DISSERTATION

Titel der Dissertation

„Phase relations and crystal structure study in various Ti, Al and Si-based systems"

Verfasser

Mag. Atta Ullah Khan

angestrebter akademischer Grad

Doktor der Naturwissenschaften (Dr. rer. nat.)

Wien, im November 2011

Dedicated to

My beloved parents who always pray for my success.

My friends who always encouraged and supported me.

Acknowledgement

All praises to Almighty Allah, most beneficent, the most merciful who bestowed me with sight to observe and utmost courage to follow the path of knowledge, discovery and to achieve the milestone of my Doctoral Thesis.

I would like to express my deepest gratitude to Prof. Peter Franz Rogl for giving me the opportunity to join his research group, for his guidance, valuable scientific discussions, and taking care of my research work throughout this project. I gratefully acknowledge Dr. X. Yan and Dr. A. Grytsiv for introducing me to all equipments, data evaluation software and valuable suggestions. Their theoretical and experimental knowledge on phase equilibria, crystal structure and expertise in sample preparations always helped me. I am also grateful to Mrs. G. Rogl for teaching me German language and especially grateful for her support in many other aspects of my life.

I would like to thank all my colleagues, especially Z. P. Malik, M. Falmbigl, W. Julia and I. Zeihringer for creating such a nice working environment. I am obliged to all my teachers and friends who encouraged me for going ahead with my Doctorate and for moral support during the course of my studies. I would like to thank my family, especially my parents for their prayers. I am also thankful to my brothers and sister, who cooperated with me during my stay in Austria.

I have to say thanks to the Higher Education Commission (HEC) of Pakistan, the Austrian Exchange Service (ÖAD) for providing me a marvelous opportunity to study in Austria. I am especially thankful to the HEC for the funding of my Doctoral studies.

Note: I didn't perform any TEM study or any physical property measurement except Vicker's hardness in the present research work.

Abstract

Ti-based alloys have a wide range of applications. They are being used not only in turbine and automotive industry but also in aerospace applications. In additional to that, they are potential candidates for hydrogen storage materials. In many cases, they are used in combination with Al. Both Ti and Al have the advantage of lightweight and are valuable constituents of high strength alloys. Al based materials are widely used in industry as well as in home appliances. Si is a very important alloying partner and Si base alloys are promising materials for high temperature applications because of their high melting points and good resistance to oxidation.

Detailed knowledge on phase equilibria and crystal structure is very important for the selection and design of high quality materials. The purpose of this research work was to provide the information on crystal structure and phase relations of Ti, Al and Si-based systems as well as to clarify the inconsistencies present in the literature.

Although the Ti-Ni-Al system has been thoroughly studied in the past, several problems prevailed and have been clarified in this work using combined XRD and neutron powder diffraction as well as EPMA analyses. Two four-phase reactions of transition type have been defined. The crystal structure of the two compounds in the Al-rich region (τ_5-TiNi$_{2-x}$Al$_5$, x = 0.48) and in the Ti-rich region [τ_6-Ti$_2$(Ti,Ni,Al)$_3$] of the Ti-Ni-Al system has been solved from X–ray powder and single crystal combined with neutron powder diffraction. In addition to that, phase relations especially those related to the Ti-rich phase [τ_6-Ti$_2$(Ti,Ni,Al)$_3$] are studied, clarified and reported in this study.

The crystal structures of phases in the Al-rich corner in the systems Mo-Cu-Al, Re-Ni-Al and Mo-Ni-Al have been determined. In the W-Ni-Al system, the presence of a new phase is reported [(WNi$_{2-x-y}$$\square_yAl_{8+x-z}$$\square_z$, (x = 0.162, y = 0.015, z = 0.010))]. ReNi$_2$Al$_{8-x}$ (x = 0.033), [MoNi$_{2-x}$Al$_{8+x}$ (x = 0.166)] and (WNi$_{2-x-y}$$\square_yAl_{8+x-z}$$\square_z$, (x = 0.162, y = 0.015, z = 0.010) have the same structure which is a superstructure of the Mo(Cu$_x$Al$_{1-x}$)$_6$Al$_4$ (x=0.416)-type. Vickers hardness (H$_v$) of Re-Ni-Al, Mo-Ni-Al, W-Ni-Al and Ni$_2$Al$_3$ has also been evaluated as part of this work.

As Pd lies in the same group with Ni, one expects some similarity in phase relations as well as in crystal structure. So the partial isothermal section at 860 °C has been studied for the Al-rich part of the Mo-Pd-Al system. Two ternary phases (named τ_1 and τ_2) were found out of which, crystal structure and micro-hardness of the τ_1-MoPd$_{2-x}$Al$_{8+x}$ phase is measured. τ_1-MoPd$_{2-x}$Al$_{8+x}$ is a

superstructure of the $Mo(Cu_xAl_{1-x})_6Al_4$ type. Inspired by these structural relations, the Al-rich part of the Zr-Cu-Al system was also studied. A single crystal study of τ_7-$Zr(Cu_{1-x}Al_x)_{12}$, x = 0.514 helped in understanding the homogeneity region of this phase, which appears as a line compound due to the Cu/Al exchange with constant Zr content. The Al-rich phase τ_9-$ZrCu_{1-x}Al_4$, x = 0.144 crystallized in a novel structure type and is a superstructure of Cu appearing from the combination of three blocks of the Cu unit cell.

Addition of boron can enhance the strength and oxidation resistance of Nb,Ta-based silicides. For this purpose, single crystal X-ray diffraction was used to find the atom site preference of B in Ta_3Si and Ta_5Si_3 phases. Similarly, B site preference for two phases [$Ta_5(SiB)_3$ and $Ta_5Si_3B_{1-x}$] was studied using Neutron Powder Diffraction (NPD). The $Ta_5Si_3B_{1-x}$-phase was proven to adopt the Ti_5Ga_4 structure type. The Ta-V-Si system was thoroughly studied and a complete isothermal section at 1500 °C and a partial isothermal section at 1200 °C have been derived. Two ternary compounds τ_1 and τ_2 were found at these two temperatures with Mn_5Si_3 type and $MgZn_2$ type, respectively. In addition to that, Si was found to stabilize a ternary $MgCu_2$-type Laves phase at this temperature, which separates from the binary Ta-V system. Constructed phase diagram agrees well with the thermodynamic modelling based on CALPHAD approach. A partial isothermal section is reported in the Ta-V-Ge system at 1500 °C. In addition to the phases also seen in the Ta-V-Si system [τ_1-Mn_5Si_3 structure type, τ_2-$MgZn_2$ structure type and $MgCu_2$ structure type], two additional ternary phases (τ_3-Nb_9Co_4Ge type structure and τ_4-unknown structure) were found. $MgZn_2$-type Laves phase was confirmed by Rietveld Refinement of X-ray Powder Diffraction and transmission electron microscopy (TEM). $V_{11}Ge_8$ ($Cr_{11}Ge_8$ type) shows a large solubility up to $(Ta_xV_{1-x})_{11}Ge_8$, x = 0.639 at 1500 °C.

The Mn-rich part of the Ti-Mn system was reinvestigated by X-ray, DTA and EDX analyses on arc melted and annealed alloys. The crystal structure of $Ti_6(Ti_{1-x}Mn_x)_6Mn_{25}$, x = 0.462 ($TiMn_{\sim 3}$) and $Ti_8(Ti_xMn_{1-x})_6Mn_{39}$, x = 0.187 ($TiMn_{\sim 4}$) was solved from X-ray single crystal diffraction data. Single phase sample of $Ti_8(Ti_xMn_{1-x})_6Mn_{39}$, x = 0.187 ($TiMn_{\sim 4}$) was prepared for the measurement of different physical properties.

Kurzfassung

Titanlegierungen haben ein breites Sortiment von Anwendungen. Sie werden nicht nur in der Turbinen- und Automobilindustrie verwendet sondern auch für Anwendungen in der Raumfahrt. Außerdem sind sie potentielle Kandidaten für Wasserstoffspeicherung. In vielen Fällen werden sie zusammen mit Aluminium verwendet. Beide Metalle, Titan und Aluminium, haben den Vorteil, dass sie leicht sind und daher wertvolle Bestandteile hochwarmfester Legierungen darstellen. Materialien, basierend auf Aluminium, werden in Industrie sowie für Geräte im Haushalt verwendet. Silicium ist ein sehr wichtiger Legierungspartner und Legierungen mit Silicium sind vielversprechende Materialien für Einsätze bei hohen Temperaturen weil sie einen hohen Schmelzpunkt in Kombination mit hoher Oxidationsbeständigkeit aufweisen.

Für die Auswahl und das Design von Materialien hoher Qualität ist die genaue Kenntnis von Phasengleichgewichten und Kristallstrukturen wichtig. Der Zweck dieser wissenschaftlichen Arbeit war daher, Information über Kristallstruktur und Phasenbeziehungen in den Systemen mit Ti, Al und Si bereit zu stellen aber auch Inkonsistenzen in der Literatur zu klären.

Obwohl das Ti-Ni-Al-system in der Vergangenheit gründlich untersucht wurde, bestanden etliche Probleme, die in dieser Arbeit mit Hilfe von XRD, kombiniert mit Neutronenpulverstreuung aber auch mittels EPMA-analysen geklärt werden konnten. Weiters wurden zwei Vierphasenreaktionen vom Übergangstyp ermittelt. Die Kristallstruktur von den zwei Verbindungen in der Al-reichen Zone (τ_5-TiNi$_{2-x}$Al$_5$, x = 0.48) und der Ti-reichen Zone [τ_6-Ti$_2$(Ti,Ni,Al)$_3$] des Ti-Ni-Al-systems wurde mittels Röntgenpulverdiffraktion kombiniert mit Einkristalluntersuchungen und Neutronenpulverdiffraktion gelöst. Zusätzlich wurden spezielle Phasenverbindungen die der Ti-reichen Phase [τ_6-Ti$_2$(Ti,Ni,Al)$_3$] artverwandt sind geklärt und in dieser Studie darüber berichtet.

Die Kristallstrukturen von Phasen im Al-reichen Bereich der Systeme Mo-Cu-Al, Re-Ni-Al und Mo-Ni-Al wurden bestimmt. Im W-Ni-Al-system, wurde eine neue Phase dokumentiert [(WNi$_{2-x-y}$□$_y$Al$_{8+x-z}$□$_z$, (x = 0.162, y = 0.015, z = 0.010)]. ReNi$_2$Al$_{8-x}$ (x = 0.033), [MoNi$_{2-x}$Al$_{8+x}$ (x = 0.166)] und (WNi$_{2-x-y}$□$_y$Al$_{8+x-z}$□$_z$, (x = 0.162, y = 0.015, z = 0.010) haben die gleiche Struktur die sich als eine Überstruktur vom Mo(Cu$_x$Al$_{1-x}$)$_6$Al$_4$(x=0.416)-typ ableitet. DieVickers Härte (H$_v$) von Re-Ni-Al, Mo-Ni-Al, W-Ni-Al und Ni$_2$Al$_3$ wurde ebenfalls in dieser Arbeit evaluiert.

Da Palladium in derselben Gruppe wie Nickel vorkommt, erwartet man sich eine Ähnlichkeit bezüglich der Phasenbeziehungen und der Kristallstrukturen. Aus diesem Grund wurde ein Teil des isothermen Bereichs des Al-reichen Bereichs des Mo-Pd-Al-systems bei 860° C studiert. Zwei ternäre Phasen (genannt τ_1 und τ_2) wurden entdeckt und über die Kristallstruktur und Mikrohärte der τ_1-MoPd$_{2-x}$Al$_{8+x}$ Phase wurde in dieser Arbeit berichtet. τ_1-MoPd$_{2-x}$Al$_{8+x}$ ist eine Überstruktur des Mo(Cu$_x$Al$_{1-x}$)$_6$Al$_4$ Typs. Inspiriert von diesen strukturellen Zusammenhängen, wurde auch der Al-reiche Teil des Zr-Cu-Al-systems erforscht. Eine Einkristalluntersuchung von τ_7-Zr(Cu$_{1-x}$Al$_x$)$_{12}$, x = 0.514 trug dazu bei, den Homogenitätsbereich dieser Phase zu verstehen, die wegen des Cu/Al-Austausches mit gleichbleibendem Zr-gehalt als „line-compound" auftritt. Die Al-reiche Phase τ_9-ZrCu$_{1-x}$Al$_4$, x = 0.144 kristallisiert in einem neuen Strukturtyp und ist eine Überstruktur des fcc-Cu Typs und besteht aus der Kombination von drei Blöcken der Kupfereinheitszelle.

Das Hinzufügen von Bor kann in Siliciden des Nb und Ta die Festigkeit und den Widerstand gegen Oxidation erhöhen. Aus diesem Grund wurde eine Röntgenstrukturanalyse am Einkristall vorgenommen um heraus zu finden, welchen Gitterplatz die Bor-atome in den Ta$_3$Si- und Ta$_5$Si$_3$-Phasen bevorzugen. Weiters wurde die Gitterplatzpräferenz für zwei Phasen [Ta$_5$(SiB)$_3$ und Ta$_5$Si$_3$B$_{1-x}$] mit Hilfe von Neutronenpulverstreuung (NPD) studiert. Für die Ta$_5$Si$_3$B$_{1-x}$ Phase wurde der Ti$_5$Ga$_4$ Strukturtyp ermittelt. Das Ta-V-Si-system wurde vollständig untersucht und ein kompletter isothermer Schnitt bei 1500° C und ein Teilschnitt bei 1200° C konnten bestimmt werden. Zwei ternäre Verbindungen τ_1 und τ_2 wurden bei diesen beiden Temperaturen gefunden die dem Mn$_5$Si$_3$ Typ und MgZn$_2$ Type entsprechen. Zusätzlich konnte gezeigt werden, dass Si eine ternäre MgCu$_2$-type Lavesphase bei dieser Temperatur stabilisiert die vom binären Ta-V-system durch Konnoden getrennt ist. Das konstruierte Phasendiagramm stimmt gut mit dem nach der CALPHAD-Methode berechneten thermodynamischen Modell überein. Ein isothermer Teilschnitt wurde im Ta-V-Ge-system bei 1500° C erstellt. Zusätzlich zu den Phasen, die auch im Ta-V-Ge-system [Strukturtyp τ_1-Mn$_5$Si$_3$, Strukturtyp τ_2-MgZn$_2$ und Strukturtyp MgCu$_2$] auftreten, wurden zwei ternäre Phasen (Strukturtyp τ_3-Nb$_9$Co$_4$Ge und eine unbekannte Struktur τ_4) gefunden. Die Struktur der Lavesphase vom MgZn$_2$-typ wurde mittels Rietveld Verfeinerung der Röntgenpulveraufnahme und unter Verwendung eines Durchstrahlelektronenmikroskops (TEM) bestätigt. V$_{11}$Ge$_8$ (Cr$_{11}$Ge$_8$-typ) zeigt bei 1500 °C eine große Löslichkeit bis zu (Ta$_x$V$_{1-x}$)$_{11}$Ge$_8$, x = 0.639.

Der Mn-reiche Teil des Ti-Mn-systems wurde unter Einsatz von Röntgenstruktur- DTA- und EDX-analysen an Hand von Proben die im Lichtbogen geschmolzen und dann geglüht wurden neu untersucht. Die Kristallstrukturen von $Ti_6(Ti_{1-x}Mn_x)_6Mn_{25}$, x = 0.462 ($TiMn_{\sim3}$) und $Ti_8(Ti_xMn_{1-x})_6Mn_{39}$, x = 0.187 ($TiMn_{\sim4}$) konnten mittels Röntgendiffraktion am Einkristall aufgeklärt werden. Eine einphasige Probe von $Ti_8(Ti_xMn_{1-x})_6Mn_{39}$, x = 0.187 ($TiMn_{\sim4}$) wurde für die Messung verschiedener physikalischer Eigenschaften hergestellt.

Table of Content

1. Introduction

Successful alloy design of materials is based on a profound knowledge of phase equilibria and crystal structures. Due to increased complexity in materials processing, detailed knowledge of phase equilibria is vital for materials engineers. The properties of materials not only depend on their crystallographic structures but also on their microstructures. The number and ratio of different phases form the microstructure. The properties of materials can be controlled and modified according to the needs of a given application by controlling the structure and composition. Many properties of the material depend strongly on the structure, even if the composition doesn't not change. The so-called materials science and engineering (MSE) tetrahedron [1] that represents this approach is shown in Fig. 1. In material science, the focus is on understanding the relationships between the structure, composition, synthesis and processing, and properties of materials.
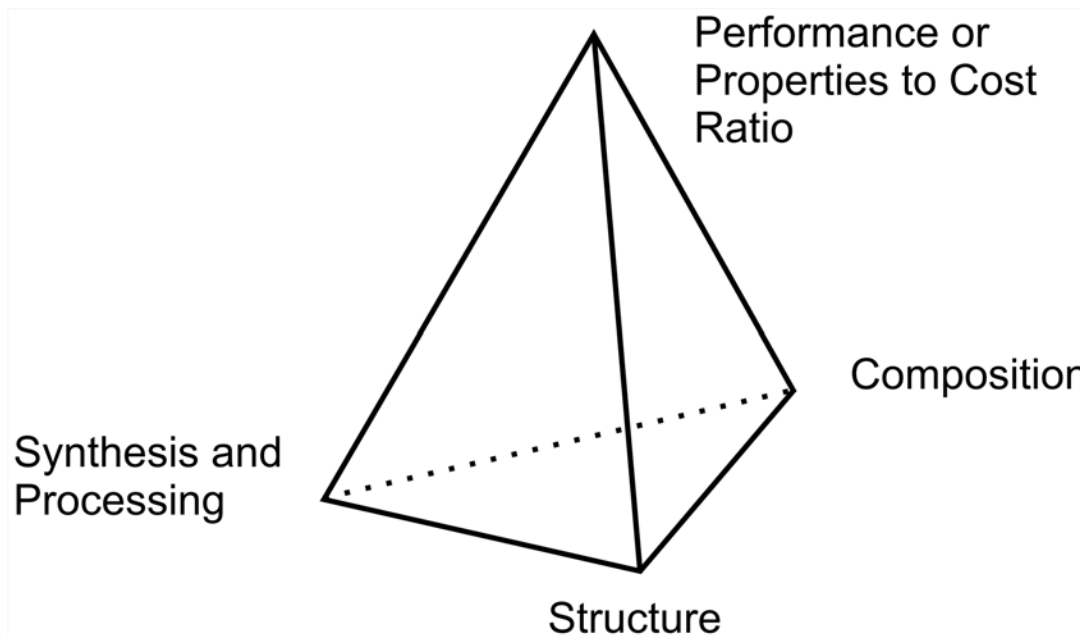
Fig. 1. The materials science and engineering (MSE) tetrahedron.

Titanium is a widely used metal due to lightweight and attractive properties. It is an essential constituent of several very important materials. It is being used in Engine design. Several parts of famous Trent Aero-engines introduced by Rolls-Royce are made of Titanium (Fig. 2).
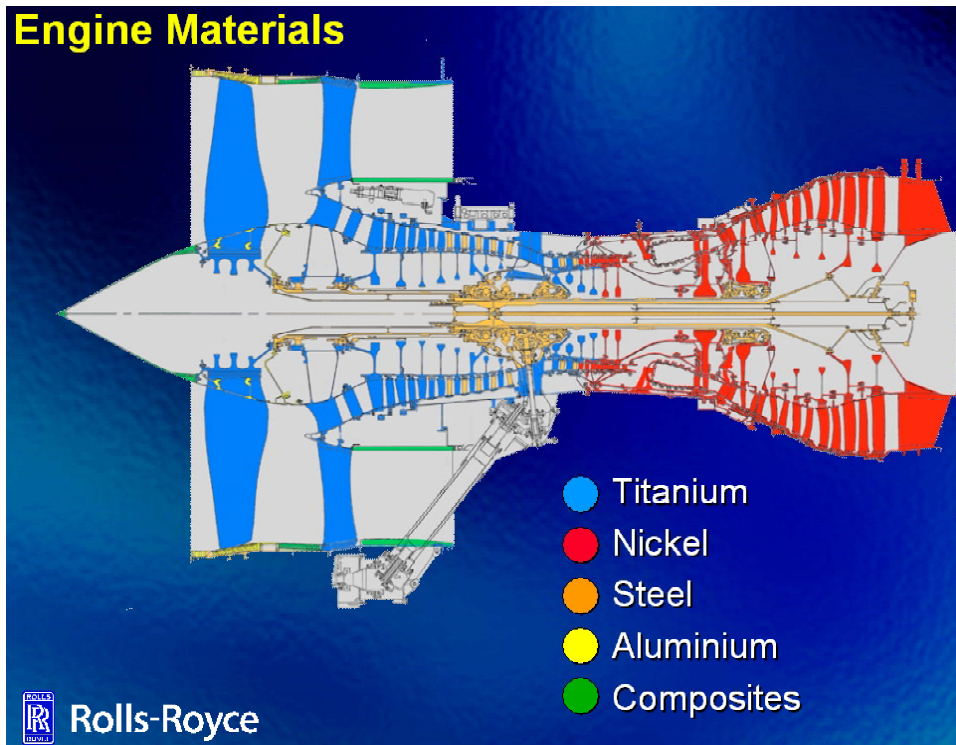
Fig. 2. Ratio of different elements or their alloys used in Trent Aero-engine [2].

Titanium exhibits a high corrosion resistance. That's why; it is being used in the petrochemical industry where high corrosion resistance is the basic requirement. In addition to that, high heat tolerance makes it suitable for use in heat exchangers and reactors (Fig. 3).

Fig. 3. Titanium is used in petroleum industry [3].

Titanium exhibits higher strength as compared to Al, steels and super alloys at room temperatures as well as at elevated temperatures. A comparison of strength versus temperature is shown in Fig. 4 [4]. Only at temperatures below 300 °C, carbon fiber reinforced plastics exhibit a

higher specific strength than titanium alloys. However, Ti-based alloys could not be used for high temperatures due to poor oxidation resistance. TiAl-based alloys have helped in this regard and compete the high temperature steels and Ni-based superalloys at high temperatures [4].
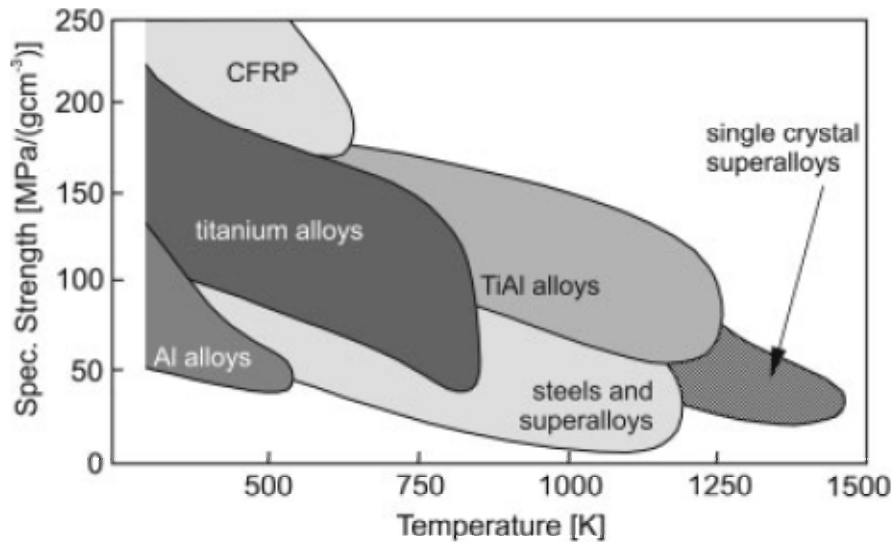
Fig. 4. Specific strength versus temperature. Comparison of different materials [4].

Titanium has a good biological compatibility not only with human bones but also with tissues. That's why; rods and wires made of titanium are ideal materials for medical applications [3].

Aluminum is very lightweight and ductile and is the essential part of many materials. Materials design of Ti$_3$Al- and TiAl-based high strength alloys involving third metal components essentially depends on a detailed knowledge of the temperature and solute dependent solubility limits as well as on the chemical and crystallographic nature of precipitates. Low-temperature brittleness has so far restricted utilization of titanium aluminides and requests further improvement of mechanical properties. In this respect group-VIII elements as alloy constituents are of interest and among them particularly nickel because it can enhance oxidation resistance and tensile strength of Ti-Al alloys [5].

Due to high strength [6, 7], good corrosion and oxidation resistance and good resistance to rupture and creep at high temperature, lightweight Ti-Ni-Al alloys are important for application in gas or steam turbine engines [8].

Molybdenum has become an important constituent for Ni-base superalloys because it can improve the creep properties [9]. Besides this, binary Al(Mo)-based alloys with less than 30%

3

Mo show melting temperatures higher than 1500°C but still are light in weight [10]. Low-temperature brittleness, however, has so far restricted utilization of molybdenum aluminides and requests further improvement of mechanical properties.

Metal silicide thin films are being used in all microelectronics devices. For metallization of integrated circuit (IC) devices, transition metal silicides, including refractory metal silicides, are used [11]. They are also used in electrical heating elements, photovoltaic and thermoelectric devices [12]. With good properties at high temperatures, boron-silicides of refractory transition metals (TM) are promising materials for high temperature applications [13]. However, no data is available on site preference of B in the phases present in Ta- and Nb-rich parts of Ta-Si-B as well as Nb-Si-B system.

Tantalum and vanadium are important constituents in martensitic steels for fusion reactors, which besides good thermal stability show low induced activity under neutron irradiation (low activation steels) [14,15]. With small amounts of Si in steels also the ternary system Ta-V-Si deserves attention, particularly as silicon is believed to be responsible for the stabilization of numerous complex phases in transition metal systems [16], including Laves phases. Many controversies exist related to Ta-V-Si system. Ge lies in the same group with Si and one can expect similar phase relations, crystal structure and properties in Ta-V-Ge system. However, no one has reported any phase relation related to Ta-V-Ge system.

1.1. Task of the present work

The thesis covers the vast field of phase equilibria in selected systems and crystal structure of intermediate compounds. It includes many ternaries as well as binary systems. It also includes selected properties in some cases. The work was accomplished as follows

    i)   Determination of exact temperatures of three different four-phase reactions in the Ti-Ni-Al system in the temperature range of 800°C and 1050°C.

    ii)   As hitherto neither phase equilibria data involving the new phase nor crystal structure data have been published, the investigation was designed to provide this information including a reinvestigation of the structure of $(Ti,Al)_2Ni$. X-ray single crystal (XSC) data were used to solve the structure of this phase along with Neutron Powder

Diffraction (NPD) and to derive high precision atom positions and particularly to check on the electron density at the centers of vacant metal octahedral.

iii) Determination of the crystal structure of another phase, already reported to be present in the Al-rich corner of the Ti-Ni-Al system. Single crystal was used in addition to NPD to solve the structure and was confirmed by Transmission Electron Microscope (TEM). After the confirmation of structure and the vacancy in this structure, similar structures in Hf-Ni-Al and Zr-Ni-Al were also reinvestigated.

iv) Solving the crystal structure of phases reported in Al-rich corners of Mo-Cu-Al, Mo-Ni-Al and Re-Ni-Al systems and reinvestigating W-Ni-Al in Al-rich corner for the presence of isostructural phase. In this regard, Single crystal study was employed to solve the structure of these phases. Vicker's hardness was also measured for these phases.

v) As Pd lies in the same group with Ni, Mo-Pd-Al system in Al-rich corner should be evaluated. Phase relations and crystal structure of one phase along with Vicker's hardness is reported. To solve the structure of phases and atom site preference in Zr-Cu-Al system. X-ray single crystal diffraction was used for this purpose.

vi) Some phases in Nb-rich part of Nb-Si-B are reported to have some attractive properties. However, no information is available on the site preference of B in this system. Similarly, no one studied the Ta-Si-B system. So my task is to report boron site preference in phases present in Nb- and Ta-rich corner with the help of X-ray single crystal diffraction (XSC) as well as neutron powder diffraction (NPD).

vii) To study the phase relations in crystal structure in Ta-V-Si system. There were many controversies present in literature regarding this system. There was a need to thoroughly study the phase equilibria and crystal structure of the phases in this system.

viii) To study the phase relations in Ta-V-Ge system. And if found some ternary phases in the Ta-V-Ge system, then to find the structure solution of these phases as well as atom site preference in all these phases. Detailed study on the presence and atom site preference of hexagonal Laves phase.

ix)   To study the phase equilibria including the homogeneity regions in the Mn-rich part of the Ti-Mn binary phase diagram. And to solve the crystal structure and to determine the atom site preference by using XSC.

For all these investigations, arc melting and in some cases, metallurgical techniques were employed for sample preparation. Light optical microscope (LOM), Scanning electron microscope (SEM) and electron probe microanalyzer (EPMA) were used for characterization of materials. X-ray Powder diffraction (XPD), neutron powder diffraction (NPD) and X-ray single crystal diffraction (XSC) were used to solve the crystal structure of phases (for details, see chapter 2).

References

[1]   D.R. Askeland and P.P. Fulay, "Essentials of Materials Science and Engineering". 2nd Edition, CENGAGE Learning, USA, (2010).

[2]   http://www.msm.cam.ac.uk/phase-trans/mphil/Trent1/index.htm.

[3]   http://www.supraalloys.com/prodapp.php.

[4]   C. Leyens and M. Peters, "Titanium and Titanium Alloys", WILLEY-VCH, (2003).

[5]   T. Tetsui, T. Miura, Mitsubishi Heavy Industries Technical Review 39(1), (2002), p. 268-271.

[6]   J.Q. Guo and K. Ohtera, Acta Mater. 46(11) (1998), p. 3829-3838.

[7]   B.N. Nobrega, T. Eberle and W. Ristow Jr., Materials Science Forum 591-593 (2008), p. 252-257.

[8]   X.H. Du, J. C. Huang and B. L. Wu, Advanced Engineering Materials 9(8) (2007), p. 684-688.

[9]   J. Zhang, J. Li, T. Jin, X. Sun, Z. Hu, Materials Science and Engineering A 527, (2010), p. 3051-3056.

[10]   T.B. Massalski, 2nd Edition, ASM International, Materials Park, Ohio, 1, (1990), p. 174-175.

[11]   L.J. Chen, Journal of the Minerals, Metals and Materials Society, 57(9), (2005), p. 24-31.

[12] A.L. Schmitt, J.M. Higgins, J.R. Szezech and S. Jin, J. Mater. Chem., **20**, (2010), p. 223-235.

[13] A.J. Thom, E. Summers and M. Akinc, Intermetallics **10** (2002), p. 555-570.

[14] P. Fernandez, A.M. Lancha, J. Lapena and M. Hernandez-Mayoral, Fusion Engineering and Design, **58-59** (2001) p. 787-792.

[15] A.-A.F. Tavassoli, Journal of Nuclear Materials **302** (2002) p. 73-88.

[16] M.V. Nevitt, in P.A. Beck (ed.), Electronic Structure and Alloy Chemistry of the Transition Elements, Willey-Interscience, New York, (1963).

2. Experimental details.

2.1. General procedure for sample preparation and characterization.

Alloy samples were prepared either by arc melting the ingots of elements (purity better than 99.9 %) under argon atmosphere or by mixing the powders of different elements, compacting and annealing at different temperatures, depending on their melting points and interaction with other elements. Then the reguli were wrapped in Mo-foil to protect them from attack by the hot quartz walls, sealed in evacuated quartz tubes and annealed at different temperatures. Temperature at the position of samples was controlled by a high quality standard thermocouple: the melting points of metal standards (5N-Ag, 5N-Cu) in the furnace used for all our annealing procedures were recorded within ±3°C of the temperature listed in the International Temperature Scale ITS-90. All samples were quenched in cold water after annealing except those annealed in high vacuum furnace where the samples were radiations cooled. As cast as well as annealed samples were examined by light optical microscopy (LOM) and scanning electron microscope (SEM). Compositions were determined by Electron Probe Micro-Analyzer (EPMA) based on Energy dispersive X-ray spectroscopy (EDX) or wavelength dispersive X-ray spectroscopy (WDX) systems. Thermal analyses were performed in a calibrated Differential Scanning Calorimeter (DSC) in Al_2O_3 crucibles under a stream of 6N argon. X-ray single crystal diffraction (XSC) was used to solve the structure of unknown phase as well as to get reliable crystallographic data for some phases with known structures.

2.2. Instrumental details:

2.2.1. Arc melting furnace.

Most of the samples were prepared by arc melting furnace. Tungsten electrode and Copper hearth is used in this furnace (Fig. 1). Continuous water flow was supplied to control the temperature of the Tungsten electrode and Copper hearth. Furnace was evacuated with the help of a vacuum pump and then filled with Argon gas and this procedure was repeated 4-5 times

prior to melting. Ti-getter was always melted first to absorb the rest of the gases and the colour of the Ti-getter was always inspected. Change in colour of the Ti-getter was always considered as an indication of the high amount of air inside the furnace. Samples were prepared only if no change in colour of the Ti-getter was observed. Arc was moved slowly towards sample and kept on sample until it is completely melted. Arc was taken back to the Ti-getter and kept there until the sample was cooled and power was turned off.

Fig. 1. Arc melting furnace.

2.2.2. X-ray diffraction.

X-ray diffraction has its beginnings in von Laue's discovery that crystals diffract X-rays. And the diffraction pattern reveals the structure of the crystal. X-ray diffraction techniques are widely used for the identification of the crystalline materials. X-ray tube is used for the production of X-rays (Fig. 2). X-ray diffraction is based on constructive interference of monochromatic X-ray beam and crystalline sample.
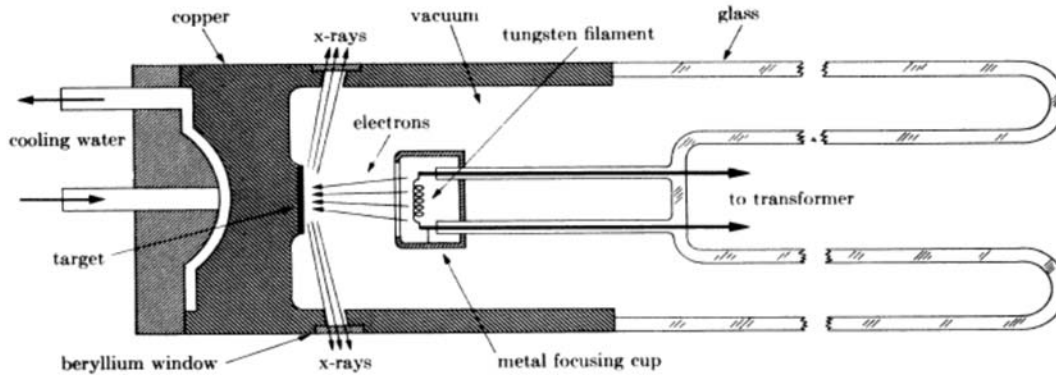
Fig. 2. Cross-section of sealed-off filament X-ray tube (schematic).

Diffraction angle depends on the d spacing between the planes of atoms in the crystal. Bragg's equation demonstrates this relationship,

$$2d\sin\theta = n\lambda \qquad\qquad (2.1)$$

where θ is the angle between the incident beam and the scattering plane and λ is the wavelength of the X-rays. X-ray powder diffraction can be used not only on a single-phase material but also on the multiphase samples. Each phase gives its own diffraction pattern and can be identified easily. X-ray powder diffraction can also be used for the calculations of crystallite size, quantitative ratio of phases, strain and for the dislocation densities etc. However, for more accurate determination of Laue symmetry, space group, site preference, vacancies and bond lengths, X-ray single crystal diffraction is preferred. It is even better to use X-ray powder diffraction (XPD) in combination with X-ray single crystal diffraction (XSC) and Neutron powder diffraction (NPD) especially when light atoms or neighbouring atoms in periodic table are present in the structure.

2.2.2.1. X-ray Powder Diffractometer and Image Plate (IP).

A Guinier Huber Image Plate (IP) camera G670 was used for the X-ray powder diffraction measurements. Both Cu $K_{\alpha 1}$ radiation ($\lambda = 0.154056$ nm) and Fe $K_{\alpha 1}$ radiation ($\lambda = 0.193631$ nm) were used depending on the elements present in the sample. G670 is constructed in such a way that it is completely shielded from the ambient light. The housing of the G670 camera contains image memory foil and laser recording unit with photomultiplier (Fig. 3). In addition to that, it has pre-amplifier as well as the halogen deleting lamp. The diffracted X-rays from the

10

sample enter the camera through a side-mounted incidence window [1]. The sample is continuously moving back and forth and X-rays are continuously diffracted and recorded by the image memory foil. This set up enables G670 to provide digital powder diffractograms in a very short time (~ 1 minute after the completion of measurement). This diffractograms is then used for the Rietveld refinement using different software. In the present research work, FULLPROF program [2] was used for the Rietveld refinement of the X-ray as well as neutron powder diffraction data. After the collection of the diffractogram, image plate is erased automatically (erasing time 10s) and is ready for reuse.

For Cu $K_{\alpha1}$ radiation ($\lambda = 0.154056$ nm), a potential of 40kV was applied with 30mA current and for Fe $K_{\alpha1}$ radiation ($\lambda = 0.193631$ nm), potential of 40 kV was employed using a current of 20mA in a 2-theta range of $8° \leq 2\theta \leq 100°$ with a step size of 0.005.
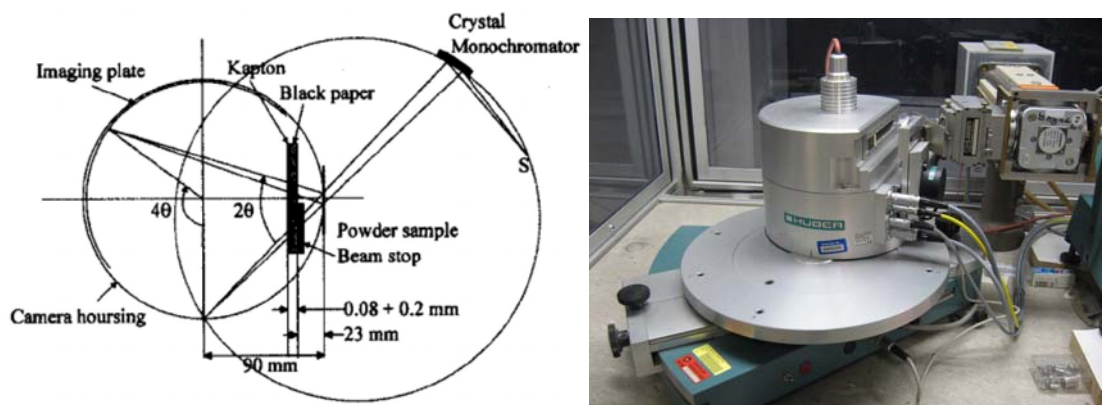
Fig. 3. Schematic diagram of Guinier Huber camera (left). An overview of Guinier Huber G670 IP (right) used in present research work.

2.2.2.2. AXS GADDS.

In the present research work, we used Bruker AXS GADDS (General Area Detector Diffraction system) system (Fig. 4). It consists of an X-ray generator to produce X-rays. X-ray optics are used to condition the X-ray beam. A goniometer and sample stage serves to establish the relationship between primary beam, sample and the detector. HI-STAR Area Detector System intercepts, records and saves the scattering X-rays from the sample. Sample alignment and monitor help the user to position the sample into the instrument center and to monitor the sample state and position. It displays the diffraction pattern in 2D image frame [3]. The whole system is

controlled by a computer that uses GADDS software. A schematic diagram is shown in Fig. 5. This detector system is almost 10,000 times faster than a point detector. Although GADDS has many different functions like, phase identification and quantification, measurement of lattice parameters and refinement, texture analysis, stress measurement and percentage of crystallinity, we have used it only for the purpose of inspection of single crystal quality to be sure that this is suitable for measurement on four-cycle diffractometer.
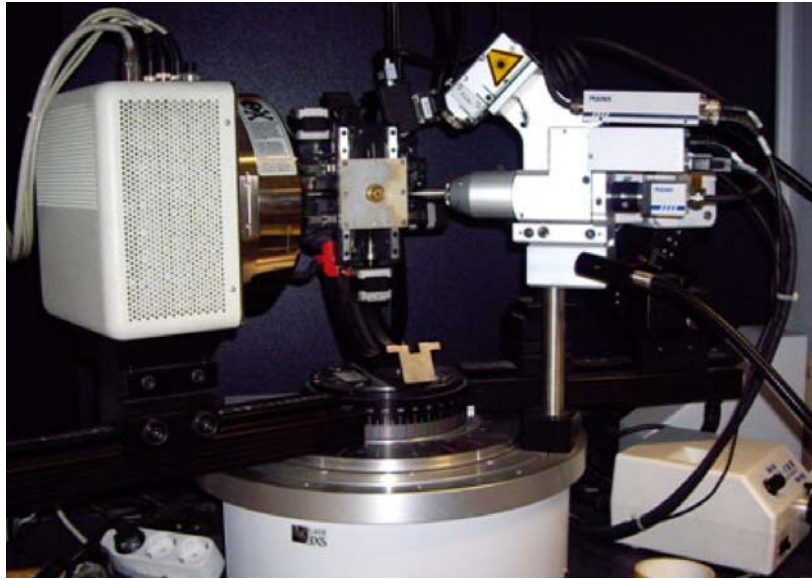
Fig. 4. An overview of GADDS used during present research work.
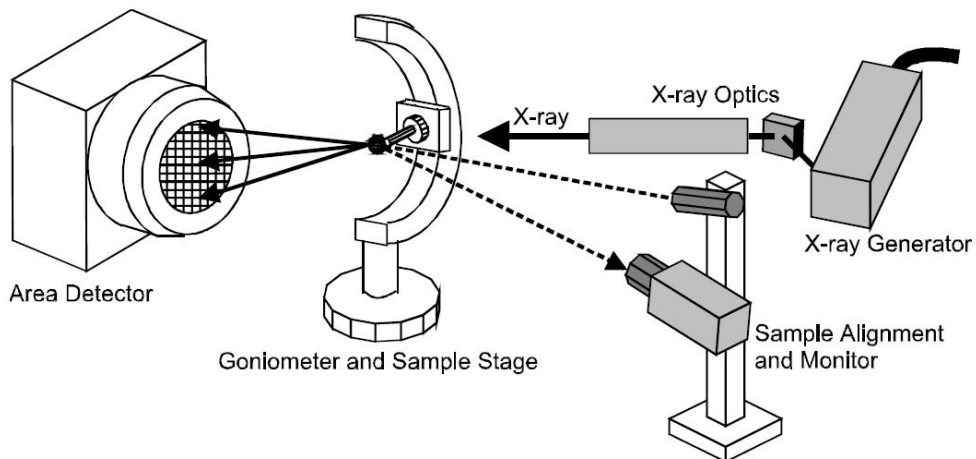
Fig. 5. Schematic diagram of AXS GADDS [3].

2.2.2.3. Nonius Kappa diffractometer with area detector CCD.

The KappaCCD consists of an X-ray source, three axes goniometer (Omega, Kappa and Phi) to position the crystal. In addition to that, a Theta axis and DX is also the part of the instrument to position the detector. The detector measures the X-rays, which are reflected from the sample. X-rays are generated by a fixed tube, which is part of the goniometer and a HV generator. A monochromator and collimator is also the part of this instrument. A microscope displays the crystal on the PC monitor. A phosphor converts the X-rays to light in the two dimensional detector. CCD measures the light signal. A Server computer controls all the system. This setting is shown in Fig. 6. The detector and X-ray tube contain windows of beryllium (for further details see [4]).
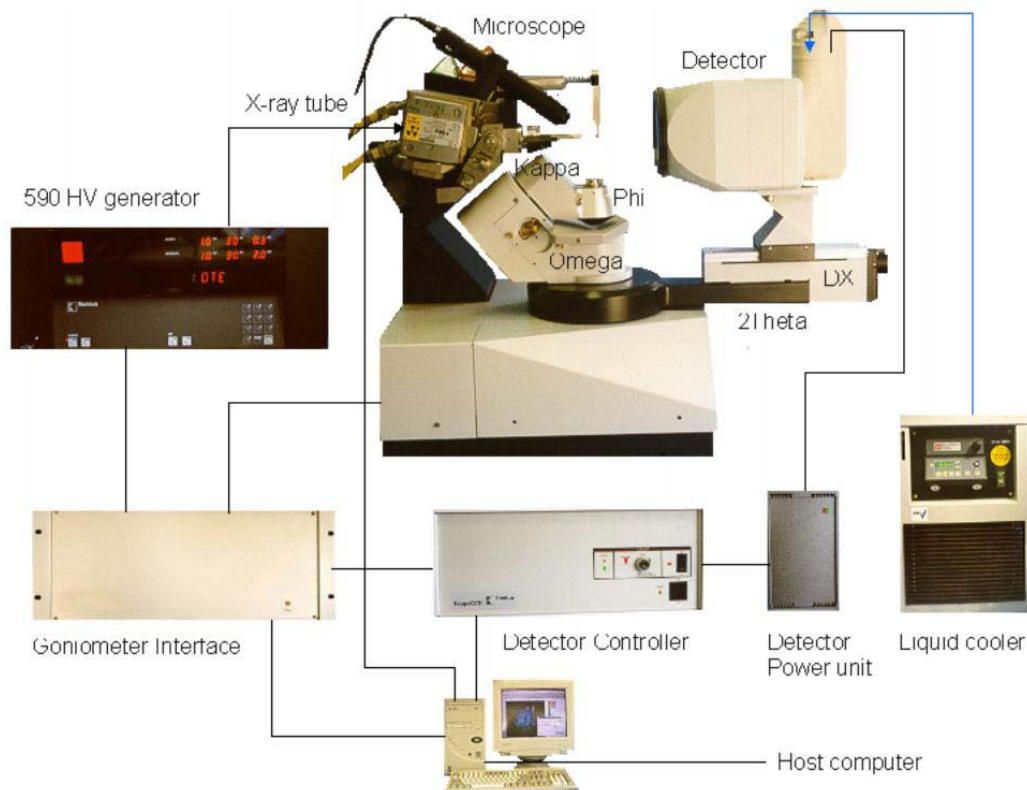
Fig. 6 illustrates the different parts and arrangement of Nonius Kappa diffractormeter [4].

Orientation matrix and unit cell parameters of single crystal in the present research work were derived by using the program DENZO [5].

2.2.3. Neutron Powder diffraction (NPD).

Neutron Powder diffraction pattern, for the first time, were observed in 1945 at the Oak Ridge. Neutrons are the basic building blocks of nucleus. Thermal neutrons ($\sim$ 1-2 $\times 10^{-10}$ m) diffract by the ordered arrangements of atoms in the crystal in a similar way to the X-rays. However, nuclear scattering lengths does not depend on atomic number and light elements as well as adjacent elements in the periodic table are easily distinguished. Penetration of neutrons is much more than electrons.
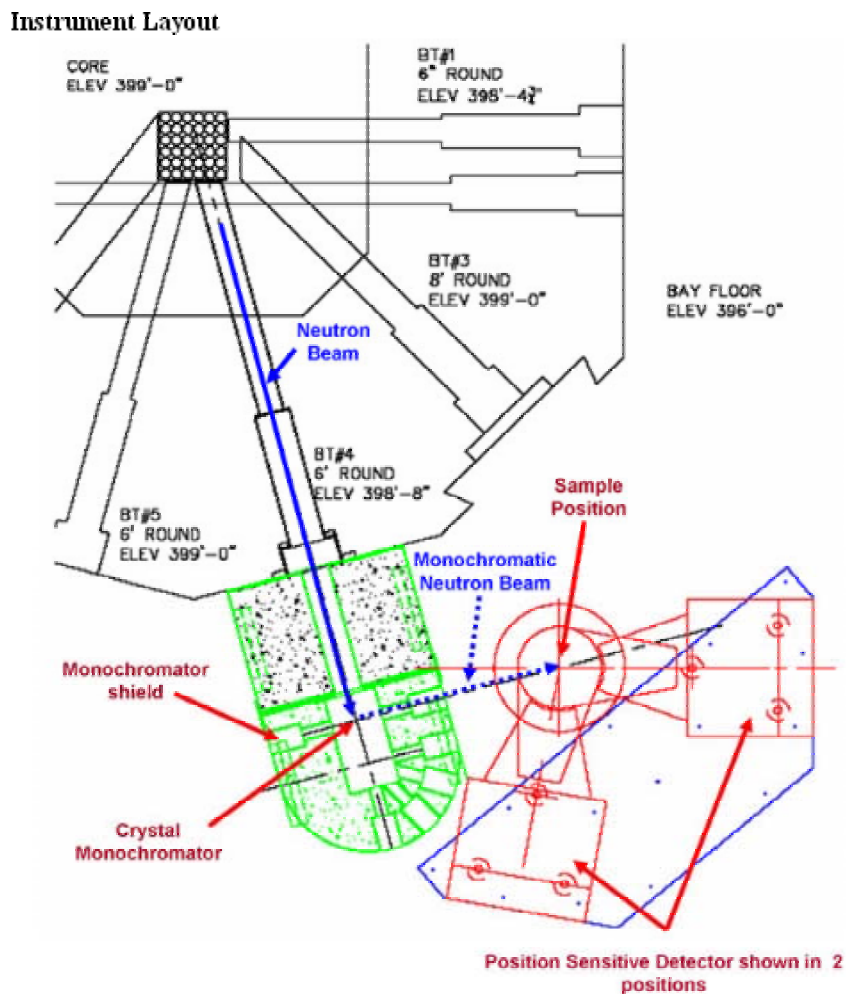
Fig. 8. Layout of instrument used for NPD [6].

A schematic view is shown in Fig. 8. Although similar to X-ray diffraction, neutron diffraction has many advantages. In case of neutrons, the strength of scattering is different for different isotopes. So isotopes substitution can be used to find the reliable site preference. Due to high penetrating powers, it is possible to put the samples even in cryo-refrigerators or furnaces and measure. Due to magnetic moment of neutrons, their scattering is sensitive to the magnetic moment of atoms making them ideal means to study magnetic moments [6].

2.2.4. Electron Probe Micro Analyzer (EPMA).

Small pieces from the samples were embedded in electroconductive resin with the help of a SIMPLIMET 3 hot molding press (Buehler, Lake Bluff, Illinois USA). Instrument was operated under a pressure of 2.9×10^7 Pa at 150°C for a duration of 1.5 min. The embedded samples were grinded using sand papers made of SiC of different grit size. The samples were polished using alumina powder with grain size 1.0, 0.3 and 0.05 micron on a fine polishing cloth. Surface of the polished samples was cleaned by using acetone in an instrument which creates supersonic waves and finally with alcohol. Samples were inspected using light optical microscope (LOM) prior to investigation in scanning electron microscopy (SEM), energy dispersive X-ray (EDX) analysis or wavelength dispersive X-ray analysis.

2.2.4.1. Working Principle

An electron probe micro-analyzer is an instrument, which is used for the non-destructive chemical analysis. It is equipped with SEM together with different detectors. Fig. 9 shows the schematic diagram as well as the overview of actual instrument used in the present research work. The basic principle of the instrument is that if a solid material is bombarded by accelerated and focused electrons, the incident beam can liberate both matter and energy from the sample. Such kind of interactions normally liberate heat but also derivative electrons and X-rays. The characteristic X-rays help to find out the type of elements and their ratio in the sample.

Fig. 9. Schematic cut-away diagram of a microprobe. Image courtesy of the University of Minnesota Electron Microprobe Lab (left side of the figure) [7] and overview of actual EPMA used in present research work.

EPMA consists of following main parts (i) a W-filament cathode also called "gun", (ii) Electromagnetic lenses located in the column to focus the electron beam; these optics operates similar to light optics, (iii) a sample chamber with moveable sample stage which is kept under vacuum, (iv) different detectors arranged around the sample chamber to collect X-rays and emitted electrons from the sample [7].

In the present research work, compositions were determined either by an Electron Probe Micro-Analyzer (EPMA) on a Carl Zeiss EVO 40 equipped with a Pentafet Link energy dispersive X-ray (EDX) system operated at 20 kV or by using a JEOL JSM 6460 scanning electron microscope equipped with both energy- and wavelength dispersive X-ray analytical systems INCA Energy and INCA Wave by Oxford Instruments. Energy dispersive X-ray (EDX) system was used for the measurement of all alloys except Ta-V-Si alloys where reliable evaluation of Si content is hindered by a strong overlap of the Si K_α peak at 1.740 keV and the Ta M_α peak at 1.710 keV in energy dispersive X-ray (EDX) spectra. Thus wavelength dispersive X-ray analysis (WDX) with well-separated wavelengths needs to be used for accurate composition measurements. Si K_α, V K_α and Ta L_α were used for quantification at an electron beam current of about 15 nA. The full width at half maximum of the Si K_α peak measured experimentally in WDX is only about 2 eV, hence no overlap with M_α Ta peak can occur.

Pure elements were used as standards to carry out the deconvolution of overlapping peaks and background subtraction. Finally the X-ray intensities were corrected for ZAF effects using the INCA-Energy 300 software package [8].

2.3. Details of programs used for data analysis

2.3.1 Rietveld Refinement of XPD and NPD.

Powder diffraction pattern obtained from Guinier Huber camera can be used directly for Rietveld refinement. Rietveld refinement can reveal several information of the compound under consideration, i.e., crystal structure, positional parameters, site preference of atoms, temperature factors and occupancies etc [9, 10]. There are many different software available for the Rietveld refinement including commercial and freeware. In the present study, Fullprof program [2] was used for the Rietveld refinement of X-ray powder diffraction pattern. In the Rietveld refinement, the observed pattern is fitted with the calculated pattern, which is based on the calculations of all the parameters related to crystal structure, type and arrangement of atoms, positional parameters, instrumental parameters etc. For the Rietveld refinement, we always a starting model which should be closer to the actual solution and that's why, it cannot be used for solving the unknown structures. Number of parameters are refined, mostly starting with background and scale factor and then proceeding with the lattice parameters, peak shapes, overall and individual temperature factors, positional parameters of atoms and occupancies etc to get best possible fit. To judge the difference between observed and calculated patterns, various R-values are used which are defined below,

$$R_F = \frac{\sum \left| (I_K(obs))^{1/2} - (I_K(calc))^{1/2} \right|}{\sum (I_K(obs))^{1/2}} \qquad \text{R-structure factor} \qquad 2.2$$

$$R_B = \frac{\sum |I_K(obs) - I_K(calc)|}{\sum I_K(obs)} \qquad \text{R-Bragg factor} \qquad 2.3$$

$$R_P = \frac{\sum |y_i(obs) - y_i(calc)|}{\sum y_i(obs)} \qquad \text{R-Pattern} \qquad 2.4$$

$$R_{wP} = \left\{ \frac{\sum w_i (y_i(obs) - y_i(calc))^2}{\sum w_i (yi(obs))^2} \right\}^{1/2} \qquad \text{R-weighted pattern} \qquad 2.5$$

Rietveld refinement of Neutron powder diffraction (NPD) and X-ray powder diffraction are slightly different because in X-rays, we should keep in mind, number of electrons present in the

atom when changing occupancy or assigning different sites to atoms while in NPD, we should focus on the scattering lengths of atoms. Best solution is obtained when both techniques are used together. Fullprof has the option to refine multiple patterns together.

2.3.2. Structure Solutions for X-ray single crystal diffraction (XSC)

In almost all the cases in the present research work, we used single crystals with a diameter around 40μm. Due to this reason, no absorption corrections were made. After the inspection of crystals on AXS GADDS and obtaining the lattice parameters, intensity data was collected on Nonius Kappa CCD diffractometer. Afterwards, this data was used for structural solution by using the program SHELXS97 and refinement by using the program SHELXL-97-2 [11]. Both these programs are integrated in Oscail interface [12]. ABSEN which is also integrated in Oscail program helped to determine the possible space group based on the extinction rules. Then the Direct methods were used to find the first solution with the help of SHELXS97 program. Then the least square refinement was performed with the help of SHELXL-97-2 to obtain the final solution.

References

[1]   http://www.xhuber.de/en/Products/diffractometers/xray/powder/g670/670.rsys.

[2]   J. Rodríguez-Carvajal, FULLPROF. Commission on Powder Diffraction (IUCr), Newsletter 26, (2001), p. 12–19.

[3]   http://depts.washington.edu/ntuf/facility/docs/GADDS%20Manual.pdf.

[4]   http://www.nonius.nl/KappaCCD/manuals/technical/userman.html.

[5]   Nonius Kappa CCD, Program Package COLLECT, DENZO, SCALEPACK,SORTAV, Nonius Delft, The Netherlands.

[6]   http://www.ne.ncsu.edu/nrp/npdf.html.

[7]   http://serc.carleton.edu/research_education/geochemsheets/techniques/EPMA.html.

[8]   INCA Energy-300, Oxford Instruments Analytical Ltd., UK 2000.

[9]   H. M. Rietveld, J. Appl. Crystallogr. 2, (1969), p. 65.

[10]   H. M. Rietveld. Acta Crystallogr. 22, (1967), p. 151.

[11]   G.M. Sheldrick, SHELXL-97, Program for crystal structure refinement. University of Göttingen, Germany; Windows version by McArdle, Natl Univ. Ireland, Galway; (1997).

[12]   http://www.softpedia.com/progDownload/Oscail-Download-171745.html.

3. On the four-phase reactions in the Ti-Ni-Al system

3.1. Introduction

Several research teams [1-9] have investigated the Ti-Ni-Al system and have presented different phase constitution at different temperatures but neither the transition temperature for the reaction among the phases NiAl, TiNiAl (τ_3), TiNiAl$_2$ (τ_2), TiNi$_2$Al (τ_4) nor among the phases TiNiAl, Ti$_3$NiAl$_8$ (τ_1), TiAl$_2$, TiNiAl$_2$ has been reported. For details, the reader may be transferred to recent critical assessments of phase diagram data by V. Raghavan [10] and J. C. Schuster [11]. According to Huneau et al. [3] and Nash and Liang [6], a tie line was found at 900°C between τ_2 and τ_4, which was also reported to exist at 800°C [1,2]. In the papers of Xu et al. [4] and J. C. Schuster et al. [5] (see Fig. 1, gray part) a tie line was reported to connect τ_3 and NiAl at 927°C and at 1000°C respectively, suggesting a transition type reaction among the four phases. However, J. C. Schuster et al. [5] were unable to observe any corresponding phase transition signal from DTA experiments.

Similarly, in the region comprising the phases τ_1, τ_2, τ_3 and TiAl$_2$, at 900°C a tie line between τ_2 and TiAl$_2$ was reported by Huneau et al. [3], whereas according to J. C. Schuster et al. [5] and Mazdiyasni et al. [8], the tie line seems to connect τ_1 and τ_3 at 1000°C and 1200°C respectively, again crossing the former one and suggesting a transition type four-phase equilibrium among the four phases. It is interesting to note that Raman and Markiv et al. [1,2] claimed the tie line $\tau_1 + \tau_3$ to exist at 800°C. Thus it is unrealistic that the same equilibrium was found at 800°C and 1000°C but a different equilibrium should exist at 900°C.

Another four-phase reaction involving the phases TiNi$_2$Al (τ_4), TiNiAl (τ_3), {Ti,Al}$_2$Ni and Ti$_3$Al (α_2) is also disputed. According to Huneau et al. [3] as well as to Markiv et al. [2], a tie line connects α_2 and τ_4 at 900°C and at 800°C, respectively, but according to J. C. Schuster et al. [5], the four-phase reaction {Ti,Al}$_2$Ni + $\tau_3 \Leftrightarrow \alpha_2 + \tau_4$ was claimed to exist at 876±2°C. The two-phase equilibrium {Ti,Al}$_2$Ni + τ_3 was also claimed by Xu and Jin [4] at 927°C and by Nash & Liang [6] at 900°C.

As hitherto no information exists on the exact temperature of these phase reactions, the current investigation is related to solve this problem. Thus the Ti-Ni-Al system is reinvestigated to

determine the three afore-mentioned four-phase reactions in the temperature range between 800°C and 1050°C and may thus present a reliable basis for fine-tuned CALPHAD-type modeling of phase relations in the Ti-Ni-Al system [9,12].

3.2. Experimental Details

In order to prove the reaction type and temperature of the four-phase reactions, we have selected alloy positions along one of the possible tie lines of the four-phase reactions and one composition for the three-phase equilibrium $\alpha_2 + \tau_3 + \tau_4$ (see alloy positions in Fig. 1). Samples were prepared from high purity metal ingots of Ti, Ni and Al (purity 99.9 mass %, Alfa Johnson Matthey GmbH, D) by arc melting under argon atmosphere and were melted three times for homogenization. Then these alloys were wrapped in Mo-foil to protect from attack by the hot quartz walls, sealed in evacuated quartz tubes and annealed for 10 days at various temperatures: 800°C, 870°C, 880°C, 900°C, 925°C, 950°C, 975°C, 990°C, 1000°C, 1010°C and 1040°C. One sample with nominal composition $Ti_{30}Ni_{11}Al_{59}$ was annealed at 800°C for 25 days to derive the phase constitution after long time annealing. Temperature at the position of samples was defined by a high quality standard thermocouple to control exact temperature. The samples were quenched in cold water after annealing. However, in order to check reaction kinetics, one sample was annealed at 1000°C for just 4 hours. Lattice parameters and standard deviations were determined by least squares refinements of room temperature X-ray powder Diffraction (XRD) data either obtained from a Guinier-Huber image plate employing monochromatic Cu $K\alpha_1$ radiation or from a Siemens D-5000 diffractometer using Win-index program TREOR [13]. Phase compositions were analyzed by Electron Probe Micro-Analyzer (EPMA) on a Carl Zeiss EVO 40 equipped with a Pentafet Link EDX system operated at 20 kV. Thermal analyses were performed in a calibrated Netzsch STA 409 PG/4/G Luxx Differential Scanning Calorimeter (DSC) employing a heating rate of 1-5 K/min in Al_2O_3 crucibles under a stream of 6N argon. Prior to DTA (differential thermal analysis) the alloys were annealed at 900°C for 10 days.

3.3. Results and discussion

3.3.1. The transition type reaction: $NiAl + \tau_3 \Leftrightarrow \tau_2 + \tau_4$

XRD and EPMA data support the existence of a tie line between τ_2 and τ_4 at 900°C as well as at 880°C, which agrees well with the findings of Huneau et al. [3]. However, on increasing temperature to 950°C, we found that the phase equilibrium changed to a tie line between τ_3 and NiAl, which agrees with the results of J. C. Schuster et al. [5] at 1000°C and Xu and Jin [4] at 927°C. Thus, a corresponding solid state four-phase reaction was supposed to occur between 900°C and 950°C.

DTA method was firstly employed in order to find out the exact phase transition temperature. But it did not yield any signal in the 880°C to 1000°C range. The failures in finding the four-phase transition temperature in our attempt and in literature J. C. Schuster [5] probably relates to: (i) high speed of heating and/or (ii) reaction kinetic is too slow. As even at our lowest speed of heating of 1 K per minute we did not find any signal, we consider the reaction to be too slow for DSC/DTA to reveal it. To check this, we took a sample previously annealed at 900°C and heat-treated it at 1000°C for 4 hours. After quenching in water, XRD did not reveal any phase change in this sample, which proves that the reaction does not proceed far even in a few hours.
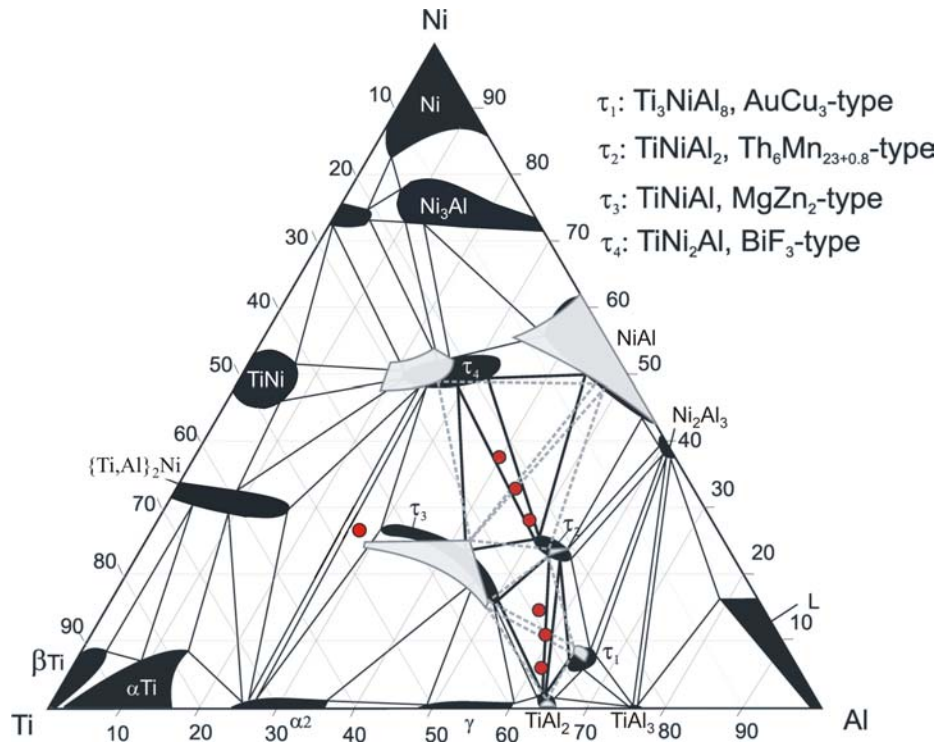
Fig. 1: Location of alloys (filled circles) in the isothermal section of 900°C after Huneau et al. [3]; a partial isothermal section of 1000°C from Schuster et al. [5] is superimposed in gray color.

Fig. 2 shows the microstructure of the alloy $Ti_{23}Ni_{33}Al_{44}$ (in at.%) in as cast condition (Fig. 2 (a)) and after annealing at 925°C (Fig. 2 (b)).
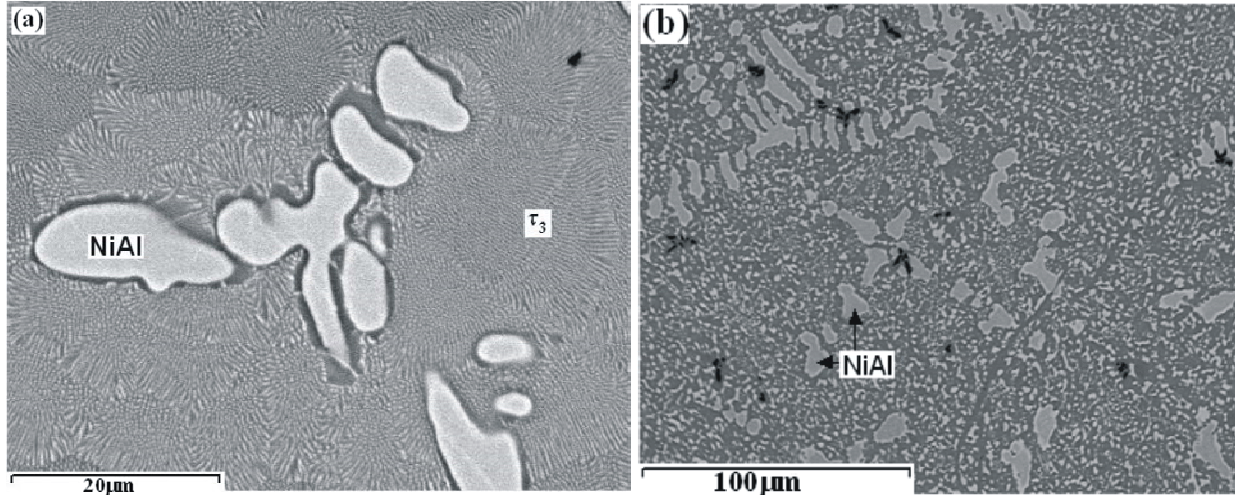
Fig. 2: Microstructures of alloy $Ti_{23}Ni_{33}Al_{44}$ (in at.%) in as cast (a) and after anneal for 10 days at 925°C (b). White primary crystals in (a) are NiAl and matrix is τ_3. The eutectic composition is $Ti_{25.5}Ni_{31.5}Al_{43}$ (from an EPMA area scan). In (b), the white phase is NiAl type with composition of $Ti_{5.95}Ni_{49.08}Al_{44.97}$, the other phases are difficult to identify by EPMA due to the fine grain size.
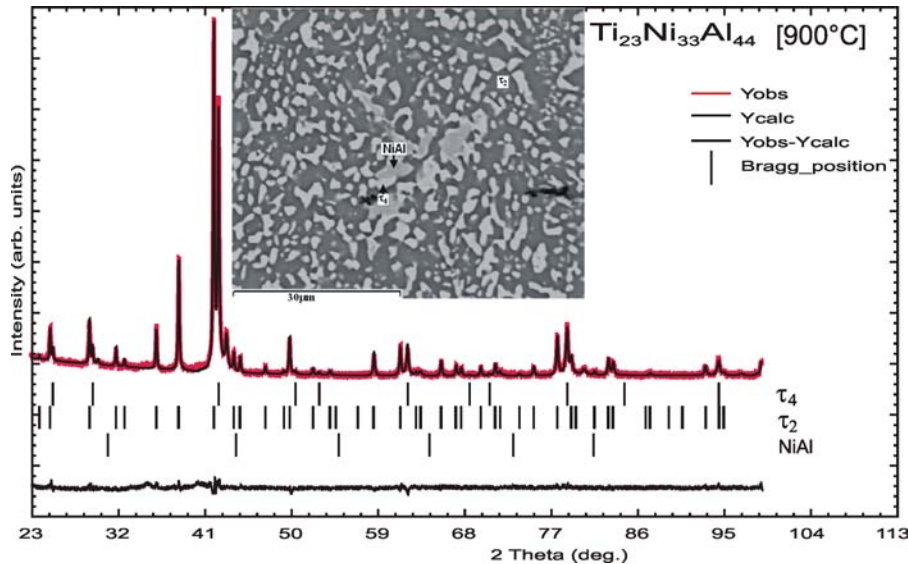
Fig. 3: Rietveld refinement of XRD data for alloy $Ti_{23}Ni_{33}Al_{44}$ annealed at 900°C revealing the three-phase equilibrium $\tau_2 + \tau_4 + NiAl$. Vertical bars represent locations of indexed peaks. Microstructure of alloy is shown in inset. White phase is τ_4 with composition $Ti_{23}Ni_{41.2}Al_{35.8}$, light gray is NiAl (due to fine grain size EPMA is unreliable) and black phase is τ_2 with composition $Ti_{24.8}Ni_{26.5}Al_{48.7}$.

Rietveld refinements for the annealed sample at 900°C and 950°C are shown in Fig. 3 and 4 along with the microstructures.
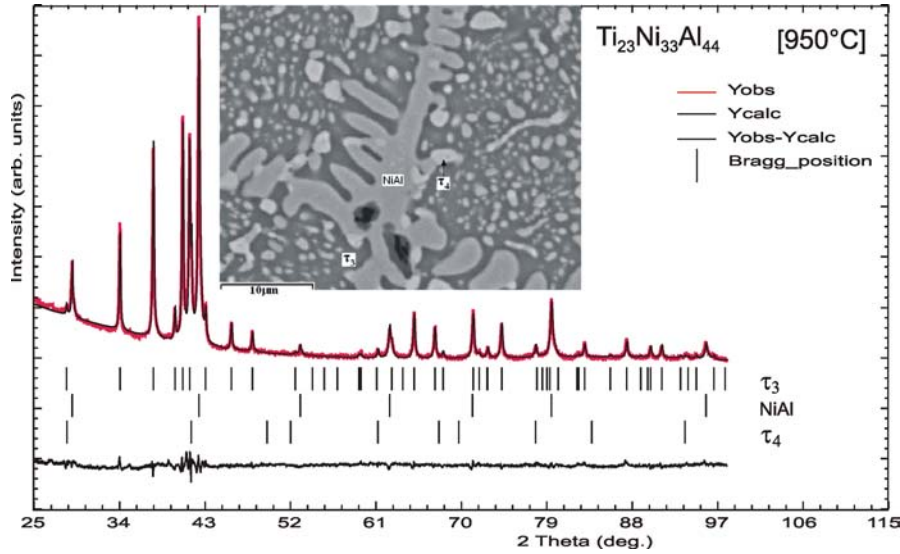
Fig. 4: Rietveld refinement of XRD data for alloy $Ti_{23}Ni_{33}Al_{44}$ annealed at 950°C revealing three phases: $\tau_3 + \tau_4$ + NiAl. Vertical bars represent locations of indexed peaks. Microstructure of alloy is shown in inset. Dark gray phase is τ_3 ($Ti_{29.6}Ni_{27.7}Al_{42.7}$), light gray phase is NiAl ($Ti_{8.3}Ni_{46}Al_{45.7}$) and white phase is τ_4 ($Ti_{23.7}Ni_{45.5}Al_{30.8}$).
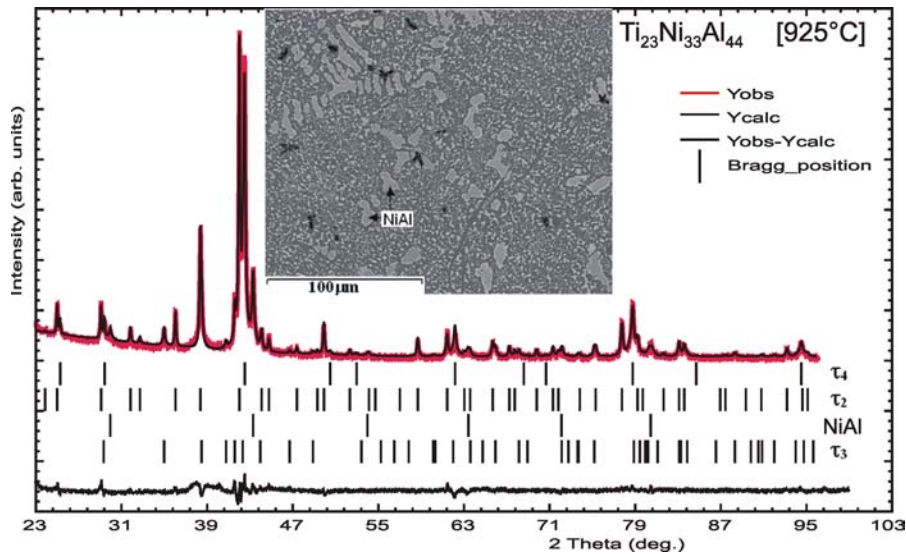
Fig. 5: Rietveld refinement of XRD data for alloy $Ti_{23}Ni_{33}Al_{44}$ annealed at 925°C revealing the four phases $\tau_2 + \tau_3 + \tau_4$ and NiAl. Vertical bars represent locations of indexed peaks. Microstructure of alloy is shown in inset.

As we found a four-phase structure at 925°C (see Fig. 5) but only the tie line between τ_2 and τ_4 at 900°C and the tie line between τ_3 and NiAl at 950°C, we locate the reaction isotherm, NiAl + τ_3 $\Leftrightarrow$ τ_2 + τ_4, at around 925°C with an uncertainty of ±15°C. However, due to a very fine-grained microstructure EPMA was incapable of delivering exact phase compositions for the tie-triangles (see Fig. 2b). The phase constitutions from the other two samples with compositions of $Ti_{24}Ni_{28}Al_{48}$ and $Ti_{23}Ni_{37.5}Al_{39.5}$ annealed at different temperatures confirmed this phase reaction. The reversibility of the reaction was proven from alloys, which were annealed at 950°C (similar result as for as-cast condition) and then at 925°C followed by annealing at 800°C. Table 1 shows the detailed information from $Ti_{23}Ni_{33}Al_{44}$ and $Ti_{30}Ni_{11}Al_{59}$ (which will be discussed in the following section) on phase constitutions at different temperatures, lattice parameters and composition of phases.

The XRD spectra of the alloy $Ti_{23}Ni_{33}Al_{44}$ annealed at 880°C, 900°C, 925°C and 950°, are presented in Fig. 6 and reveal the gradual phase change with the increase in temperature.
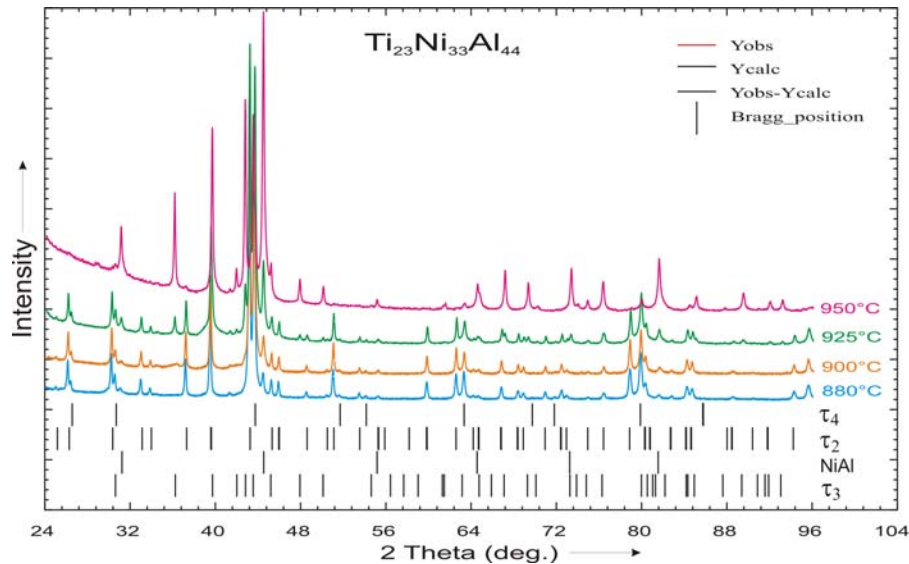
Fig. 6: XRD spectra of the alloy $Ti_{23}Ni_{33}Al_{44}$ annealed at 880°C, 900°C, 925°C and 950°. Vertical bars represent locations of indexed peaks for the four phases.

3.3.2. The transition type reaction $\tau_1 + \tau_3 \Leftrightarrow TiAl_2 + \tau_2$

New X-ray and EPMA data in the present investigation confirmed the tie line between τ_2 and $TiAl_2$ at 900°C as stated by Huneau et al. [3]. The tie line prevails up to a temperature of 975°C

and then a phase change starts. Rietveld refinement of the sample $Ti_{30}Ni_{11}Al_{59}$ after annealing at 975°C and its microstructure are shown in Fig. 7.
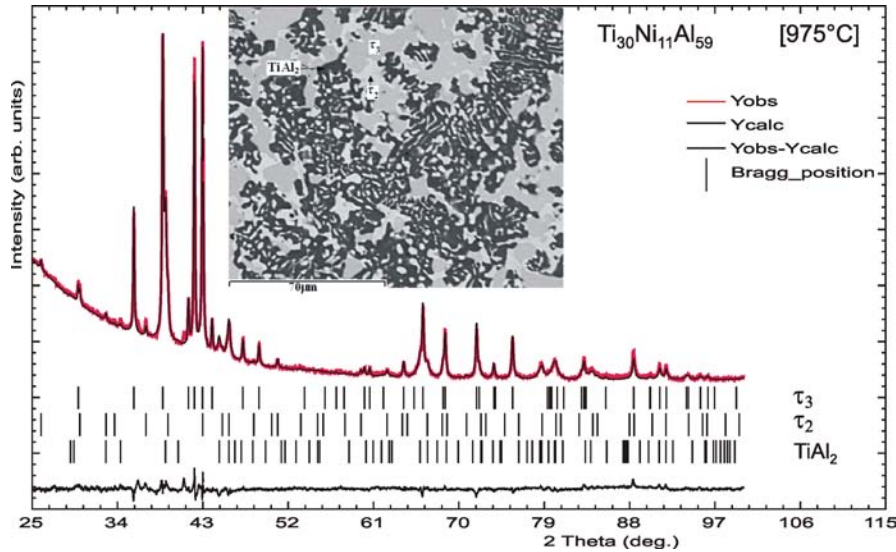
Fig. 7: Rietveld refinement for alloy $Ti_{30}Ni_{11}Al_{59}$ annealed at 975°C revealing the three-phase equilibrium $\tau_2 + \tau_3 + TiAl_2$. Vertical bars represent locations of indexed peaks. Microstructure of alloy is shown in inset. White phase is τ_2 ($Ti_{22.7}Ni_{23.6}Al_{53.7}$), light gray phase is τ_3 ($Ti_{34.7}Ni_{16.2}Al_{49.1}$) and dark gray phase is $TiAl_2$ ($Ti_{35.6}Ni_{2.6}Al_{61.8}$).
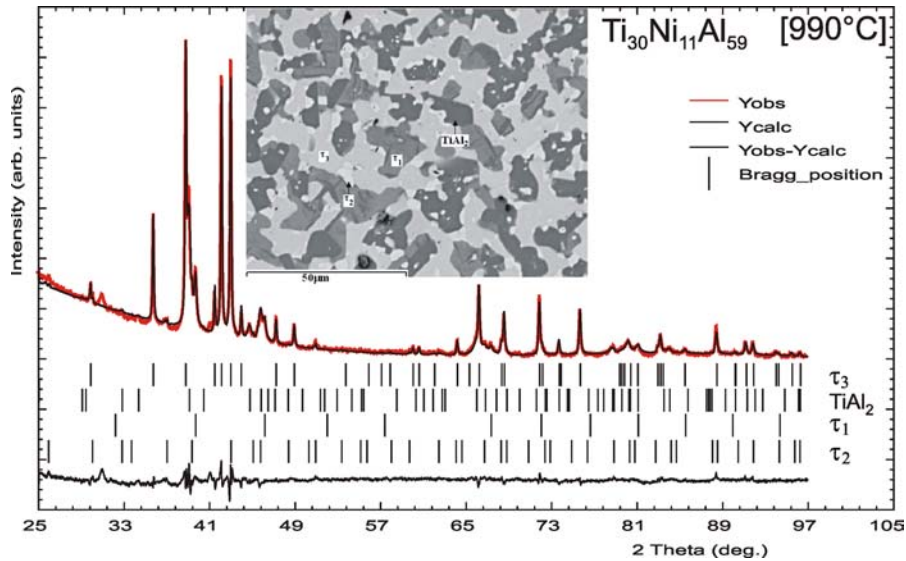
Fig. 8: Rietveld refinement for the alloy $Ti_{30}Ni_{11}Al_{59}$ annealed at 990°C revealing four phases. Vertical bars represent locations of indexed peaks. Microstructure of alloy is shown in inset. White phase shows τ_2 ($Ti_{24.2}Ni_{22.3}Al_{53.5}$); light gray is τ_3 ($Ti_{34.9}Ni_{16.1}Al_{49}$); medium gray phase is τ_1 ($Ti_{29.5}Ni_{7.9}Al_{62.6}$) and dark gray phase is $TiAl_2$ ($Ti_{35.8}Ni_2Al_{62.2}$)

Four phases were found to co-exist at 990°C and 1000°C (see Fig. 8) although J. C. Schuster et al. [5] claimed that there is no solid evidence for the existence of a four-phase reaction between

$\tau_1 + \tau_3$ and $TiAl_2 + \tau_2$. Therefore we suggested a temperature for the four-phase transition reaction $\tau_1 + \tau_3 \Leftrightarrow TiAl_2 + \tau_2$ around 995°C.
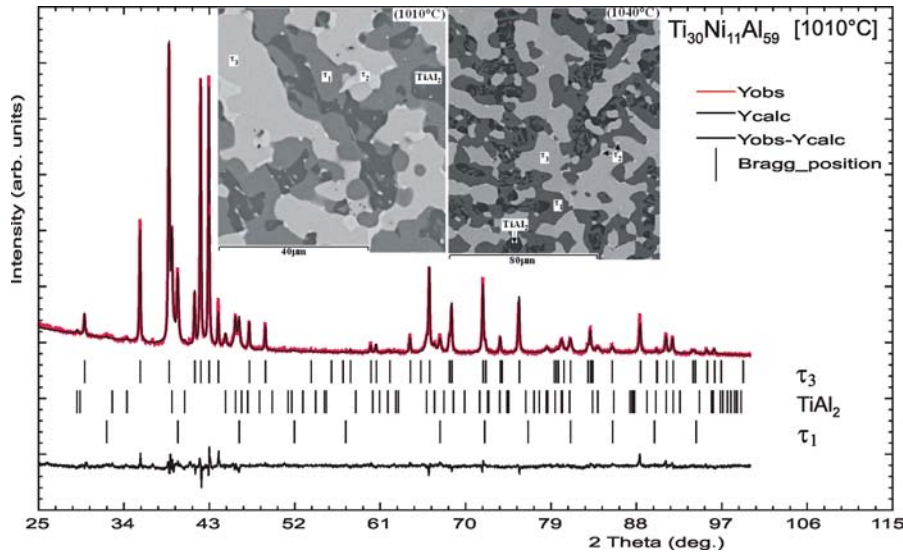
Fig. 9: Rietveld refinement of XRD data for alloy $Ti_{30}Ni_{11}Al_{59}$ annealed at 1010°C revealing three phases. Vertical bars represent locations of indexed peaks. Microstructure of alloy at 1010°C and 1040°C is shown in inset. Light gray shows τ_3 ($Ti_{34.4}Ni_{15.6}Al_{50}$), medium gray phase is τ_1 ($Ti_{27.2}Ni_{9.5}Al_{63.3}$) and dark gray phase is $TiAl_2$ ($Ti_{34.9}Ni_{1.9}Al_{63.2}$). Traces of τ_2 (White phase) are also present.
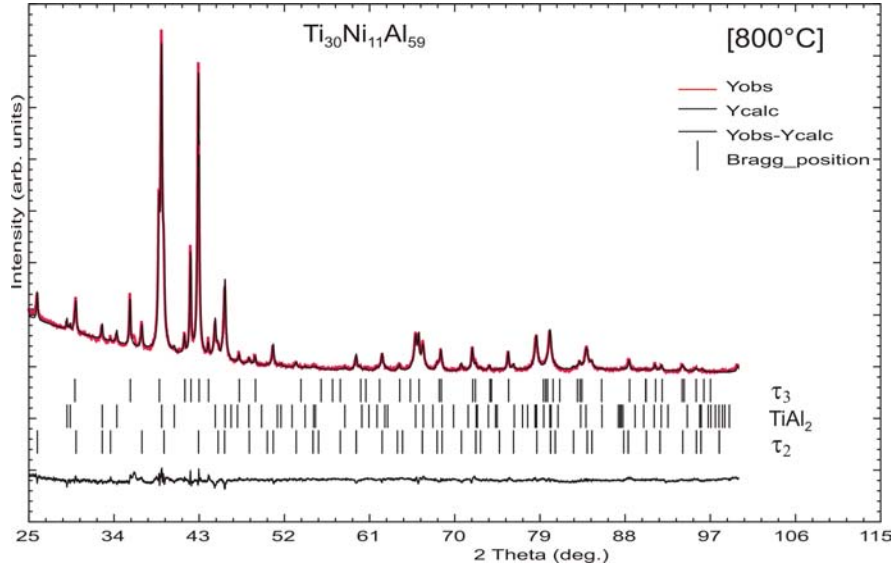
Fig. 10: Rietveld refinement of alloy $Ti_{30}Ni_{11}Al_{59}$ annealed at 800°C revealing the three-phase equilibrium $\tau_2 + \tau_3 + TiAl_2$. Vertical bars represent locations of indexed peaks.

At 1010°C, we found only the tie line between τ_1 and τ_3 to exist (along with a little amount of $TiAl_2$ and τ_2 which practically disappeared at 1040°C (see Fig. 9 and Table 1). This result is also in agreement with the findings of Mazdiyasni et al. [8]. The phase constitutions from the other

two samples with compositions of $Ti_{29.3}Ni_{14.7}Al_{56}$ and $Ti_{33}Ni_6Al_{61}$ annealed at different temperatures confirmed this phase reaction. In order to recheck the relevant phase relations at 800°C, a sample was annealed at 800°C for 25 days and then examined by XRD. Rietveld refinement of this sample, as shown in Fig. 10, clearly reveals three phases $\tau_2 + \tau_3 + TiAl_2$ in equilibrium thereby disapproving the findings of Markiv et al. [2].
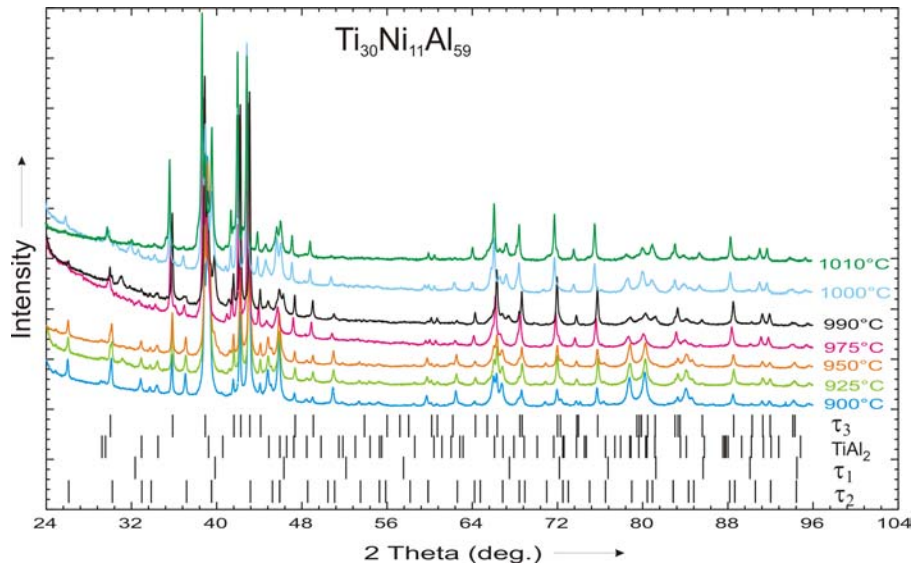
Fig. 11: Rietveld refinement for the alloy $Ti_{30}Ni_{11}Al_{59}$ (in at.%) annealed at 900°C, 925°C, 950°C, 975°C, 990°C, 1000°C and 1010°C. Vertical bars represent locations of indexed peaks for the four phases.

Fig. 11 shows the continuous phase change through the XRD spectra at different temperatures in sequence. From the XRD spectra, it is obvious that the four-phase reaction occurs at a temperature about 995°C with an uncertainty of ±15°C. EPMA data and lattice parameters for the phases at temperature above and below the tie lines change are shown in Table 1.

Table 1

Crystallographic and EPMA data of selected Ti-Ni-Al alloys annealed and quenched from different temperatures.

Ti-Ni-Al alloy (in at. %)	Heat treatment	Phase(s)	Space group	Structure type	Lattice parameters (nm)		EPMA data in at. % Ti-Ni-Al
					a	*c*	
23-33-44	900°C, 10 days	$TiNiAl_2$ (τ_2) $TiNi_2Al$ (τ_4) NiAl	Fm-3m Fm-3m Pm-3m	Th_6Mn_{23} BiF_3 CsCl	1.19065(6) 0.58889(6) 0.28965(9)	- - -	24.8-25.6-49.6 23.2-40.3-36.5 24.6-26.8-48.6

23-33-44	950°C, 10 days	TiNiAl (τ_3) TiNi$_2$Al (τ_4) NiAl	P6$_3$/mmc Fm-3m Pm-3m	MgZn$_2$ BiF$_3$ CsCl	0.49992(7) 0.58916(4) 0.28955(2)	0.80642(8) - -	29.6-27.7-42.7 23.7-45.5-30.8 8.3-46-45.7
30-11-59	975°C, 10 days	TiNiAl (τ_3) TiNiAl$_2$ (τ_2) TiAl$_2$	P6$_3$/mmc Fm-3m I4$_1$/amd	MgZn$_2$ Th$_6$Mn$_{23}$ HfGa$_2$	0.50259(6) 1.18943(9) 0.39656(2)	0.82330(9) - 2.42800(2)	34.7-16.2-49.1 22.7-23.6-53.7 35.6-02.6-61.8
30-11-59	1010°C, 10 days	TiNiAl (τ_3) TiAl$_2$ Ti$_3$NiAl$_8$ (τ_1)	P6$_3$/mmc I4$_1$/amd Pm-3m	MgZn$_2$ HfGa$_2$ AuCu$_3$	0.50254(4) 0.39595(6) 0.39335(7)	0.82347(7) 2.4321(7) -	34.4-15.6-50 34.9-1.9-63.2 27.2-9.5-63.3

3.3.3. The phase equilibrium $\alpha_2 + \tau_3 + \tau_4$ at 900°C

Evaluation of X-ray data on alloys in this region gave evidence of a tie line between $\alpha_2 + \tau_4$ at 870°C and 900°C. In the sample Ti$_{46}$Ni$_{27}$Al$_{27}$, at 900°C, we found τ_3, τ_4 and α_2 to coexist (see Fig. 12), which agrees with the results presented by Huneau et al. [3] but disagrees with the four-phase reaction (Ti,Al)$_2$Ni + $\tau_3 \Leftrightarrow \tau_4 + \alpha_2$ claimed at 876±2°C J. C. Schuster [5].
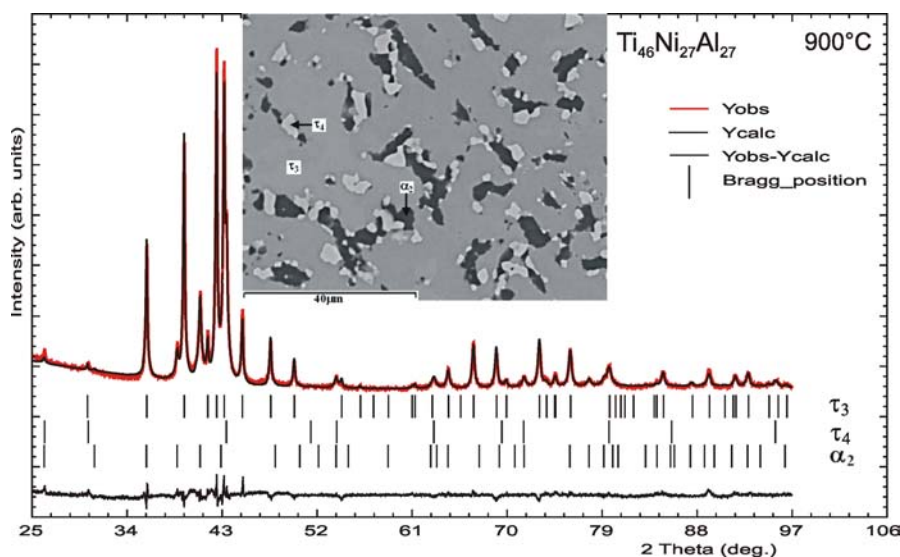
Fig. 12: Rietveld refinement for alloy Ti$_{46}$Ni$_{27}$Al$_{27}$ annealed at 900°C revealing the three-phase equilibrium $\tau_4 + \tau_3 + \alpha_2$. Vertical bars represent locations of indexed peaks. Microstructure of alloy is shown in inset. White phase is τ_4 (Ti$_{27.9}$Ni$_{47.3}$Al$_{24.8}$), light gray phase is τ_3 (Ti$_{45.4}$Ni$_{28}$Al$_{26.6}$) and dark gray phase is α_2 (Ti$_{70.5}$Ni$_{3.3}$Al$_{26.1}$).

However, when we tried to resolve the four-phase equilibrium, a new phase Werner et. al. [13], entered the equilibria with the Laves phase τ_3 at temperatures higher than 900°C. Details about

the new phase with hitherto unknown crystal structure will be the subject of a forthcoming publication.

3.4. Conclusion

Two four-phase transition type reactions were established in the Ti-Ni-Al system. The temperature for the four-phase reaction τ_3 + NiAl $\Leftrightarrow$ τ_2 + τ_4 is 925±15°C. The temperature for the four-phase reaction τ_1 + τ_3 $\Leftrightarrow$ τ_2 + TiAl$_2$ is at 995±15°C. The present results confirm the phase relations as presented at 900°C by Huneau et al. [3] with respect to both four-phase reactions defined above. It was shown, that neither of the two solid four-phase reactions mentioned above could be detected by DTA because reaction kinetics is too slow. Furthermore, we also confirmed the three-phase field τ_4 + α_2 + τ_3 at 900°C as reported by Huneau et al. [3].

References

[1]   A. Raman and K. Schubert, Z. Metallkde **56** (1965), p. 99-104.

[2]   V.Y. Markiv, V.V. Burnashova and V.R. Ryabov, Metallofizika **46** (1973), p. 103-110.

[3]   B. Huneau, P. Rogl, K. Zeng, R. Schmid-Fetzer, M. Bohn and J. Bauer. Intermetallics **7** (1999), p. 1337-1345.

[4]   H.H. Xu and Z. Jin, Trans Nonferrous Met Soc China **7** (1997), p. 24-29.

[5]   J.C. Schuster, Z. Pan, S. Liu, F. Weitzer and Y. Du, Intermetallics **15** (2007), p. 1257-1267.

[6]   P. Nash and W.W. Liang, Metallurgical Transitions **16A** (1985), p. 319-322.

[7]   J.J. Ding, P. Rogl and H.Schmidt, Journal of Alloys and Compounds **317-318** (2001), p. 379-384.

[8]   S. Mazdiyasni, D.B. Miracle, D.M. Dimiduk, M.G. Mendiratta and P.R. Subramanian, Scripta Met. **23** (1989), p. 327-331.

[9]   K. Zeng, R. Schmid-Fetzer, B. Huneau, P. Rogl and J. Bauer, Intermetallics **7** (1999), p. 1347-1359.

[10] V. Raghavan, Journal of Phase Equlibria and Diffusion **26** (2005), p. 268-272.

[11] J.C. Schuster, Intermetallics **14(10-11)** (2006), p. 1304-1311.

[12] N. Dupin, PhD-thesis, Institut National Polytechnique Grenoble, France (1995).

[13] P.E. Werner, L. Eriksson and M. Westdahl, J. App. Crystallography **18** (1985), p. 367-370.

[14] A. Grytsiv, Xing-Qiu Chen, V.T. Witusiewicz, P. Rogl, R. Podloucky, V. Pomjakushin, D. Maccio, A. Saccone, G. Giester and F. Sommer, Z. Kristallografie **221** (2006), p. 334-348.

4. Crystal Structure of τ_5-TiNi$_{2-x}$Al$_5$ (x= 0.48) and Isotypic {Zr,Hf}Ni$_{2-x}$Al$_{5-y}$

4.1. Introduction

Although several research teams [1-3] have identified an Al-rich phase in the Ti-Ni-Al system (labelled as τ_5 with a composition around Ti$_{14.5}$Ni$_{20.5}$Al$_{65}$ (at. %)), structure solution has so far not been achieved. The τ_5 phase was first mentioned by Ding et al. [1] as a metastable phase in the temperature range of 600°C-900°C. In a reinvestigation τ_5 was registered as a stable phase with a possibly decagonal structure [2]. Electron Back Scatter Diffraction (EBSD) by Bursik et al. [3] confirmed the τ_5-phase but ruled out any decagonal symmetry. Recent critical assessments [4,5] of the Hf-Ni-Al system list a phase HfNi$_2$Al$_5$, for which an original composition Hf$_3$Ni$_6$Al$_{16}$ was termed by Markiv et al. [6]. Although HfNi$_2$Al$_5$ was said to be isostructural with the ZrNi$_2$Al$_5$ type [7,8], no crystallographic details of sufficient precision were presented. In continuation of our systematic research on the Ti-Ni-Al system [9,10], the current investigation was designed to provide detailed structural information on the τ_5-phase as well as on the isostructural compounds {Zr,Hf}Ni$_2$Al$_5$.

4.2. Experimental Details

Alloys were prepared (each of 1-2 grams) by argon arc melting from metal ingots of Ti, Zr, Hf, Ni and Al with purity higher than 99.9 mass % (Alfa Johnson Matthey GmbH, Germany) and were melted three times for homogenisation (weight loss less than 0.1 %). As-cast alloys were individually wrapped in Mo-foil to protect from attack by the hot quartz walls, sealed in evacuated quartz tubes and annealed for 1-15 days at 1050°C, 1020°C, 1000°C, 950°C and 900°C followed by quenching the capsules in cold water. However, at annealing temperatures of 1000°C or higher, the samples lost significant amounts of Al from the outer surface. Temperature at the position of samples was controlled by a high quality standard thermocouple. Lattice parameters and standard deviations were determined by least squares refinements of room temperature X-ray powder diffraction (XRD) data obtained from a Guinier-Huber image

plate employing monochromatic Cu Kα_1 radiation. Samples were polished using standard procedures and were examined by optical metallography and scanning electron microscopy (SEM). Compositions were determined in an Electron Probe Micro-Analyzer (EPMA) on a Carl Zeiss EVO 40 equipped with a Pentafet Link energy dispersive X-ray (EDX) system operated at 20 kV. Pure elements were used as standards to carry out the deconvolution of overlapping peaks and background subtraction. Finally the X-ray intensities were corrected for ZAF effects using the INCA-Energy 300 software package [for details see Chapter 2]. A Philips CM12 STEM transmission electron microscope (TEM) was used with an EDX analyzer and Phoenix software to corroborate unit cell, symmetry and formation of superstructures. TEM investigations were performed on particles (0.1−2 μm), which were obtained by mechanically crunching alloy pieces under ethanol and transferring the particles on a thin holey carbon film supported by a copper grid. Single crystals of τ_5 suitable for X-ray diffraction were mechanically isolated from an arc-melted specimen $Ti_{13.9}Ni_{19.7}Al_{66.4}$, which was annealed at 1020°C for 5 days. The crystals were inspected on an AXS-GADDS texture goniometer for quality and crystal symmetry prior to X-ray intensity data collection on a four-circle Nonius Kappa diffractometer (CCD area detector and graphite monochromated MoK$_\alpha$ radiation, λ = 0.071069 nm). Orientation matrix and unit cell parameters were derived using the program DENZO [for details see Chapter 2]. No absorption correction was necessary because of the rather regular crystal shape and small dimensions of the investigated specimens. The structures were solved by direct methods and refined with the SHELXS-97 and SHELXL-97 programs [for details see Chapter 2] respectively. A 10 g sample $Ti_{13.9}Ni_{19.7}Al_{66.4}$ was prepared for neutron powder diffraction (NPD) by annealing at 1020°C for 4 days and was powdered to a grain size below 40 μm in order to reduce preferential orientation effects. Neutron diffraction was performed at room temperature on the high-resolution HRPT diffractometer [11] at the SINQ spallation source of the Paul Scherrer Institute (Switzerland). The HRPT diffractometer was used in high intensity mode ($\Delta d/d \geq 2 \times 10^{-3}$) with two neutron wavelengths $\lambda_{neutron}$= 0.14940 nm and 0.18857 nm within the angular 2θ range from 4° to 164°. Combined quantitative Rietveld refinement of the X-ray and neutron powder diffraction data was performed with the FULLPROF program [for details see Chapter 2], with the use of its internal tables for scattering lengths and atomic form factors.

4.3. Results and discussion

4.3.1. The crystal structure of τ_5-TiNi$_{2-x}$Al$_5$, x = 0.48

Compositions derived from EPMA-data by several research groups confirmed the formation of the τ_5 phase at about Ti$_{14}$Ni$_{21}$Al$_{65}$ (at. %) without a significant homogeneity region [1-3]. The various EPMA compositions found in the literature for τ_5 are drawn in Fig. 1 on the Al-rich part of the most recent isothermal section at 1000°C published by Schuster et al. [2]. The τ_5 phase was reported to form in a peritectic reaction at 1107°C: L + τ_1 + Ni$_2$Al$_3$ $\Leftrightarrow$ τ_5 Schuster et al. [2], where τ_1 represents the AuCu$_3$-type phase at about Ti$_{25.6}$Ni$_{7.7}$Al$_{66.7}$ (at. %).
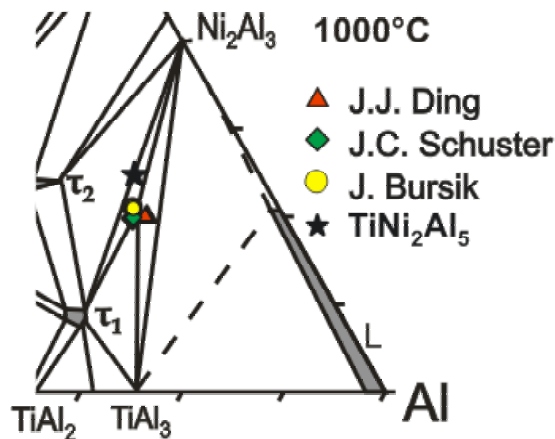
Fig. 1. Isothermal section of the Al-rich part of the system Ti-Ni-Al [2]. The symbols indicate the compositions of the τ_5 phase obtained by three different research groups [1-3]. The position of stoichiometric TiNi$_2$Al$_5$ is denoted by a star.

Attempts to obtain single crystals from slowly cooled melts within the primary crystallization field of τ_5 Schuster et al. [2] failed due to the rather small field of crystallization. Therefore several samples (about 2g) near the τ_5 composition were arc-melted and subdued to annealing at 1020°C for 5 days. A single crystal (SC) of τ_5, although small (27×23×20 µm) but suitable for X-ray structure analysis, was mechanically isolated from the specimen with nominal composition Ti$_{13.9}$Ni$_{19.7}$Al$_{66.4}$ (at.%). The SC-diffraction pattern was completely indexed on the basis of a tetragonal unit cell [a = 0.3984(2) nm and c = 1.4073(3) nm] and revealed extinctions of only a body-centred Bravais lattice compatible with *I*4/*mmm* (No.139) as the highest symmetric space

group type. TEM analyses confirmed the crystal symmetry, the dimensions of the unit cell and the absence of superstructure reflections (Fig. 2, for details see below). Direct methods yielded an atomic arrangement, which according to Pearson's Crystal Data [12] was recognized to be isotypic with the structure type of $ZrNi_2Al_5$ [8].

a) τ_5-TiNi$_{2-x}$Al$_5$

b) ZrNi$_{2-x}$Al$_{5-y}$
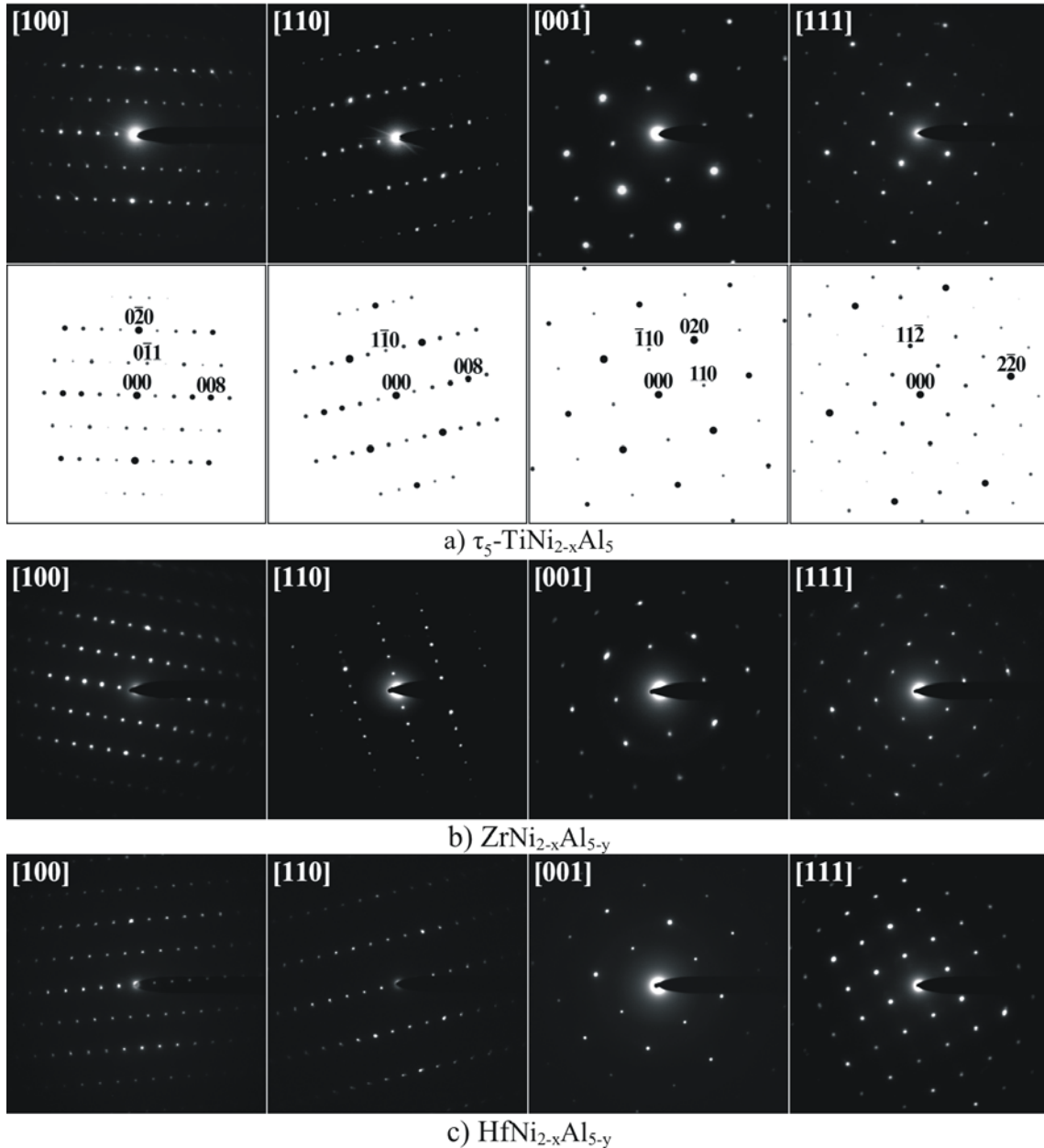
c) HfNi$_{2-x}$Al$_{5-y}$

Fig. 2. TEM selected area diffraction patterns of low index zone axes [100], [110], [001] and [111] together with their simulations for a) τ_5-TiNi$_{2-x}$Al$_5$, b) ZrNi$_{2-x}$Al$_{5-y}$ and c) HfNi$_{2-x}$Al$_{5-y}$.

Refinement with anisotropic atom displacement parameters (ADP) converged to $R_{F^2} = 0.013$ with residual electron densities smaller than ±0.6 e⁻/Å³. Whereas the 2a site is fully occupied by Ti atoms and the 2b and 8g sites are fully occupied by Al atoms, a partial occupancy was revealed for Ni-atoms in the 4e-site (occ. = 0.76 Ni). We tested the structural arrangement with respect to further atom/defect ordering in a series of space groups with lower symmetry ($I\bar{4}2m$, $I4/m$, $I\bar{4}$). However, these attempts did not provide any further possibilities for atom/defect ordering.

A check for missing symmetry via program PLATON in all cases prompted $I4/mmm$ as the proper space group. Results of the final refinement are summarized in Table 1 yielding the structural formula τ_5-Ti(Ni$_{0.76}$)$_2$Al$_5$.

Table 1a. Structural data for TiNi$_{2-x}$Al$_5$, x = 0.48 [SC with μ_{abs} (mm⁻¹) = 9.34 for XRD] (ZrNi$_2$Al$_5$ type, SG: $I4/mmm$, #139), ZrNi$_{2-x}$Al$_{5-y}$, x = 0.4, y = 0.4 (XRD) and HfNi$_{2-x}$Al$_{5-y}$, x = 0.5, y = 0.2 (XRD); data standardized with program Structure Tidy [13].

Parameter/compound	Ti-Ni-Al XSC	Ti-Ni-Al NPD	Ti-Ni-Al XRD	Zr-Ni-Al XRD	Hf-Ni-Al XRD
Composition from EPMA in (at.%)	Ti$_{14.1}$Ni$_{20.6}$Al$_{65.3}$	Ti$_{14.1}$Ni$_{20.6}$Al$_{65.3}$		Zr$_{14.4}$Ni$_{23.2}$Al$_{62.4}$	Hf$_{14.3}$Ni$_{21.7}$Al$_{64.0}$
Composition from refinement (at.%)	Ti$_{13.3}$Ni$_{20.2}$Al$_{66.5}$	Ti$_{13.3}$Ni$_{20.2}$Al$_{66.5}$		Zr$_{13.9}$Ni$_{22.1}$Al$_{64.0}$	Hf$_{13.7}$Ni$_{20.6}$Al$_{65.7}$
Formula from refinement	TiNi$_{2-x}$Al$_5$, x = 0.48	TiNi$_{2-x}$Al$_5$, x = 0.48		ZrNi$_{2-x}$Al$_{5-y}$, x = 0.4, y = 0.4	HfNi$_{2-x}$Al$_{5-y}$, x = 0.5, y = 0.2
Radiation, λ (nm)	Mo Kα	$\lambda_n = 0.14940$	Cu Kα$_1$	Cu Kα$_1$	Cu Kα$_1$
a (nm)	0.3984(2)	0.39578(1)	0.39578(4)	0.40193(1)	0.40073(1)
c (nm)	1.4073(3)	1.40538(4)	1.40599(2)	1.44304(2)	1.42909(2)
Reflections in refinement	160≥4σ(F$_o$) of 182	111	56	56	56
Number of variables	14	36	36	23	23
$R_F = \Sigma|F_0-F_c|/\Sigma F_0$	-	0.020	0.041	0.078	0.032
$R_B = \Sigma|I_0-I_c|/\Sigma I_0$	-	0.036	0.038	0.085	0.026
$R_{wP} = [\Sigma w_i|y_{0i}-y_{ci}|^2/\Sigma w_i|y_{0i}|^2]^{1/2}$	-	0.085	0.082	0.103	0.098
$R_P = \Sigma|y_{0i}-y_{ci}|/\Sigma|y_{0i}|$	-	0.078	0.104	0.101	0.099
$R_e = [(N-P+C)/\Sigma w_i y_{0i}^2]^{1/2}$	-	0.043	0.059	0.046	0.015
$\chi^2 = (R_{wP}/R_e)^2$	GOF = 1.12	-	-	-	-
$R_F^2 = \Sigma|F_0^2-F_c^2|/\Sigma F_0^2$	0.0133	-	-	-	-
R_{Int}	0.0390	-	-	-	-
wR2	0.0225	-	-	-	-
Extinction (Zachariasen)	0.0078(7)	-	-	-	-
Residual density e⁻/Å³; max; min.	0.38; -0.55	-	-	-	-
Atom parameters					
M; 2a (0, 0, 0); Occ.;	1.00(1) Ti	1.00(1) Ti		1.00(1) Zr	1.00(1) Hf
$U_{11} = U_{22}$; U_{33}[1]	0.0046(2); 0.0059(2)	B$_{iso}^2$ = 0.12(3)		B$_{iso}$ = 0.77(2)	B$_{iso}$ = 0.62(1)
Ni; 4e (0, 0, z); Occ.,	0.763(2),	0.757(9), 0.23898(7)		0.792(1),	0.750(2),

36

z;	0.23917(3)		0.23817(6)	0.23860(7)
$U_{11}= U_{22}; U_{33}$	0.0077(1); 0.0069(2)	$B_{iso} = 0.40(2)$	$B_{iso} = 0.35(1)$	$B_{iso} = 0.59(2)$
Al1; 8g (0, 1/2, z); Occ., z;	1.00(0), 0.14595(4)	1.00, 0.14609(7)	0.90(2), 0.14984(6)	0.952(2), 0.15073(7)
$U_{11};U_{22}; U_{33}$	0.0071(3), 0.0099(3) 0.0095(2)	$B_{iso} = 0.44(2)$	$B_{iso} = 0.42(2)$	$B_{iso} = 0.41(3)$
Al2; 2b (0, 0, 1/2); Occ.;	1.00(1)	1.00(1)	1.00(1)	1.00(1)
$U_{11}= U_{22}; U_{33}$	0.0064(3); 0.0094(4)	$B_{iso} = 0.20(4)$	$B_{iso} = 0.34(5)$	$B_{iso} = 0.54(5)$

[1]$U_{23} = U_{13} = U_{12} = 0$ for all sites. [2]B_{iso} is given in (10^2 nm^2).

Table 1b: Interatomic distances (nm) for $TiNi_{2-x}Al_5$, x = 0.48 from XSC. Standard deviation ≤ 0.0001

Ti–	−4Al2	0.2817
CN = 12	−8Al1	0.2861
Ni–	4Al1	0.2385
CN = 12	−4Al1	0.2566
	−4Ni	0.2834
Al1–	2Ni	0.2385
CN = 13	−2Ni	0.2566
	−4Al1	0.2817
	−2 Ti	0.2861
	−2Al2	0.2861
	−1Al1	0.2929
Al2–	-4Ti	0.2817
CN = 12	−8Al1	0.2861

Although interatomic distances favour Ni in the 4e-site, the occupancy level yields only 21.3 electrons in this site close to the X-ray scattering power of a Ti-atom. Due to the negative neutron scattering length of natural Ti, neutron powder diffraction data are very sensitive to the location of Ti atoms in the crystal structure. Therefore a combined Rietveld refinement of NPD and XRD (Fig. 3) data was employed to unambiguously locate Ti-atoms in the structure. Indeed the combined refinement confirmed the fully ordered atom arrangement with Ti in 2a, Al in 2b and 8g sites and Ni in a partially filled 4e-site (occ. = 0.76 Ni). The combined refinement is in perfect agreement with the X-ray single crystal data.

A summary of the results on the structure of τ_5-TiNi$_{2-x}$Al$_5$ is given in Table 1a. It should be noted that neutron spectra of this sample were taken for two neutron wavelengths (0.14940 and 0.18857 nm) and both prompted identical results. The large sample used for NPD shows the τ_2– phase (filled Th$_6$Mn$_{23+1}$-type at Ti$_{19.8}$Ni$_{23.0}$Al$_{57.2}$) in addition to the phases present in the specimen used for XPD. Due to evaporation losses of Al during annealing in the evacuated quartz tube at 1020°C, the overall composition in a thin surface layer of the reguli shifted to the phase triangle, $\tau_1 + \tau_2 + $ Ni$_2$Al$_3$ (Fig. 4a). At the centre of the alloy buttons, there is no τ_2 present (Fig. 4a) and consequently the small amount of powders necessary for XPD was taken from the

central piece of the alloy specimen (Fig. 5). Although attempts were made to grind off the outer portion of the annealed samples, still some of it was left in the alloys used for neutron powder diffraction.
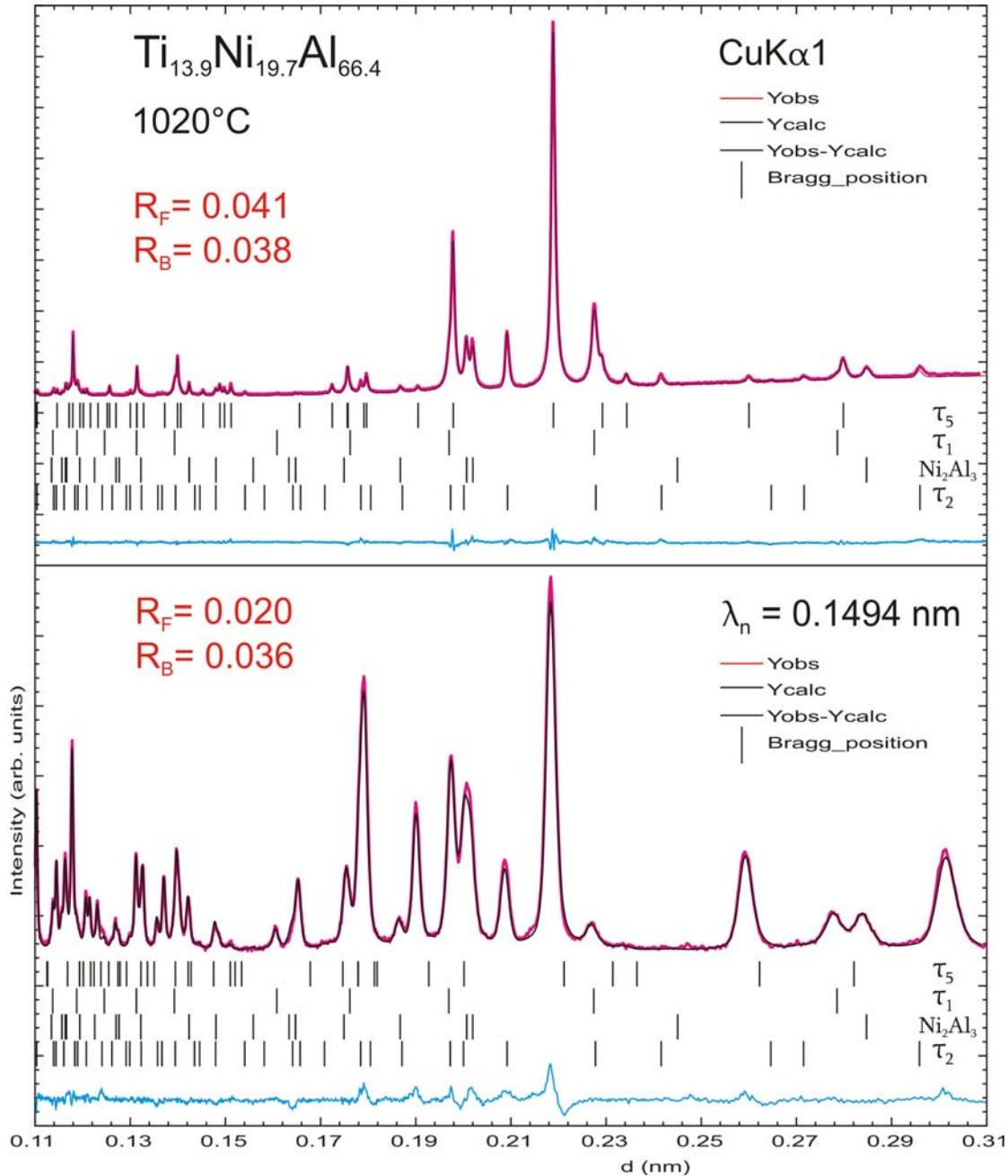
Fig. 3. Combined Rietveld refinement of neutron and X-ray powder diffraction for τ_5-TiNi$_{2-x}$Al$_5$.

The Ni-defects found yield a composition $Ti_{13.3}Ni_{20.2}Al_{66.5}$ (in at.%) consistent with EPMA data for the τ_5-phase ($Ti_{14.1}Ni_{20.6}Al_{65.3}$), which centres a narrow three-phase triangle formed by τ_1 - $TiAl_3$ - Ni_2Al_3.
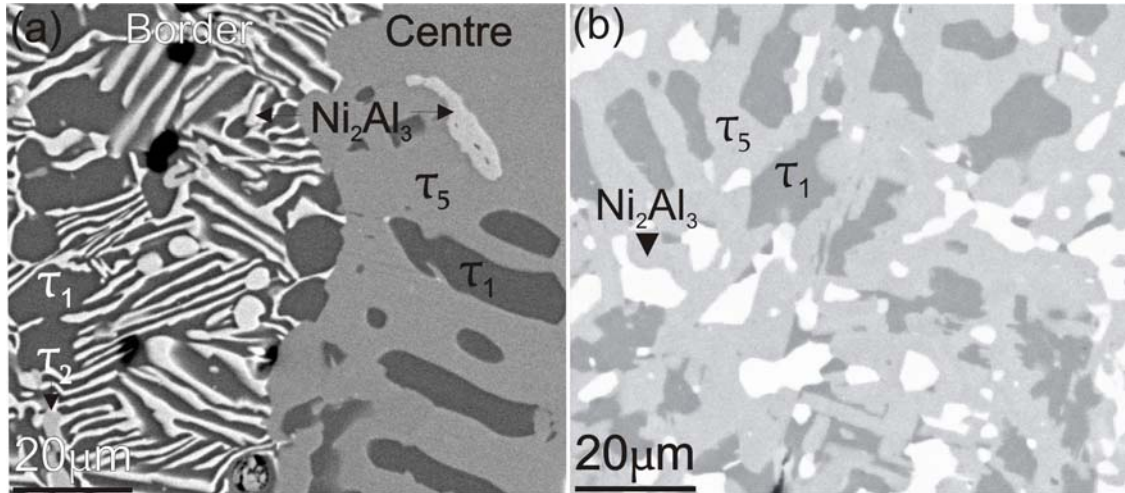
Fig. 4: SEM images for a) $Ti_{13.9}Ni_{19.7}Al_{66.4}$ (annealed at 1020°C) and b) $Ti_{16.7}Ni_{23.1}Al_{60.2}$ (annealed at 900°C).
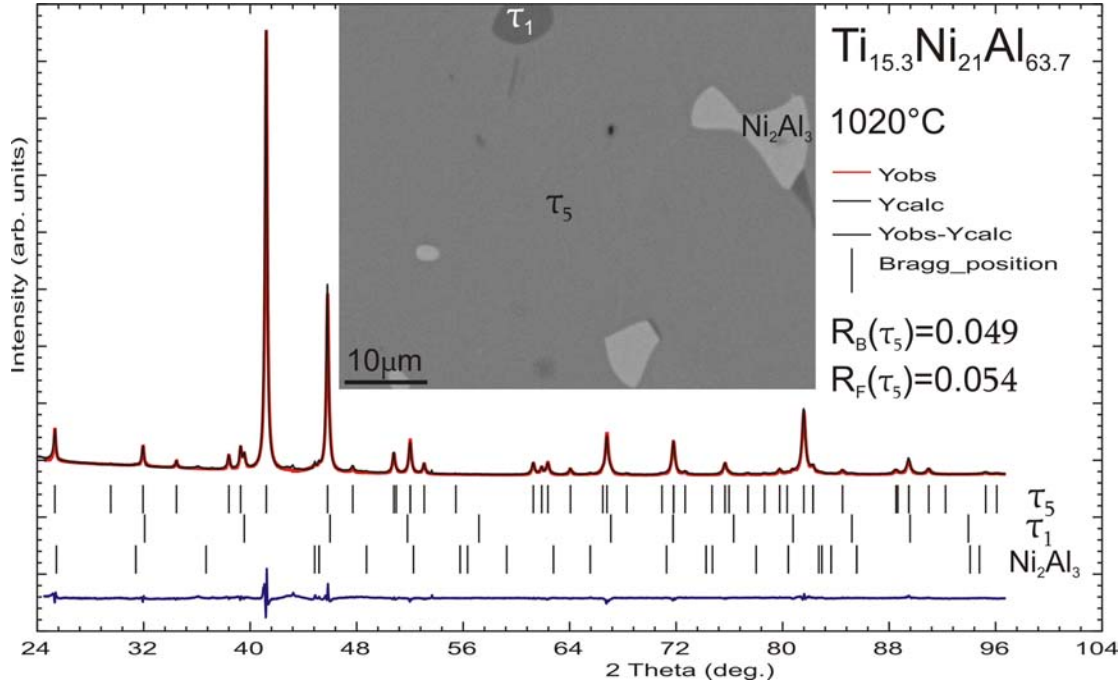
Fig. 5: Rietveld refinement for alloy $Ti_{15.3}Ni_{21}Al_{63.7}$ (EPMA, at. %) annealed at 1020°C and quenched, revealing the three-phase equilibrium $\tau_5 + \tau_1 + Ni_2Al_3$. Vertical bars represent the location of indexed peaks. A micrograph of this sample is shown as insert.
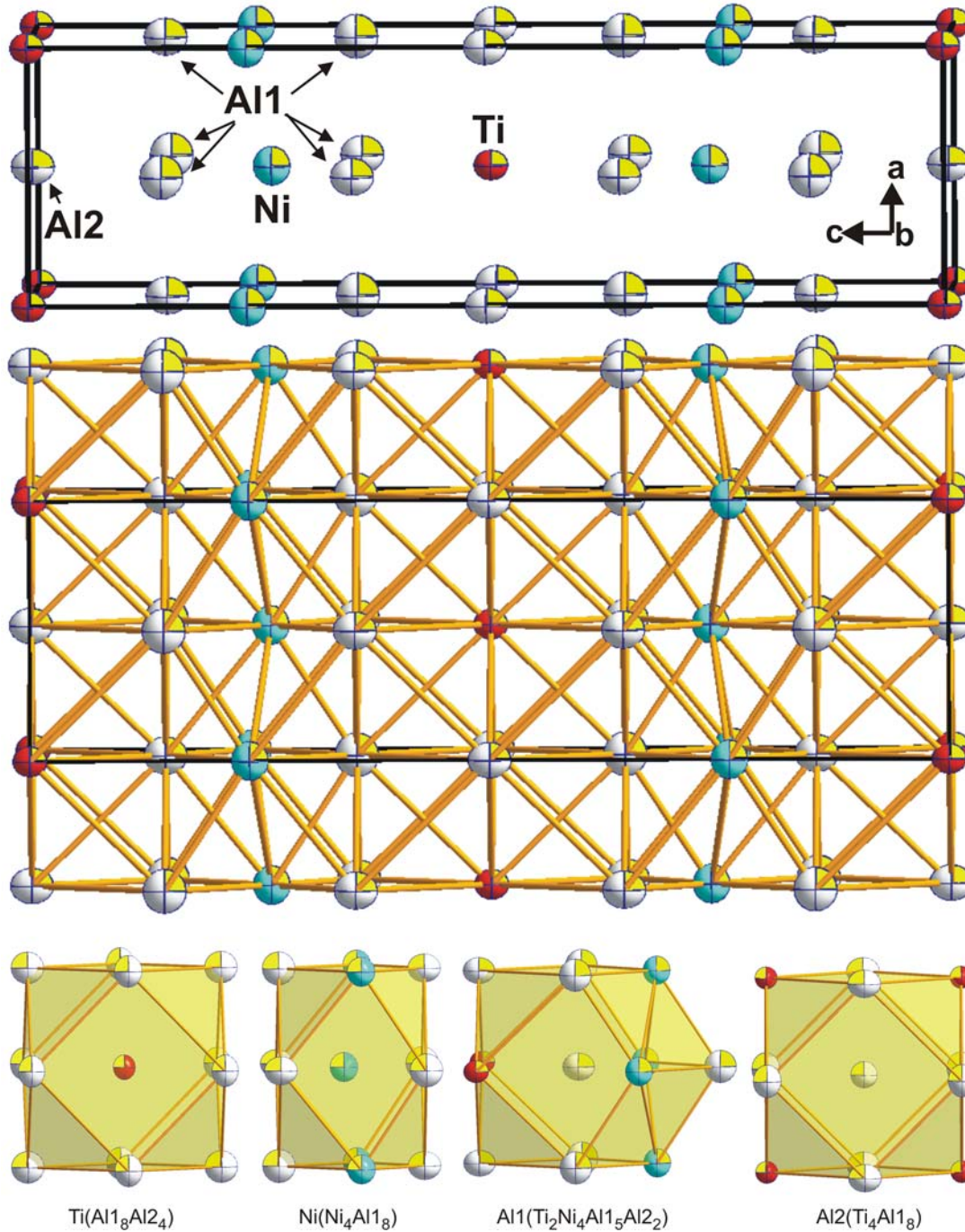
Fig. 6: Crystal structure and coordination polyhedra of τ_5-TiNi$_{2-x}$Al$_5$ in three-dimensional view with anisotropic displacement parameters from X-ray single crystal refinement. Solid black lines outline the unit cell. Note the corrugated defect Ni - layers in the lattice.

According to the phase equilibria derived for the Al-rich region [1-3], stoichiometric "TiNi$_2$Al$_5$" (= Ti$_{12.5}$Ni$_{25}$Al$_{62.5}$ at.%) would appear at the tie line connecting τ_1 + Ni$_2$Al$_3$ (Fig. 1). Indeed,

Rietveld refinement of a sample $Ti_{15.3}Ni_{21}Al_{63.7}$ (composition from EPMA) with a Ni-content slightly lower than for the stoichiometric formula ($TiNi_2Al_5$) documents the equilibrium $\tau_5 + \tau_1 + Ni_2Al_3$ (Fig. 5) in perfect agreement with the Ni-deficiency in τ_5-$TiNi_{2-x}Al_5$.

The crystal structure of τ_5-$TiNi_{2-x}Al_5$ along with the coordination polyhedra for each atom site is presented in Figure 6. Bonding distances in Table 1b are in the range of 0.2385-0.2929 nm. The shortest bond length was found between Ni-Al1 and the longest bond length between Al1-Al1. These values are close to interatomic distances given for Ni_2Al_3 (0.2442-0.2899 nm) in the literature [14], which is in equilibrium with τ_5-$TiNi_{2-x}Al_5$. The puckered layers of Ni-atoms inside the lattice are shown in Fig. 6. The maximum number of ligands (13) was found around Al1 (mono-capped cuboctahedron). In all other cases, slightly distorted cuboctahedra were formed with 12 ligands (Fig. 6).

4.3.2. Transmission electron microscopy.

Grains of τ_5-$TiNi_{2-x}Al_5$, $ZrNi_{2-x}Al_{5-y}$ and $HfNi_{2-x}Al_{5-y}$ were identified via the internal EDX system of the TEM-apparatus. A series of selected area diffraction (SAD) patterns was then taken at various sample tilts. Figures 2(a,b,c) summarize the most representative diffraction patterns with low index zone axes [100], [110], [001] and [111] and their simulations using software JEMS [15]. All diffraction patterns were fully indexed using the lattice parameters found by X-ray and neutron diffraction techniques. No superstructure spots were detected confirming the unit cell dimensions given in Table 1. The observed intensities of diffraction spots correlate well with the simulations based on atomic positions given in Table 1.

4.3.3. Phase reactions involving τ_5-$TiNi_{2-x}Al_5$.

Table 2 contains the EPMA results of a series of samples near τ_5, which were annealed in the temperature range of 1050°C to 900°C. These analyses prove that there is no change in phase equilibria between 900°C and 1050°C. The micrograph of a sample annealed at 900°C is shown in Fig. 4b, which furthermore suggests that earlier claims Schuster et al. [2] on the proposed four-phase reactions: $\tau_1 + Ni_2Al_3 \Leftrightarrow \tau_2 + \tau_5$ at $\leq$1000°C and $\tau_1 + \tau_5 \Leftrightarrow \tau_2 + TiAl_3$ at 800°C < T < 1000°C Schuster et al. [2] may only hold for temperatures lower than 900°C.

Table 2. EPMA (at. %) and X-rays results of selected Ti-Ni-Al samples involving τ_5.

Nominal composition			H. T.*	Phases	Structure type	Space group	Lattice parameters (nm)		EPMA		
Ti	Ni	Al					a	c	Ti	Ni	Al
13.9	19.7	66.4	1050	τ_5	$ZrNi_2Al_5$	$I4/mmm$	0.39542(4)	1.40682(9)	13.9	20.5	65.6
				τ_1	Cu_3Au	Pm-$3m$	0.39338(8)		25.6	7.7	66.7
				Ni_2Al_3	Ni_2Al_3	P-$3m1$	0.40403(3)	0.49025(8)	0.7	41.1	58.2
14.3	20.4	65.3	1020	τ_5	$ZrNi_2Al_5$	$I4/mmm$	0.39567(5)	1.40698(9)	14.0	20.1	65.9
				τ_1	Cu_3Au	Pm-$3m$	0.39368(3)		25.3	7.5	67.2
				Ni_2Al_3	Ni_2Al_3	P-$3m1$	0.40409(5)	0.49027(6)	0.6	39.9	59.5
15	17	68	1020	τ_5	$ZrNi_2Al_5$	$I4/mmm$	0.39578(7)	1.40455(8)	14.0	19.8	66.2
				τ_1	Cu_3Au	Pm-$3m$	0.39381(3)		25.2	7.4	67.4
				$TiAl_3$	$TiAl_3$	$I4/mmm$	0.38474(2)	0.86079(7)	23.4	3.8	72.8
14	20	66	950	τ_5	$ZrNi_2Al_5$	$I4/mmm$	0.39549(6)	1.40781(9)	13.9	20.9	65.2
				τ_1	Cu_3Au	Pm-$3m$	0.39385(1)		25.9	8.0	66.1
				Ni_2Al_3	Ni_2Al_3	P-$3m1$	0.40373(5)	0.49025(9)	0.7	41.3	58.0
16	22	62	900	τ_5	$ZrNi_2Al_5$	$I4/mmm$	0.39573(2)	1.40822(8)	13.9	21.2	64.9
				τ_1	Cu_3Au	Pm-$3m$	0.39366(6)		25.9	8.3	65.8
				Ni_2Al_3	Ni_2Al_3	P-$3m1$	0.40407(4)	0.48986(4)	0.7	40.9	58.4

*Heat Treatment at temperatures (°C).
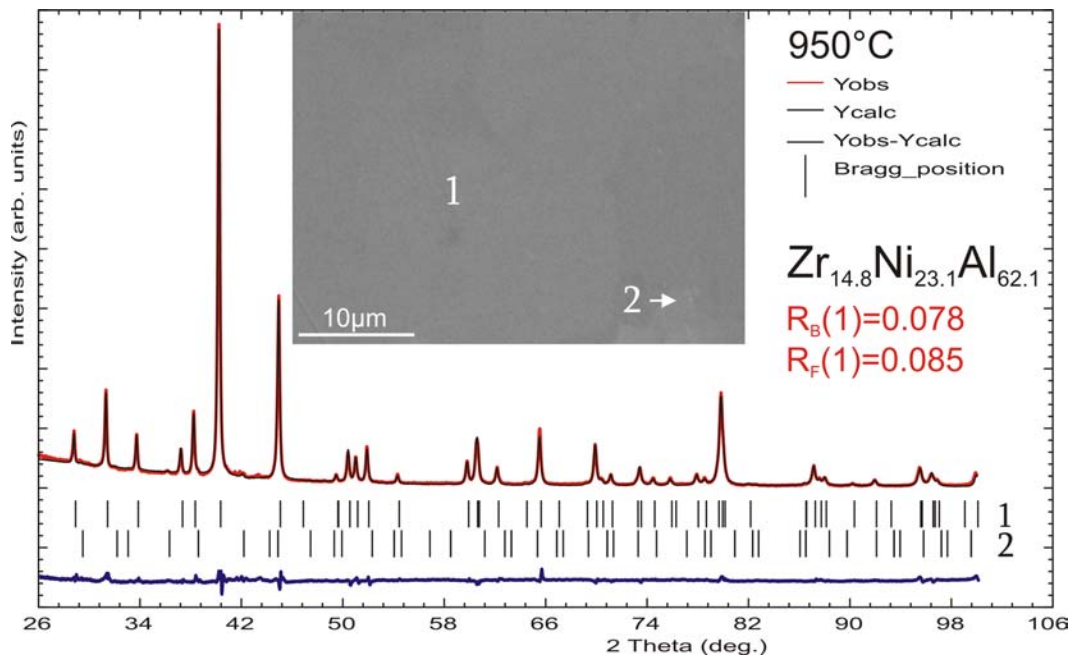
Fig. 7: Rietveld refinement for alloy $Zr_{14.8}Ni_{23.1}Al_{62.1}$ (EPMA, at. %), annealed at 950°C and quenched, revealing the two-phase equilibrium between $ZrNi_2Al_5$ (phase 1) and traces of the Th_6Mn_{23}-type phase (phase 2).

4.3.4. Refinement of ZrNi$_{2-x}$Al$_{5-y}$, x = 0.4, y = 0.4 and of isotypic HfNi$_{2-x}$Al$_{5-y}$, x = 0.5, y = 0.2.

Although the crystal structure of ZrNi$_2$Al$_5$ was described by Markiv et al. [8] on the basis of X-ray single crystal photographs [R$_F$(h0l)=0.116], the rather high R-value might have masked details on atom site occupancies. Our refinement of an X-ray powder spectrum for the alloy Zr$_{14.8}$Ni$_{23.1}$Al$_{62.1}$ (Fig. 7; composition in at. % from EPMA) unambiguously revealed the presence of vacancies for the Ni-site 4e and a composition Zr$_{13.3}$Ni$_{20.1}$Al$_{66.6}$ in contrast to a significantly lower Al-content obtained by EPMA (Zr$_{14.4}$Ni$_{23.2}$Al$_{62.4}$, at %). Therefore considering the high temperature factors for Al on the 8g site, the presence of additional vacancies was suggested. Subsequent refinement of the Al-occupancy in this site reveals the composition ZrNi$_{2-x}$Al$_{5-y}$, x = 0.4, y = 0.4 (Zr$_{13.9}$Ni$_{22.1}$Al$_{64.0}$, Table 1a) which is in good agreement with EPMA (Zr$_{14.4}$Ni$_{23.2}$Al$_{62.4}$, at %). It has to be noted that atomic coordinates agree well with those reported by Markiv [8] (Table 3).
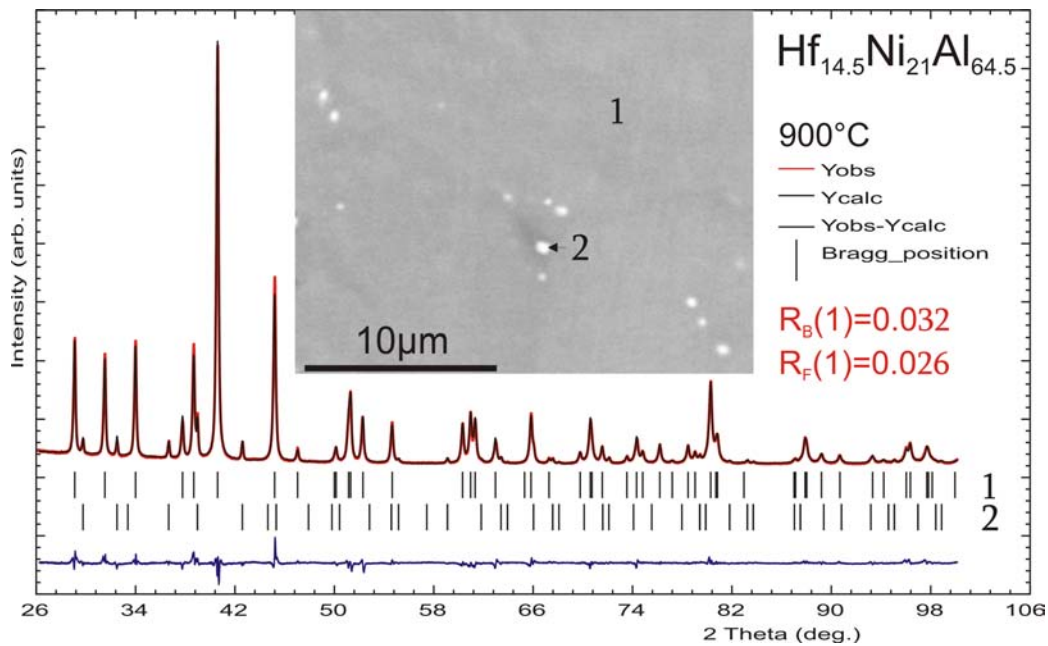
Fig. 8: Rietveld refinement for alloy Hf$_{14.5}$Ni$_{21}$Al$_{64.5}$ (nominal composition, annealed at 900°C and quenched), revealing the two-phase equilibrium between Hf$_{14.3}$Ni$_{21.7}$Al$_{64.0}$ (EPMA, at. %, ZrNi$_2$Al$_5$-type, phase 1) and Hf$_{22.0}$Ni$_{25.7}$Al$_{52.3}$ (EPMA, at. %, Th$_6$Mn$_{23}$-type, phase 2).

Although no details besides lattice parameters have been given, the $ZrNi_2Al_5$ structure type was also reported to be present in the system Hf-Ni-Al [6,7]. Alloys prepared at nominal compositions identical with either stoichiometric $HfNi_2Al_5$ or at the position of the Ti-compound, $HfNi_{1.52}Al_5$, both revealed XRD spectra consistent with a $ZrNi_2Al_5$ type lattice. Albeit no considerable homogeneity region was reported for $HfNi_2Al_5$ [6], our lattice parameters [a = 0.40073(1), c = 1.4291(1) nm] differ considerably from those given earlier [7] [a = 0.401, c = 1.412 nm]. Figure 8 shows the Rietveld refinement of a two-phase sample at the nominal composition of $Hf_{14.5}Ni_{21}Al_{64.5}$ revealing the $HfNi_2Al_5$-phase in equilibrium with a Th_6Mn_{23}-type phase ($Hf_{22.0}Ni_{25.7}Al_{52.3}$).

Results of the refinement are summarized in Table 1a and yield vacancies on two crystallographic sites ($4e$ and $8g$) corresponding to the overall formula $HfNi_{2-x}Al_{5-y}$, x = 0.5, y = 0.2. Ni-vacancies on the $4e$ site yield the composition $Hf_{13.3}Ni_{20}Al_{66.7}$, which is inconsistent with the data from EPMA ($Hf_{14.3}Ni_{21.7}Al_{64.0}$). An additional vacancy on the Al-site $8g$ (similar to isotypic $ZrNi_{1.6}Al_{4.6}$) is indicated by the high temperature factor and reveals a final composition $Hf_{13.7}Ni_{20.6}Al_{65.7}$, which is close to the composition $Hf_{14.3}Ni_{21.7}Al_{64.0}$ obtained by EPMA. It needs to be emphasized that indexing of the powder spectra for both compounds $\{Zr,Hf\}Ni_{2-x}Al_{5-y}$ was complete and is backed by the TEM diffraction data (Fig. 2), which prove the absence of any superstructures for metal/vacancy ordering.

4.3.5. Structural chemistry of τ_5-$TiNi_{2-x}Al_5$ and related phases.

The crystal structure of τ_5-$TiNi_{2-x}Al_5$ is one of the few representatives of the $ZrNi_2Al_5$ type [8,16], which was also reported to exist in the Hf-Ni-Al system [13]. An occupation variant of this structure was encountered recently among rare earth and actinoid members: $CePd_5Al_2$ [17], UPd_5Al_2, $NpPd_5Al_2$ (the first heavy fermion superconductor among neptunium compounds) [18] and $PuPd_5Al_2$ [19,20]. A search for structural relations of $ZrNi_2Al_5$ in TYPIX [16] shows that this structure is a deformation and substitution derivative of Cu and $TiAl_3$ (double unit cell of Cu) and further symmetry reduction leads to the $ZrNi_{1.3}Ga_{5.7}$-type (S.G. *Immm*) [21] (Fig. 9).

$Fm\bar{3}m$
Cu

Cu: 4a $m\bar{3}m$
0
0
0

↓ t3
a, b, 2c

$I4/mmm$
TiAl$_3$

Ti: 2a 4/mmm	Al1: 2b 4/mmm	Al2: 4d -4m2
0	0	0
0	0	½
0	½	¼

↓ i2
a, b, 2c

$I4/mmm$
ZrNi$_2$Al$_5$

Zr: 2a 4/mmm	Al1: 2b 4/mmm	Ni: 4e 4mm	Al1: 8g 2mm
0	0	0	0
0	0	0	½
0	½	0.238	0.149

↓ t2

$Immm$
ZrNi$_{1.3}$Ga$_{5.7}$

Zr: 2a mmm	M1: 2c mmm	M2: 4i mm2	M3: 4j mm2	M4: 4j mm2
0	½	0	½	½
0	½	0	0	0
0	0	0.228	0.144	0.352
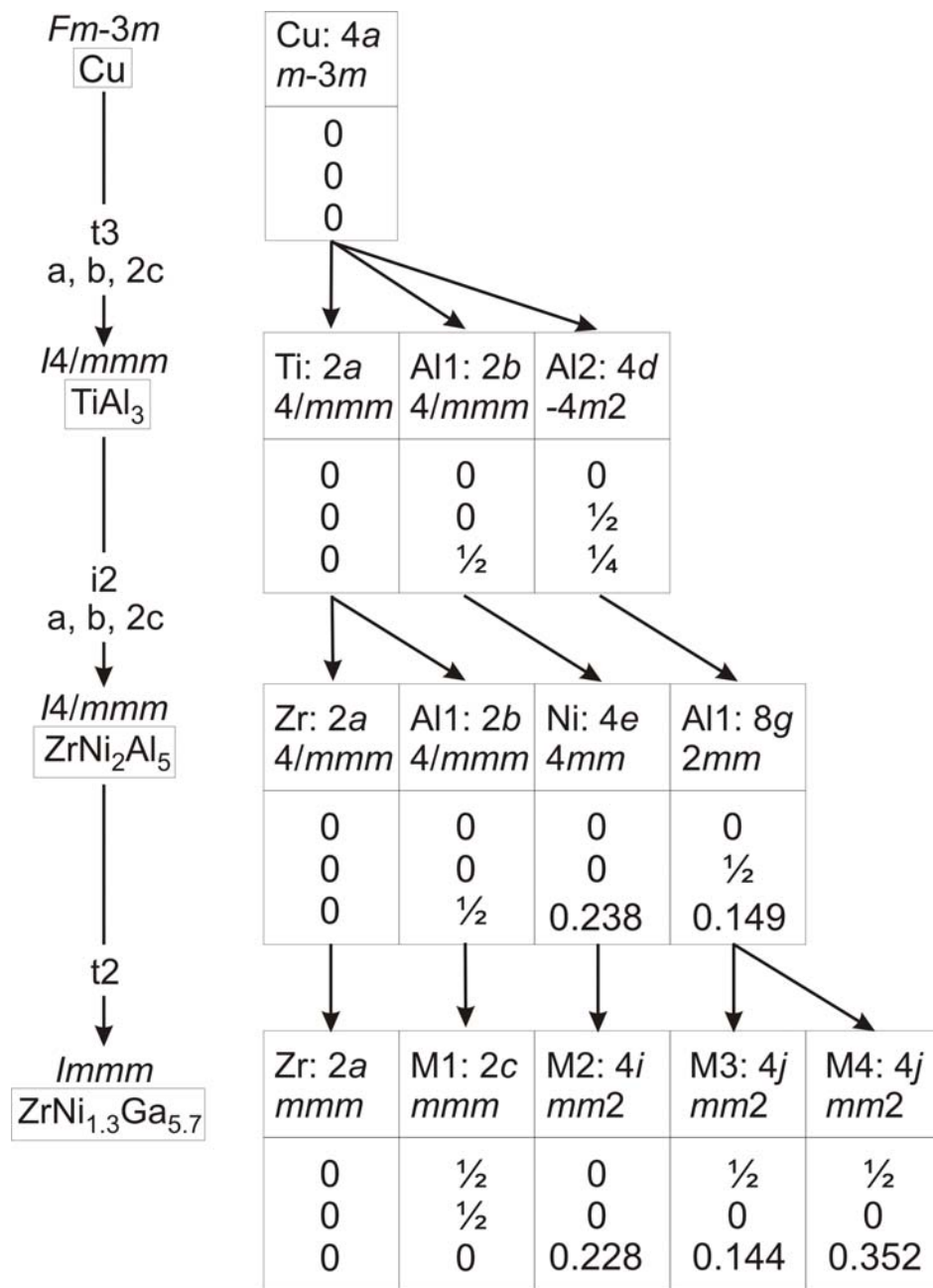
Fig. 9: Bärnighausen tree relating the structure types of Cu, TiAl$_3$, ZrNi$_2$Al$_5$ and Zr(Ni,Ga)$_7$.

Interestingly, a metal cuboctahedron is the coordination figure in Al and Ni (Cu–type) as well as in τ_1 (AuCu$_3$ type structure) and these polyhedra dominate in almost all titanium and nickel binary aluminides. However, this atom environment is rare in Ti-Ni compounds. Respectively no Ti-Ni bonds are encountered for τ_5-TiNi$_{2-x}$Al$_5$. The crystallographic group-subgroup relationship

among the structure types of Cu, TiAl$_3$, ZrNi$_2$Al$_5$ and Zr(Ni,Ga)$_7$ have been defined in terms of a Bärnighausen scheme (see Fig. 9).

4.4. Conclusion

The crystal structure of τ_5-TiNi$_{2-x}$Al$_5$ was solved from X-ray single crystal data (space group $I4/mmm$, a = 0.3984(2) nm, c = 1.4073(3) nm). TEM data assured the unit cell dimensions, the crystal symmetry and the absence of superstructures. Combined refinement of XPD and NPD data confirmed the full atom order as well as the partially defect Ni-site 4e (occ. = 0.76). The structure of τ_5-TiNi$_{2-x}$Al$_5$ is isostructural with the ZrNi$_2$Al$_5$ type. Rietveld X-ray powder data refinement of the homologous compounds ZrNi$_{2-x}$Al$_{5-y}$, x = 0.4, y = 0.4 and HfNi$_{2-x}$Al$_{5-y}$, x = 0.5, y = 0.2 showed full atom order for Ti (2a) and Al (2b) as well as defects on Ni (4e) and Al (8g)-sites. A Bärnighausen scheme has been derived, which depicts the evolution of the crystallographic group-subgroup relationship among the structure types of Cu, TiAl$_3$, ZrNi$_2$Al$_5$ and Zr(Ni,Ga)$_7$.

References

[1] J.J. Ding, P. Rogl and H. Schmidt, Journal of Alloys and Compounds **317-318** (2001), p. 379-384.

[2] J.C. Schuster, Z. Pan, S. Liu, F. Weitzer and Y. Du, Intermetallics **15** (2007), p. 1257-1267.

[3] J. Bursik and P. Broz, Intermetallics **17** (2009), p. 591-595.

[4] G. Ghosh, G. Effenberg and S. Ilyenko, Springer Materials-The Landolt-Börnstein Database, DOI: 10.1007/10915998_10, (2005).

[5] V. Raghavan, Journal of Phase Equilibria and Diffusion **30(1)** (2009) p. 64-66.

[6] V.Ya. Markiv and V.V. Burnashova, Russ. Metall. **6** (1969) p. 113-115.

[7] V.Ya. Markiv and V.V. Burnashova, Dopov. Akad. Nauk Ukr. RSR, **A5** (1969) p. 463-446.

[8] V.Ya. Markiv, P.I. Kripjakevich, N.N. Beljavina, Dopov. Akad. Nauk Ukr. RSR, Ser. A, **44**, Fiziko-Matematichni Ta Tekhnichni Nauki, (1982), p. 78.

[9] A.U. Khan, X. Yan, P. Rogl and A. Saccone, Intermetallics **17** (2009) p. 1000-1006.

[10] A.U. Khan, A. Grytsiv, X. Yan, P. Rogl, A. Saccone, V. Pomjakushin and G. Giester, Inorganic Chemistry 50, (2011), p. 4537-4547.

[11] P. Fischer, G. Frey, M. Koch, M. Koennecke, V. Pomjakushin, J. Schefer, R. Thut, N. Schlumpf, R. Buerge, U. Greuter, S. Bondt and E. Berruyer, Physica B, **146** (2000) p. 276-278.

[12] P. Villars, K. Cenzual, Pearson's Crystal Data, Release 2010, ASM International, Ohio, USA.

[13] L.M. Gelato and E. Parthé, J. Appl. Crystallogr. **20** (1987), p. 139-143.

[14] M. Ellner, U. Kattner and B. Predel, Journal of Less-Common Metals, **87** (1982), p. 305-325.

[15] P. Stadelmann, JEMS: Java Electron Microscopy Software (2007). Available from: http://cimewww.epfl.ch/people/stadelmann/jemswebsite/jems.html.

[16] E. Parthe, L. Gelato, B. Chabot, M. Penzo, K. Cenzual and R. Gladyshevskii, TYPIX in Gmelin Handbook of Inorganic and Organometallic Chemistry, **1994**, Volume 4, 8th edition, Springer-Verlag.

[17] R.A. Ribeiro, T. Onimaru, K. Umeo, M.A. Avila, K. Shigetoh and T. Takabatake, J. Phys. Soc. Jpn. **76** (2007), 123710.

[18] Y. Haga, D. Aoki, Y. Homma, S. Ikeda, T.D. Matsuda, E. Yamamoto, H. Sakai, N. Tateiwa, N. Dung, A. Nakamura, Y. Shiokawa and Y. Onuki, Journal of Alloys and Compounds **464** (2008), p. 47-50.

[19] J.-C. Griveau, K. Gofryk, E. Colineau, J. Rebizant, Journal of Nuclear Materials **385** (2009), p. 11-14.

[20] K. Gofryk, J-C. Griveau, E. Colineau, and J. Rebizant, Physical Review B **77** (2008) 092405.

[21] V.Y. Markiv, N.N. Belyavina and A.A. Babenko, Dopov. Akad. Nauk Ukr. RSR **Ser. B** (1983) 7-41.

5. Phase Relations and Crystal Structure of τ_6-Ti$_2$(Ti$_{0.16}$Ni$_{0.43}$Al$_{0.41}$)$_3$

5.1. Introduction

Although several research teams have investigated the Ti-Ni-Al system, different phase constitution has been presented [1-9]. For details, the reader may be referred to recent assessments of phase diagram data by Raghavan [10,11] and by Schuster [12]. Thermodynamic calculations of the Ti-Ni-Al system were performed by three different groups [9,13,14]. In our recent reinvestigation [15], two four-phase reactions have been elucidated, which have solved some of the hitherto puzzling data: (i) NiAl + τ_3-TiNiAl (Laves phase) $\Leftrightarrow$ τ_2-TiNiAl$_2$ + τ_4-TiNi$_2$Al (Heusler-phase) at 925°C $\pm$ 15°C and (ii) τ_3-TiNiAl + τ_1-Ti$_3$NiAl$_8$ (AuCu$_3$-type) $\Leftrightarrow$ TiAl$_2$ + τ_2-TiNiAl$_2$ at 990°C $\pm$ 15°C. Furthermore we confirmed the three-phase field τ_4 + α_2-Ti$_3$Al + τ_3, as reported at 900°C by Huneau et al. [6], whilst Schuster et al. [9] claimed a four-phase reaction {Ti,Al}$_2$Ni + τ_3 $\Leftrightarrow$ α_2 + τ_4 at 876±2°C. For the Ti-rich region, we confirmed the findings of Grytsiv et al. [16] on a hitherto unknown phase τ_6 (near "Ti$_2$NiAl"(Ti$_{47-49}$Ni$_{27}$Al$_{26-24}$), which at that time was named τ_5). In the meantime another phase in the Al-rich corner "Ti$_{15}$Ni$_{20}$Al$_{65}$" was labeled as τ_5 [12]. In order to reduce confusion, we will keep the Al-rich phase as τ_5 and will label the Ti-rich phase reported by Grytsiv et al. [16] as τ_6. As hitherto neither phase equilibria data involving the τ_6-phase nor crystal structure data have been published for τ_6, the current investigation was designed to provide this information including a reinvestigation of the structure of (Ti,Al)$_2$Ni on the basis of X-ray single crystal (XSC) data. Although atom distribution in η-(Ti$_{0.81}$Al$_{0.19}$)$_2$Ni has been defined from X-ray Rietveld powder refinement [17], single crystal data were used to derive high precision atom positions and particularly to check on the electron density at the centers of vacant metal octahedra.

5.2. Experimental Details

In order to find the reaction types and reaction temperatures related to τ_6, we have prepared 60 alloys (each of 1-2 grams) from high purity metal ingots of Ti, Ni and Al (purity 99.9 mass %,

Alfa Johnson Matthey GmbH, D) by arc melting under argon atmosphere. Alloys were melted three times for homogenization (weight loss less than 0.1 %). Then the reguli were wrapped in Mo-foil to protect them from attack by the hot quartz walls, sealed in evacuated quartz tubes and annealed for 10 days at temperatures from 850°C to 1000°C in steps of 5-10°. Temperature at the position of samples was controlled by a high quality standard thermocouple: the melting points of metal standards (5N-Ag, 5N-Cu) in the furnace used for all our annealing procedures were recorded within ±3°C of the temperature listed in the International Temperature Scale ITS-90. All samples were quenched in cold water after annealing. Lattice parameters and standard deviations were determined by least squares refinements of room temperature X-Ray powder Diffraction (XRD) data recorded with a Guinier-Huber image plate employing monochromatic Cu Kα_1 radiation. As cast and annealed samples were polished using standard procedures and were examined by optical metallography and scanning electron microscopy (SEM). Compositions were determined in an Electron Probe Micro-Analyzer (EPMA) on a Carl Zeiss EVO 40 equipped with a Pentafet Link EDX system operated at 20 kV. Pure elements were used as standards to carry out the deconvolution of overlapping peaks and background subtraction. Finally the X-ray intensities were corrected for ZAF effects using the INCA-Energy 300 software package [For details, see chapter 2]. Overall composition of the samples derived from EPMA area scans agree with the nominal values within 0.5 at. %.

Thermal analyses were performed in a calibrated Netzsch STA 409 PG/4/G Luxx Differential Scanning Calorimeter (DSC) employing a heating rate of 1-5 K/min in Al_2O_3 crucibles under a stream of 6N argon. Prior to DTA (differential thermal analysis), the alloys were annealed at 850°C for 10 days.

Single crystals of τ_6 (30×35×35 nm) as well as of η-$(Ti,Al)_2Ni$ (60×50×50 nm) were mechanically isolated from arc-melted specimens $Ti_{54}Ni_{25}Al_{21}$ and $Ti_{54.3}Ni_{32.3}Al_{13.4}$, which were annealed at 975°C and 980°C respectively. The crystals were inspected on an AXS-GADDS texture goniometer for quality and crystal symmetry prior to X-ray intensity data collection on a four-circle Nonius Kappa diffractometer (CCD area detector and graphite monochromated MoK$_\alpha$ radiation, λ = 0.071069 nm). Orientation matrix and unit cell parameters were derived using the program DENZO [For details, see chapter 2]. No absorption correction was necessary because of the rather regular crystal shape and small dimensions of the investigated specimens. The

structures were solved by direct methods and refined with the SHELXS-97 and SHELXL-97 programs [For details, see chapter 2], respectively.

As for neutron powder diffraction (NPD), a sample with a total mass of about 6 grams was necessary, ten individual alloys of smaller mass (1 g) to facilitate quenching were prepared (at the nominal composition $Ti_{51}Ni_{25}Al_{24}$ and annealed at 925°C), from which six specimens with identical lattice parameters for the τ_6-phase were selected and powdered to a grain size below 40 µm in order to reduce preferential orientation effects. Neutron diffraction was performed at room temperature on the high resolution HRPT diffractometer [18] at the SINQ spallation source of the Paul Scherrer Institute (Switzerland). The diffractometer was used in high intensity mode ($\Delta d/d \geq 2\times10^{-3}$) with a neutron wavelength $\lambda_{neutron}$=0.188570 nm within the angular 2θ range from 3.85° to 164.2°. Combined Rietveld multi-pattern refinements of the X-ray and neutron powder diffraction data were performed with the FULLPROF program [For details, see chapter 2] with the use of its internal tables for scattering lengths and atom form factors.

5.3. Results and discussion

5.3.1. The crystal structure of τ_6-$Ti_2(Ti_{0.16}Ni_{0.43}Al_{0.41})_3$ from combined X-ray single crystal, X-ray powder and neutron powder diffraction analyses.

Unit cell parameters [a=1.85383(7), b=0.49970(2), c=0.81511(3) nm, ß=99.597(3)°] and systematic extinctions for a C-centered lattice are compatible with three monoclinic space group symmetries: $C2$, Cm and $C2/m$. Solution of the structure by direct methods in all these space groups revealed the same atomic order in the crystal lattice. As practically identical reliability factors and residual electron densities were obtained for these three refinements and as an analysis of missing symmetry by program PLATON confirmed $2/m$, we describe the structure in the highest symmetric space group $C2/m$. Including anisotropic atomic displacement parameters for all atoms, the refinement converged to $R_{F2} = 0.038$ with residual electron densities ≤ 1.4 e⁻/10⁻³nm³. At this stage, the composition of τ_6, as derived from the single crystal refinement, was $Ti_{53.22}Ni_{25.26}Al_{21.22}$, close to the formula "$Ti_2NiAl$" and within 2 to 3 atom % of the EPMA data. Although XRD intensities collected from a polycrystalline sample are in perfect agreement with the intensities calculated from the structural model taken from the single crystal, a corresponding

neutron powder spectrum showed severe discrepancies and was not explained to satisfaction. Due to the negative neutron scattering length of natural titanium, neutron powder diffraction data are very sensitive to the location of Ti atoms in the lattice, whereas the occupation of a random mixture of Ni and Al atoms in proper proportions may constitute the X-ray scattering power of a titanium atom (at $\dfrac{\sin\theta}{\lambda} = 0$: $0.60 \times f_{Ni} + 0.40 \times f_{Al} = f_{Ti}$). Therefore a combined analysis of XRD and NPD data is necessary to unambiguously define the site preference. Albeit refinement of the neutron powder data unambiguously confirmed the five crystallographic positions (Ti1-Ti5, see Table 1) completely occupied by Ti, refinements of random mixtures of two atom species for the remaining six crystallographic sites were unsuccessful.

Table 1a: X-ray single crystal data for τ_6-Ti$_2$(Ti$_{0.16}$Ni$_{0.43}$Al$_{0.41}$)$_3$, space group $C2/m$, #12 (V$_2$(Co$_{0.57}$Si$_{0.43}$)$_3$ structure type) standardized with program *Structure Tidy* [19]. XSC; $2 \leq 2\Theta \leq 72.05$; ω-scans, scan width $2°$; 150 sec/frame, NPD; $3.85 \leq 2\Theta \leq 164.8$ and XRD; $8 \leq 2\Theta \leq 100$.

Parameter/Diff. Technique	XSC	NPD	XRD
Composition from EPMA in (at.%)	Ti$_{50}$Ni$_{26.4}$Al$_{23.6}$	Ti$_{48.6}$Ni$_{27.3}$Al$_{24.1}$	
Composition from refinement (at.%)	Ti$_{49.5}$Ni$_{26.1}$Al$_{24.4}$	Ti$_{49.0}$Ni$_{27.2}$Al$_{23.8}$	
Formula from refinement	Ti$_{2.48}$Ni$_{1.30}$Al$_{1.22}$ = Ti$_2$(Ti$_{0.16}$Ni$_{0.43}$Al$_{0.41}$)$_3$	Ti$_{2.45}$Ni$_{1.36}$Al$_{1.19}$ = Ti$_2$(Ti$_{0.15}$Ni$_{0.45}$Al$_{0.40}$)$_3$	
Radiation, λ (nm)	Mo Kα = 0.071069	λ_n = 0.18857	Cu Kα_1 = 0.154056
a (nm)	1.85383(7)	1.84668(9)	1.84685(3)
b (nm)	0.49970(2)	0.49895(3)	0.49890(1)
c (nm)	0.81511(3)	0.81411(4)	0.81380(1)
β (°)	99.597(3)	99.541(4)	99.560(1)
V (nm^3)	0.74452	0.75012	0.74982
Reflections in refinement	1185>4σ(F$_o$) of 1888	529	501
Mosaicity	0.45	-	-
Number of variables	89	54	54
$R_F = \Sigma|F_0\text{-}F_c|/\Sigma F_0$	-	0.055	0.036
$R_I = \Sigma|I_0\text{-}I_c|/\Sigma I_0$	-	0.034	0.043
$R_{wP} = [\Sigma w_i|y_{0i}\text{-}y_{ci}|^2/\Sigma w_i|y_{0i}|^2]^{1/2}$	-	0.117	0.065
$R_P = \Sigma|y_{0i}\text{-}y_{ci}|/\Sigma|y_{0i}|$	-	0.097	0.072
$R_e = [(N\text{-}P+C)/\Sigma w_i y_{0i}^2]^{1/2}$	-	0.012	0.009
$\chi^2 = (R_{wP}/R_e)^2$	-	8.00	4.82
$R_F^2 = \Sigma|F_0^2\text{-}F_c^2|/\Sigma F_0^2$	0.0375	-	-
R_{Int}	0.075	-	-
wR2	0.086	-	-
GOF	1.047	-	-
Extinction (Zachariasen)	0.0004(1)	-	-
Residual density e$^-$/Å^3; max; min.	1.40; -1.35	-	-
Atom parameters			
Ti1 in 4i (x, 0, z); x, z	0.28542(5), 0.08003(10)	0.2859(3), 0.0771(7)	
U$_{11}$, U$_{22}$, U$_{33}$	0.0127(4), 0.0111(4), 0.0129(4)	B$_{iso}$ = 0.41(3)	
U$_{23}$ = U$_{12}$ = 0, U$_{13}$	0.0009(3)	-	
Ti2 in 4i (x, 0, z); x, z	0.55163(4), 0.36002(10)	0.5478(3), 0.3684(7)	
U$_{11}$, U$_{22}$, U$_{33}$	0.0131(4), 0.0115(4), 0.0135(4)	B$_{iso}$ = 0.87(2)	
U$_{23}$ = U$_{12}$ = 0, U$_{13}$	0.0025(3)	-	
Ti3 in 4i (x, 0, z); x, z	0.28915(4), 0.45288(10)	0.2917(3), 0.4533(7)	
U$_{11}$, U$_{22}$, U$_{33}$	0.0137(4), 0.0110(4), 0.0127(4)	B$_{iso}$ = 0.67(2)	
U$_{23}$ = U$_{12}$ = 0, U$_{13}$	0.0031(3)	-	
Ti4 in 4i (x, 0, z); x, z	0.02358(4), 0.16884(10)	0.02754(3), 0.1767(6)	
U$_{11}$, U$_{22}$, U$_{33}$	0.0132(4), 0.0109(4), 0.0114(4)	B$_{iso}$ = 0.84(2)	
U$_{23}$ = U$_{12}$ = 0, U$_{13}$	0.0026(3)	-	

Ti5 in 4i (x, 0, z); x, z	0.43475(4), 0.01961(10)		0.4316(3), 0.0153(6)	
U_{11}, U_{22}, U_{33}	0.0129(4), 0.0128(4), 0.0163(4)		$B_{iso} = 0.73(2)$	
$U_{23} = U_{12} = 0, U_{13}$	0.0038(3)		-	
M1 in 4i (x, 0, z); Occ., x, z	0.073(1) Ti + 0.462 Ni + 0.465 Al		0.073(1) Ti + 0.462 Ni + 0.465 Al	
	0.86891(4), 0.04377(10)		0.8706(3), 0.0446(7)	
U_{11}, U_{22}, U_{33}	0.0128(4), 0.0110(4), 0.0128(4)		$B_{iso} = 0.43(1)$	
$U_{23} = U_{12} = 0, U_{13}$	0.0022(3)		-	
M2 in 8j (x, y, z); Occ., x, y, z	0.136(1) Ti + 0.421 Ni + 0.443 Al		0.110(1) Ti + 0.482 Ni + 0.407 Al	
	0.16874(3), 0.25531(11), 0.21856(7)		0.1685(2), 0.2600(8), 0.2202(4)	
U_{11}, U_{22}, U_{33}	0.0134(3), 0.0083(3), 0.0112(3)		$B_{iso} = 0.31(1)$	
U_{23}, U_{13}, U_{12}	-0.0003(2), 0.0013(2), -0.0017(2)		-	
M3 in 8j (x, y, z); Occ., x, y, z	0.164(1) Ti + 0.507 Ni + 0.329 Al		0.165(1) Ti + 0.503 Ni + 0.332 Al	
	0.40763(3), 0.23586(11), 0.30969(6)		0.4060(2), 0.2343(6), 0.3073(4)	
U_{11}, U_{22}, U_{33}	0.0134 (3), 0.0105(3), 0.0121(3)		$B_{iso} = 0.81(2)$	
U_{23}, U_{13}, U_{12}	-0.0012(2), 0.0022 (2), -0.0002(2)		-	
M4 in 2c (0, 0, ½); Occ.	0.262(2) Ti + 0.440 Ni + 0.298 Al		0.248(2) Ti + 0.496 Ni + 0.256 Al	
U_{11}, U_{22}, U_{33}	0.0118(6), 0.0133(6), 0.0128(6)		$B_{iso} = 0.26(3)$	
$U_{23} = U_{12} = 0, U_{13}$	0.0027(4)		-	
M5 in 4i (x, 0, z); Occ., x, z	0.151(2) Ti + 0.488 Ni + 0.361 Al		0.150(2) Ti + 0.465 Ni + 0.385 Al	
	0.13348(4), 0.45100(10)		0.1295(3), 0.4552(7)	
U_{11}, U_{22}, U_{33}	0.0125(4), 0.0138(4), 0.0136(4)		$B_{iso} = 0.73(3)$	
$U_{23} = U_{12} = 0, U_{13}$	0.0013(3)		-	
M6 in 4i (x, 0, z); Occ., x, z	0.238(1) Ti + 0.237 Ni + 0.525 Al		0.232(1) Ti + 0.258 Ni + 0.510 Al	
	0.21332(5), 0.73533(11)		0.2158(4), 0.7340(8)	
U_{11}, U_{22}, U_{33}	0.0124(4), 0.0144(5), 0.0133(5)		$B_{iso} = 0.26(3)$	
$U_{23} = U_{12} = 0, U_{13}$	0.0024(4)		-	

* B_{iso} (10^2 nm^2)

Table 1b: Inter atomic distances (nm) for τ_6 taken from XSC refinement (upper right column), standard deviation ≤0.0001 nm.

Ti1-	2M1	0.2871		2M3	0.2916		1Ti1	0.3015
CN = 16	1Ti5	0.2891		2M2	0.2944	M3-	1M3	0.2357
	3M2	0.2897		2Ti2	0.2944	CN = 12	1M4	0.2489
	1M6	0.2902		2Ti5	0.3098		1M1	0.2537
	3M6	0.2915		2Ti5	0.3125		1M5	0.2537
	2M3	0.2935	Ti5-	1Ti5	0.2494		1M6	0.2575
	1M1	0.2980	CN = 14	2M3	0.2761		1M3	0.2640
	2Ti1	0.3015		2M2	0.2775		1Ti5	0.2761
	1Ti3	0.3029		2M1	0.2801		1Ti2	0.2885
Ti2-	2M3	0.2885		1Ti1	0.2891		1Ti3	0.2903
CN = 16	2M2	0.2893		2Ti4	0.3098		1Ti4	0.2916
	2M3	0.2921		2Ti4	0.3125		1Ti2	0.2921
	2Ti4	0.2944		1Ti2	0.3146		1Ti1	0.2935
	2M5	0.2953		1Ti2	0.3223	M4-	4M3	0.2489
	2M4	0.2971	M1-	2M2	0.2487	CN = 12	2M5	0.2571
	1Ti3	0.3088	CN = 12	2M3	0.2537		2Ti4	0.2805
	1Ti5	0.3146		1M6	0.2546		4Ti2	0.2971
	1Ti2	0.3215		2Ti5	0.2801	M5-	2M2	0.2462
	1Ti5	0.3223		1Ti4	0.2850	CN = 12	1M6	0.2534
Ti3-	1M5	0.2884		1Ti1	0.2871		1M4	0.2571
CN = 16	1M6	0.2891		1Ti4	0.2878		2M3	0.2574
	2M3	0.2903		2Ti1	0.2980		1Ti4	0.2806
	2M5	0.2922	M2-	1M2	0.2445		1Ti3	0.2884
	2M6	0.2929	CN = 12	1M5	0.2462		2Ti3	0.2922
	2M2	0.2929		1M6	0.2478		2Ti2	0.2953
	2M2	0.2973		1M1	0.2487	M6-	2M2	0.2478
	1Ti1	0.3029		1M2	0.2552	CN = 12	1M5	0.2534
	2Ti3	0.3051		1Ti5	0.2775		1M1	0.2546
	1Ti2	0.3088		1Ti2	0.2893		2M3	0.2575
Ti4-	1Ti4	0.2746		1Ti1	0.2915		1Ti3	0.2891
CN = 15	1M4	0.2805		1M5	0.2922		1Ti1	0.2902
	1M5	0.2806		1Ti3	0.2929		2Ti1	0.2915
	1M1	0.2850		1Ti3	0.2973		2Ti3	0.2929
	1M1	0.2878						
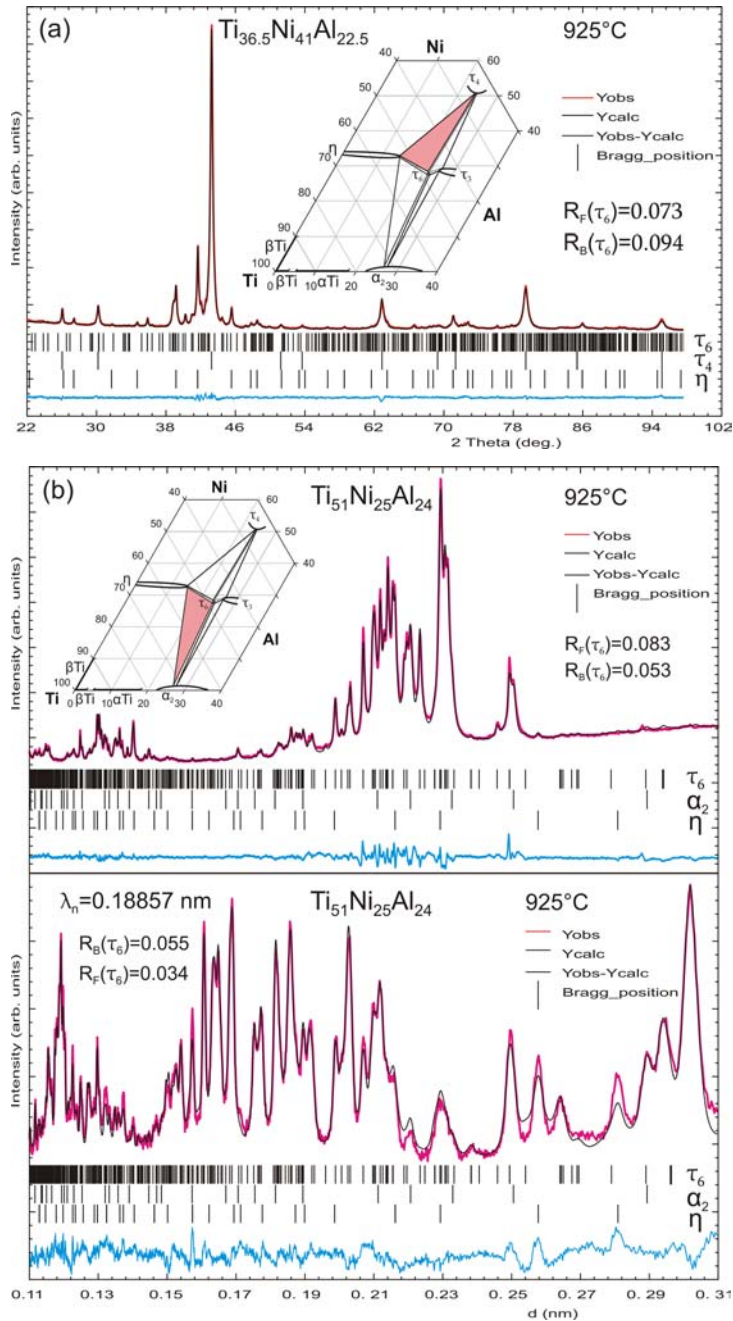
Fig. 1: Rietveld refinements on room temperature spectra (a) for $Ti_{36.5}Ni_{41}Al_{22.5}$ (annealed and quenched from 925°C) showing the three-phase equilibrium $\tau_6 + \tau_4 + \eta$. (b) for $Ti_{51}Ni_{25}Al_{24}$ (annealed and quenched from 925°C) revealing the three-phase equilibrium $\tau_6 + \alpha_2 + \eta$. (b) shows the pattern resulting from the combined refinement of XRD and NPD presented as intensities versus d values for both spectra. Vertical bars represent location of indexed peaks.

Again atom ordering in lower symmetry (space group types *Cm* and *C*2) was pursued to no avail. Therefore returning to the higher symmetry *C2/m* and in order to define the combination of atoms per site (keeping the five Ti-sites already determined), we simply refined the electron density and the nucleon density on every site M1 to M6 (Table 2).

This procedure yields for each site a system of two equations with two variables, the solution of which presents the corresponding random mixture of atoms for each site. The calculations, which are summarized in Table 2, unambiguously imply a mix of the three atom species Ti, Ni, Al on all these sites. A combined XRD and NPD refinement of this model was satisfactory (see Fig. 1, Table 2): (i) it confirmed the atom arrangement derived from the calculation, and (ii) without using the phase composition as a constraint, the proper atom concentrations were obtained. It should be emphasized that crystallographic models that involve a random mixture of only two atom species in sites M1-M6 (Ti + Ni or Ti + Al; for details see Table 2) result in negative occupancies.

Table 2. Observed scattering power and collected occupancies for different models of site preference in τ_6.

Site	Observed scattering power		Calculated occupancy														
			Ti + Ni + Al			Ti + Ni				Ti + Al				Ni + Al			
			X-rays + Neutrons			X-rays		Neutrons		X-rays		Neutrons		X-rays		Neutrons	
	Neutrons	X-rays	Ti	Ni	Al	Ti	Ni	Ti	Ni	Ti	Al	Ti	Al	Ni	Al	Ni	Al
M1	0.574	19.88	0.08	0.41	0.51	1.35	-0.35	0.33	0.67	0.76	0.24	-0.33	1.33	0.46	0.54	0.33	0.67
M2	0.595	20.44	0.08	0.45	0.47	1.26	-0.26	0.32	0.68	0.83	0.17	-0.36	1.36	0.50	0.50	0.37	0.63
M3	0.545	21.56	0.17	0.47	0.36	1.07	-0.07	0.35	0.65	0.95	0.05	-0.29	1.29	0.57	0.43	0.29	0.71
M4	0.403	21.56	0.31	0.39	0.31	1.07	-0.07	0.46	0.54	0.95	0.05	-0.08	1.08	0.57	0.43	0.08	0.92
M5	0.573	21.56	0.15	0.48	0.37	1.07	-0.07	0.33	0.67	0.95	0.05	-0.33	1.33	0.57	0.43	0.33	0.67
M6	0.375	17.92	0.18	0.22	0.60	1.68	-0.68	0.48	0.52	0.55	0.45	-0.04	1.04	0.33	0.67	0.04	0.96

Even for M1 and M2-sites, for which the calculation yielded a minor amount of Ti as a third element, a random mix of three atom species is clearly required in order to achieve a proper ADP (atomic displacement parameter). Based on this atom distribution, the refinement of the X-ray single crystal data gained only marginal improvement with R_{F2} = 0.037 and residual electron densities ≤ 1.4 e$^-$/10^{-3}nm^3. However, as a final composition from the refinement, we arrive at τ_6-Ti$_2$(Ti$_{0.16}$Ni$_{0.43}$Al$_{0.41}$)$_3$, now within 1 atom % of the EPMA data (Table 1a,b).
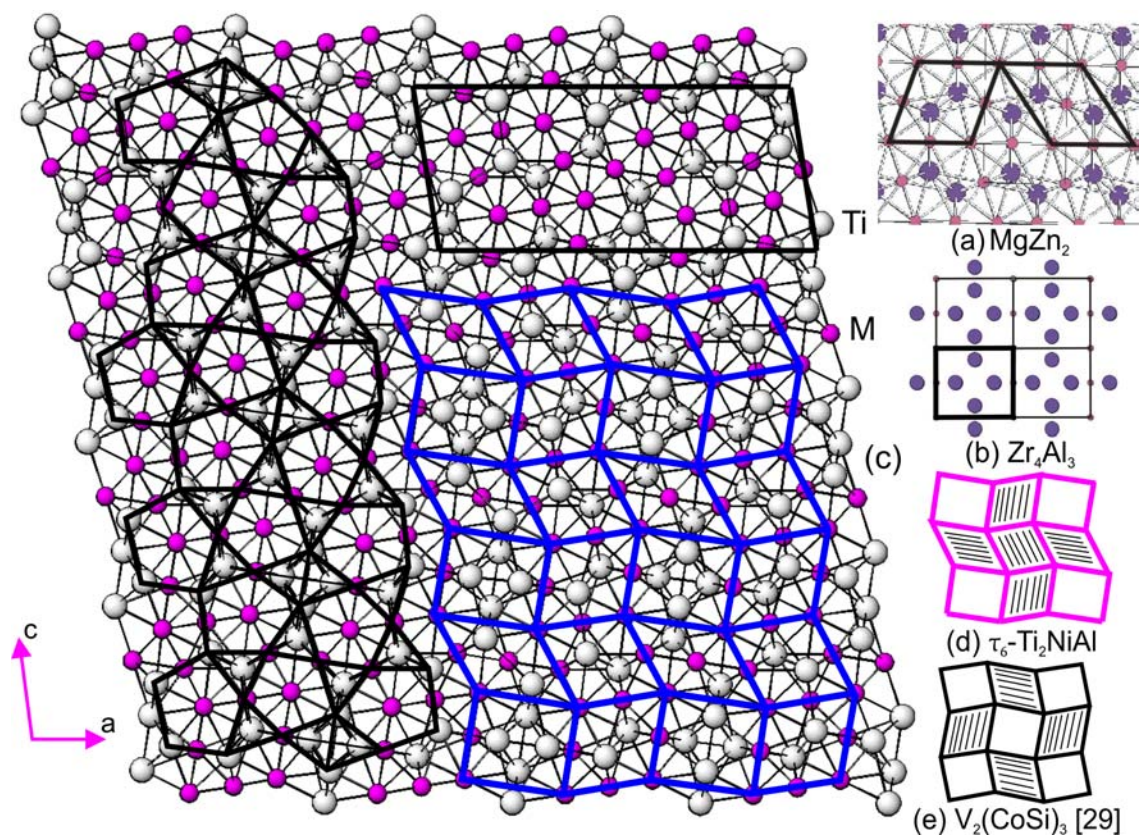
Fig. 2. Crystal structure of $Ti_2(Ti_{0.16}Ni_{0.43}Al_{0.41})_3$ as seen in projection along the [010] axis, a) thick lines highlighting the building blocks of $MgZn_2$, b) Zr_4Al_3-unit highlighted with thick lines, c) unit cell of $Ti_2(Ti_{0.16}Ni_{0.43}Al_{0.41})_3$ shown in upper right part, left part indicates the pentagon-triangle main layers and right part shows blocks of $MgZn_2$ and Zr_4Al_3 forming the structure of τ_6, d) schematic arrangement of $MgZn_2$ (hexagonal ruled boxes) and Zr_4Al_3 units (square unruled boxes) according to this work is outlined in contrast to e) the version shown for $V_2(Co_{0.57}Si_{0.43})_3$ in Typix [24].

A search for the structure type (Pearson symbol: mS50) in Pearson's Crystal Data [20] prompted two compounds, which adopt the same crystal symmetry and Wyckoff sequence i.e. the structures of $V_2(Co_{0.57}Si_{0.43})_3$ [21] and $Mg_{2.3}Ir_{2.7}$ [22]. A comparison of the atom site occupation in τ_6 with these structures is consistent with the fact that the larger polyhedral centers (CN = 14, 15 and 16; distorted Franck-Kasper polyhedra) are occupied by the larger and more electropositive elements V, Mg and Ti.

The crystal structure of τ_6-$Ti_2(Ti_{0.16}Ni_{0.43}Al_{0.41})_3$ is presented in Fig. 2 as seen along the [010] axis and clearly shows the pentagon-triangle main layers of metal atoms. Krypyakevich [21] recognized units of $MgZn_2$ and Zr_4Al_3 (shown in the lower left part of Fig.2) as the building blocks of $V_2(Co_{0.57}Si_{0.43})_3$. The arrangement of these building blocks of corresponding units of

MgZn$_2$ (τ_3 in the Ti-Ni-Al system) and Zr$_4$Al$_3$ is outlined by thick solid lines in the right part of the crystal structure of τ_6 in Fig.2. A comparison of the schematic arrangement of MgZn$_2$ and Zr$_4$Al$_3$ units according to this work with the version given in Typix for V$_2$(Co$_{0.57}$Si$_{0.43}$)$_3$ [24] is outlined in the upper left part of Fig.2 and questions the correctness of the stacking sequence presented earlier [24].

A listing of the inter atomic distances in Ti$_2$(Ti$_{0.16}$Ni$_{0.43}$Al$_{0.41}$)$_3$ is presented in Table 1b. The bonds between Ti-Ti, Ti-M and M-M are in the range of 0.249-0.322 nm, 0.276-0.301 nm and 0.236-0.264 nm, respectively. Shortest interatomic distances are associated with M sites containing higher Ni content. Due to the lack of precise atom positions for V$_2$(Co$_{0.57}$Si$_{0.43}$)$_3$ [21], no comparison can be made. The coordination polyhedra for all independent crystal sites in τ_6 are presented in Fig. 3.
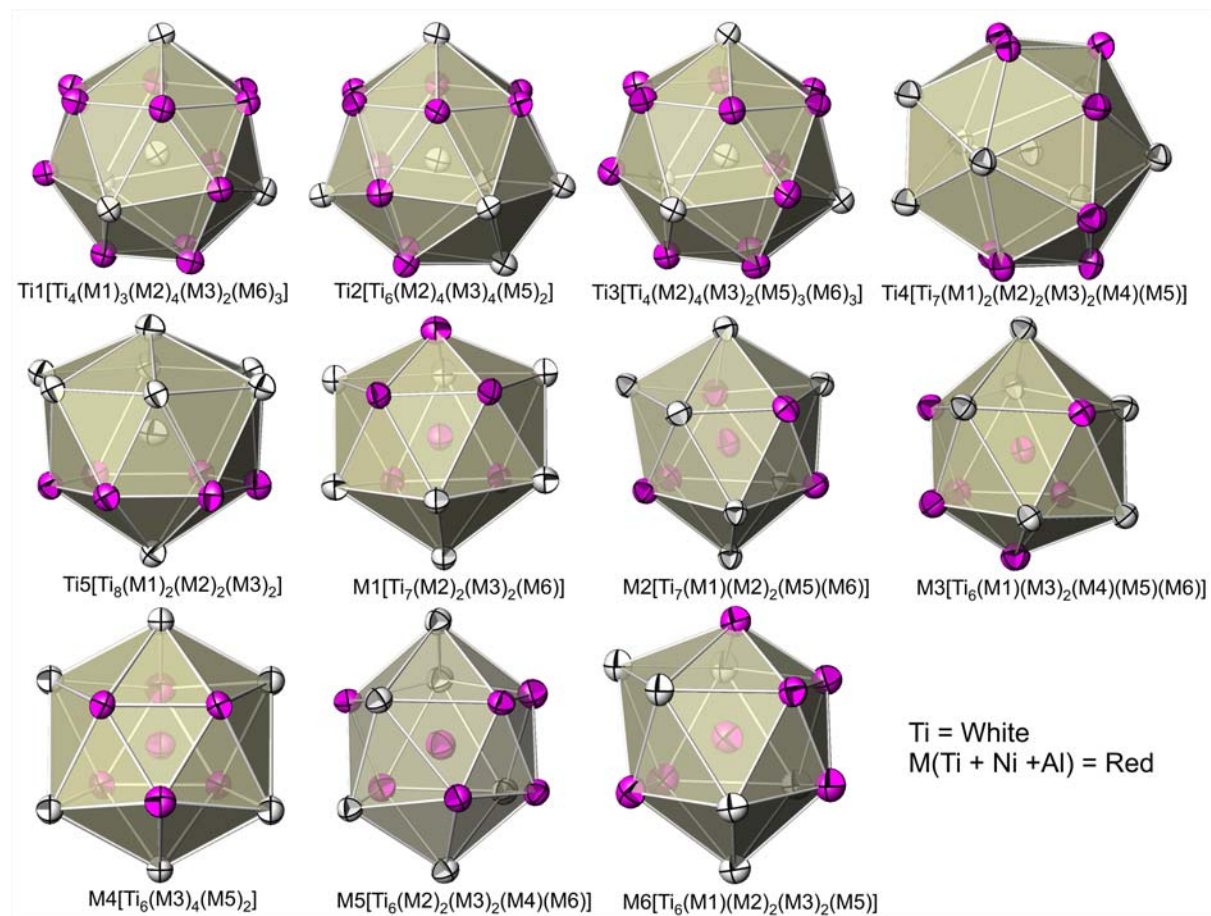
Fig. 3. Coordination polyhedra of τ_6 with anisotropic displacement parameters from single crystal refinement: white atoms represent a position occupied by Ti atoms only and red atoms (dark gray in black & white print) represent the mixed positions of Ti + Ni + Al.

From the comparison of the atom site occupation in τ_6 with the isopointal structures of $V_2(Co_{0.57}Si_{0.43})_3$ [21] and $Mg_{2.3}Ir_{2.7}$ [22] in Table 3, we conclude that the larger polyhedral centers (CN = 14, 15 and 16; distorted Franck-Kasper polyhedra) are occupied by the larger and more electropositive elements V, Mg and Ti, whilst all the smaller M atom combinations are found at the centers of distorted icosahedra. Atoms Ti1, Ti2 and Ti3 in τ_6 adopt the same polyhedra like Mg in $MgZn_2$, M7, M8 and M11 correspond to polyhedra of Zn2 in $MgZn_2$ but M1 and M2 were found to be surrounded by identical polyhedra like Al in Zr_4Al_3.

Table 3: Architecture of crystal structures derived from the $V_2(Co_{0.57}Si_{0.43})_3$-type; all with space group $C12/m1$ (# 12).

Compound	$Ti_2(Ti_{0.16}Ni_{0.43}Al_{0.41})_3$	$V_2(Co_{0.57}Si_{0.43})_3$	$Mg_{2.30}Ir_{2.70}$	$Mg_{1.93}Ir_{3.07}$
Reference	This work	[21]	[22]	[23]
Composition from refinement	$Ti_2(Ti_{0.16}Ni_{0.43}Al_{0.41})_3$	$V_2(Co_{0.57}Si_{0.43})_3$	$Mg_2(Mg_{0.1}Ir_{0.9})_3$	$(Mg_{0.97}Ir_{0.03})_2Ir_3$
a (nm)	1.85383 (7)	1.717	1.8582(2)	1.85699(2)
b (nm)	0.49970(2)	0.466	0.52308(6)	0.518715(4)
c (nm)	0.81511(3)	0.755	0.8551(1)	0.849233(6)
β (°)	99.597(3)	99.2	97.645(9)	97.2209(5)
4i (x, 0, z)	Ti	V	Mg	Mg
x, z	0.28539(4), 0.07994(10)	0.294, 0.091	0.2803(3), 0.0851(8)	0.281(1), 0.067(2)
4i (x, 0, z)	Ti	V	Mg	Mg
x, z	0.55166(4), 0.35996(10)	0.553, 0.369	0.5543(3), 0.3831(7)	0.562(1), 0.382(2)
4i (x, 0, z)	Ti	V	Mg	Mg
x, z	0.28916(4), 0.45292(10)	0.294, 0.440	0.2913(3), 0.4474(7)	0.286(1), 0.435(2)
4i (x, 0, z)	Ti	V	Mg	Mg
x, z	0.02360(4), 0.16885(10)	0.015, 0.144	0.0227(3), 0.1803(7)	0.025(1), 0.174(2)
4i (x, 0, z)	Ti	V	Mg	0.167(5) Ir + 0.833 Mg
x, z	0.43472(4), 0.01964(10)	0.427, 0.015	0.4218(3), 0.0093(7)	0.4228(5), 0.007(1)
4i (x, 0, z)	0.073(1) Ti + 0.462 Ni + 0.465 Al	0.57 Co + 0.43 Si	0.926(5) Ir + 0.074 Mg	Ir
x, z	0.86894(4), 0.0437(1)	0.873, 0.037	0.87163(3), 0.03192(7)	0.8702(2), 0.0294(3)
8j (x, y, z)	0.136(1) Ti + 0.421 Ni + 0.443 Al	0.57 Co + 0.43 Si	Ir	Ir
x, y, z	0.1687(1), 0.2553(1), 0.2185(1)	0.164, 0.25, 0.225	0.16641(2), 0.25347(7), 0.22635(5)	0.1676(1), 0.2496(4), 0.2271(2)
8j (x, y, z)	0.164(1) Ti + 0.507 Ni + 0.329 Al	0.57 Co + 0.43 Si	Ir	Ir
x, y, z	0.4076(1), 0.2358(1), 0.3097(1)	0.407, 0.25, 0.308	0.40958(2), 0.23369(7), 0.29747(4)	0.4095(1), 0.2357(3), 0.2957(2)
2c (0,0,½)	0.262(2) Ti + 0.440 Ni + 0.298 Al	0.57 Co + 0.43 Si	0.694(8) Ir + 0.306 Mg	Ir
4i (x, 0, z)	0.151(2) Ti + 0.488 Ni + 0.361 Al	0.57 Co + 0.43 Si	0.836(6) Ir + 0.164 Mg	Ir
x, z	0.13347(4), 0.45101(10)	0.129, 0.464	0.13530(3), 0.46351(7)	0.1351(2), 0.4655(3)
4i (x, 0, z)	0.238(1) Ti + 0.237 Ni + 0.525 Al	0.57 Co + 0.43 Si	0.652(6) Ir + 0.348 Mg	Ir
x, z	0.21334(5), 0.73538(11)	0.206, 0.735	0.21513(3), 0.7443(1)	0.2144(2), 0.7408(3)
R_F^2	0.0376	Not given	0.0335	$R_B = 0.056$
Technique of measurement	XSC + NPD + XRD	XSC	XSC	XRD

5.3.2. The crystal structure of η-(Ti$_{0.84}$Al$_{0.16}$)$_2$Ni

A single crystal was selected from the alloy $Ti_{55.7}Ni_{33.1}Al_{11.2}$ (composition from EPMA) annealed at 980°C to derive high precision atom positions and particularly to check on the electron density at the centers of vacant metal octahedra. X-ray single crystal data were completely indexed on a cubic face centered lattice and extinctions *(0kl)* for *k + l = 4n + 1, (h00)* for *h = 4n + 1* confirm *Fd*-3*m* as the space group with the highest symmetry. Direct methods confirm atom order isotypic with the Ti_2Ni-type. For anisotropic atomic displacement parameters, the refinement converged to $R_{F2} = 0.023$ with residual electron densities smaller than 1.5 $e^-/10^{-3}nm^3$. Results are compiled in Table 4. In agreement with the extension of the solid solution η-$(Ti_{1-x}Al_x)_2Ni$, Al atoms at x = 0.16 substitute for 20 % of the Ti atoms in the 48*f* position (x,1/8,1/8), whereas Al atoms in the 16*c* position (0,0,0) at the centres of metal icosahedra substitute for 5.6 % of the Ti atoms. Ni-atoms occupy the 32*e* site (x,x,x). It should be noted that residual densities (1.5 $e^-/10^{-3}nm^3$) are insignificant and demonstrate that there is a negligible concentration of non-metal atoms at the centres of Ti/Al octahedra (16*d* sites (1/2,1/2,1/2) and 8*b* sites (3/8,3/8,3/8)). Thus stabilisation of the solid solution η-$(Ti_{1-x}Al_x)_2Ni$ by interstitials can safely be ruled out. The composition obtained from the structure refinement, $Ti_{56.7}Ni_{32.3}Al_{11}$, is almost identical with the EPMA value (see Table 4a).

Table 4a: X-Ray single crystal data for η-$(Ti_{1-x}Al_x)_2Ni$ (x=0.16), space group *Fd*-3*m*, #227 (Ti_2Ni structure type) standardized with program *Structure Tidy* [19]. (MoKα; 2°$\leq$2$\Theta$$\leq$72.05°; ω-scans, scan width 2°; 150 sec/frame.

Parameter/compound	$(Ti_{0.84}Al_{0.16})_2Ni$
Composition from EPMA in at.%	$Ti_{56.7}Ni_{32.3}Al_{11.0}$
Composition from refinement (at.%)	$Ti_{55.7}Ni_{33.3}Al_{11.0}$
Formula from refinement	$(Ti_{1-x}Al_x)_2Ni$; x = 0.16
a (nm)	1.12543(3)
μ_{abs} (mm^{-1})	17.41
V (nm^3)	1.4255
ρ_x (gcm^{-3})	5.50
Reflections in refinement	168>4σ(F$_o$) of 196
Mosaicity	0.55
Number of variables	15
$R_F^2 = \Sigma|F_0^2\text{-}F_c^2|/\Sigma F_0^2$	0.0222
R_{Int}	0.060
wR2	0.050
GOF	1.151
Extinction (Zachariasen)	0.00026(7)
Residual density e$^-$/Å^3; max; min.	1.49; -0.68
Atom parameters	
Ni1 in 32e (x, x, x); x; Occ.	1.00 Ni; x=0.21369(3)
$U_{11} = U_{22} = U_{33}$	0.0106(2)
$U_{23} = U_{13} = U_{12}$	0.0010(1)

M1 (Ti1/Al1) in 48f (x, 1/8, 1/8) ; x;	$0.800(4)$ Ti + 0.200 Al; x=$0.44013(6)$
U_{11}; $U_{22} = U_{33}$	$0.0101(3)$; $.0088(2)$
U_{23}, $U_{13} = U_{12}$	$0.0006(2)$, 0.0000
M2 (Ti2/Al2) in 16c (0,0,0) Occ.	$0.944(4)$ Ti + 0.056 Al
$U_{11} = U_{22} = U_{33}$	$0.0101(2)$
$U_{23} = U_{13} = U_{12}$	$0.0016(2)$

Table 4b: Inter atomic distances (nm) for τ_6 taken from XSC refinement (upper right column), standard deviation ≤ 0.0001 nm.

Ni1–	3M2	0.2473	M1–	2Ni1	0.2581		4M1	0.2998
CN = 12	3M1	0.2581	CN = 14	2Ni1	0.2913	M2-	6Ni1	0.2473
	3Ni1	0.2823		2M2	0.2922	CN = 12	6M1	0.2922
	3M1	0.2913		4M1	0.2943			

The coordination polyhedra for η-$(Ti_{0.84}Al_{0.16})_2Ni$ are shown in Fig. 4. Interatomic distances are listed in Table 4b. Shortest bond distances are observed between Ni1 and Ti4, whereas longest distances are observed between Ti2 and Al3 or Ti2 with Ti2 itself. Ti-Ni, Ti-Al and Ni-Al bonds are found to be in the range of 0.247-0.291 nm, 0.292-0.294 nm and 0.258 nm respectively. A comparison of interatomic distances of η-$(Ti_{0.84}Al_{0.16})_2Ni$ with binary Ti_2Ni shows that our bond distances, $d_{Ni-M}=0.2473$-0.2913 nm, $d_{Ni-Ni}=0.2823$ nm and $d_{M-M}=0.2922$-0.2998 nm, are in good agreement with data in the literature [20, 24]. It should be noted, that although Ti sites are partially occupied by Al atoms, still the bond distance remains the same because of the similar size of Ti and Al atoms.

Ni[M1₆Ni₃M2₃]   M1[M1₈Ni₄M2₂]   M2[M1₆Ni₆]
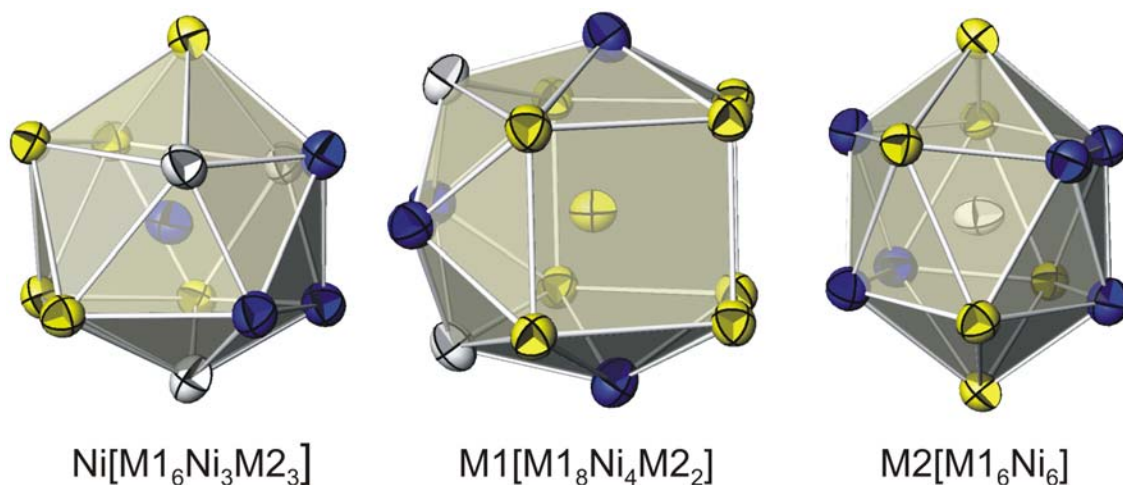
Fig. 4. Coordination polyhedra of the atom sites in η-$(Ti_{0.84}Al_{0.16})_2Ni$ with anisotropic displacement parameters from single crystal refinement. Blue atoms (dark gray in black & white print) represent a position occupied by Ni atoms only, yellow atoms (light gray in black & white print) represent the mixed position M1 (0.80Ti + 0.20Al) and white atoms represent the mixed position M2 (0.94Ti + 0.06Al).

5.3.3. Phase equilibria and reactions involving the τ_6-phase.

In previous investigation [6], the Laves phase (τ_3-TiNiAl) was found to form equilibrium with α_2-Ti$_3$Al and τ_4-TiNi$_2$Al at 900°C, whilst alloys annealed at 1000°C contained the Laves phase together with the liquid. At temperatures between 980°C and 870°C, a new X-ray powder diffractogram was recognized suggesting the formation of a novel ternary compound for which X-ray and EPMA data revealed a formula "Ti$_2$NiAl". XRD spectra are consistent with the spectra collected by Grytsiv et al. [16] on a new phase near "Ti$_2$NiAl" (Ti$_{47-49}$Ni$_{27}$Al$_{26-24}$). Rietveld refinement of the XRD intensities undoubtedly identified the spectra with the crystal structure of τ_6-Ti$_2$(Ti$_{0.16}$Ni$_{0.43}$Al$_{0.41}$)$_3$. According to EPMA, a small homogeneity region (~1 at. %) (Table 5, Fig. 5) was found.

Table 5. Composition (EPMA) and lattice parameters for selected alloys.

#	Nominal (at. %)			Overall (at. %)			H. T.* (°C)	Phases	S.G., Str. Type	Cell parameters (nm)			Composition (at. %)		
	Ti	Ni	Al	Ti	Ni	Al				a	b	c	Ti	Ni	Al
1	44	33	23	42.3	33.4	24.3	1000	τ_3	$P6_3/mmc$, MgZn$_2$	0.50127(3)	-	0.80675(8)	47.5	28.4	24.1
								η	$Fd\text{-}3m$, Ti$_2$Ni	1.12348(5)	-	-	54.1	30.4	15.5
								τ_4	$Fm\text{-}3m$, MnCu$_2$Al	0.59032(8)	-	-	27.0	49.0	24.0
2	51	25	24	49.1	25.4	25.5	1000	α_2	$P6_3/mmc$, Mg$_3$Cd	0.57946(7)	-	0.46686(0)	75.0	0.9	24.1
								τ_3	$P6_3/mmc$, MgZn$_2$	0.50161(6)	-	0.80753(9)	47.5	27.8	24.7
								η	$Fd\text{-}3m$, Ti$_2$Ni	1.12362(4)	-	-	54.4	30.1	15.5
3	49.5	26	24.5	50.2	25.7	24.1	975	α_2	$P6_3/mmc$, Mg$_3$Cd	0.57912(5)	-	0.46523(6)	73.3	1.1	25.6
								τ_3	$P6_3/mmc$, MgZn$_2$	0.50168(9)	-	0.80905(9)	46.6	28.6	24.8
								τ_6	$C2/m$, V$_2$(Co,Si)$_3$	1.84801(5)	0.49899(1)	0.81468(2)	49.5	27.1	23.4
4	50	28	22	51.1	28.1	20.8	975	η	$Fd\text{-}3m$, Ti$_2$Ni	1.12367(3)	-	-	54.2	30.8	15.0
								τ_6	$C2/m$, V$_2$(Co,Si)$_3$	1.84921(8)	0.49903(2)	0.81504(3)	49.6	27.1	23.3
								τ_3	$P6_3/mmc$, MgZn$_2$	0.50148(4)	-	0.80790(8)	46.7	29.0	24.3
5	51	25	24	50.8	25.5	23.7	975	α_2	$P6_3/mmc$, Mg$_3$Cd	0.57922(4)	-	0.46642(4)	73.8	1.0	25.2
								η	$Fd\text{-}3m$, Ti$_2$Ni	1.12414(4)	-	-	54.8	30.1	15.1
								τ_6	$C2/m$, V$_2$(Co,Si)$_3$	1.84777(5)	0.49917(1)	0.81415(2)	50.0	26.4	23.6
6	47	30	23	47.6	37.1	22.3	975	τ_3	$P6_3/mmc$, MgZn$_2$	0.50141(4)	-	0.80745(7)	46.4	29.0	24.6
								η	$Fd\text{-}3m$, Ti$_2$Ni	1.12380(3)	-	-	54.0	31.6	14.4
								τ_4	$Fm\text{-}3m$, MnCu$_2$Al	0.58967(20)	-	-	27.0	49.0	24.0
7	50	28	22	51.5	27.5	21.0	950	η	$Fd\text{-}3m$, Ti$_2$Ni	1.12333(9)	-	-	53.8	32.1	14.1
								τ_6	$C2/m$, V$_2$(Co,Si)$_3$	1.84835(6)	0.49902(1)	0.81384(3)	49.3	27.7	23.0
								τ_3	$P6_3/mmc$, MgZn$_2$	0.50139(6)	-	0.80839(7)	46.9	28.7	24.4

8	51	25	24	52.1	25.1	22.8	950	α_2	$P6_3/mmc$, Mg_3Cd	0.57879(9)	-	0.46551(8)	72.8	1.1	26.1
								η	$Fd\text{-}3m$, Ti_2Ni	1.12383(9)	-	-	53.8	31.6	14.6
								τ_6	$C2/m$, $V_2(Co,Si)_3$	1.84741(3)	0.49887(1)	0.81387(1)	49.2	26.6	24.2
9	49.5	26	24.5	50.2	25.7	24.1	950	α_2	$P6_3/mmc$, Mg_3Cd	0.57855(5)	-	0.46499(8)	72.6	1.1	26.3
								τ_3	$P6_3/mmc$, $MgZn_2$	0.50154(7)	-	0.80848(9)	46.2	28.6	25.2
								τ_6	$C2/m$, $V_2(Co,Si)_3$	1.84821(5)	0.49892(1)	0.81440(2)	49.2	26.9	23.9
10	47	30	23	47.8	30.5	21.7	950	τ_3	$P6_3/mmc$, $MgZn_2$	0.50128(3)	-	0.80779(8)	46.4	28.7	24.9
								η	$Fd\text{-}3m$, Ti_2Ni	1.12300(7)	-	-	54.2	31.7	14.1
								τ_4	$Fm\text{-}3m$, $MnCu_2Al$	0.58990(4)	-	-	27.0	49.0	24.0
11	51	25	24	52.3	24.2	23.5	925	α_2	$P6_3/mmc$, Mg_3Cd	0.57860(5)	-	0.46509(8)	72.4	1.1	26.5
								η	$Fd\text{-}3m$, Ti_2Ni	1.12310(9)	-	-	53.3	32.2	14.5
								τ_6	$C2/m$, $V_2(Co,Si)_3$	1.84618(3)	0.49893(1)	0.81385(1)	48.6	27.3	24.1
12	36.5	41	22.5	38.1	39.9	21.9	925	τ_4	$Fm\text{-}3m$, $MnCu_2Al$	0.59014(5)	-	-	26.6	49.5	23.9
								η	$Fd\text{-}3m$, Ti_2Ni	1.12336(9)	-	-	52.8	33.2	14.0
								τ_6	$C2/m$, $V_2(Co,Si)_3$	1.84716(9)	0.49916(3)	0.81424(4)	48.5	28.2	23.3
13	49	25	26	50.4	24.4	25.2	925	α_2	$P6_3/mmc$, Mg_3Cd	0.57882(3)	-	0.46544(9)	72.3	1.0	26.7
								τ_3	$P6_3/mmc$, $MgZn_2$	0.50132(4)	-	0.80862(7)	45.1	28.6	26.3
								τ_6	$C2/m$, $V_2(Co,Si)_3$	1.84653(9)	0.49914(3)	0.81509(4)	48.3	27.0	24.7
14	44	30	26	45.4	29.3	25.3	925	τ_3	$P6_3/mmc$, $MgZn_2$	0.50135(5)	-	0.80829(8)	45.1	28.6	26.3
								τ_4	$Fm\text{-}3m$, $MnCu_2Al$	0.58997(8)	-	-	26.8	49.0	24.2
								α_2	$P6_3/mmc$, Mg_3Cd	0.57891(5)	-	0.46597(9)	71.7	1.4	26.9
								η	$Fd\text{-}3m$, Ti_2Ni	1.12321(9)	-	-	51.6	32.3	16.1
15	51	25	24	52.3	24.2	23.5	900	α_2	$P6_3/mmc$, Mg_3Cd	0.57895(4)	-	0.46531(6)	72.1	1.0	26.9
								η	$Fd\text{-}3m$, Ti_2Ni	1.12368(9)	-	-	53.3	32.8	13.9
								τ_6	$C2/m$, $V_2(Co,Si)_3$	1.84604(3)	0.49867(1)	0.81329(1)	48.1	27.9	24.0
16	48	25	27	49.1	24.5	26.4	900	α_2	$P6_3/mmc$, Mg_3Cd	0.57881(7)	-	0.46510(6)	71.9	1.0	27.1
								τ_4	$Fm\text{-}3m$, $MnCu_2Al$	0.58982(9)	-	-	26.4	49.0	24.6
								τ_3	$P6_3/mmc$, $MgZn_2$	0.50116(6)	-	0.80757(7)	44.3	28.7	27.0
17	36.5	41	22.5	38.5	39.9	21.6	900	τ_4	$Fm\text{-}3m$, $MnCu_2Al$	0.58995(8)	-	-	25.4	50.6	24.0
								η	$Fd\text{-}3m$, Ti_2Ni	1.12332(9)	-	-	52.4	33.8	13.8
								τ_6	$C2/m$, $V_2(Co,Si)_3$	1.84684(9)	0.49976(5)	0.81403(8)	48.1	28.0	23.9
18	49.5	26	24.5	51.0	25.1	23.9	900	α_2	$P6_3/mmc$, Mg_3Cd	0.57865(6)	-	0.46510(8)	71.9	1.1	27.0
								τ_4	$Fm\text{-}3m$, $MnCu_2Al$	0.58958(8)	-	-	26.0	50.0	24.0
								τ_6	$C2/m$, $V_2(Co,Si)_3$	1.84579(4)	0.49859(1)	0.81306(2)	48.3	27.7	24.0
19	46	27	27	47.9	25.6	26.5	865	α_2	$P6_3/mmc$, Mg_3Cd	0.57865(7)	-	0.46407(5)	71.7	1.0	27.3
								τ_4	$P6_3/mmc$, $MgZn_2$	0.59021(1)	-	-	25.3	50.6	24.1
								τ_3	$P6_3/mmc$, $MgZn_2$	0.50161(5)	-	0.80754(7)	42.1	29.0	28.9
20	47	31	22	48.7	29.5	21.8	865	α_2	$P6_3/mmc$, Mg_3Cd	0.57935(8)	-	0.46389(5)	72.3	1.0	26.7
								τ_4	$Fm\text{-}3m$, $MnCu_2Al$	0.59006(7)	-	-	25.4	51.0	23.6

								η	Fd-3m, Ti$_2$Ni	1.12355(9)	-	-	52.8	34.2	13.0

* Heat treatment

Fig. 5. Temperature dependence of vertex-composition of η, τ$_3$, τ$_6$; line a represents triangle η + τ$_3$ + τ$_4$, b represents triangle η + α$_2$ + τ$_3$, c represents triangle η + τ$_3$ + τ$_6$, d represents triangle α$_2$ + τ$_3$ + τ$_6$, e represents triangle η + α$_2$ + τ$_6$, f represents triangle η + τ$_4$ + τ$_6$, g represents triangle τ$_3$ + τ$_4$ + τ$_6$, h represents triangle α$_2$ + τ$_4$ + τ$_6$, i represents triangle α$_2$ + τ$_3$ + τ$_4$ and j represents triangle η + α$_2$ + τ$_4$.

Fig. 6. Partial phase diagrams at (a) sub-solidus (slightly below solidus) temperature, (b) 975°C, (c) 950°C, (d) 925°C, (e) 900°C and (f) 865°C. Equilibria at 1000° after [9] are shown in gray color (Figure a).

62

Figure 5 presents the temperature dependence of the composition of the phases involved in equilibria with the τ_6-phase. The corresponding change in lattice parameters is in most cases small as the phases mainly shift their composition with respect to Ti/Al substitution with similar atom radii for Ti and Al.
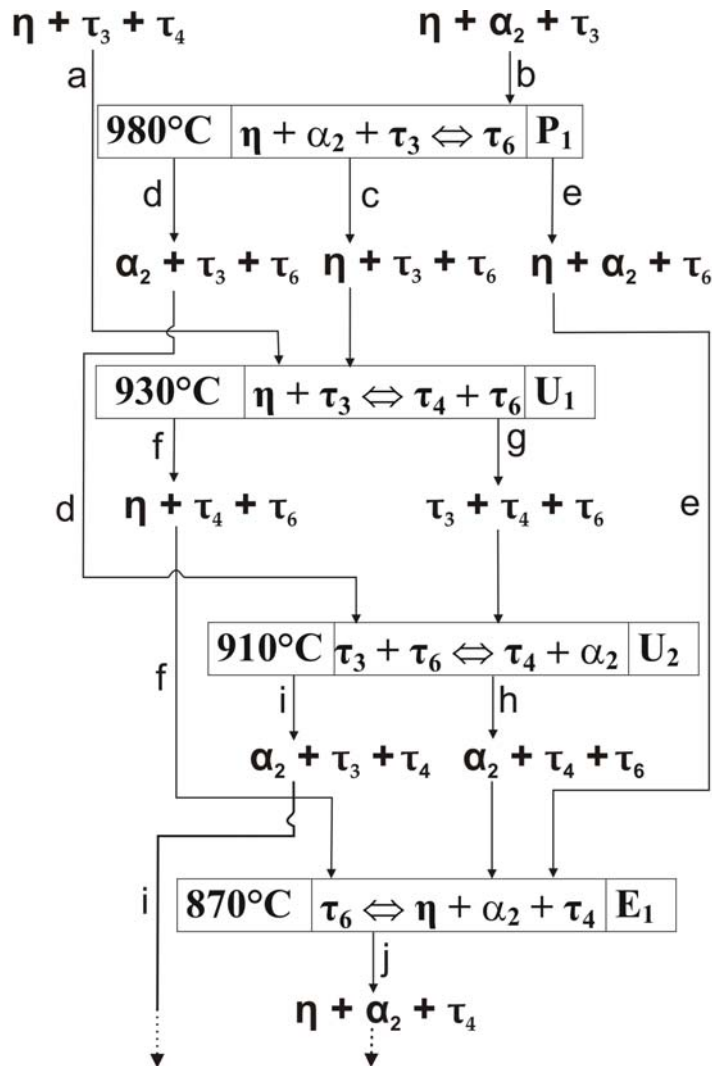
Fig. 7 Schultz-Scheil diagram involving the phase τ_6-Ti$_2$(Ti$_{0.16}$Ni$_{0.43}$Al$_{0.41}$)$_3$. Letters a, b… correspond to three-phase triangles for which composition dependence as a function of temperature is shown in Fig. 5.

X-ray and EPMA results of selected samples to prove isothermal equilibria at various temperatures are summarized in Table 5. Due to slow reaction kinetics, even at very slow heating rates (1 K/min), it was very difficult to interpret DSC measurements. Therefore X-ray and EPMA on isothermally treated alloys served to construct isothermal phase relations for the

region confined by the phases TiNi$_2$Al (τ_4), (Ti$_{1-x}$Al$_x$)$_2$Ni (η), α_2-Ti$_3$Al and the Laves phase Ti(Ti,Ni,Al)$_2$ (τ_3) and finally to derive a Schultz-Scheil diagram. Evaluations are summarized in a set of partial isothermal sections at 865, 900, 925, 950, 975°C, in a sub-solidus diagram (see Fig. 6) and resulted in the Schultz-Scheil reaction scheme presented in Fig. 7.
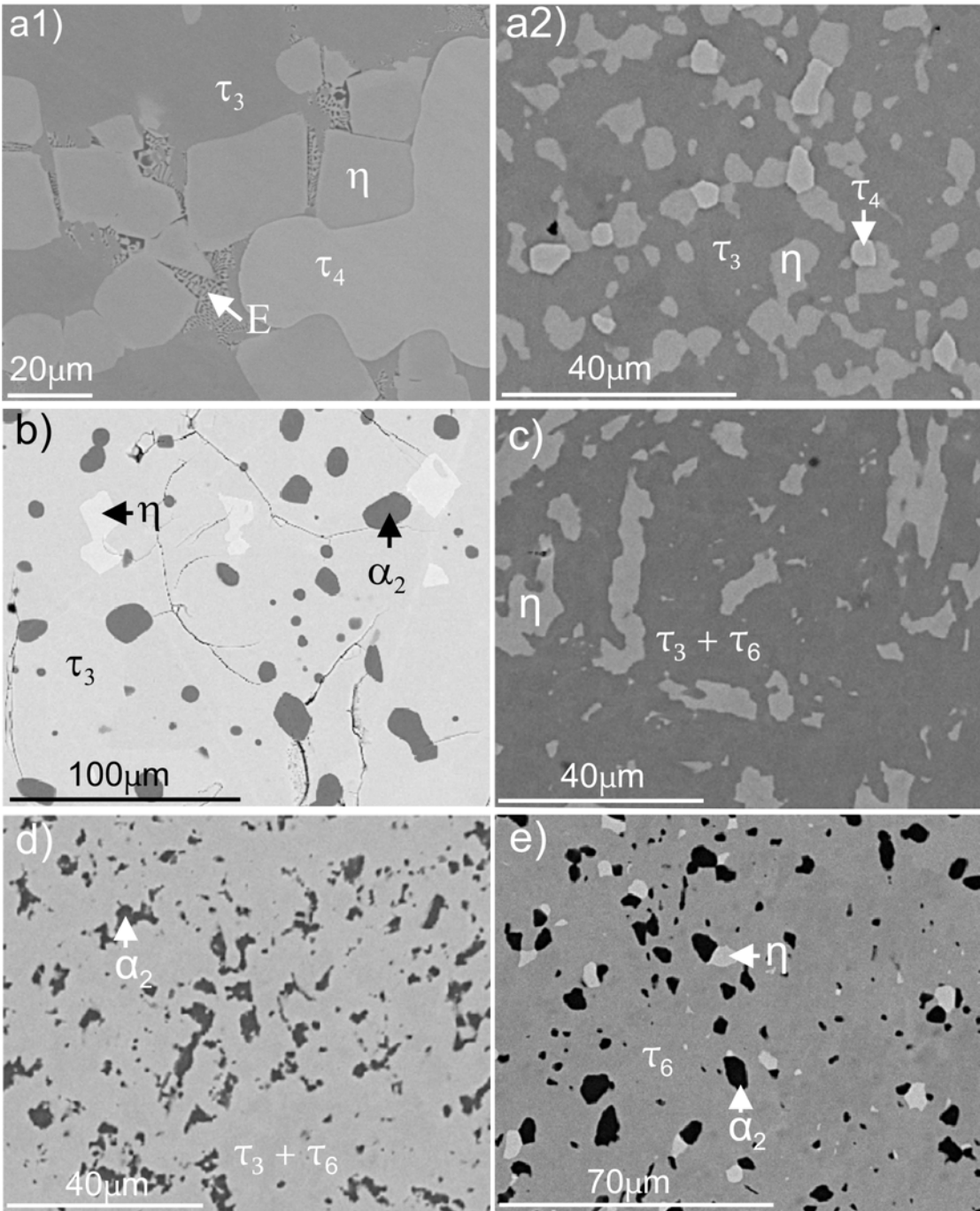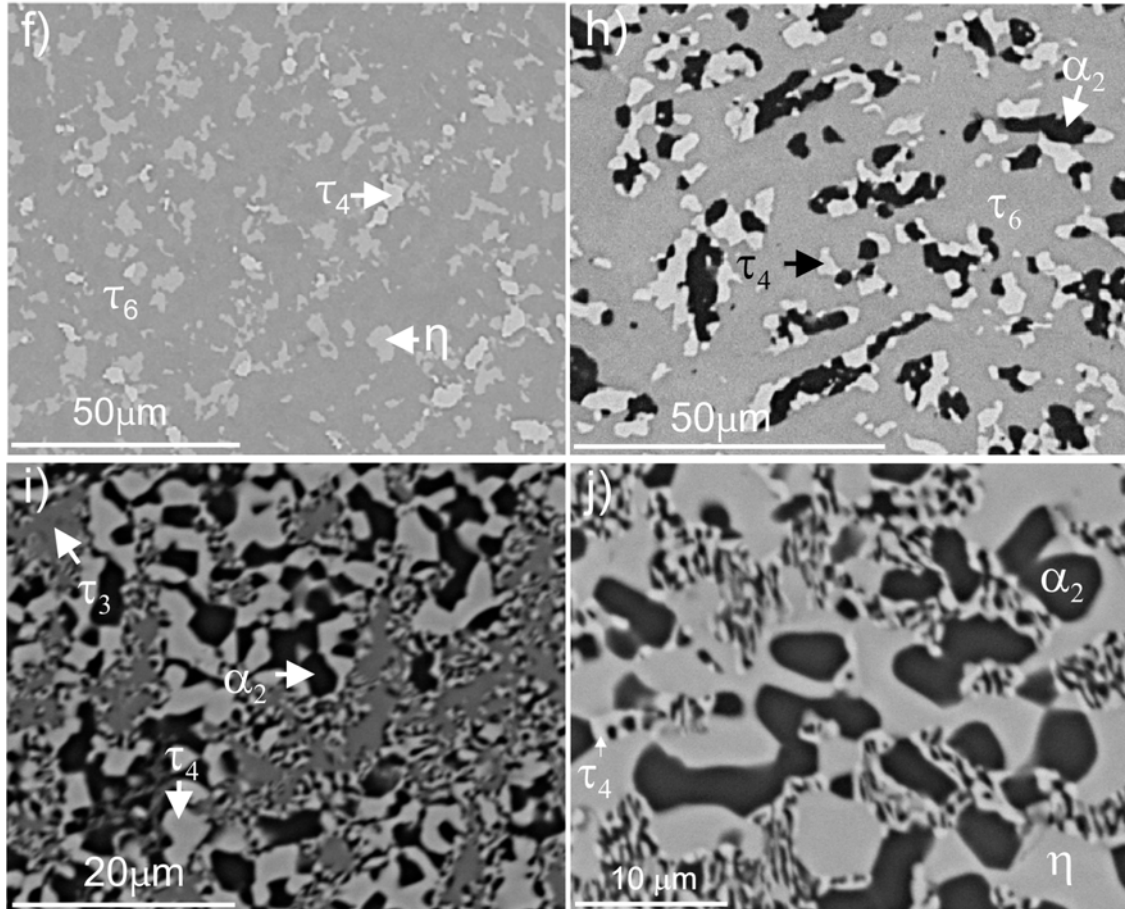
Fig. 8. Microstructures of selected samples with phases identified by EPMA: (a1) $Ti_{47}Ni_{30}Al_{23}$ (1000°C), (a2) $Ti_{47}Ni_{30}Al_{23}$ (950°C), (b) $Ti_{51}Ni_{25}Al_{24}$ (1000°C), (c) $Ti_{50}Ni_{28}Al_{22}$ (975°C), (d) $Ti_{49}Ni_{25}Al_{26}$ (975°C), (e) $Ti_{51}Ni_{25}Al_{24}$ (975°C), (f) $Ti_{48}Ni_{29}Al_{23}$ (925°C), (h) $Ti_{49.5}Ni_{26}Al_{24.5}$ (900°C), (i) $Ti_{46}Ni_{27}Al_{27}$ (865°C), (j) $Ti_{56}Ni_{25.0}Al_{19}$ (865°C). Phase compositions and lattice parameters are available in Table 5.

Alloys annealed at 1000°C (Fig. 8a1, b) show big grains of equilibrium phases ($\eta + \tau_3 + \tau_4$ and $\eta + \alpha_2 + \tau_3$, respectively) and little amount of a eutectic-like structure indicating that these alloys were close to the melting temperature. This observation agrees with data [9] on the existence of liquid in this part of the phase diagram at 1000°C.

With decrease of temperature to 975°C, alloys from the phase field $\eta + \alpha_2 + \tau_3$ undergo a phase transformation with formation of the new phase τ_6. Accordingly, we observe at this temperature three new phase tie-triangles $\eta + \tau_3 + \tau_6$, $\alpha_2 + \tau_3 + \tau_6$ and $\eta + \alpha_2 + \tau_6$ (Fig. 8c,d,e) inferring the existence of the invariant reaction P_1: $\eta + \alpha_2 + \tau_3 \Leftrightarrow \tau_6$, which was defined to occur at 980±10 °C (Table 6, Fig. 7, 9).

Table 6. Invariant equilibria involving τ_6.

Invariant Equilibrium	Phase	Composition (at. %)		
		Ti	Ni	Al
P_1: 980°C	α_2	73.6	~1.0*	25.4
$\eta + \alpha_2 + \tau_3 \Leftrightarrow \tau_6$	η	54.5	30.4	15.1
	τ_3	46.8	29.0	24.2
	τ_6	49.9	26.7	23.4
U_1: 930°C	η	52.7	33.2	14.1
$\eta + \tau_3 \Leftrightarrow \tau_4 + \tau_6$	τ_3	46.4	28.5	25.1
	τ_4	27.0	~49.0	24.0
	τ_6	49.2	28.0	22.8
U_2: 910°C	α_2	72.2	~1.0	26.8
$\tau_3 + \tau_6 \Leftrightarrow \tau_4 + \alpha_2$	τ_3	44.8	28.7	26.5
	τ_4	26.8	~49.0	24.2
	τ_6	48.2	27.2	24.6
E_1: 870°C	α_2	72.4	~1.0	26.6
$\tau_6 \Leftrightarrow \eta + \alpha_2 + \tau_4$	η	52.9	34.0	13.1
	τ_4	27.2	~49.0	23.8
	τ_6	47.6	28.3	24.1

* Ni is approximate due to small amount of α_2 and τ_4 in most of samples.

Alloys $\eta + \tau_3 + \tau_4$ (Fig. 8a1) do not change phase composition up to 950°C (Fig. 8a2). However, the samples annealed at 925°C for this triangle already reveal τ_6 (Fig. 6d, 8f). Therefore a temperature of 930°C was assigned to the invariant equilibrium U_1: $\eta + \tau_3 \Leftrightarrow \tau_4 + \tau_6$ that is responsible for the observed change of phase equilibria. The three phase field $\tau_3 + \tau_4 + \tau_6$ that forms during this reaction is very narrow and exists in a small temperature range. Attempts to quench any equilibrated three phase sample from this field were unsuccessful and resulted in four-phase microstructures containing α_2, τ_3, τ_4 and η (Fig. 6d). However, from the interpretation of all other phase triangles at 925°C (Fig. 6d), it is obvious that also the equilibrium $\tau_3 + \tau_4 + \tau_6$ exists. Further decrease of annealing temperature to 910°C results in different phase equilibria and τ_6 does not participate anymore in equilibria with τ_3 (Fig. 6e, 8h, i). Phase equilibria observed, $\alpha_2 + \tau_4 + \tau_6$ (Fig. 8h) and $\alpha_2 + \tau_3 + \tau_4$ (Fig. 8i), result from the transition reaction U_2 at 910°C: $\tau_3 + \tau_6 \Leftrightarrow \tau_4 + \alpha_2$. The τ_6-phase decomposes at 870°C in a eutectoid invariant reaction $\tau_6 \Leftrightarrow \eta$–$(Ti,Al)_2Ni + \alpha_2 + \tau_4$ with the formation of subsequent phase field $\eta + \alpha_2 + \tau_4$ at lower temperatures (Fig. 8j). Consequently, we can not confirm the reaction η-$(Ti,Al)_2Ni + \tau_3 \Leftrightarrow \alpha_2 +$

τ_4 at 876±2°C claimed by Schuster et al. [9], who did not consider the data [16] on the existence of τ_6. A significant discrepancy also occurs on the extension of the τ_3 phase field at 900°C, which was reported [9] to exist at a Ti content higher than 50 at. %, whilst the maximum solubility of 47 at. % Ti at 1000°C [9] agrees well with our data (Fig. 5).

A three-dimensional view of the phase diagram for the composition-temperature range investigated is shown in Figure 9.
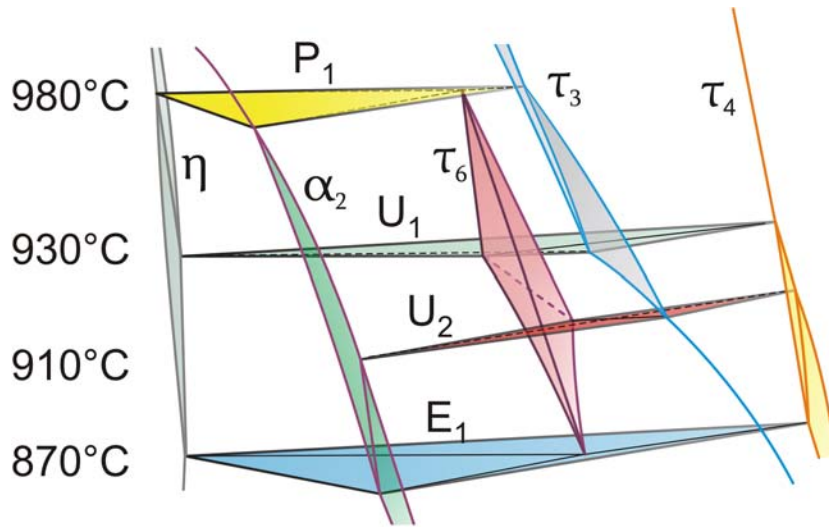
Fig. 9. 3D-phase diagram for region of existence of τ_6-Ti$_2$(Ti$_{0.16}$Ni$_{0.43}$Al$_{0.41}$)$_3$. Composition of equilibrium phases is available from Fig. 5 and Table 5.

It is worth noticing that τ_6 is not reported yet in literature in any homologous system of Ti-Ni-Al like Zr-Ni-Al, [25] Hf-Ni-Al, [26] Ti-Pd-Al, [27], Ti-Co-Al, [28] Ti-Ni-Si [29] etc.

5.4. Conclusion

The crystal structure of τ_6-Ti$_2$(Ti$_{0.16}$Ni$_{0.43}$Al$_{0.41}$)$_3$ was solved via combined evaluation of XRD and NPD data. τ_6-Ti$_2$(Ti,Ni,Al)$_3$ was found to be an isotypic variant of the V$_2$(Co$_{0.57}$Si$_{0.43}$)$_3$-type. The structure is composed of slabs of the MgZn$_2$-Laves type and slabs of the Zr$_4$Al$_3$-type forming a tetrahedrally close-packed Frank-Kasper structure. Phase relations in the temperature interval from 1000°C to 865°C were determined for a set of isothermal sections at 865, 900, 925,

950, 975°C and in a sub-solidus diagram. A Schultz-Scheil reaction scheme has been derived which comprises four isothermal reactions all involving the new phase τ_6. The τ_6 phase forms on cooling in a peritectoid reaction at 980°C: η-(Ti,Al)$_2$Ni + τ_3 + α_2 $\Leftrightarrow$ τ_6 and decomposes on cooling in a eutectoid reaction at about 870°C: τ_6 $\Leftrightarrow$ η-(Ti,Al)$_2$Ni + τ_4 + α_2.

Atomic positions and distribution of Al in η-(Ti,Al)$_2$Ni were evaluated from X-ray single crystal data.

References

[1]   A. Raman, K. Schubert, Z. Metallkde **56**, (1965), p. 99-104.

[2]   V.Y. Markiv, V.V. Burnashova, V.R. Ryabov, Metallofizika **46**, (1973), p. 103-110.

[3]   P. Nash, W.W. Liang, Metallurgical Transactions **16/A**, (1985), p. 319-322.

[4]   S. Mazdiyasni, D.B. Miracle, D.M. Dimiduk, M.G. Mendiratta, P.R. Subramanian, Scripta Met. **23**, (1989), p. 327-331.

[5]   H.H. Xu, Z. Jin, Trans Nonferrous Met Soc China **7**, (1997), p. 24-29.

[6]   B. Huneau, P. Rogl, K. Zeng, R. Schmid-Fetzer, M. Bohn, J. Bauer, Intermetallics **7**, (1999), p. 1337-1345.

[7]   K. Zeng, R. Schmid-Fetzer, B. Huneau, P. Rogl, J. Bauer, Intermetallics **7**, (1999), p. 1347-1359.

[8]   J.J. Ding, P. Rogl, H. Schmidt, Journal of Alloys and Compounds **317-318**, (2001), p. 379-384.

[9]   J.C. Schuster, Z. Pan, S. Liu, F. Weitzer, Y. Du, Intermetallics **15**, (2007), p. 1257-1267.

[10] V. Raghavan, Journal of Phase Equilibria and Diffusion **26**, (2005), p. 268-272.

[11] V. Raghavan, Journal of Phase Equilibria and Diffusion **31**, (2010), p. 55-56.

[12] J.C. Schuster, Intermetallics **14/(10-11)**, (2006), p. 1304-1311.

[13] N. Dupin, PhD-thesis, Institut National Polytechnique Grenoble, France (1995).

[14] J. Bursik, P. Broz, Intermetallics **17**, (2009), p. 591-595.

[15] A.U. Khan, X. Yan, P. Rogl Saccone, A. Intermetallics **17/12**, (2009), p. 1000-1006.

[16] A. Grytsiv, Xing-Qiu Chen, V.T. Witusiewicz, P. Rogl, R. Podloucky, V. Pomjakushin, D. Maccio, A. Saccone, G. Giester, F. Sommer, Z. Kristallografie **221**, (2006), p. 334-348.

[17] B. Huneau, J.J. Ding, P. Rogl, J. Bauer, X.Y. Ding, M. Bohn, J. Solid State Chemistry, **155**, (2000), p. 71-77.

[18] P. Fischer, G. Frey, M. Koch, M. Koennecke, V. Pomjakushin, J. Schefer, R. Thut, N. Schlumpf, R. Buerge, U. Greuter, S. Bondt, E. Berruyer, Phys. B. **276-278**, (2000), p. 146.

[19] L.M. Gelato, E. Parthe, J. Appl. Cryst. **20**, (1987), p. 139-143.

[20] P. Villars, K. Cenzual, Pearson's Crystal Data, ASM International, Ohio, USA, Release (2010/11).

[21] P.I. Krypyakevich Y.P. Yarmolyuk, Dopov. Akad. Nauk. Ukr. RSR, Ser. **A 32**, (1970), p. 948-950.

[22] V. Hlukhyy Pöttgen, R. Solid State Sciences **6/10**, (2004), p. 1175-1180.

[23] R. Cerny, G. Renaudin, Y. Tokaychuk, V. Z. Favre-Nicolin, Kristallogr. Suppl. (2006), **23**, p. 411-416.

[24] Gmelin Handbook of Inorganic and Organometallic Chemistry, Typix, **1993**, Volume 1, 169.

[25] G. Ghosh, G. Effenberg S. Ilyenko, SpringerMaterials-The Landolt-Börnstein Database, DOI: 10.1007/10915998_35, (2005).

[26] V. Raghavan, Journal of Phase Equilibria and Diffusion **30/1**, (2009), p. 64-66.

[27] O.V. Zaikina, V.G. Khorujaya, D. Pavlyuchkov, B. Grushko T.Ya. Velikanova, Journal of Alloys and Compounds **509**, (2011), p. 43-51.

[28] V. Raghavan, Journal of Phase Equilibria and Diffusion **26/2**, (2005), p. 175-177.

[29] N. Lebrun, G. Effenberg, S. Ilyenko (ed.), SpringerMaterials - The Landolt-Börnstein Database DOI: 10.1007/11008514_38, (1999).

6. The crystal structures of hexagonal Mo(Cu$_x$Al$_{1-x}$)$_6$Al$_4$, MoCu$_2$Al$_{8-x}$ and orthorhombic {Mo,W,Re}Ni$_{2-x}$Al$_{8+x}$

6.1. Introduction

For the Al-Mo-Ni system, two recent assessments [1,2] have summarized all information existing in the literature confirming two ternary compounds in the Al-rich part of the phase diagram: the so-called N-phase and the X-phase. The N-phase exists in a small homogeneity region, Mo(Al$_{1-x}$Ni$_x$)$_3$ with 0.53≤x≤2 in as cast alloys [3] and was identified as TiAl$_3$-type by Markiv et al. [4]. The crystal structure of the X-phase (earlier denoted as Mo$_5$Ni$_{18}$Al$_{77}$ [4]), however, remained unknown, although a detailed TEM (Transmission Electron Microscope) study [3] revealed orthorhombic symmetry (possible space groups: *Pbm*2, *Pb2$_1$m or Pbmm*) and lattice parameters (a=1.0054, b=1.5288, c=0.8519 nm) for a composition Mo$_{11}$Ni$_{14}$Al$_{75}$ (from EPMA in at.%).

A recent critical assessment on the Al-Ni-Re system by V. Raghavan [5], which was based on the work of B. Grushko et al. [6, 7], interestingly revealed a ternary phase with composition close to the X-phase from the Al-Mo-Ni system. A detailed TEM-investigation indeed determined crystal symmetry and lattice dimensions corresponding to the X-phase [6, 7] (possible space groups: *Pbm*2, *Pb2$_1$m* or *Pbmm*; a=1.0048, b=1.5423, c=0.8367 nm for a composition Re$_8$Ni$_{18.5}$Al$_{73.5}$). From DTA-data this phase was reported to melt incongruently at 888°C [6, 7]. Although the X-ray powder diffraction pattern was indexed by Grushko et al. [7], no structure refinement was carried out. For the W-Ni-Al system, where one could expect the formation of an isotypic X-phase, recent critical assessments showed that the Al rich part of the system was not well studied [8, 9].

Some inconsistencies seem also to concern the Al-rich phases in the systems Al-Cu-{Mo,W} [10]. Whereas A.P. Prevarskiy et al. [11, 12] claimed the existence of two isotypic orthorhombic compounds with unknown crystal structure {Mo,W}Cu$_2$Al$_7$ [a = 0.505, b = 0.841, c = 1.968 nm for MoCu$_2$Al$_7$, but no parameters were given for WCu$_2$Al$_7$], a reinvestigation with TEM by B. Grushko et al. [13, 14] revealed a hexagonal lattice for both these compounds [a = 0.86796(8) and c = 1.51948(12) nm for MoCu$_2$Al$_7$ (no detailed composition given) and a = 0.86594(13) and

c = 1.52677(21) nm for WCu_2Al_7 ($W_{12}Cu_{21}Al_{67}$)]. From composition as well as lattice parameters, one can, however, expect a close structural relationship of these hexagonal phases with the X-phases existing in the Al-Ni-Re and Al-Mo-Ni systems.

As hitherto no crystal structure data have been published for the X-phases in the systems Al-Ni-{Mo,Re}, Al-Cu-{Mo,W} and as the Al rich part of the Al-Ni-W system is needed to be reinvestigated, the current investigation was designed to provide this information.

6.2. Experimental Details

Alloys were prepared (each of 1-2 grams) from high purity metal ingots of Mo, Cu, Ni and Al (purity 99.9 mass %, Alfa Johnson Matthey GmbH, D) by arc melting under argon atmosphere and were melted several times for homogenization (weight loss less than 0.1 %). Samples from the Al-Ni-{W, Re} and Al-Cu-W systems were prepared from metal powder blends (purity > 99 mass %), compacted and then arc melted to get homogenized samples. Then the reguli were wrapped in Mo-foil to protect from attack by the hot quartz walls, sealed in evacuated quartz tubes and annealed for 5-23 days at various temperatures starting from 865°C to 930°C. All samples were quenched in cold water after annealing. Lattice parameters and standard deviations were determined by least squares refinements of room temperature X-ray powder Diffraction (XRD) data obtained from a Guinier-Huber image plate employing monochromatic Cu Kα_1 radiation. Rietveld refinements of the X-ray powder diffraction data were performed with the FULLPROF program [For details, see chapter 2] with the use of its internal tables for atom form factors. Annealed samples were polished using standard procedures and were examined by optical metallography and scanning electron microscopy (SEM). Compositions were determined in an Electron Probe Micro-Analyzer (EPMA) on a Carl Zeiss EVO 40 equipped with a Pentafet Link EDX system operated at 20 kV. Pure elements were used as standards to carry out the deconvolution of overlapping peaks and background subtraction. Finally the X-ray intensities were corrected for ZAF effects using the INCA-Energy 300 software package [For details, see chapter 2]. Overall composition of the samples derived from EPMA area scans agree with the nominal values within 1.0 at. %.

Single crystals of the Al-Mo-Ni X-phase as well as of Ni_2Al_3 were mechanically isolated from a specimen with nominal composition $Mo_8Ni_{17}Al_{75}$, which was annealed at 925 °C for 4 days in

order to stay below the incongruent decomposition temperature of 1015 °C, reported for the X-phase ($Mo_{10.7}Ni_{14.2}Al_{75.1}$) [3]. Similarly a single crystal of the Al-Ni-Re X-phase was taken from a specimen with nominal composition $Re_{6.6}Ni_{20}Al_{73.4}$, which was annealed at 865 °C for 7 days, below the incongruent decomposition temperature of 888 °C, reported for the X-phase ($Re_8Ni_{18.5}Al_{73.5}$) [3]. Following this procedure, a single crystal of the Al-Ni-W X-phase was selected from the alloy with nominal composition $W_5Ni_{15}Al_{80}$ (annealed at 930 °C for 7 days). Finally a single crystal of the hexagonal X-phase in Mo-Cu-Al system was selected from the alloy $Mo_{9.5}Cu_{20.5}Al_{70}$ (Nom. composition), which was annealed at 710 °C for 14-23 days. All crystals were inspected on an AXS-GADDS texture goniometer for quality and crystal symmetry prior to X-ray single crystal (XSC) intensity data collection on a four-circle Nonius Kappa diffractometer (CCD area detector and graphite monochromatic Mo K_α radiation, $\lambda = 0.071069$ nm). Orientation matrix and unit cell parameters were derived using the program DENZO [For details, see chapter 2]. No individual absorption correction was necessary because of the rather regular crystal shape and small dimensions of the investigated specimens. The structures were solved by direct methods and refined with the SHELXS-97 and SHELXL-97 programs [For details, see chapter 2], respectively.

6.3. Results and discussion

6.3.1. The crystal structure of $Mo(Cu_xAl_{1-x})_6Al_4$ (x=0.416)

In order to solve the still unknown crystal structure of the hexagonal phase identified by B. Grushko et al. [13] in the Al-rich part of the Al-Cu-Mo system, a sample with the nominal composition $Mo_{7.5}Cu_{20.5}Al_{72.0}$ was prepared and annealed for 14 days. The practically single-phase X-ray powder pattern was found to agree essentially with the diffractogram reported by B. Grushko et al. [13], however, single crystals obtained from this alloy (a = 0.867, c = 1.52 nm) were of insufficient quality for structure determination. For better crystals, the alloy was annealed for further 23 days. Surprisingly, but consistent with a simpler X-ray powder pattern, the unit cell of the single crystal specimens with lattice parameters a = 0.50030(1) and c = 0.76279(3) nm was smaller than that reported by B. Grushko et al. [13] ($a_0 = 0.86796(8)$ and $c_0 = 1.51948(12)$ nm). A simple relation exists among the two lattice geometries: $a = a_0/\sqrt{3}$, $c = c_0/2$.
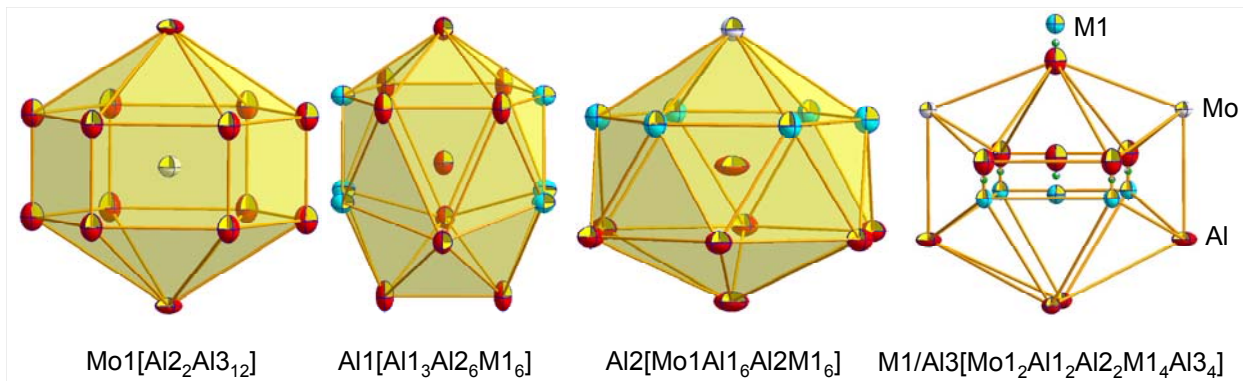
Fig. 1. Coordination polyhedra in $Mo(Cu_xAl_{1-x})_6Al_4$. The small green circles in between the blue and red atoms in the M1/Al3 polyhedra are hypothetical representing the center of split $6i$ site.
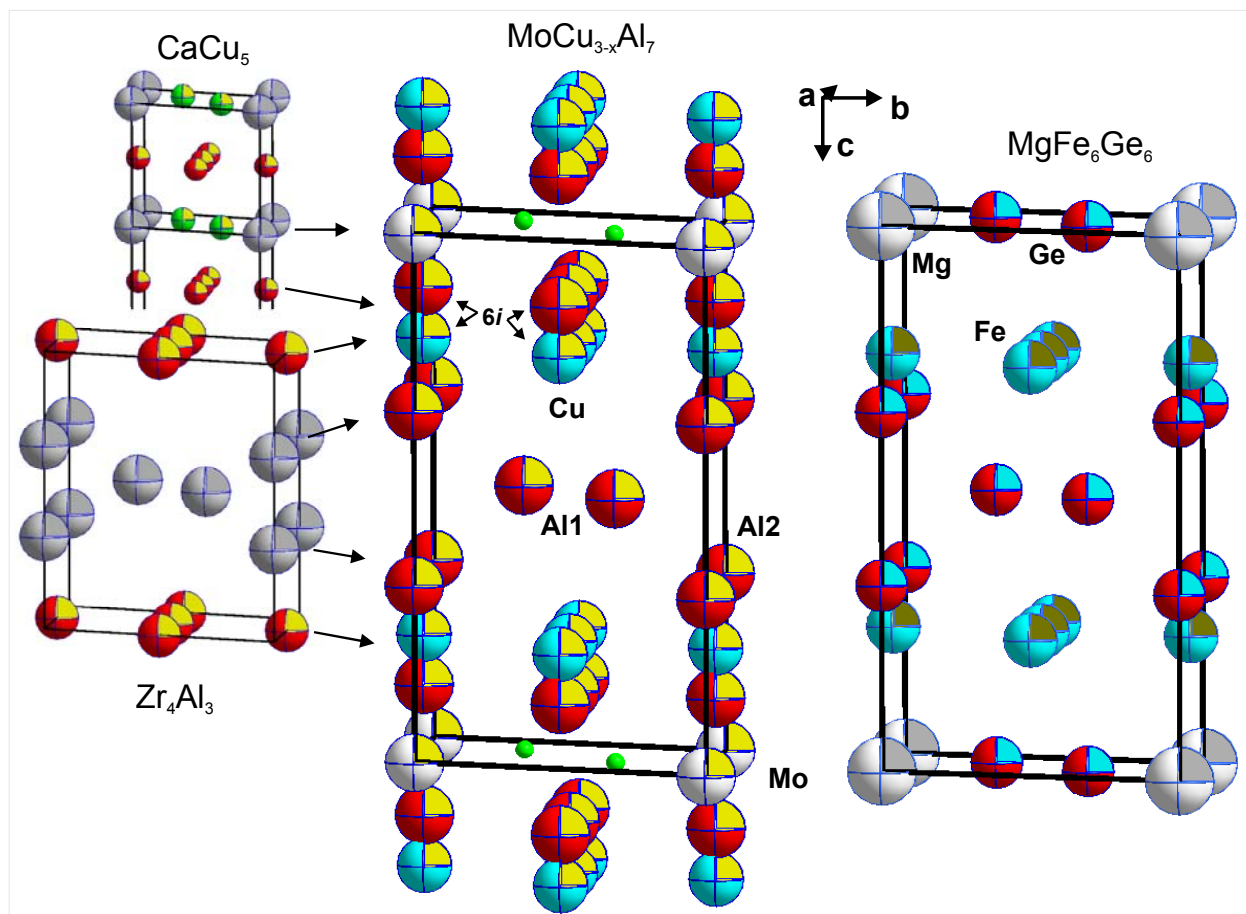
Fig. 2. Structural relation between $Mo(Cu_xAl_{1-x})_6Al_4$ and $MgFe_8Ge_8$ composed of slabs of $CaCu_5$ and Zr_4Al_3. Small greens balls in $Mo(Cu_xAl_{1-x})_6Al_4$ are hypothetical to indicate the void which should be occupied to complete the $CaCu_5$ block.

It should, however, be noted that the composition shifted to $Mo_{9.0}Cu_{22.8}Al_{68.1}$ (from EPMA). Systematic extinctions revealed a primitive unit cell with eight possible space group symmetries, *P6/mmm* (No. 191), *P-62m* (No. 189), *P-6m2* (No. 187), *P622* (No. 177), *P6mm* (No. 183), *P-6* (No. 174), *P6* (No. 168), *P6/m* (No. 175). As structure solution using direct methods in all these space groups revealed practically identical solutions, we describe the structure in the space group with the highest symmetry *P6/mmm* (No. 191). In total, 5 crystallographic sites were obtained out of which, 1*a* was fully occupied by Mo, 2*d* and 2*e* were fully occupied by Al and two 6*i* sites were partially occupied by Cu and Al atoms. Independent refinement of atom occupation in the latter two sites yielded 50.5 % for Al in one site, leaving a small defect in the Cu-site (45%). Therefore in the following refinements the occupation of Al was kept at 50 %, whereas the vacancy on the Cu-site was filled with Al. With this atom arrangement the refined composition ($Mo_{9.1}Cu_{22.7}Al_{68.2}$) was close to the EPMA value ($Mo_{9.1}Cu_{22.8}Al_{68.1}$).

It must be noted that the distance between these latter two sites was only 0.07241 nm indicating that we deal with one site split into an Al site (6*i*1; 50.0 %) and a random mixture of Cu+Al in the second site (6*i*2; 50.0 %). The split site is positioned between the 1*a* site (occupied by Mo) and the 2*e* site (occupied by Al). Consistent with the chemical affinity of the three elements, Al atoms from the 6*i*1 site move closer to the 1*a* site (Mo), whereas Cu atoms in site 6*i*2 move closer to the 2*e* site (Al). Although atoms neighbouring the split site (Al in 2*e*) show a moderate elliptical shape, a difference Fourier map revealed a correspondingly broadened but single peak structure. With anisotropic displacement parameters, the structure refinement finally converged to $R_{F2} = 0.022$ with negligible residual electron density (0.89 and –0.82 $e^-/10^{-3}nm^3$). Results are summarized in Table 1a,b. X-ray powder diffraction intensities collected from a polycrystalline sample are in good agreement with the intensities calculated from the structural model taken from the single crystal. Fig. 1 shows the coordination polyhedra for $Mo(Cu_xAl_{1-x})_6Al_4$. The crystal structure of $Mo(Cu_xAl_{1-x})_6Al_4$ is a unique structure type, which is made of alternate blocks of Zr_4Al_3 and $CaCu_5$ (Fig. 2), however, the 2*c* site in $CaCu_5$ is vacant. A closely related combination of these two structural blocks is obvious from the structure type of $MgFe_6Ge_6$ [15]. Although the distances between Mo and Cu atoms ($d_{Mo(1a)-Cu(2c)} = 0.2888$ nm) would satisfy the sum of metal atom radii, splitting of the 6*i* site, however, diminished the distances between neighboring 6*i* sites ($d_{Cu,Al(6i)-Cu,Al(6i)} = 0.189$ nm) resulting in vacant 2*c* sites (Fig. 2). The crystal

structure of $Mo(Cu_xAl_{1-x})_6Al_4$ can thus be considered as an unfilled structure variant of the $MgFe_6Ge_6$-type.

Table 1a: XSC data for $Mo(Cu_xAl_{1-x})_6Al_4$ (x=0.416), $MoCu_2Al_{8-x}$ (x = 0.080) and Ni_2Al_3 standardized with program *Structure Tidy* [15]. Mo Kα; 2Θ range (°) = 3$\leq$2$\Theta$$\leq$70; ω-scans, scan width 1.7° = 150 sec/frame; Anisotropic displacement parameters in (10^2nm^2).

Parameter/compound	$Mo(Cu_xAl_{1-x})_6Al_4$ (x=0.416)	$MoCu_2Al_{8-x}$, x = 0.080	Ni_2Al_3
Space Group	*P6/mmm*, #191	*P6*, #168	*P-3m*1, #164
Composition from EPMA	$Mo_{9.1}Cu_{22.8}Al_{68.1}$	$Mo_{9.5}Cu_{19.0}Al_{71.5}$	$Ni_{39.2}Al_{60.8}$
Composition from refinement	$Mo_{9.1}Cu_{22.7}Al_{68.2}$	$Mo_{9.2}Cu_{18.3}Al_{72.5}$	Ni_2Al_3
Formula from refinement	$Mo(Cu_xAl_{1-x})_6Al_4$ (x=0.416)	$MoCu_2Al_{8-x}$, x = 0.080	Ni_2Al_3
a, c (nm)	0.50030(1), 0.76279(3)	0.86769(1), 1.52149(2)	4.0533(2), 4.9038(3)
Reflections in refinement	181$\geq$4σ(F_o) of 187	394	136$\geq$4σ(F_o) of 139
Number of variables	20	92	9
$R_F^2 = \Sigma|F_0^2-F_c^2|/\Sigma F_0^2$	0.022	$R_B = \Sigma|I_0-I_c|/\Sigma I_0 = 0.049$	0.0166
R_{Int}	0.016	$R_F = \Sigma|F_0-F_c|/\Sigma F_0 = 0.058$	0.0292
wR2	0.049	$R_{wP} = [\Sigma w_i|y_{0i}-y_{ci}|^2/\Sigma w_i|y_{0i}|^2]^{1/2}$ = 0.045	0.0379
$R_e = [(N-P+C)/\Sigma w_i y_{0i}^2]^{1/2}$	-	0.009	-
GOF	1.173	$R_P = \Sigma|y_{0i}-y_{ci}|/\Sigma|y_{0i}| = 0.029$	1.914
Residual density e$^-$/Å^3; max; min.	0.87; -0.82	$\chi^2 = (R_{wP}/R_e)^2 = 24.3$	0.69; -1.19
Atom parameters **Atom site 1**	**Mo1** in 1*a* (0, 0, 0)	**Mo1** in 1*a* (0, 0, z)	**Ni** in 2*d*(⅓, ⅔, z)
Occ.;	1.00	1.00	1.00
z;	-	0.001(9)	0.1444(1)
U_{11}= U_{22}; U_{33}	0.0126(2); 0.0109(2)	$^1B_{iso}$ = 0.60(2)	0.0054(1); 0.0043(1)
U_{23} = U_{13} = 0, U_{12}	0	-	0.0027(1)
Atom site 2	**Al1** in 2*d* (⅓, ⅔, ½)	**Mo2** in 1*a* (0, 0, z)	**Al1** in 2*d*(⅓, ⅔, z)
Occ.;	1.00	1.00	1.00
z;	-	0.49(2)	0.6462(2)
U_{11}= U_{22}; U_{33}	0.0161(4); 0.0107(4)	B_{iso} = 0.60(2)	0.0086(3); 0.0042(4)
U_{23} = U_{13} = 0, U_{12}	0.0080(2)	-	0.0043(1)
Atom site 3	**Al2** in 2*e* (0, 0, z)	**Mo3** in 2*b* (⅓, ⅔, z)	**Al2** in 1*a*(0, 0, 0)
Occ.;	1.00	1.00	1.00
z;	0.3348(1)	0.49(2)	-
U_{11}= U_{22}; U_{33}	0.0272(5); 0.0088(5)	B_{iso} = 0.60(2)	0.0059(3); 0.0148(7)
U_{23} = U_{13} = 0, U_{12}	0.0137(3)	-	0.0029(2)
Atom site 4	M in 6*i*2 (½, 0, z)	**Mo4** in 2*b* (⅓, ⅔, z)	-
Occ.;	M = 0.416(4) Cu + 0.084 Al	1.00	-
z;	0.2188(1)	0.99(2)	-
U_{11}; U_{22}; U_{33}	0.0128(2); 0.0114(3); 0.0147(4)	B_{iso} = 0.60(2)	-

$U_{23} = U_{13} = 0$, U_{12}	0.0057(1)	-	-
Atom site 5	**Al3** in $6i1$ (½, 0, z)	**Al1** in $6d$ (x, y, z)	-
Occ.;	0.500(6)	1.00	-
x, y, z;	z = 0.1238(3)	0.000(3), 0.353(2), 0.74(2)	-
U_{11}; U_{22}; U_{33}	0.0190(7); 0.0186(8); 0.030(1)	B_{iso} = 0.78(3)	-
$U_{23} = U_{13} = 0$, U_{12}	0.0093(4)	-	-
Atom site 6	-	**Al2** in $6d$ (x, y, z)	-
Occ.;	-	1.00	-
x, y, z;	-	0.007(3), 0.340(1), 0.24(2)	-
B_{iso};	-	0.78(3)	-
Atom site 7	-	**Al3** in $1a$ (0, 0, z)	-
Occ.;	-	1.00	-
z;	-	0.16(2)	-
B_{iso};	-	0.78(3)	-
Atom site 8	-	**Al4** in $1a$ (0, 0, z)	-
Occ.;	-	1.00	-
z;	-	0.32(2)	-
B_{iso};	-	0.78(3)	-
Atom site 9	-	**Al5** in $1a$ (0, 0, z)	-
Occ.;	-	1.00	-
z;	-	0.82(2)	-
B_{iso};	-	0.78(3)	-
Atom site 10	-	**Al6** in $1a$ (0, 0, z)	-
Occ.;	-	0.52(1)	-
z;	-	0.65(2)	-
B_{iso};	-	0.78(3)	-
Atom site 11	-	**Al7** in $2b$ (⅓, ⅔, z)	-
Occ.;	-	1.00	-
z;	-	0.66(2)	-
B_{iso};	-	0.78(3)	-
Atom site 12	-	**Al8** in $2b$ (⅓, ⅔, z)	-
Occ.;	-	1.00	-
z;	-	0.82(2)	-
B_{iso};	-	0.78(3)	-
Atom site 13	-	**Al9** in $2b$ (⅓, ⅔, z)	-
Occ.;	-	1.00	-
z;	-	0.32(2)	-
B_{iso};	-	0.78(3)	-
Atom site 14	-	**Al10** in $2b$ (⅓, ⅔, z);	-
Occ.;	-	1.00	-
z;	-	0.15(2)	-

B_{iso};	-	0.78(3)	-
Atom site 15	-	**Al11** in 6*d* (x, y, z)	-
Occ.;	-	1.00	-
x, y, z;	-	0.328(1), 0.164(2), 0.87(2)	-
B_{iso};	-	0.78(3)	-
Atom site 16	-	**Al12** in 6*d* (x, y, z)	-
Occ.;	-	1.00	-
x, y, z;	-	0.341(1), 0.175(2), 0.08(2)	-
B_{iso};	-	0.78(3)	-
Atom site 17	-	**Cu1** in 6*d* (x, y, z)	-
Occ.;	-	1.00	-
x, y, z;	-	0.3356(5), 0.176(1), 0.59(2)	-
B_{iso};	-	0.90(5)	-
Atom site 18	-	**Al13** in 6*d* (x, y, z)	-
Occ.;	-	1.00	-
x, y, z;	-	0.347(1), 0.179(2), 0.42(2)	-
B_{iso};	-	0.78(3)	-
Atom site 19	-	**Cu2** in 3*c* (½, 0, z)	-
Occ.;	-	1.00	-
z;	-	0.10(2)	-
B_{iso};	-	0.90(5)	-
Atom site 20	-	**Cu3** in 3*c* (½, 0, z)	-
Occ.;	-	1.00	-
z;	-	0.38(2)	-
B_{iso};	-	0.90(5)	-
Atom site 21	-	**Al14** in 3*c* (½, 0, z)	-
Occ.;	-	1.00	-
z;	-	0.55(2)	-
B_{iso};	-	0.78(3)	-
Atom site 22	-	**Al15** in 3*c* (½, 0, z)	-
Occ.;	-	1.00	-
z;	-	0.94(2)	-
B_{iso};	-	0.78(3)	-

[1] B_{iso} is given in $(10^2 \ nm^2)$.

Table 1b: Interatomic distances (nm) for Ni_2Al_3, standard deviation ≤0.0002.

Ni–	1Al1	0.2443		–3Al1	0.2556	CN = 11	–1Ni	0.2461			–3Al2	0.2913
CN = 11	–3Al2	0.2445		–3Ni	0.2735		–3Ni	0.2556	Al2–	6Ni	0.2445	
	–1Al1	0.2461	Al1–	1Ni	0.2443		–3Al1	0.2744	CN = 12	–6Al1	0.2913	
$Mo(Cu_xAl_{1-x})_6Al_4$												
Mo1–	2Al2	0.2553		–6Al2	0.3151		–6Al1	0.3151			–2Al2	0.2799

CN = 14	−12Al3	0.2674	Al2−	1Al2	0.2521	Cn*−	4Cn	0.2501		−2Mo1	0.2818
Al1−	6M1	0.2587	CN = 14	−1Mo1	0.2553	CN = 11	−1Cn	0.2593		−2Al1	0.2902
CN = 15	−3Al1	0.2888		−6M1	0.2654						

*Represents the central position of M1 and Al3 and distances were taken from this central position.

6.3.2. The crystal structure of $MoCu_2Al_{8-x}$, x = 0.080

After the crystal structure of $Mo(Cu_xAl_{1-x})_6Al_4$ had been solved, we returned to the XPD data of the sample with the nominal composition $Mo_{7.5}Cu_{20.5}Al_{72}$, which was annealed at 720° C for 14 days only and which was completely indexed on the bigger hexagonal unit cell [a = 0.86769(1), c = 1.52149(2) nm] earlier reported by B. Grushko et al. [13]. Inspection of the extinctions resulted in the diffraction symbol *P---* with 8 possible space group types [*P6/mmm* (191), *P-62m* (189), *P-6m2* (187), *P6mm* (183), *P622* (177), *P6/m* (175), *P-6* (174) and *P6* (168)]. Rietveld refinement of the structure model transferred from the $Mo(Cu_xAl_{1-x})_6Al_4$ type sub-cell (taking only the center position of the split sites 6i1 and 6i2) in all these space groups, gave the best agreement for *P6* (168) with the lowest R-value = 0.049, whilst refinements for all other space groups arrived at higher residual values: R > 0.10. According to the larger size (a = $a_0\sqrt{3}$, c = $2c_0$), the unit cell contains 6 times the number of atoms present in $Mo(Cu_xAl_{1-x})_6Al_4$ and is defined by the formula $MoCu_2Al_{8-x}$ due to a small amount of vacancies in the 1*a* site (Al6). The lower symmetry allows slight positional changes for the atoms in relation to the atom arrangement in the subcell. Therefore all interatomic distances are similar to the distances obtained in $Mo(Cu_xAl_{1-x})_6Al_4$). The Rietveld refinement in Figure 3 shows that the X-ray spectrum can satisfactorily describe all the weak superstructure reflections. Results are summarized in Table 1a. A Bärnighausen tree describing the crystallographic group-subgroup relations between the structure types of $Mo(Cu_xAl_{1-x})_6Al_4$ and $MoCu_2Al_{8-x}$ via a series of hypothetical structure types is shown in Fig. 4. The essential difference between the parent structure and the superstructure is the split of the 6*i* position (deriving from the central position of sites 6*i*1 and 6*i*2, which in the parent structure are occupied by Al and (Cu+Al) atoms, respectively). In the superstructure this split is removed and full atom order is restored among the 8 independent sites as they are separately occupied by Cu (Cu1, Cu2, Cu3) and Al atoms (Al11, Al12, Al14, Al15, Al16) (Fig. 4). Cu atoms move closer to Al atoms and Al atoms move closer to Mo resulting in

little displacement of other Mo and Al atoms. It is interesting to note that the composition has shifted from $Mo_{9.5}Cu_{19.0}Al_{71.5}$ for the small hexagonal cell to $Mo_{9.1}Cu_{22.8}Al_{68.1}$ for the supercell.
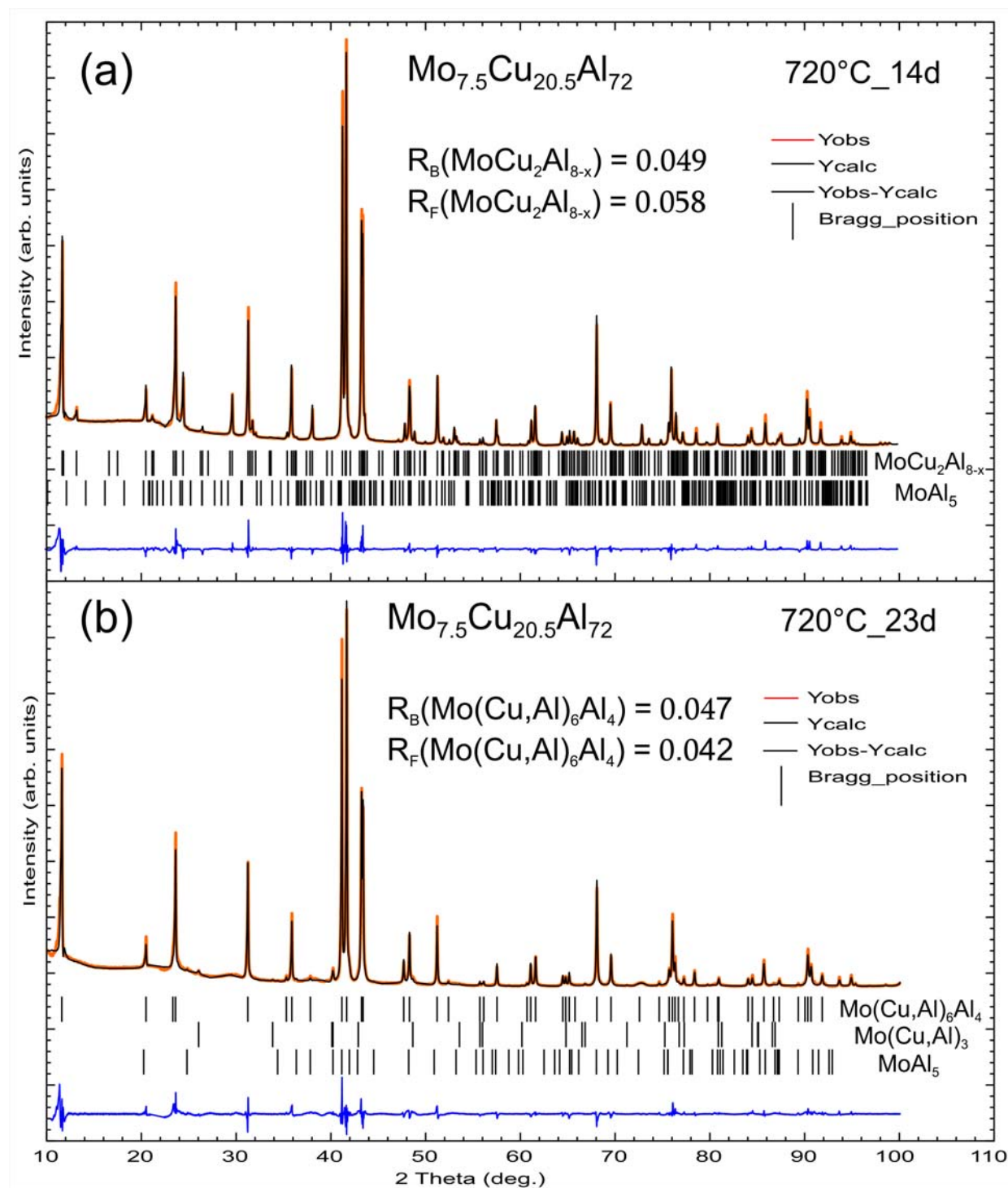
Fig. 3. Refinement of X-ray spectrum of $Mo_{7.5}Cu_{20.5}Al_{72}$ (nominal composition) quenched from 720°C (a) after annealing for 14 days, represents $MoCu_2Al_{8-x}$ and $MoAl_5$ phase (traces) and (b) after annealing for

23 days, showing equilibrium between $Mo(Cu_xAl_{1-x})_6Al_4$ and little amounts of the $Mo(Cu,Al)_3$-N-phase ($TiAl_3$-type) and $MoAl_5$.

Although the main features of the X-ray spectrum in Fig.3 agree essentially with the diffractogram reported by B. Grushko et al. [13], some of the weaker reflections show differences to our observed spectrum suggesting further structure variants as a function of Cu/Al exchange in the homogeneity region. It should be mentioned in this context that the X-ray diffractograms for the homologous W-Cu-Al alloys indicate further structure variants, which are under investigation but will be subject of a forthcoming publication.

P6/mmm
MoAl₄(Cu,Al)₆
|
i(3x2)
a+b, -a+2b, 2c

Mo: 1a 6/mmm	Al1: 2d -6m2	Al2: 2e 6mm	M1: 6i 2mm
0	1/3	0	1/2
0	2/3	0	0
0	1/2	0.335	0.17

P6/mmm
|
t2
a, b, c

Mo1: 1a 6/mmm	Mo2: 1b 6/mmm	Mo3: 2c -6m2	Mo4: 2d -6m2	Al1: 12n ..m	Al2: 2e 6mm	Al3: 2e 6mm	Al3: 4h 3m.	Al3: 4h 3m.	M1: 6i 2mm	M2: 6i 2mm	M3: 12o .m.	M4: 12o .m.
0	0	1/3	1/3	0	0	0	1/3	1/3	1/2	1/2	0.334	0.334
0	0	2/3	2/3	0.333	0	0	2/3	2/3	0	0	0.167	0.167
0	1/2	0	1/2	0.25	0.167	0.667	0.167	0.667	0.085	0.585	0.085	0.585

P6/m
|
t2

Mo1: 1a 6/m..	Mo2: 1b 6/m..	Mo3: 2c -6..	Mo4: 2d -6..	Al1: 12l 1	Al2: 2e 6..	Al3: 2e 6..	Al3: 4h 3..	Al3: 4h 3..	M1: 6i 2..	M2: 6i 2..	M3: 12l 1	M4: 12l 1
0	0	1/3	1/3	0.0	0	0	1/3	1/3	1/2	1/2	0.334	0.334
0	0	2/3	2/3	0.333	0	0	2/3	2/3	0	0	0.167	0.167
0	1/2	0	1/2	0.25	0.167	0.667	0.167	0.667	0.085	0.585	0.085	0.585

P6
MoCu₂Al₈

Mo1: 1a 6..	Mo2: 1a 6..	Mo3: 2b 3..	Mo4: 2b 3..	Al1: 6d 1	Al2: 6d 1	Al3: 1a 6..	Al5: 1a 6..	Al6: 1a 6..	Al4: 1a 6..	Al10: 2b 3..	Al8: 2b 3..	Al7: 2b 3..	Al9: 2b 3..	Cu2: 3c 2..	Al16: 3c 2..	Cu3: 3c 2..	Al15: 3c 2..	Al12: 6d 1	Al11: 6d 1	Cu1: 6d 1	Al14: 6d 1
0	0	1/3	1/3	0.0	0.0	0	0	0	0	1/3	1/3	1/3	1/3	1/2	1/2	1/2	1/2	0.341	0.327	0.335	0.347
0	0	2/3	2/3	0.353	0.338	0	0	0	0	2/3	2/3	2/3	2/3	0	0	0	0	0.171	0.165	0.173	0.178
0.0	0.487	0.987	0.495	0.742	0.244	0.155	0.814	0.653	0.315	0.152	0.821	0.659	0.319	0.095	0.940	0.376	0.551	0.078	0.873	0.594	0.423

Fig. 4. Bärnighausen tree relating the structure types of $Mo(Cu_xAl_{1-x})_6Al_4$ and $MoCu_2Al_{8-x}$.

6.3.3. The crystal structure of $ReNi_2Al_{8-x}$, x = 0.268.

The X-phase in Re-Ni-Al system was first reported by B. Grushko et al. [7], who from TEM assigned an orthorhombic unit cell [a = 1.0048(3), b = 1.5423(8), c = 0.8367(3) nm] with three possible space group symmetries: *Pbm*2 (No. 28), *Pb*2₁*m* (No. 26) and *Pbmm* (No. 51). Our unit cell parameters [a = 1.00320(2), b = 1.51258(3), c = 0.83890(2) nm], derived from a single crystal suitable for X-ray structure analysis, are consistent with the unit cell parameters given by

B. Grushko et al. [7]. Systematic extinctions revealed a primitive lattice with two possible space group symmetries, *Pba*2 (No. 32) and *Pbam* (No. 55), which, however, differ from the space group types suggested earlier [7]. Solution of the structure by direct methods in both these space groups revealed identical atomic order in the crystal lattice. As practically identical reliability factors and residual electron densities were obtained for these two refinements and as an analysis of missing symmetry by program PLATON confirmed *Pbam*, we describe the structure in the highest symmetry space group *Pbam*. Results are summarized in Table 2a,b.
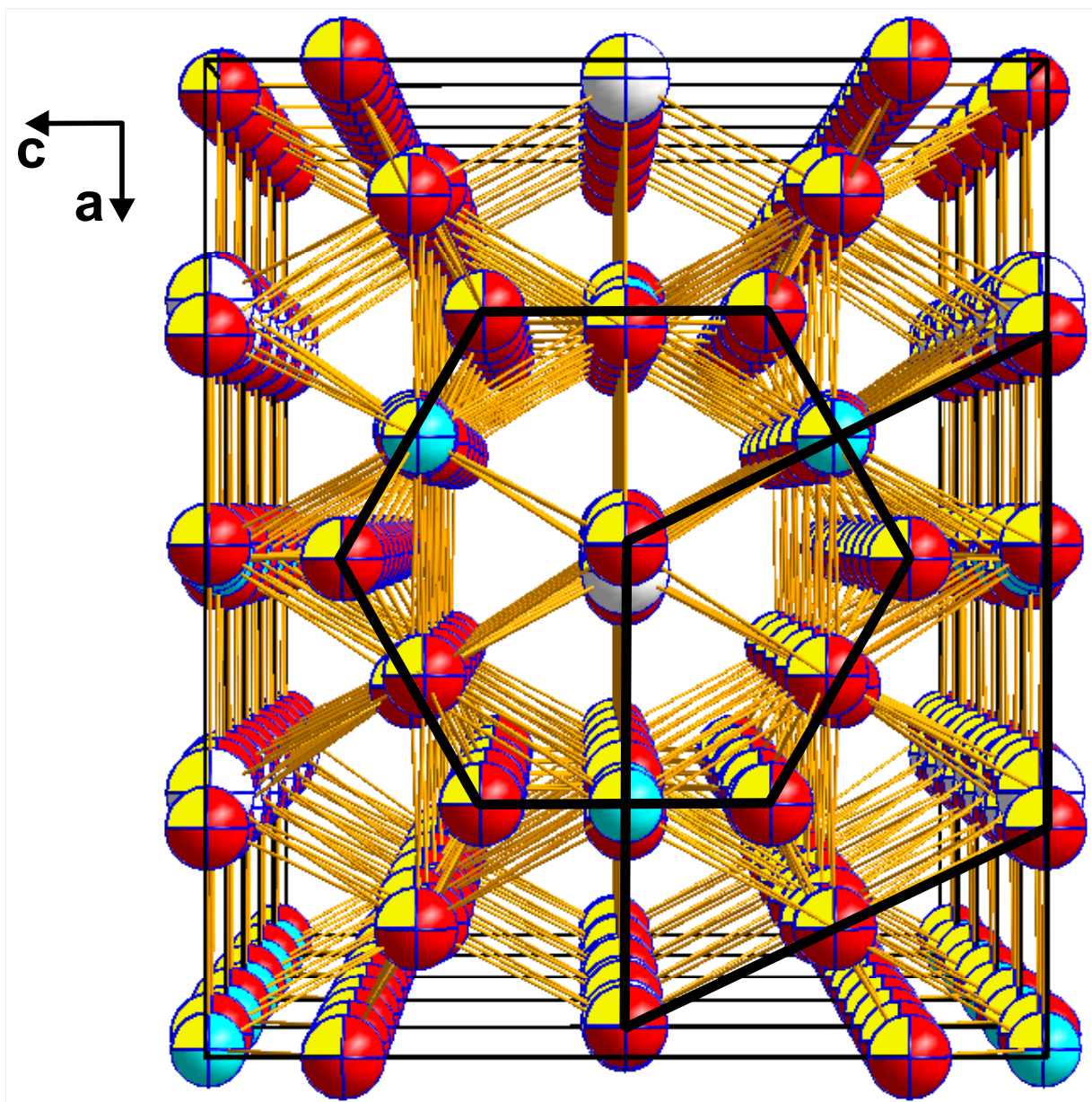
Fig. 5. Projection of the crystal structure of ReNi$_2$Al$_{8-x}$ (x = 0.033) along the b-axis.
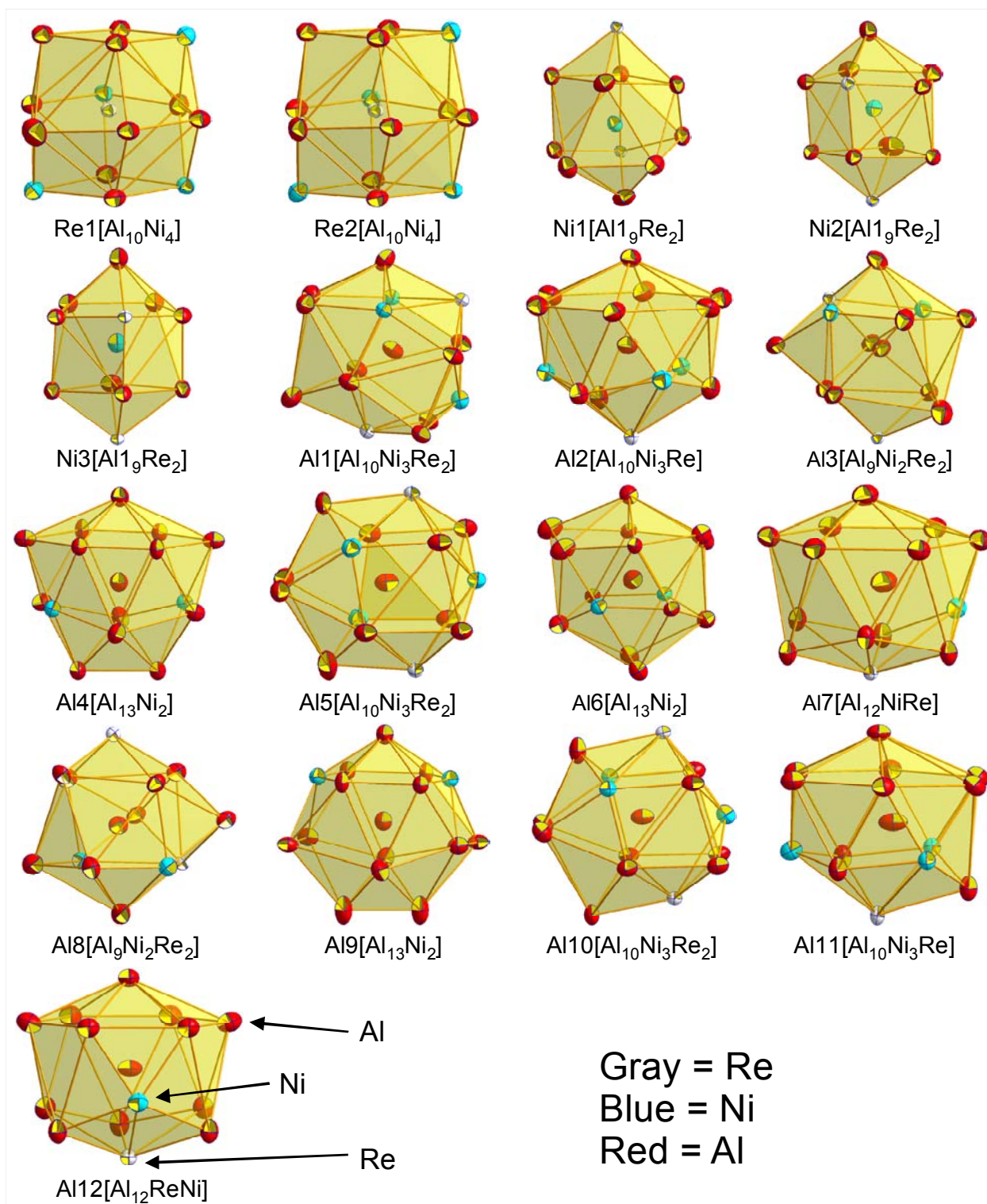
Fig. 6. Coordination polyhedra of the 17 atom sites in $ReNi_2Al_{8-x}$.

Figure 5 represents a projection of ReNi$_2$Al$_{8-x}$ along the b-axis showing an infinite channel running through the structure. Furthermore, X-ray powder diffraction intensities collected from a polycrystalline sample are in good agreement with the intensities calculated from the structural model taken from the single crystal. Coordination polyhedra for ReNi$_2$Al$_{8-x}$ are shown in Fig. 6.
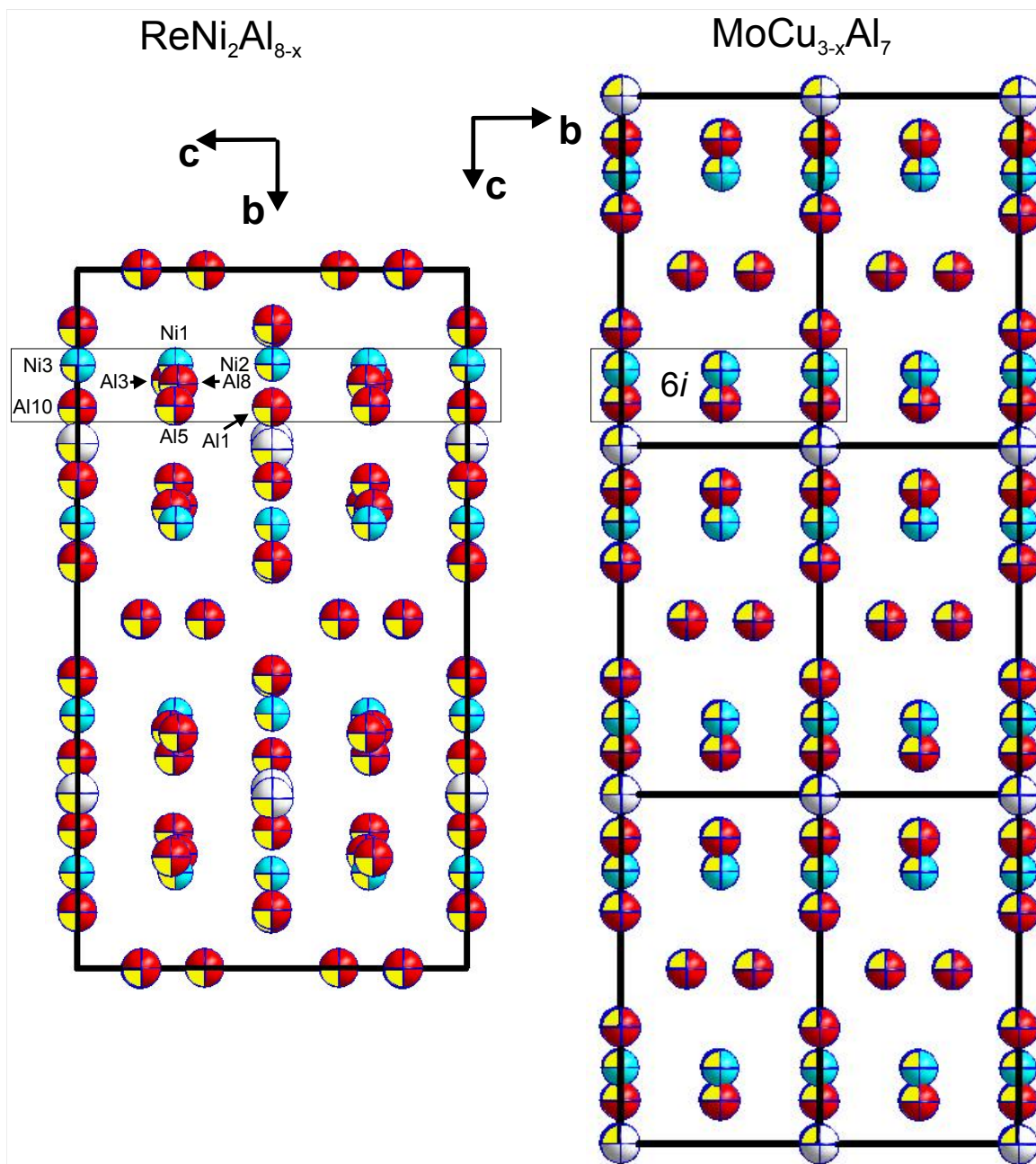
Fig. 7. Structural relation between the structure types of Mo(Cu$_x$Al$_{1-x}$)$_6$Al$_4$ and ReNi$_2$Al$_{8-x}$. Three unit cells of Mo(Cu$_x$Al$_{1-x}$)$_6$Al$_4$ are shown on the right side. Doubling of c-axis and shift of origin by ½c of Mo(Cu$_x$Al$_{1-x}$)$_6$Al$_4$ form the b-axis of ReNi$_2$Al$_{8-x}$.

Bärnighausen tree (left-side group–subgroup chain):

$P6/mmm$ — MoAl$_4$(Cu,Al)$_6$
| t3
| $a+b$, $-a+b$, c
| Origin shift ½, 0, 0
$Cmmm$
| k2
| a, b, c
$Pmmm$
| k2
| $2a$, $-c$, b
| Origin shift 0, ½, 0
$Pmam$ ($Pmma$)
| k2
| a, $2b$, c
$Pbam$ — ReNi$_2$Al$_8$

$P6/mmm$ level:

Mo: 1a 6/mmm	Al1: 2d -6m2	Al2: 2e 6mm	M1: 6i 2mm
0	⅓	0	½
0	⅔	0	0
0	½	0.335	0.17

$Cmmm$ level:

Mo: 2b mmm	Al1: 4j m2m	Al2: 4l mm2	M1: 8m ..2	M2: 4k mm2
½	0	0	¼	0
0	0.167	½	¼	0
0	½	0.335	0.17	0.17

$Pmmm$ level:

Mo1: 1b mmm	Mo2: 1e mmm	Al1: 2n m2m	Al2: 2p m2m	Al3: 2r mm2	Al4: 2s mm2	M1: 8α 1	M2: 2t mm2	M3: 2q mm2
½	0	0	½	0	½	0.25	½	0
0	½	0.167	0.333	½	0	0.25	½	0
0	0	½	½	0.335	0.335	0.17	0.17	0.17

$Pmam$ ($Pmma$) level:

Mo1: 2e mm2	Mo2: 2d .2/m.	Al1: 4g .2.	Al2: 4k m..	Al3: 4j .m.	Al4: 2e mm2	Al5: 2e mm2	M2: 8l 1	M2: 8l 1	M3: 2f mm2	M4: 2f mm2	M5: 4i .m.
¼	½	0	¼	0.0	¼	¼	0.125	0.125	¼	¼	0.0
0.50	½	0	0.0	0.165	0.165	0.835	0.330	0.670	0.67	0.33	0.33
0	½	0.167	0.333	½	0	0	0.250	0.250	½	½	0

$Pbam$ — ReNi$_2$Al$_8$ level:

Re2: 4g ..m	Re1: 4h ..m	Al9: 4e ..2	Al4: 4f ..2	Al6: 8i 1	Al7: 4h ..m	Al2: 4h ..m	Al12: 4g ..m	Al11: 4g ..m	Al5: 8i 1	Al3: 8i 1	Ni1: 8i 1	Al8: 8i 1	Al1: 4h ..m	Ni2: 4h ..m	Ni3: 4g ..m	Al10: 4g ..m
0.262	0.489	0	0	0.254	0.028	0.014	0.229	0.226	0.125	0.368	0.123	0.381	0.234	0.251	0.003	0.014
0.250	0.257	0	½	0.002	0.079	0.416	0.084	0.420	0.196	0.342	0.363	0.164	0.303	0.135	0.138	0.302
0	½	0.164	0.164	0.328	½	½	0	0	0.248	0.240	0.252	0.259	½	½	0	0

Fig. 8. Bärnighausen tree relating the structure types of Mo(Cu$_x$Al$_{1-x}$)$_6$Al$_4$ and ReNi$_2$Al$_{8-x}$.

Table 2a: XSC data for MoNi$_{2-x}$Al$_{8+x}$ (x = 0.165), WNi$_{2-x-y}$Al$_{8+x-z}$, (x = 0.162, y = 0.015, z = 0.010) and isotypic ReNi$_2$Al$_{8-x}$, x = 0.033, space group $Pbam$, #55, standardized with program *Structure Tidy* [15]. Mo Kα-radiation 2Θ range (°) = 3≤2Θ≤70; ω-scans, scan width 1.7°; 150 sec/frame; Anisotropic displacement parameters in (10^2nm^2).

Parameter/compound	ReNi$_2$Al$_{8-x}$, x = 0.033	MoNi$_{2-x}$Al$_{8+x}$, x = 0.165	WNi$_{2-x-y}$Al$_{8+x-z}$, (x = 0.162, y = 0.015, z = 0.010)
Composition from EPMA	Re$_{9.5}$Ni$_{19.5}$Al$_{71.4}$	Mo$_{10.1}$Ni$_{16.7}$Al$_{73.2}$	W$_{9.5}$Ni$_{17.5}$Al$_{73.0}$
Composition from refinement	Re$_{9.1}$Ni$_{18.2}$Al$_{72.7}$	Mo$_{9.1}$Ni$_{16.7}$Al$_{74.2}$	W$_{9.1}$Ni$_{16.5}$Al$_{74.4}$
Formula from refinement	ReNi$_2$Al$_{8-x}$, x = 0.033	MoNi$_{2-x}$Al$_{8+x}$, x = 0.165	WNi$_{2-x-y}$Al$_{8+x-z}$, (x = 0.162, y = 0.015, z = 0.010)
a (nm)	1.00320(2)	1.00664(2)	1.00683(2)
b (nm)	1.51258(3)	1.53108(2)	1.53236(3)

c (nm)	0.83890(2)	0.85205(2)	0.85232(2)
μ_{abs} (mm^{-1})	25.81	8.07	23.5
Reflections in refinement	2357≥4σ(F$_o$) of 2956	2396≥4σ(F$_o$) of 2910	2171≥4σ(F$_o$) of 3049
Number of variables	119	127	128
$R_F^2 = \Sigma|F_0^2 - F_c^2|/\Sigma F_0^2$	0.017	0.035	0.024
R_{Int}	0.034	0.038	0.020
wR2	0.040	0.060	0.055
GOF	1.134	1.155	0.975
Extinction (Zachariasen)	0.00093(3)	0.00142(7)	0.00099(4)
Residual density e$^-$/Å^3; max; min.	1.62; -1.31	1.42; -1.79	1.99; -1.78

Atom parameters

Atom site 1	**Re1** in 4h (x, y, ½);	**Mo1** in 4h (x, y, ½);	**W1** in 4h (x, y, ½);
Occ.;	1.00	1.00	1.00
x, y	0.48787(2), 0.25684(1)	0.48878(4), 0.25658(2)	0.48819(2), 0.25657(1)
U$_{11}$; U$_{22}$; U$_{33}$	0.00355(9), 0.00427(2); 0.00389(7)	0.0048(1), 0.0051(1); 0.0045(1)	0.0071(1), 0.0063(1); 0.0063(1)
U$_{23}$ = U$_{13}$ = 0, U$_{12}$	0.00000(4)	0.0002(1)	0.0003(1)
Atom site 2	**Re2** in 4g (x, y, 0);	**Mo2** in 4g (x, y, 0);	**W2** in 4g (x, y, 0);
Occ.;	1.00	1.00	1.00
x, y	0.26220(2), 0.24957(1)	0.26028(4), 0.25074(2)	0.26056(2), 0.25037(1)
U$_{11}$; U$_{22}$; U$_{33}$	0.00337(9); 0.00432(6), 0.00398(8)	0.0086(2); 0.0066(1), 0.0044(1)	0.0105(1); 0.0081(1), 0.0062(1)
U$_{23}$ = U$_{13}$ = 0, U$_{12}$	-0.00017(3)	0.0025(1)	0.0027(1)
Atom site 3	**Ni1** in 8i (x, y, z);	**Ni1** in 8i (x, y, z);	**Ni1** in 8i (x, y, z);
Occ.;	1.00	1.00	1.00
x, y, z	0.12326(3), 0.36345(2), 0.25200(4)	0.12341(3), 0.36650(2), 0.25271(4)	0.12344(4), 0.36635(2), 0.25260(5)
U$_{11}$; U$_{22}$; U$_{33}$	0.0051(1); 0.0057(1); 0.0059(1)	0.0061(1); 0.0068(1); 0.0071(1)	0.0083(2); 0.0084(2); 0.0093(2)
U$_{23}$, U$_{13}$, U$_{12}$	-0.0001(1), 0.0001(1), 0.0001(1)	0.0001(1), 0.0001(1), 0.0002(1)	0.0001(1), -0.0001(1), 0.0004(1)
Atom site 4	**Ni2** in 4h (x, y, ½);	**Ni2** in 4h (x, y, ½);	**Ni2** in 4h (x, y, ½);
Occ.;	1.00	1.00	0.966(2)
x, y	0.25051(5), 0.13548(3)	0.25287(5), 0.13420(3)	0.25345(6), 0.13436(4)
U$_{11}$; U$_{22}$; U$_{33}$	0.0070(2); 0.0067(2); 0.0065(2)	0.0084(2); 0.0089(2); 0.0079(2)	0.0102(3); 0.0096(3); 0.0088(3)
U$_{23}$ = U$_{13}$ = 0, U$_{12}$	-0.0006(1)	-0.0006(2)	-0.0008(2)
Atom site 5	**Ni3** in 4g (x, y, 0);	**M** in 4g (x, y, 0);	**M** in 4g (x, y, 0);
Occ.;	**Ni** = 1.00	**M** = 0.668(1) Ni + 0.332 Al	**M** = 0.632(1) Ni + 0.368 Al
x, y	0.00332(5), 0.13753(3)	0.00168(6), 0.13873(4)	0.00082(7), 0.13899(5)
U$_{11}$; U$_{22}$; U$_{33}$	0.0080(2); 0.0065(2); 0.0063(2)	0.0094(3); 0.0135(3); 0.0069(3)	0.0111(3); 0.0153(3); 0.0086(4)
U$_{23}$ = U$_{13}$ = 0, U$_{12}$	0.0009(2)	0.0020(2)	0.0025(3)
Atom site 6	**Al1** in 4h (x, y, 1/2);	**Al1** in 4h (x, y, 1/2);	**Al1** in 4h (x, y, 1/2);
Occ.;	1.00	1.00	1.00
x, y	0.2341(1), 0.30342(7)	0.2332(1), 0.3040(1)	0.2329(1), 0.3045(1)
U$_{11}$; U$_{22}$; U$_{33}$	0.0055(5); 0.0100(5); 0.0058(5)	0.0067(5); 0.0164(5); 0.0086(5)	0.0090(6); 0.0193(7); 0.0097(7)
U$_{23}$ = U$_{13}$ = 0, U$_{12}$	0.0001(4)	0.0007(4)	0.0001(5)
Atom site 7	**Al2** in 4h (x, y, 1/2);	**Al2** in 4h (x, y, 1/2);	**Al2** in 4h (x, y, 1/2);
Occ.;	1.00	1.00	1.00
x, y	0.0143(1), 0.41637(7)	0.0121(1), 0.4160(1)	0.0122(2), 0.41625(9)
U$_{11}$; U$_{22}$; U$_{33}$	0.0119(6), 0.0056(4); 0.0073(6)	0.0130(5); 0.0064(4); 0.0086(5)	0.0151(7), 0.0089(6); 0.0105(7)
U$_{23}$ = U$_{13}$ = 0, U$_{12}$	0.0007(4)	-0.0005(4)	0.0006(5)
Atom site 8	**Al3** in 8i (x, y, z);	**Al3** in 8i (x, y, z);	**Al3** in 8i (x, y, z);
Occ.;	1.00	1.00	1.00
x, y, z	0.3684(1), 0.34207(5), 0.2406(1)	0.3668(1), 0.3422(1), 0.2465(1)	0.3669(1), 0.34176(7), 0.2473(1)
U$_{11}$; U$_{22}$; U$_{33}$	0.0054(3), 0.0091(3); 0.0068(4)	0.0066(3), 0.0124(3); 0.0106(3)	0.0088(4), 0.0136(4); 0.0123(5)
U$_{23}$, U$_{13}$, U$_{12}$	0.0002(3),0.0001(3), 0.0003(3)	0.0026(3),-0.0015(3), -0.0006(3)	0.0028(5),-0.0012(3), -0.0003(4)
Atom site 9	**Al4** in 4f (0, ½, z);	**Al4** in 4f (0, ½, z);	**Al4** in 4f (0, ½, z);
Occ.,	1.00	1.00	1.00
Z	0.1636(1)	0.1649(1)	0.16523(2)

U_{11}; U_{22}; U_{33}	0.0086(7), 0.0073(4); 0.0083(6)	0.0111(6), 0.0080(4); 0.0097(5)	0.0130(7), 0.0094(6); 0.0118(8)
$U_{23} = U_{13} = 0$, U_{12}	0.0017(4)	0.0020(4)	0.0009(5)
Atom site 10	**Al5** in 8*i* (x, y, z);	**Al5** in 8*i* (x, y, z);	**Al5** in 8*i* (x, y, z);
Occ.;	1.00	1.00	1.00
x, y, z	0.12456(8), 0.19573(5), 0.2483(1)	0.1270(1), 0.2004(1), 0.2522(1)	0.1270(1), 0.20009(6), 0.2521(1)
U_{11}; U_{22}; U_{33}	0.0059(3); 0.0098(3); 0.0053(3)	0.0087(3); 0.0118(3); 0.0114(3)	0.0109(4); 0.0140(4); 0.0139(5)
U_{23}, U_{13}, U_{12}	-0.0003(3), 0.0004(2), 0.0001(3)	0.0020(3), 0.0035(3), 0.0008(3)	0.0012(4), 0.0035(3), 0.0016(4)
Atom site 11	**Al6** in 8*i* (x, y, z);	**Al6** in 8*i* (x, y, z);	**Al6** in 8*i* (x, y, z);
Occ.;	1.00	1.00	1.00
x, y, z	0.25408(7), 0.00154(5), 0.3278(1)	0.2551(1), 0.0021(1), 0.3284(1)	0.25536(8), 0.00208(5), 0.3281(2)
U_{11}; U_{22}; U_{33}	0.0089(6); 0.0070(3); 0.0099(5)	0.0104(5); 0.0077(3); 0.0113(4)	0.0125(6); 0.0091(4); 0.0131(7)
U_{23}, U_{13}, U_{12}	-0.0016(2), 0.0004(2), 0.0000(4)	-0.0015(2), 0.0009(3), -0.0001(3)	-0.0015(3), 0.0009(3), 0.0010(4)
Atom site 12	**Al7** in 4*h* (x, y, ½);	**Al7** in 4*h* (x, y, ½);	**Al7** in 4*h* (x, y, ½);
Occ.;	1.00	1.00	0.977(7)
x, y	0.0281(1), 0.07920(8)	0.0292(1), 0.0801(1)	0.0303(2), 0.0793(1)
U_{11}; U_{22}; U_{33}	0.0111(7), 0.0066(5); 0.0173(7)	0.0129(6), 0.0065(5); 0.0215(6)	0.0152(9), 0.0082(7); 0.0218(9)
$U_{23} = U_{13} = 0$, U_{12}	-0.0011(4)	-0.0007(4)	-0.0001(5)
Atom site 13	**Al8** in 8*i* (x, y, z);	**Al8** in 8*i* (x, y, z);	**Al8** in 8*i* (x, y, z);
Occ.;	1.00	1.00	1.00
x, y, z	0.3814(1), 0.16357(5), 0.2586(1)	0.3826(1), 0.1654(1), 0.2597(1)	0.3823(1), 0.16494(7), 0.2587(1)
U_{11}; U_{22}; U_{33}	0.0052(3); 0.0083(3); 0.0067(3)	0.0066(3); 0.0115(3); 0.0076(3)	0.0091(4); 0.0129(4); 0.0089(5)
U_{23}, U_{13}, U_{12}	0.0005(3), -0.0001(3), 0.0003(3)	0.0006(3), 0.0004(3), 0.0002(3)	0.0009(4), -0.0002(3), 0.0001(4)
Atom site 14	**Al9** in 4*e* (0, 0, z);	**Al9** in 4*e* (0, 0, z);	**Al9** in 4*e* (0, 0, z);
Occ.;	1.00	1.00	1.00
Z	0.1637(1)	0.1648(1)	0.1649(2)
U_{11}; U_{22}; U_{33}	0.0097(7); 0.0063(4); 0.0075(6)	0.0125(6); 0.0091(4); 0.0095(5)	0.0137(7); 0.0102(6); 0.0123(8)
$U_{23} = U_{13} = 0$, U_{12}	0.0004(5)	0.0004(4)	0.0009(5)
Atom site 15	**Al10** in 4*g* (x, y, 0);	**Al10a** in 4*g* (x, y, 0);	**Al10a** in 4*g* (x, y, 0);
Occ.;	1.00	0.65(1)	0.63(2)
x, y	0.0140(1), 0.30200(7)	0.0128(2), 0.3003(3)	0.0127(2), 0.2999(4)
U_{iso}/ (U_{11}; U_{22}; U_{33} for Re-Ni-Al)	0.0053(5); 0.0104(4), 0.0060(5)	0.0064(6)	0.0080(9)
$U_{23} = U_{13} = 0$, U_{12}	0.0001(4)	-	-
	-	**Al10b** in 4*g* (x, y, 0);	**Al10b** in 4*g* (x, y, 0);
Occ.;	-	0.35(1)	0.37(2)
x, y; U_{iso}	-	0.0152(4), 0.3276(5); 0.008(1)	0.0146(4), 0.3271(7); 0.009(1)
Atom site 16	**Al11** in 4*g* (x, y, 0);	**Al11a** in 4*g* (x, y, 0);	**Al11a** in 4*g* (x, y, 0);
Occ.;	0.975(6)	0.44(3)	0.52(4)
x, y	0.2256(1), 0.42032(8)	0.248(1), 0.4193(2)	0.2460(1), 0.4195(2)
U_{iso}/ (U_{11}; U_{22}; U_{33} for Re-Ni-Al)	0.0142(8); 0.0053(5), 0.0069(6)	0.007(1)	0.009(1)
$U_{23} = U_{13} = 0$, U_{12}	-0.0004(4)	-	-
	-	**Al11b** in 4*g* (x, y, 0);	**Al11b** in 4*g* (x, y, 0);
Occ.;	-	0.56(3)	0.48(4)
x, y; U_{iso}	-	0.2161(9), 0.4215(2); 0.0089(9)	0.213(1), 0.4216(2); 0.009(1)
Atom site 17	**Al12** in 4*g* (x, y, 0);	**Al12a** in 4*g* (x, y, 0);	**Al12a** in 4*g* (x, y, 0);
Occ.;	0.958(6)	0.73(2)	0.69(3)
x, y	0.2287(1), 0.08431(7)	0.2288(6), 0.0860(1)	0.2260(9), 0.0851(2)
U_{iso}/ (U_{11}; U_{22}; U_{33} for Re-Ni-Al)	0.0095(7); 0.0040(5); 0.0096(7)	0.0106(7)	0.0129(9)
$U_{23} = U_{13} = 0$, U_{12}	0.0001(4)	-	-
	-	**Al12b** in 4*g* (x, y, 0);	**Al12b** in 4*g* (x, y, 0);
Occ.;	-	0.27(2)	0.31(3)
x, y; U_{iso}	-	0.264(1), 0.0839(4); 0.007(2)	0.260(2), 0.0832(4); 0.009(2)

Table 2b: Interatomic distances (nm) for ReNi$_2$Al$_{8-x}$ (x = 0.165), Standard deviation ≤0.0002.

Re1–	1Al7	0.2543		–1Al11	0.2932	CN = 15	–1Ni3	0.2600		–1Al2	0.2742
CN = 14	–1Al1	0.2645		–1Re2	0.2980		–1Al8	0.2633		–1Re2	0.2833

	−2Al5	0.2649		−1Re2	0.3120		−1Al3	0.2644		−1Al6	0.2854
	−1Al1	0.2652	Al1–	2Ni1	0.2560		−1Re1	0.2649		−1Al4	0.2890
	−1Al2	0.2665	CN = 15	−1Ni2	0.2576		−1Ni2	0.2656		−1Al12	0.2948
	−2Al8	0.2724		−1Re1	0.2645		−1Re2	0.2660		−1Al5	0.3262
	−2Al3	0.2835		−1Re1	0.2652		−1Al10	0.2892		−1Al1	0.3319
	−1Ni2	0.3027		−2Al3	0.2658		1Al12	0.2913	Al9–	2Ni3	0.2526
	−1Ni2	0.3116		−1Al2	0.2808		−1Al1	0.2921	CN = 15	−1Al9	0.2790
	−2Ni1	0.3117		−2Al5	0.2921		−1Al7	0.2954		−2Al3	0.2834
Re2–	1Al12	0.2553		−2Al8	0.3319		−1Al8	0.3262		−2Al6	0.2915
CN = 14	−1Al10	0.2625		−2Al6	0.3372		−1Al6	0.3316		−2Al12	0.2985
	−1Al11	0.2640		−1Al7	0.3463		−1Al3	0.3324		−2Al7	0.3124
	−1Al10	0.2654	Al2–	2Ni1	0.2515		−1Al9	0.3328		−2Al11	0.3326
	−2Al5	0.2660	CN = 14	−1Al2	0.2577	Al6–	1Ni2	0.2521		−2Al5	0.3328
	−2Al3	0.2711		−1Re1	0.2665	CN = 15	−1Ni1	0.2532	Al10–	1Ni3	0.2520
	−2Al8	0.2833		−2Al8	0.2742		−1Al3	0.2834	CN = 15	−2Ni1	0.2590
	−1Ni3	0.2980		−1Ni2	0.2771		−1Al4	0.2844		−1Re2	0.2625
	−2Ni1	0.3099		−1Al1	0.2808		−1Al8	0.2854		−2Al8	0.2629
	−1Ni3	0.3120		−2Al6	0.3048		−1Al9	0.2915		−1Re2	0.2654
Ni1–	1Al8	0.2470		−2Al4	0.3143		−1Al6	0.2934		−1Al11	0.2796
CN = 11	−1Al3	0.2491		−2Al6	0.3254		−1Al7	0.2956		−2Al5	0.2892
	−1Al2	0.2515	Al3–	1Ni3	0.2479		−1Al2	0.3048		−2Al4	0.3340
	−1Al6	0.2532	CN = 13	−1Ni1	0.2491		−1Al11	0.3065		−2Al3	0.3349
	−1Al11	0.2536		−1Al5	0.2644		−1Al12	0.3078		−1Al12	0.3358
	−1Al4	0.2545		−1Al1	0.2658		−1Al2	0.3254	Al11–	2Ni1	0.2536
	−1Al1	0.2560		−1Re2	0.2711		−1Al5	0.3316	CN = 15	−1Al12	0.2553
	1Al5	0.2568		−1Al8	0.2740		−1Al1	0.3372		−1Re2	0.2640
	−1Al10	0.2590		−1Al11	0.2775		−1Al7	0.3428		−2Al3	0.2775
	−1Re2	0.3099		−1Al9	0.2834	Al7–	−1Ni2	0.2399		−1Al10	0.2796
	−1Re1	0.3117		−1Al6	0.2834	CN = 14	−1Al7	0.2490		−2Al4	0.2931
Ni2–	1Al7	0.2399		−1Re1	0.2835		−1Re1	0.2543		−1Ni3	0.2932
CN = 11	−2Al8	0.2480		−1Al7	0.2988		−2Al5	0.2954		−2Al6	0.3065
	−2Al6	0.2521		−1Al5	0.3324		−2Al6	0.2956		−2Al9	0.3326
	−1Al1	0.2576		−1Al10	0.3349		−2Al3	0.2988	Al12–	1Ni3	0.2411
	−2Al5	0.2656	Al4–	2Ni1	0.2545		−2Al9	0.3124	CN = 14	−1Al11	0.2553
	−1Al2	0.2771	CN = 15	−1Al4	0.2788		−2Al6	0.3428		−1Re2	0.2553
	−1Re1	0.3027		−2Al6	0.2844		−1Al1	0.3463		−2Al5	0.2913
	−1Re1	0.3116		−2Al8	0.2890	Al8–	1Ni1	0.2470		−2Al8	0.2948
Ni3–	1Al12	0.2411		−2Al11	0.2931	CN = 13	−1Ni2	0.2480		−2Al9	0.2985
CN = 11	−2Al3	0.2479		−2Al2	0.3143		−1Al10	0.2629		−2Al6	0.3078
	−1Al10	0.2520		−2Al12	0.3327		−1Al5	0.2633		−2Al4	0.3327
	−2Al9	0.2526		−2Al10	0.3340		−1Re1	0.2724		−1Al10	0.3358
	−2Al5	0.2600	Al5–	1Ni1	0.2568		−1Al3	0.2740			

A search for the structure type (Pearson symbol: oP88) in Pearson's Crystal Data [17] prompted no results suggesting $ReNi_2Al_{8-x}$ to be a unique structure type. Comparing the structures of $ReNi_2Al_{8-x}$ and $Mo(Cu_xAl_{1-x})_6Al_4$, we observed a close structural relationship documented in Fig. 7. A Bärnighausen tree for the crystallographic group-subgroup relations between the structure types of $Mo(Cu_xAl_{1-x})_6Al_4$ and $ReNi_2Al_{8-x}$ via a series of hypothetical structure types is shown in Fig. 8. The main reason for the orthorhombic superstructure is the ordering of the 6i site, which in $Mo(Cu_xAl_{1-x})_6Al_4$ is a split site and separates into eight fully ordered sites comprising the atoms Ni1, Ni2, Ni3, Al1, Al3, Al5, Al8 and Al10 in $ReNi_2Al_{8-x}$ (Fig. 7). This causes the other atoms to retreat slightly from their ideal locations and results in the orthorhombic distortions observed in $ReNi_2Al_{8-x}$.

6.3.4. The crystal structure of $MoNi_{2-x}Al_{8+x}$, x = 0.165.

Although B. Grushko et al. [3] have derived (a) the unit cell parameters for the Mo-Ni-Al X-phase from TEM [a = 1.0054(4), b = 1.5288(4), c = 0.8519(2) nm] as well as (b) possible space group symmetries for a primitive orthorhombic lattice, *Pbm*2 (No. 26), *Pb*2*m* (No. 29) and *Pbmm* (No. 51), no complete structure analysis was made. Our unit cell parameters [a = 1.00664(2), b = 1.53108(2), c = 0.85205(2) nm] obtained from a single crystal suitable for X-ray structure determination are close to the unit cell parameters given by B. Grushko et al. [3]. Systematic extinctions revealed a primitive lattice with two possible space group symmetries, *Pba*2 (No. 32) and *Pbam* (No. 55), which, however, differ from the space groups suggested earlier [3]. Solution of the structure by direct methods in both these space groups revealed the same atomic order in the crystal lattice. As practically identical reliability factors and residual electron densities were obtained for these two refinements and as an analysis of missing symmetry by program PLATON confirmed *Pbam*, we describe the structure in the highest symmetric space group *Pbam*. Employing anisotropic atomic displacement parameters the refinement converged to $R_{F2} = 0.037$. However, a strongly anisotropic thermal ellipsoid became obvious for three Al-sites Al11, Al12, Al13 which are all neighboring the site M randomly shared by 0.668 Ni + 0.332 Al. The combination of larger Al atoms with smaller Ni-atoms causes a displacement of the neighboring Al atoms. Splitting these sites into two positions reduced the residual value to $R_{F2} = 0.035$ with residual electron densities less than 1.5 $e^-/10^{-3}nm^3$. Results are summarized in Table 2a,b.

The structure formula obtained from single crystal refinement is $MoNi_{2-x}Al_{8+x}$, $x = 0.165$ yielding a corresponding composition $Mo_{9.1}Ni_{16.7}Al_{74.2}$ in good agreement with the composition of the X-phase obtained from EPMA ($Mo_{10.1}Ni_{16.7}Al_{73.2}$, in at.%). Furthermore, X-ray powder diffraction intensities collected from a polycrystalline sample are in good agreement with the intensities calculated from the structural model taken from the single crystal. Thus, lattice parameters, crystal symmetry and atom positions prove for $MoNi_{2-x}Al_{8+x}$ isotypism with the structure type of $ReNi_2Al_{8-x}$.

6.3.5. Phase relations and the crystal structure of $WNi_{2-x-y}Al_{8+x-z}$, (x = 0.162, y = 0.015, z = 0.010).

Although till now, no ternary phase near a composition characteristic for the $ReNi_2Al_{8-x}$-type has been reported in the W-Ni-Al system [8,9], we checked the presence of a homologous phase. Indeed, EPMA of a sample with nominal composition, $W_5Ni_{15}Al_{80}$, annealed at 930°C showed the existence of a ternary phase at $W_{9.1}Ni_{16.3}Al_{74.6}$ (Fig. 9) with an X-ray spectrum similar to the X-phase present in Re-Ni-Al. The new phase was found to be in equilibrium with Ni_2Al_3 and liquid, which on quenching yields a eutectic consisting of $NiAl_3$ and (Al). The new phase is furthermore in equilibrium with practically W-free Ni_2Al_3 ($Ni_{39.1}Al_{60.9}$, EPMA) and with WAl_4, which exhibits little solubility for Ni ($W_{21.5}Ni_2Al_{76.5}$, EPMA).

The partial isothermal section for the Al-rich corner of the W-Ni-Al system is presented in Figure 10. The micrograph in Figure 9 represents equilibria in one of the triangles shown in this partial isothermal section.

A single crystal was selected from the alloy (annealed at 930° C) with nominal composition $W_5Ni_{15}Al_{80}$ (for big crystal grains see the microstructure in Fig. 9). Unit cell parameters [a = 1.00683(2), b = 1.53236(3), c = 0.85232(2) nm] as well as systematic extinctions revealed a primitive lattice with two possible space group symmetries, *Pba*2 and *Pbam* similar to the $ReNi_2Al_{8-x}$ phase. Solution of the structure by direct methods in both these space groups revealed an atomic order corresponding to the structure of $ReNi_2Al_{8-x}$. Characteristic for the $ReNi_{2-x}Al_{8+x}$-type seems to be the site M, which also for the W-Ni-Al-phase exhibits a random replacement of 0.632 Ni + 0.368 Al. As a consequence the adjacent three Al sites show high anisotropic atomic displacement parameters suggesting a split position for these three atom sites. In addition to that,

a few sites showed rather high temperature factors. Occupation refinement of these sites yielded full occupancy except for the two sites $4h$ (Ni2) and $4h$ (Al7). Including anisotropic atomic displacement parameters, the refinement converged to $R_{F2} = 0.024$ with residual electron densities less than 2.0 e^{-}/10^{-3}nm^{3}. Results are summarized in Table 2a,b. Rietveld refinement of the X-ray spectrum of alloy $W_5Ni_{15}Al_{80}$ proved good agreement with the single crystal data (Fig. 9). The composition derived from the refinement agrees well with the EPMA data (see Table 2a,b). Due to similar unit cell dimensions and atom parameters, coordination polyhedra are practically identical with those for the $ReNi_2Al_{8-x}$-type. Accordingly bonding distances are not much different and therefore are not listed here.
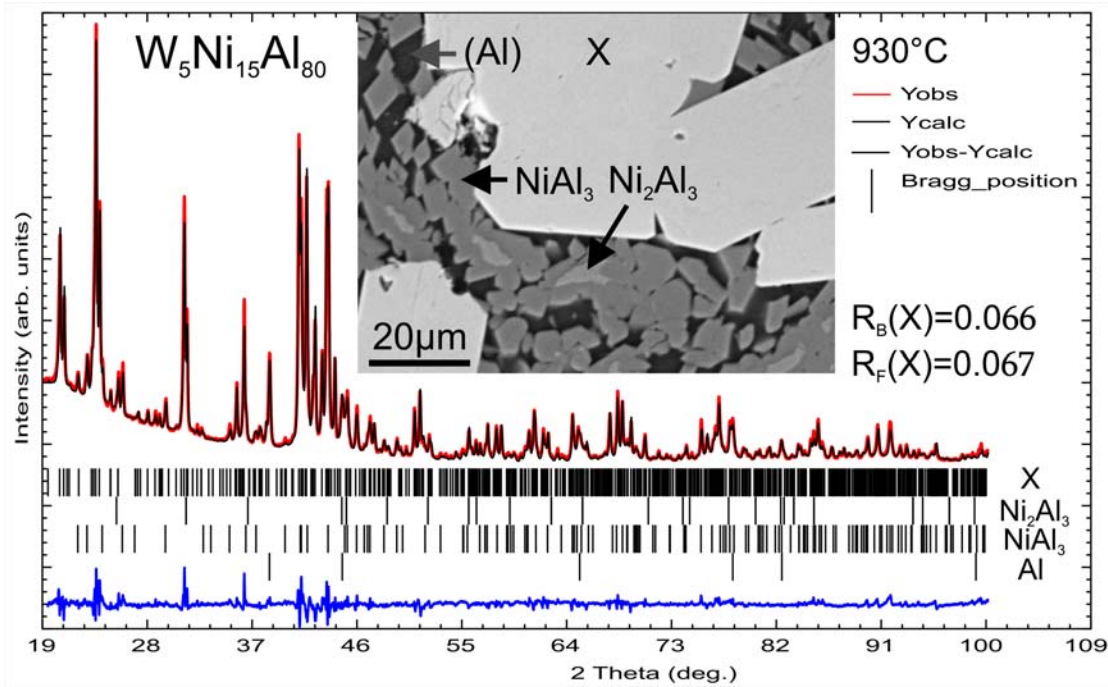
Fig. 9: Refinement of X-ray spectrum of $W_5Ni_{15}Al_{75}$ (nominal composition) quenched from 930°C. Insert reveals the microstructure: white big grains are the $WNi_{2-x-y}\square_yAl_{8+x-z}\square_z$ phase with composition $W_{9.5}Ni_{18.5}Al_{72.0}$ (in at. %), light gray phase is Ni_2Al_3 with composition $Ni_{39.1}Al_{60.9}$ (in at. %), dark gray phase is $NiAl_3$ with composition $Ni_{25.8}Al_{74.2}$ (in at. %) and black particles are Al with composition $Ni_{0.6}Al_{99.4}$ (in at. %).

From the observation of all structural models for both X-phases in the W-Ni-Al and the Re-Ni-Al system, it is obvious that the new phase in the W-Ni-Al system also adopts the structure type of the X-phase present in the Re-Ni-Al system.

It must be noted that a "ReNi$_2$Al$_{8-x}$-type" phase was not reported in the homologous systems Mn-Ni-Al [6], Cr-Ni-Al [18], Cr-Pd-Al [19], Cr-Pt-Al [20], Ta-Ni-Al [21] or Nb-Ni-Al [22].
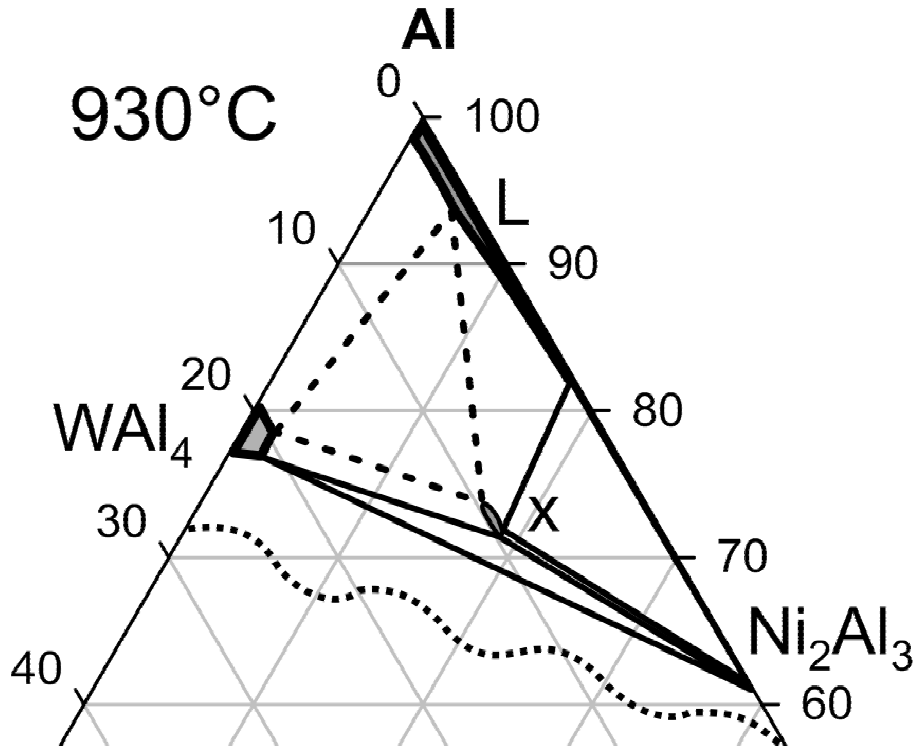
Fig. 10: System W-Ni-Al: Partial isothermal section of the Al-rich corner at 930°C. X represents the WNi$_{2-x-y}$Al$_{8+x-z}$ phase.

6.3.6. The crystal structure of Ni$_2$Al$_3$

Although the structure of Ni$_2$Al$_3$ has been solved from X-ray powder diffraction data [23], no single crystal measurement was made yet. As the alloy with nominal composition Mo$_8$Ni$_{17}$Al$_{75}$ contained large grains of the Ni$_2$Al$_3$ phase, a single crystal was selected for which XSC data were completely indexed on a trigonal lattice. Extinctions confirmed the space group $P\bar{3}m1$ with the highest symmetry. Direct methods prompted an atom arrangement fully consistent with the Ni$_2$Al$_3$-type. For anisotropic atomic displacement parameters, the refinement converged to R$_{F2}$ = 0.0166 with residual electron densities smaller than 0.7 e$^-$/10^{-3}nm^3. Bond lengths were found in the range of 0.2443-0.2913 nm with the shortest bond between Ni-Al and the longest bond between Al-Al. Apparently, Ni-Al bonds look to be shorter than normal but it should be noted

that even shorter bonds between Ni and Al are reported in literature [24]. Results are compiled in Table 1 a,b.
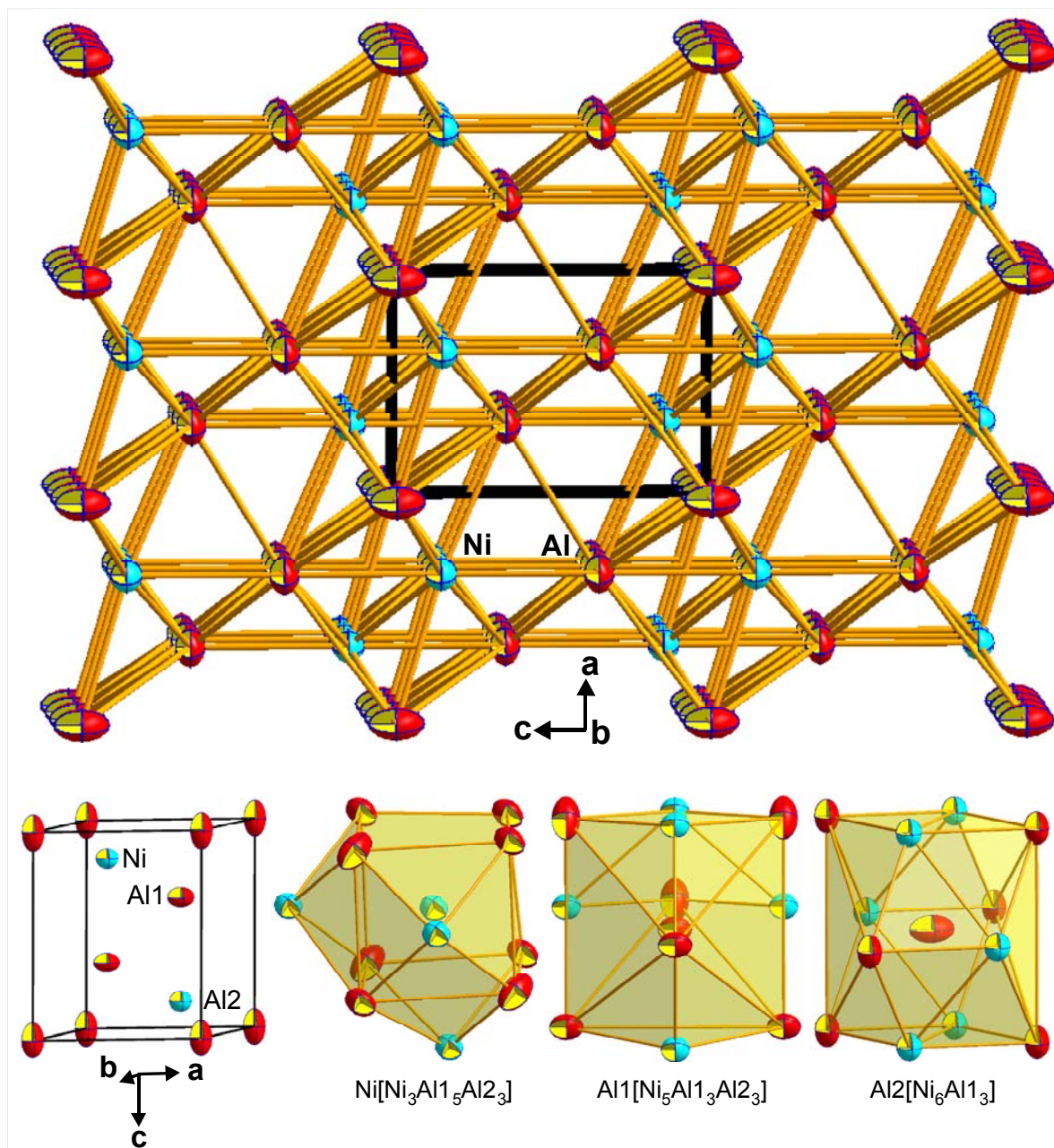
Fig. 11: Unit cell and environment of the atoms in Ni_2Al_3. Ni atoms are slightly out of the (–1 0 2) plane. Coordination polyhedra are shown for all crystallographic sites of Ni_2Al_3.

As no solubility of Mo was observed in the single crystal refinement as well as by EPMA, the structure determination refers to binary Ni_2Al_3. It should be noted that residual densities are

insignificant and demonstrate that there is a negligible concentration of Mo-atoms, although Grushko et al. [3] reported a small solubility of Mo (~0.2 at. %) in the Ni_2Al_3 phase. The composition obtained from the structure refinement, $Ni_{39.2}Al_{60.8}$, is almost identical with the EDX value (see Table 1). The coordination polyhedra for Ni_2Al_3 along with the unit cell are shown in Fig. 11. The crystal structure of $Ni_2Al_3$ (isopointal with La_2O_3) has been described as an ACB stacking of triangular Al-layers parallel to (001) with Ni-atoms in the B and C sites [25]. It is interesting to note that Ni atoms come out of the (-1 0 2) Ni-Al plane and form rather short bonds (Fig. 11). We have already reported such kind of behavior for the Al-rich phase $TiNi_{2-x}Al_5$ [26].

6.4. Conclusion.

The crystal structures of the socalled X-phases, $Mo(Cu_xAl_{1-x})_6Al_4$ (x=0.416), $ReNi_2Al_{8-x}$ (x = 0.033) and of homologous $MoNi_{2-x}Al_{8+x}$ (x = 0.166) and $WNi_{2-x-y}Al_{8+x-z}$, (x = 0.162, y = 0.015, z = 0.010) were defined from X-ray single crystal data and were found to adopt unique structure types. The crystal structure of $Mo(Cu_xAl_{1-x})_6Al_4$ can be considered as an unfilled variant of the $MgFe_6Ge_6$ type. This structure appears after 23 days of annealing, whereas with shorter annealing (14 days), a superstructure was observed with formula $MoCu_2Al_{8-x}$, x = 0.080, which was defined by Rietveld refinement of X-ray powder diffraction data. A completely ordered structure was observed for $ReNi_2Al_{8-x}$ with small defects in the two 4g sites (Al). For the homologous isotypes $MoNi_{2-x}Al_{8+x}$ and $WNi_{2-x-y}Al_{8+x-z}$, (Ni + Al) atoms randomly share one crystallographic site. $WNi_{2-x-y}Al_{8+x-z}$ and phase equilibria at 930 °C for the Al-rich region of the W-Ni-Al phase diagram were reported for the first time.

X-ray single crystal data for binary Ni_2Al_3 confirmed the space group $P\overline{3}m1$ (No. 164), the atom positions and lattice parameters: a = 0.40533(2), c = 0.49038(3) nm, which are very close to the parameters reported in the literature from powder diffraction.

References

[1]   K. Korniyenko, V. Kublii, G. Effenberg, S. Ilyenko, SpringerMaterials-The Landolt-Börnstein Database, (2005), DOI: 10.1007/10915998_25.

[2]   V. Raghavan, Journal of Phase Equilibria and Diffusion **27(4)**, (2006), p. 393-396.

[3]   B. Grushko, S. Mi, J.G. Highfield, Journal of Alloys and Compounds **334**, (2002), p. 187-191.

[4]   V.Y. Markiv, V.V. Burnashova, L.I. Pryakhina, K.P. Myasnikova, Izv. Akad. Nauk SSSR Metals **5**, (1969), p. 117-119.

[5]   V. Raghavan, Journal of Phase Equilibria and Diffusion **31(1)**, (2010), p. 53-54.

[6]   B. Grushko, W. Kowalski, S. Balanetskyy, Journal of Alloys and Compounds **479**, (2009), p. L59-L61.

[7]   B. Grushko, S. Balanetskyy, Powder Diffraction **23**, (2008), p. 251-254.

[8]   N. Bochvar, O. Fabrichnaya, K. Korniyenko, V. Kublii, G. Effenberg, S. Ilyenko, SpringerMaterials-The Landolt-Börnstein Database (2005), DOI: 10.1007/10915998_34.

[9]   V. Raghavan, Journal of Phase Equilibria and Diffusion **30(3)**, (2009), p. 281-282.

[10]   V. Raghavan, Journal of Phase Equilibria and Diffusion **32(3)**, (2011), p. 245-246.

[11]   A.P. Prevarskiy, Y.B. Kuzma, M.M. Onyshkevich, Russ. Metall. **4**, (1977), p. 162-164.

[12]   A.P. Prevarskiy, Y.B. Kuzma, Russ. Metall. **5** (1983) p. 187-189.

[13]   B. Grushko, S.B. Mi, Journal of Alloys and Compounds **509**, (2011), p. L30-L33.

[14]   B. Grushko, S.B. Mi, Powder Diffraction **26(1)**, (2011), p. 70-73.

[15]   W. Buchholz, H.U. Schuster, Z. Anorg. Allg. Chem. **482**, (1981), p. 40-48.

[16]   L.M. Gelato, E. J. Parthé, Appl. Crystallogr. **20**, (1987), p. 139-143.

[17]   P. Villars, K. Cenzual, Pearson's Crystal Data, Release 20010/11, ASM International, Materials Park, Ohio, USA.

[18]   V. Raghavan, Journal of Phase Equilibria and Diffusion **31(3)**, (2010), p. 279-281.

[19]   V. Raghavan, Journal of Phase Equilibria and Diffusion **31(6)**, (2010), p. 546-547.

[20]   V. Raghavan, Journal of Phase Equilibria and Diffusion **32(3)**, (2011), p. 243-244.

[21]   V. Raghavan, Journal of Phase Equilibria and Diffusion **27(4)**, (2006), p. 405-407.

[22]   L. Cornish, D.M. Cupid, J. Gröbner, A. Malfliet, G. Effenberg, S. Ilyenko, SpringerMaterials - The Landolt-Börnstein Database, DOI: 10.1007/978-3-540-88053-0_11, (2009).

[23]   A. Taylor, N.J. Doyle, Journal of Appl. Crystallogr. **5** (1972), p. 201-209.

[24]   F.A. Hinutdinov, S.K. Khairitdinov, A.V. Vakhobov, Doklady Akademii Nauk Tadzhikskoi SSR **30** (1987), p. 169-172.

[25]   W.B. Pearson, "The Crystal Chemistry and Physics of Metals and Alloys", Wiley Interscience, N.Y. (1972).

[26]   A.U. Khan, J. Bursik, A. Grytsiv, V. Pomjakushin, H. Effenberger, P. Rogl, Intermetallics **19** (2011), p. 1340-1347.

7. Crystal structure of novel compounds in the systems Zr-Cu-Al, Mo-Pd-Al and partial phase equilibria in the Mo-Pd-Al system

7.1. Introduction

According to our continuous interest in metal-based ternary aluminides [1-4], we report here our investigation on the systems: Mo-Pd-Al and Zr-Cu-Al.

We recently discussed the crystal structure and micro-hardness of a series of compounds in the Al-rich part of the systems Mo-Cu-Al, Mo-Ni-Al, W-Ni-Al and Re-Ni-Al [4]. One may expect similar metallurgical and structural chemical behavior from homologous palladium-based compounds. So far neither phase relations nor crystal structures have been reported for the Mo-Pd-Al system.

Y. Markiv et al. [5] reported two isothermal sections of the Zr-Cu-Al system at 500 °C and 800 °C. DTA experiments [6] revealed the presence of an additional phase, which was reported to form in a peritectic reaction at 740±10 °C. The powder pattern of this phase was tentatively indexed on a body centred tetragonal unit cell with lattice parameters a = 0.579 and c = 0.396 nm for $Zr_{17.1}Cu_{15.7}Al_{67.2}$ [8]. The phase was labelled as $\tau_9–(Zr_{17.1}Cu_{15.7}Al_{67.2})$ in the most recent critical assessment of the Zr-Cu-Al system (see ref. [7] and references therein), however, no crystal structure has yet been assigned to this phase. Similarly, the τ_7-phase was claimed to adopt the $ThMn_{12}$ structure type, but no refinement was given and thus no data on site preference of elements were provided. It should be noted, that the sequence of lattice parameters presented in this assessment for τ_7 should be modified [7] as the parameters *a* and *c* have been interchanged.

As hitherto no phase equilibria of the Mo-Pd-Al system was reported and as crystal structure data in the Zr-Cu-Al system are neither available for the τ_9-phase nor for the τ_7-phase, the current investigation was designed to provide this information.

7.2. Experimental Details

Alloys were prepared (each of 1-2 grams) from high purity metal ingots of Zr, Mo, Pd, Cu, and Al (min. purity 99.9 mass %, Alfa Johnson Matthey GmbH, D) by arc melting under argon and were melted several times for homogenization (weight loss less than 0.1 %). Then the reguli

were wrapped in Mo-foil to protect from attack by the hot quartz walls, sealed in evacuated quartz tubes and annealed for 5h to 30 days at various temperatures in the range of 700 °C to 910 °C. All samples were quenched in cold water after annealing.

Single crystals of the τ_1-phase in the Mo-Pd-Al system were mechanically isolated from a specimen with nominal composition $Mo_8Pd_{18.5}Al_{73.5}$, which was annealed at 860 °C for 10 days. Similarly a single crystal of the τ_7-phase in the Zr-Cu-Al system was taken from a specimen with nominal composition $Zr_{6.6}Cu_{20}Al_{73.4}$, which was annealed at 910 °C for 3 days. Following this procedure, a single crystal of the τ_9-phase in Zr-Cu-Al system was obtained from a specimen with nominal composition $Zr_{6.6}Cu_{20}Al_{73.4}$, which was annealed at 700 °C for 20 days.

Details of the various techniques of characterization such as light optical microscopy (LOM), electron probe microanalysis (EPMA, pure elements were used as standards), of crystal structure (X-ray powder diffraction (XPD) and single crystal determination (XSCD)) and of Vicker's hardness measurements have been described in detail in our previous paper on the systems Mo-Cu-Al, Mo-Ni-Al, Re-Ni-Al and W-Ni-Al [4].

7.3. Results and discussion

7.3.1. The crystal structure of τ_1-MoPd$_{2-x}$Al$_{8+x}$, x = 0.067

We report for the first time the presence of a ternary phase in the Al-rich corner of the Mo-Pd-Al system and we label it as $\boldsymbol{\tau_1}$. The crystal structure of $\boldsymbol{\tau_1}$-MoPd$_{2-x}$Al$_{8+x}$ has been solved from X-ray single crystal CCD intensity data (lattice parameters: a = 0.78153(2), b = 1.02643(3) and c = 0.86098(2) nm). Systematic extinctions prompted a primitive unit cell with two possible space group symmetries, *Pbcm* and *Pbc*2_1. As structure solution using direct methods in both these space groups revealed practically identical solutions and as an analysis of missing symmetry by program PLATON confirmed *Pbcm*, we describe the structure in the space group with the highest symmetry *Pbcm* (No. 57). In total, 9 crystallographic sites were obtained, out of which, only site 4*d* was fully occupied by Mo, one 4*c* site was completely occupied by Pd, one 4*d* position was randomly shared by Pd and Al atoms and the rest of the positions were fully occupied by Al. With this atom arrangement, the refined composition ($Mo_{9.1}Pd_{17.6}Al_{73.3}$) was close to the EPMA value ($Mo_{9.3}Pd_{17.7}Al_{73.0}$) and results in the formula MoPd$_{2-x}$Al$_{8+x}$, x = 0.067.

With anisotropic displacement parameters, the structure refinement finally converged to R_{F2} = 0.0287 with negligible residual electron density (2.41; -1.65 $e^-/10^{-3}nm^3$). The full set of crystallographic data is presented in Table1.

Table 1a: XSC data for τ_1-MoPd$_{2-x}$Al$_{8+x}$, x = 0.067, τ_7-Zr(Cu$_{1-x}$Al$_x$)$_{12}$, x = 0.514 and τ_9-ZrCu$_{1-x}$Al$_4$, x = 0.144, standardized with program *Structure Tidy* [9]. Anisotropic displacement parameters in (10^2nm^2).

Parameter/compound	τ_1-MoPd$_{2-x}$Al$_{8+x}$, x = 0.067	τ_7-Zr(Cu$_{1-x}$Al$_x$)$_{12}$, x = 0.514	τ_9-ZrCu$_{1-x}$Al$_4$, x = 0.144
Space Group	*Pbcm*, #57	*I4/mmm*, #139	*P4/nmm*, #129
Composition from EPMA	Mo$_{9.3}$Pd$_{17.7}$Al$_{73.0}$	Zr$_{8.5}$Cu$_{45.0}$Al$_{46.5}$	Zr$_{17.5}$Cu$_{16.1}$Al$_{66.4}$
Composition from refinement	Mo$_{9.1}$Pd$_{17.6}$Al$_{73.3}$	Zr$_{7.7}$Cu$_{44.9}$Al$_{47.4}$	Zr$_{17.1}$Cu$_{14.6}$Al$_{68.3}$
Formula from refinement	MoPd$_{2-x}$Al$_{8+x}$, x = 0.067	Zr(Cu$_{1-x}$Al$_x$)$_{12}$, x = 0.514	ZrCu$_{1-x}$Al$_4$, x = 0.144
a (nm)	0.78153(2)	0.85243(2)	0.40275(3)
b (nm)	1.02643(3)	0.85243(2)	0.40275(3)
c (nm)	0.86098(2)	0.50862(3)	1.17688(4)
Reflections in refinement	1295$\geq$4σ(F$_o$) of 1667	247$\geq$4σ(F$_o$) of 277	271$\geq$4σ(F$_o$) of 301
Number of variables	62	19	18
$R_F^2 = \Sigma|F_0^2-F_c^2|/\Sigma F_0^2$	0.0287	0.0187	0.0124
R_{Int}	0.0340	0.0210	0.0173
wR2	0.437	0.0346	0.0215
GOF	1.043	1.155	1.121
Extinction	0.0012(1)	0.0106(5)	0.033(1)
Residual density e^-/Å^3; max; min.	2.41; -1.65	1.91; -0.99	0.78; -0.54
Atom parameters			
Atom site 1	4*d* (x, y, ¼)	2*l* (0, 0, 0)	2*c* (¼, ¼, z)
Occ.;	1.00 **Mo1**	1.00 **Zr1**	1.00 **Zr1**
x, y, z;	0.50327(4), 0.11158(3)	-	0.30822(2)
U$_{11}$; U$_{22}$; U$_{33}$	U$_{11}$= 0.0052(1), U$_{22}$ = 0.0060(1), U$_{33}$ = 0.0047(1)	U$_{11}$= U$_{22}$ = 0.0059(2), U$_{33}$ = 0.0070(3)	U$_{11}$ = U$_{22}$ = 0.00461(8), U$_{33}$ = 0.0048(1)
U$_{23}$; U$_{13}$; U$_{12}$;	U$_{23}$ = U$_{13}$ = 0, U$_{12}$ = 0.0009(1)	U$_{23}$ = U$_{13}$ = U$_{12}$ = 0	U$_{23}$ = U$_{13}$ = U$_{12}$ = 0
Atom site 2	4*d* (x, y, ¼)	8*f* (¼, ¼, ¼)	2*c* (¼, ¼, z)
Occ.;	**M1** = 0.933(2) **Pd** + 0.067 **Al**	1.00 **Cu1**	0.856(2) **Cu1**
x, y, z;	0.73677(4), 0.36597(3)	-	0.01008(3)
U$_{11}$; U$_{22}$; U$_{33}$;	U$_{11}$= 0.0075(1), U$_{22}$ = 0.0078(1), U$_{33}$ = 0.0060(1)	U$_{11}$ = U$_{22}$ = 0.0088(1), U$_{33}$ = 0.0067(2);	U$_{11}$ = U$_{22}$ = 0.0083(1), U$_{33}$ = 0.0075(2)
U$_{23}$; U$_{13}$; U$_{12}$;	U$_{23}$ = U$_{13}$ = 0, U$_{12}$ = 0.0002(1)	U$_{23}$ = U$_{13}$ = 0.0014(1), U$_{12}$ = 0.0001(1)	U$_{23}$ = U$_{13}$ = U$_{12}$ = 0

Atom site 3	4c (x, ¼, 0)	8i (x, 0, 0)	4f (¾, ¼, z)	
Occ.;	1.00 **Pd2**	1.00 **Al1**	1.00 **Al1**	
x, y, z;	0.26283(4)	0.3434(1)	0.13319(5)	
U_{11}; U_{22}; U_{33};	U_{11}= 0.0068(1), U_{22} = 0.0060(1), U_{33} = 0.0069(1)	U_{11}= 0.0066(4), U_{22} = 0.0078(4), U_{33} = 0.0140(5)	0.0070(2), 0.0080(2); 0.0087(2)	
U_{23}; U_{13}; U_{12};	U_{23} = -0.0003(1), U_{13} = U_{12} = 0,	U_{23} = U_{13} = U_{12} = 0	U_{23} = U_{13} = U_{12} = 0	
Atom site 4	4d (x, y, ¼)	8j (x, ½, 0)	2c (¼, ¼, z)	
Occ.;	1.00 **Al1**	**M1** = 0.450(3) **Cu** + 0.550 **Al**	1.00 **Al2**	
x, y, z;	0.1690(2), 0.6262(1)	x_{Cu} = 0.2668(1), x_{Al} = 0.3107(3)	0.68047(7)	
U_{11}; U_{22}; U_{33};	U_{11} = 0.0071(5), U_{22} = 0.0165(7), U_{33} = 0.0164(7)	U_{11} = 0.0065(7), U_{22} =0.0062(3), U_{33} = 0.0086(3)	U_{11} = U_{22} = 0.0052(2), U_{33} = 0.0146(4)	
U_{23}; U_{13}; U_{12};	U_{23} = U_{13} = 0, U_{12} = 0.0003(5)	U_{23} = U_{13} = U_{12} = 0	U_{23} = U_{13} = U_{12} = 0	
Atom site 5	4d (x, y, ¼)	-	2b (¾, ¼, ½)	
Occ.;	1.00 **Al2**	-	1.00 **Al3**	
x, y;	0.3964(2), 0.3598(1)	-	-	
U_{11}; U_{22}; U_{33};	U_{11}= 0.0154(6), U_{22} = 0.0060(5), U_{33} = 0.0066(5)	-	U_{11} = U_{22} = 0.0069(2), U_{33} = 0.0071(3)	
U_{23}; U_{13}; U_{12};	U_{23} = U_{13} = 0, U_{12} = -0.0008(4)	-	U_{23} = U_{13} = U_{12} = 0	
Atom site 6	4c (x, ¼, 0)	-	-	
Occ.;	1.00 **Al3**	-	-	
x;	0.6021(2)	-	-	
U_{11}; U_{22}; U_{33};	U_{11} = 0.0093(5), U_{22} = 0.0073(5), U_{33} = 0.0085(5)	-	-	
U_{23}; U_{13}; U_{12};	U_{23} = 0.0008(4), U_{13} = U_{12} = 0,	-	-	
Atom site 7	8e (x, y, z)	-	-	
Occ.;	1.00 **Al4**	-	-	
x, y, z;	0.3272(1), 0.00329(9), 0.0045(1)	-	-	
U_{11}; U_{22}; U_{33};	U_{11}= 0.0121(4), U_{22} = 0.0063(3), U_{33} = 0.0071(3)	-	-	
U_{23}; U_{13}; U_{12};	U_{23} = -0.0001(3), U_{13} = 0.0019(3), U_{12} = 0.0003(3),	-	-	
Atom site 8	4d (x, y, ¼)	-	-	
Occ.;	1.00 **Al5**	-	-	
x, y;	0.1628(1), 0.1301(1)	-	-	
U_{11}; U_{22}; U_{33};	U_{11}= 0.0059(5), U_{22} = 0.0172(7), U_{33} = 0.0079(6)	-	-	
U_{23}; U_{13}; U_{12};	U_{23} = U_{13} = 0, U_{12} = -0.0010(4),	-	-	

Atom site 9	8e (x, y, z)	-	-
Occ.;	1.00 **Al6**	-	-
x, y, z;	0.0007(1), 0.38245(8), 0.0793(1)	-	-
U_{11}; U_{22}; U_{33};	U_{11}= 0.0087(4), U_{22} = 0.0119(4), U_{33} = 0.0124(4)	-	-
U_{23}; U_{13}; U_{12};	U_{23} = 0.0020(3), U_{13} = 0.0030(3), U_{12} = 0.0023(3),	-	-

[1]B_{iso} is given in (10^2 nm^2).

Table 1b: Interatomic distances (nm), standard deviation ≤0.0002.

τ₁-MoPd₂₋ₓAl₈₊ₓ, x = 0.067											

τ_1-MoPd$_{2-x}$Al$_{8+x}$, x = 0.067

Mo1–	1Al1	0.2566		–1Al3	0.2652	CN = 15	–2Al4	0.2658		–1Mo1	0.2667
CN = 14	–1Al5	0.2667		–2Mo1	0.3191		–2M1	0.2675		–2Al4	0.2796
	–1Al2	0.2681	Al1–	1Mo1	0.2566		–2Mo1	0.2692		–1M1	0.2823
	–2Al3	0.2692	CN = 14	–1M1	0.2569		–2Al2	0.2913		–1Al2	0.2981
	–1Al2	0.2701		1Al5	0.2594		–2Al1	0.3074		–2Al6	0.3108
	–2Al4	0.2756		–2Al4	0.2845		–2Al4	0.3321		–2Al6	0.3203
	–2Al4	0.2819		–2Al3	0.3074		–2Al6	0.3467		–2Al6	0.3236
	–1M1	0.3142		–2Al6	0.3131	Al4–	1Pd2	0.2582	Al6–	1M1	0.2539
	–1M1	0.3186		–2Al6	0.3186	CN = 13	–1M1	0.2589	CN = 15	–1Pd2	0.2551
	–2Pd2	0.3191		–1Al2	0.3261		–1Al3	0.2658		–1Al6	0.2773
M1–	2Al6	0.2539		–2Al6	0.3292		–1Al2	0.2658		–1Al4	0.2900
CN = 11	–1Al1	0.2569	Al2–	2Pd2	0.2644		–1Al4	0.2702		–1Al4	0.2919
	–2Al4	0.2589	CN = 15	–2Al4	0.2658		–1Mo1	0.2756		–1Al6	0.2940
	–1Al2	0.2661		–1M1	0.2661		–1Al5	0.2796		–1Al6	0.3042
	–2Al3	0.2675		–1Mo1	0.2681		–1Mo1	0.2819		–1Al5	0.3108
	–1Al5	0.2823		–1Mo1	0.2701		–1Al1	0.2845		–1Al1	0.3131
	–1Mo1	0.3142		–2Al3	0.2913		–1Al6	0.2900		–1Al1	0.3186
	–1Mo1	0.3186		–1Al5	0.2981		–1Al6	0.2919		–1Al5	0.3203
Pd2–	2Al6	0.2551		–1Al1	0.3261		–1Al3	0.3321		–1Al5	0.3236
CN = 11	–2Al4	0.2582		–2Al4	0.3362		–1Al2	0.3362		–1Al1	0.3292
	–2Al5	0.2599		–2Al6	0.3432	Al5–	1Al1	0.2594		–1Al2	0.3432
	–2Al2	0.2644	Al3–	1Pd2	0.2652	CN = 14	–2Pd2	0.2599		–1Al3	0.3466

τ_7-Zr(Cu$_{1-x}$Al$_x$)$_{12}$, x = 0.514

Zr1–	4Al1	0.2927		–2Al1	0.2781		–4Al1	0.2606		–2M1	0.2801
CN = 20	–8M1	0.3116		–2Al1	0.2801		–2Zr1	0.3271		–1Zr1	0.2927
	–8Cu1	0.3271		–2Zr1	0.3116	Al1–	4Cu1	0.2606		–4Al1	0.3167
M1–	4Cu1	0.2503	Cu1–	4M1	0.2503	CN = 14	–1Al1	0.2670			
CN = 12	–2M1	0.2546	CN = 12	–2Cu1	0.2543		–2M1	0.2781			

τ_9-ZrCu$_{1-x}$Al$_4$, x = 0.144

Zr1–	4Al2	0.2851		–4Cu1	0.2858		–2Al2	0.2977	Al3–	4Al3	0.2848
CN = 12	–4Al1	0.2881	Al1–	2Cu1	0.2481		–1Al1	0.3135	CN = 12	–4Al2	0.2927
	–4Al3	0.3025	CN = 13	–2Cu1	0.2626	Al2–	4Zr1	0.2851		–4Zr1	0.3025
Cu1–	4Al1	0.2481		–4Al1	0.2848	CN = 12	–4Al3	0.2927			
CN = 12	–4Al1	0.2626		–2Zr1	0.2881		–4Al1	0.2977			
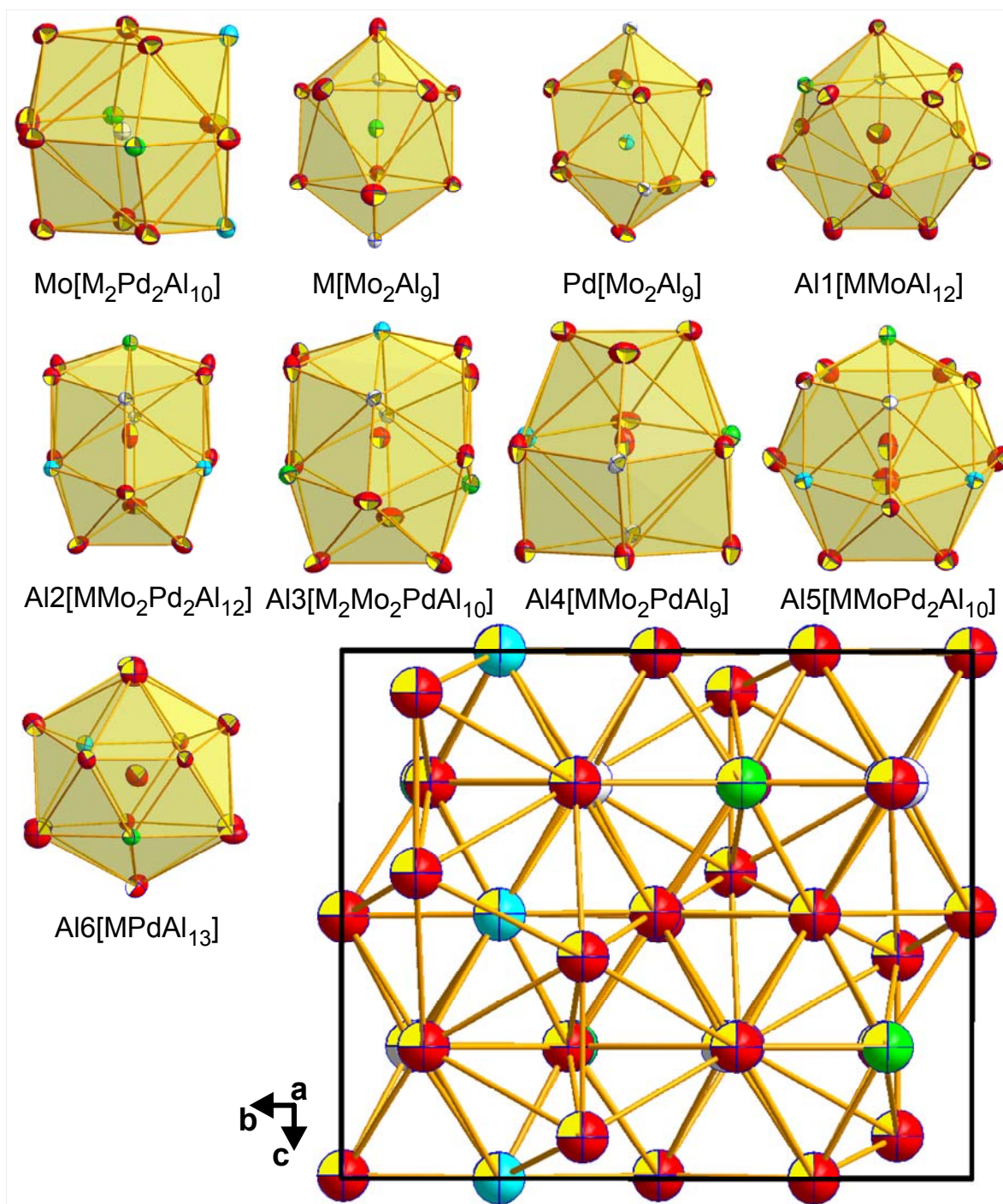
Fig. 1. Polyhedra of τ_1-MoPd$_{2-x}$Al$_{8+x}$, x = 0.067. A projection of the unit cell along [100] is shown in the right lower corner revealing hexagonal channels centered by puckered strings of metal atoms.

X-ray powder diffraction intensities collected from a polycrystalline sample are in good agreement with the intensities calculated from the structural model taken from the single crystal. Figure 1 shows the Voronoi coordination polyhedra for τ_1-MoPd$_{2-x}$Al$_{8+x}$ constructed with the

help of the program DIDO95 [10]. A projection of the unit cell along the a-axis shows hexagonal channels running through the entire structure, which are surrounded by tetrahedra (Fig. 1) and are centered along the channel axis by a string of metal atoms.

A search for the structure type (Pearson symbol: oP44) in Pearson's Crystal Data [11] delivered no results suggesting τ_1-$MoPd_{2-x}Al_{8+x}$, x = 0.067 to be a unique structure type. Comparing the structure motives and unit cell geometries of τ_1 with $Mo(Cu_xAl_{1-x})_6Al_4$, we observed a close structural relationship between these structures: a = c_0, b = $2a_0$, c = $a_0/\sqrt{3}$. Consequently we concluded that the τ_1-phase exhibits a superstructure of the $Mo(Cu_xAl_{1-x})_6Al_4$ type [4]. A Bärnighausen tree for the crystallographic group-subgroup relations between the structure types of $Mo(Cu_xAl_{1-x})_6Al_4$ and τ_1 via a series of hypothetical intermediate structures is shown in Fig. 2.
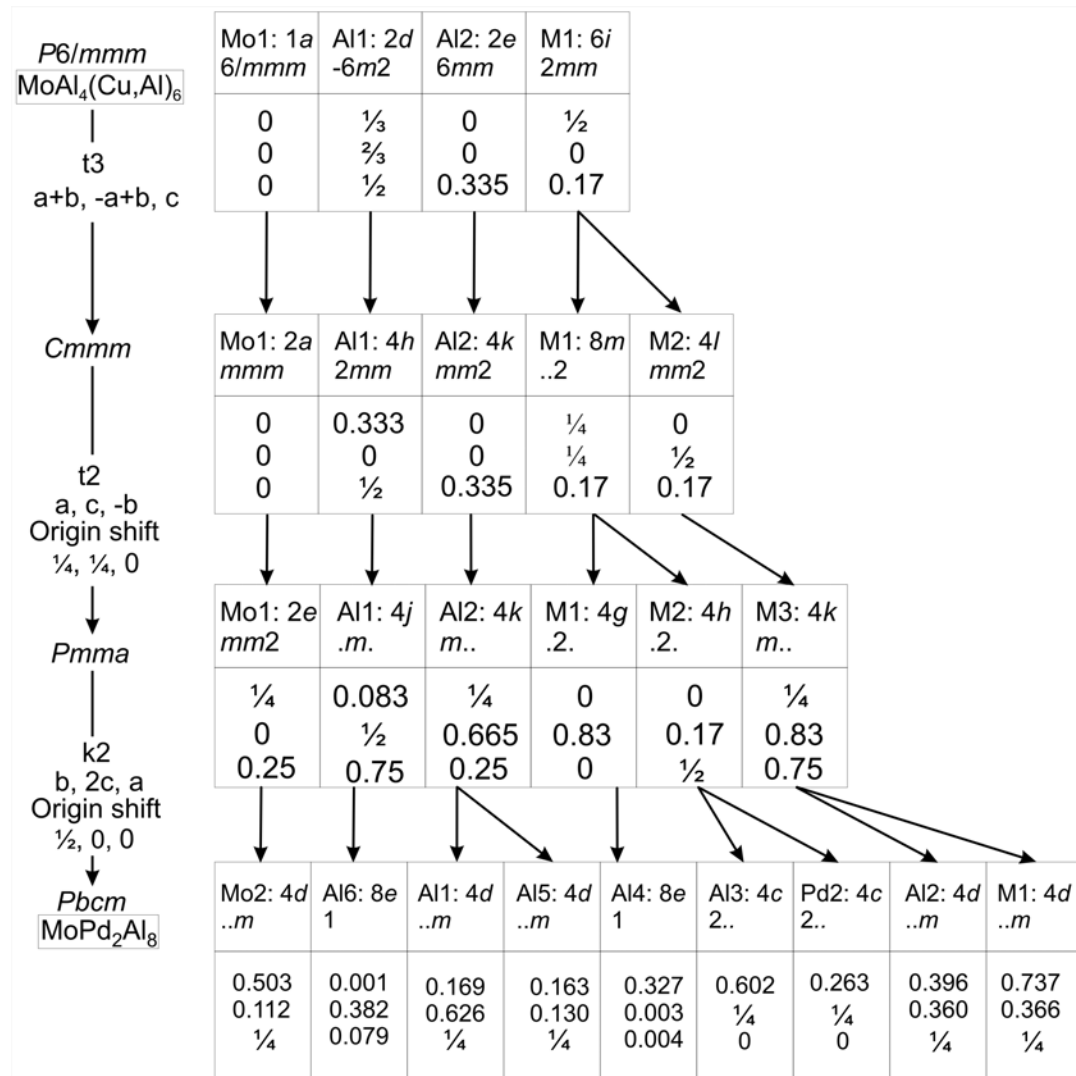
P6/mmm — MoAl₄(Cu,Al)₆

Mo1: 1a 6/mmm	Al1: 2d -6m2	Al2: 2e 6mm	M1: 6i 2mm
0	⅓	0	½
0	⅔	0	0
0	½	0.335	0.17

t3
a+b, -a+b, c

Cmmm

Mo1: 2a mmm	Al1: 4h 2mm	Al2: 4k mm2	M1: 8m ..2	M2: 4l mm2
0	0.333	0	¼	0
0	0	0	¼	½
0	½	0.335	0.17	0.17

t2
a, c, -b
Origin shift ¼, ¼, 0

Pmma

Mo1: 2e mm2	Al1: 4j .m.	Al2: 4k m..	M1: 4g .2.	M2: 4h .2.	M3: 4k m..
¼	0.083	¼	0	0	¼
0	½	0.665	0.83	0.17	0.83
0.25	0.75	0.25	0	½	0.75

k2
b, 2c, a
Origin shift ½, 0, 0

Pbcm — MoPd₂Al₈

Mo2: 4d ..m	Al6: 8e 1	Al1: 4d ..m	Al5: 4d ..m	Al4: 8e 1	Al3: 4c 2..	Pd2: 4c 2..	Al2: 4d ..m	M1: 4d ..m
0.503	0.001	0.169	0.163	0.327	0.602	0.263	0.396	0.737
0.112	0.382	0.626	0.130	0.003	¼	¼	0.360	0.366
¼	0.079	¼	¼	0.004	0	0	¼	¼

Fig. 2. Bärnighausen tree relating the structure types of $Mo(Cu_xAl_{1-x})_6Al_4$ and τ_1-$MoPd_{2-x}Al_{8+x}$, x = 0.067.

It seems that the 6*i* site (randomly shared by Cu and Al atoms) in $Mo(Cu_xAl_{1-x})_6Al_4$ arranges itself into a higher order in the τ_1-phase and decomposes into four fully ordered sites (Al2, Al3, Al4 and Pd2) and one shared position (4*d*). This moves the other atoms slightly away from their ideal locations and results in the orthorhombic distortions of τ_1. Pd atoms move closer to Al atoms and Al atoms move closer to Mo atoms similar to the parent structure where Cu moved closer to Al and away from Mo and Al atoms moved closer to Mo atoms. The Mo-Pd maximum bond length (0.3191 nm) is slightly longer than the Re-Ni bond (0.3120 nm) reported earlier [4] and merely reflects the size of the metal atom radii, whereas maximum Al-Al bond distances (0.3463 nm) reported in $ReNi_2Al_{8-x}$ (x = 0.165) [4] closely correspond to those in τ_1-$MoPd_{2-x}Al_{8+x}$ (0.3467 nm). It should be mentioned, that the structure of $ReNi_2Al_{8-x}$ is also a superstructure of the $Mo(Cu_xAl_{1-x})_6Al_4$ type (a = $2a_0$, b = $2c_0$, c = $a_0\sqrt{3}$) i.e. the coordination polyhedron for Mo in τ_1 is similar to the polyhedra for the Re-atoms in $ReNi_2Al_{8-x}$. Similarly, the polyhedron for Pd in τ_1 corresponds to the polyhedra for the Ni atoms in $ReNi_2Al_{8-x}$ but only some of the Al polyhedra are similar in both structures.

7.3.2. The crystal structure of τ_7-$Zr(Cu_{1-x}Al_x)_{12}$, x = 0.514.

Although, Markiv et al. [7] claimed the $ThMn_{12}$ type for the solution τ_7-$Zr(Cu,Al)_{12}$, no structure refinement was published for this phase. In order to find the detailed atom site preferences, we collected X-ray single crystal CCD intensity data. The lattice parameters for the single crystal were a = 0.85243(2) and c = 0.50862(3) nm. Systematic extinctions revealed a body centered unit cell with 8 possible space group symmetries, $I4/mmm$, $I\bar{4}2m$, $I\bar{4}m2$, $I4mm$, $I422$, $I4/m$, $I\bar{4}$ and $I4$. As structure solution using direct methods in all these space groups revealed practically identical results and as an analysis of missing symmetry by program PLATON confirmed $I4/mmm$, we describe the structure in the space group type with the highest symmetry $I4/mmm$ (139). Structure solution yielded a total of 4 crystallographic sites, out of which, site 2*l* was fully occupied by Zr, the 8*f* site was fully occupied by Cu, the 8*i* site was entirely occupied by Al, but the 8*j* site turned out to comprise a random mixture of Cu and Al atoms (Table 1). This atom arrangement confirms the $ThMn_{12}$ structure type [12] and is in accordance with the homogeneity region for the solution $Zr(Cu_{1-x}Al_x)_{12}$ reported in the literature [7] where a line compound is shown presenting an exchange of Cu and Al at a constant Zr-content. With this atom

arrangement, the refined composition ($Zr_{7.7}Cu_{44.9}Al_{47.4}$) was close to the EPMA value ($Zr_{8.5}Cu_{45.0}Al_{46.5}$) resulting in a formula of $Zr(Cu_{1-x}Al_x)_{12}$, x = 0.514. With anisotropic displacement parameters, the structure refinement finally converged to R_{F2} = 0.0187 with negligible residual electron density (1.91; -0.99 $e^-/10^{-3}nm^3$). All relevant crystallographic data are summarized in Table 1. X-ray powder diffraction intensities collected from a polycrystalline sample are in good agreement with the intensities calculated from the structural model obtained from the single crystal (Fig. 3).
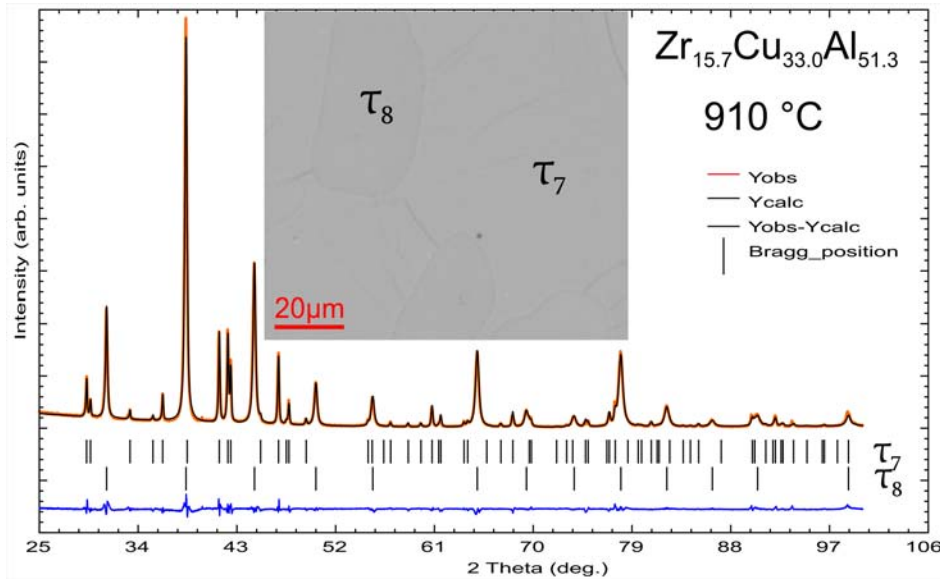

Fig. 3. Refinement of the X-ray powder spectrum for the alloy $Zr_{15.7}Cu_{33.0}Al_{51.3}$ (composition from EPMA, at. %) reveals a two-phase equilibrium between τ_7 and τ_8. The micrograph confirms the presence of these two phases τ_7-($Zr_{8.5}Cu_{45.0}Al_{46.5}$, at. %) and τ_8-($Zr_{27.5}Cu_{12.9}Al_{59.6}$, at. %).

Zr1[M1$_8$Cu1$_8$MAl1$_4$]   Cu1[Zr1$_2$Cu1$_2$Al1$_4$M$_4$]   Al1[Zr1Cu1$_4$Al1$_5$M1$_4$]   M1[Zr1$_2$Cu1$_4$Al1$_4$M1$_2$]
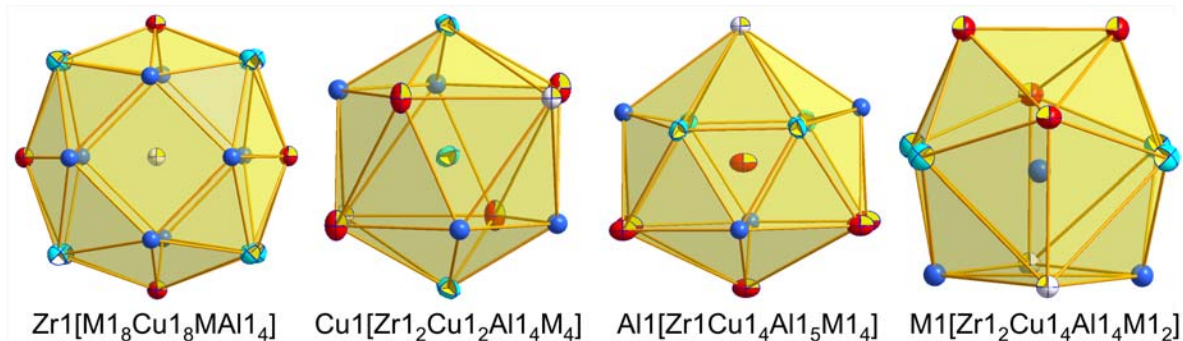
Fig. 4. Polyhedra of τ_7-$Zr(Cu_{1-x}Al_x)_{12}$, x = 0.514. Isotropic atoms represent the central position of the split site 8*j*.

Voronoi-type coordination polyhedra for τ_7 were constructed by use of the program DIDO95 [10] and these are shown in Fig. 4. Although, Zr-Cu bonds apparently are long (0.3271 nm), they

reflect the large size of the Zr atom. Maximum Al-Al distances (0.3167) are shorter than the maximum Al-Al bond distances (0.3463 nm) reported in $ReNi_2Al_{8-x}$ [4] and in τ_1-$MoPd_{2-x}Al_{8+x}$ (0.3467 nm) and suggest strong bonding.

7.3.3. The crystal structure of τ_9-$ZrCu_{1-x}Al_4$, x = 0.144

As the crystal structure of τ_9–($Zr_{17.1}Cu_{15.7}Al_{67.2}$) is yet unsolved [7], X-ray structure analysis was employed. The X-ray data for the single crystal selected were fully indexed on a tetragonal crystal system with the lattice parameters a = 0.40275(3) and c = 1.17688(4) nm. Systematic extinctions revealed a primitive unit cell with two possible space group symmetries, *P4/nmm* and *P4/n*. As structure solutions using direct methods in both these space groups revealed practically identical results and as an analysis of missing symmetry by program PLATON confirmed *P4/nmm*, we describe the structure in the space group with the highest symmetry *P4/nmm* (129). Refinement showed that τ_9 is a fully ordered structure except for a vacancy (14.4 %) on the 2c site, which is shared with Cu atoms (Table 1). With this atom arrangement, the composition from refinement ($Zr_{17.1}Cu_{14.6}Al_{68.3}$) was close to the EPMA value ($Zr_{17.5}Cu_{16.1}Al_{66.4}$) resulting in the formula $ZrCu_{1-x}Al_4$, x = 0.144. With anisotropic displacement parameters, the structure refinement finally converged to R_{F2} = 0.0124 with a negligible residual electron density (0.78; -0.54 $e^-/10^{-3}nm^3$). Results are summarized in Table 1. X-ray powder diffraction intensities collected from a polycrystalline sample are in good agreement with the intensities calculated from the structural model taken from the single crystal (Fig. 5).

From the composition and the phase equilibria documented in Figs 3 and 5, we can safely assume that the structure of $ZrCu_{1-x}Al_4$ in fact is consistent with the phase labelled τ_9 in the most recent critical assessment of the Zr-Cu-Al system [7]. Consequently τ_9-$ZrCu_{1-x}Al_4$ is likely to replace the compound found by Soares et al. [8], who tentatively indexed the X-ray spectrum of this phase with a body centred tetragonal unit cell (a = 0.579 and c = 0.396 nm for $Zr_{17.1}Cu_{15.7}Al_{67.2}$). Although our X-ray pattern for the τ_9-phase looks different at a first glance, four out of the 6 peaks reported by Soares et al. [8] were indexed on the unit cell of τ_9-$ZrCu_{1-x}Al_4$ revealing lattice parameters [~a = 0.406, c = 1.1747 nm] very close to those obtained from our single crystal (Table 1).
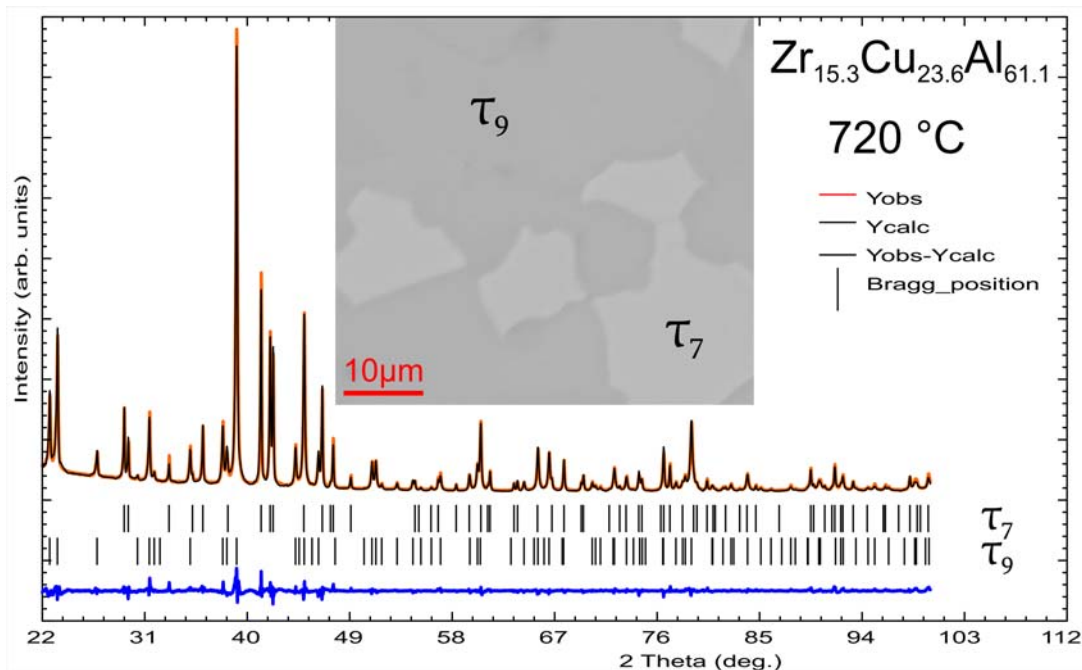
Fig. 5. Refinement of the X-ray powder spectrum for the alloy $Zr_{15.7}Cu_{33.0}Al_{51.3}$ (composition from EPMA, at. %) reveals a two-phase equilibrium between τ_8 and τ_7. The micrograph confirms the presence of these two phases τ_8-$Zr_{27.5}Cu_{12.9}Al_{59.6}$ (at. %) and τ_7-($Zr_{8.5}Cu_{45.0}Al_{46.5}$, at. %).

By using the program DIDO95 [10], we were able to accurately calculate the number of ligands for all the atoms present in the unit cell and Fig. 6 shows the Voronoi coordination polyhedra for τ_9-$ZrCu_{1-x}Al_4$. A search for the structure type (Pearson symbol: oP12) in Pearson's Crystal Data [11] prompted no results with these lattice parameters, crystal symmetry and atomic arrangement suggesting τ_9 to be a unique structure type. However, from the lattice parameters, we guessed that the unit cell of the τ_9-phase has some structure resemblance with the structure of fcc-Cu, as in τ_9 c $\cong$ 3a and a is similar to the lattice parameters of Cu. Comparing the structure motives of τ_9 with Cu, we observed a close structural relationship and concluded that τ_9 is a superstructure of Cu. In fact the structure of τ_9 is made up of 3 blocks of Cu face-connected in one direction to form the c axis of τ_9 (Fig. 6).
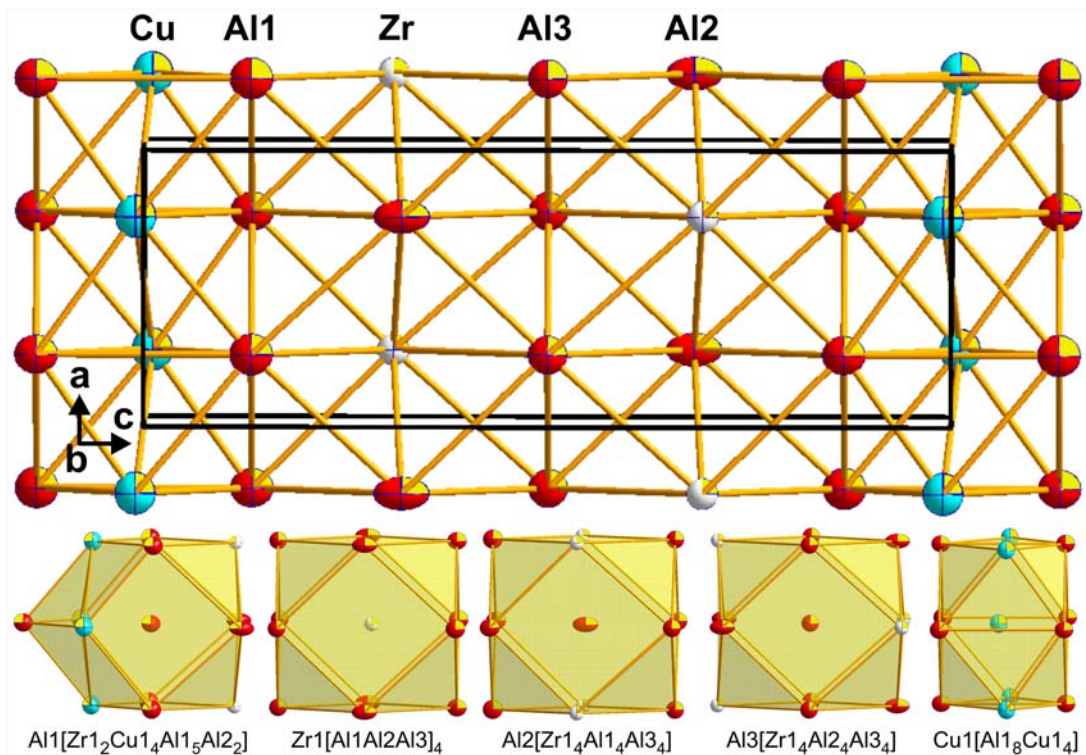
106

Fig. 6. Polyhedra of τ_9-$ZrCu_{1-x}Al_4$, x = 0.144.

A Bärnighausen tree for the crystallographic group-subgroup relation between the structure of Cu and τ_9 is given in Fig. 7. The superstructure appears due to the replacement of Cu by Al and Zr atoms in the unit cell, giving rise to the structure of τ_9. We have already reported that $TiAl_3$ appears by the combination of two blocks of Cu and τ_5-$TiNi_{2-x}Al_5$ appears by the combination of 4 blocks of the Cu unit cell [2]. In this series, τ_9 is the first representative with 3 blocks of Cu-type unit cells. We could not find any structure with a combination of 5 blocks, but we found the structures of $HfGa_2$ [13] and Cu_3Pd [14] appearing by the combination of 6 and 7 blocks of Cu unit cells in one direction, respectively.

It is also important to note that the vacancy found on the Cu site is similar to the vacancy found on the Ni-site in τ_5-$TiNi_{2-x}Al_5$ and the isotypic Zr and Hf representatives. Also the wavelike arrangement of Cu atoms in the lattice (Fig. 6) is similar to the wavelike arrangement of Ni atoms in the lattices of τ_5-$TiNi_{2-x}Al_5$ (x=0.48), $ZrNi_{2-x}Al_{5-y}$ (x=0.4, y=0.4) and $HfNi_{2-x}Al_{5-y}$ (x=0.5, y=0.2) [2].
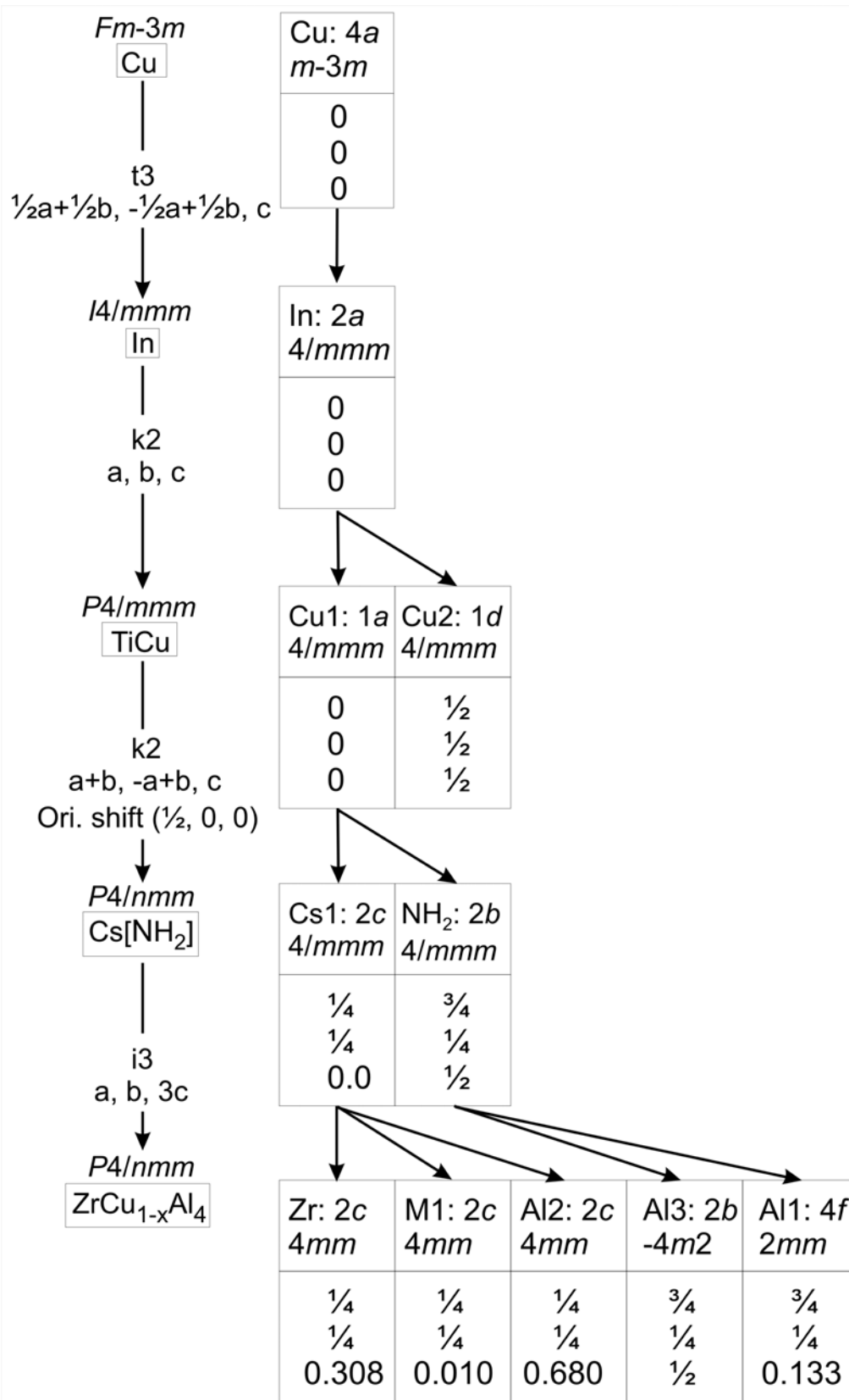
Fig. 7. Bärnighausen tree relating the structure types of Cu and ZrCu$_{1-x}$Al$_4$.

7.3.4. Partial isothermal section for the Al-rich corner of the Mo-Pd-Al system

In the attempt to elucidate the phase equilibria and the homogeneity region of the τ_1-phase we established four equilibrium triangles surrounding τ_1. A sample with composition $Mo_{9.2}Pd_{9.7}Al_{81.1}$ (all compositions mentioned in this section are obtained from EPMA and are presented in at. %) revealed in addition to τ_1 ($Mo_{9.5}Pd_{16.3}Al_{73.2}$) and $MoAl_4$ ($Mo_{19.5}Pd_{1.0}Al_{79.5}$) a eutectic structure with the overall composition $Mo_{0.5}Pd_{8.0}Al_{91.5}$ consisting of (Al) + Pd_8Al_{21} (Table 2), indicating that the τ_1–phase at 860 °C was in equilibrium with the liquid (Fig. 8a).

Table 2. EPMA (at. %) results of selected Mo-Pd-Al samples.

Overall composition (at.%)			H. T.*	Phases	Structure type	Space group	EPMA (at.%)		
Mo	Pd	Al					Mo	Pd	Al
9.2	9.7	81.1	860	τ_1	$MoPd_{2-x}Al_{8+x}$	$Pbcm$	9.5	16.3	73.2
				$MoAl_4$	WAl_4	$C1m1$	19.5	1.0	79.5
				Eutectic	-	-	0.5	8.0	91.5
7.7	26.6	65.7	860	τ_1	$MoPd_{2-x}Al_{8+x}$	$Pbcm$	9.5	19.0	71.5
				τ_2	Unknown	-	17.2	16.8	66.0
				Pd_2Al_3	Ni_2Al_3	$P\bar{3}m1$	0.2	40.8	59.0
5.4	18.6	76.0	860	τ_1	$MoPd_{2-x}Al_{8+x}$	$Pbcm$	9.1	19.2	71.7
				Pd_8Al_{21}	Pt_8Al_{21}	$I4_1/a$	0.2	28.9	70.9
				Liquid	-	-	0.2	9.2	90.6
6.1	22.9	71.0	860	τ_1	$MoPd_{2-x}Al_{8+x}$	$Pbcm$	9.1	19.0	71.9
				Pd_2Al_3	Ni_2Al_3	$P\bar{3}m1$	40.5	0.0	59.5
				Pd_8Al_{21}	Pt_8Al_{21}	$I4_1/a$	0.0	28.2	71.8
13.9	13.8	72.3	860	τ_1	$MoPd_{2-x}Al_{8+x}$	$Pbcm$	9.6	17.9	72.5
				τ_2	Unknown	-	17.3	16.9	65.8
				$MoAl_4$	WAl_4	$C1m1$	20.0	1.0	79.0
11.3	33.0	55.7	860	τ_2	Unknown	-	19.0	18.8	62.2
				PdAl	CsCl	$Pm\bar{3}m$	0.0	54.0	46.0
-	23.3	76.7	860	Pd_8Al_{21}	Pt_8Al_{21}	$I4_1/a$	-	28.3	71.7
				Liquid	-	-	-	8.5	91.5

*Heat Treatment at temperatures (°C).

A second ternary phase τ_2-($Mo_{17.2}Pd_{16.8}Al_{66.0}$) was found to exist in the sample with composition $Mo_{7.7}Pd_{26.6}Al_{65.7}$ and revealed the equilibrium with τ_1 ($Mo_{9.5}Pd_{19.0}Al_{71.5}$) and Pd_2Al_3 ($Mo_{0.2}Pd_{40.8}Al_{59.0}$) (Fig. 8b). The alloy $Mo_{5.4}Pd_{18.6}Al_{76.0}$ shows the presence of two phases τ_1 ($Mo_{9.1}Pd_{19.2}Al_{71.7}$) and Pd_8Al_{21} ($Mo_{0.2}Pd_{28.9}Al_{70.9}$) in equilibrium with the liquid (Fig. 8c).
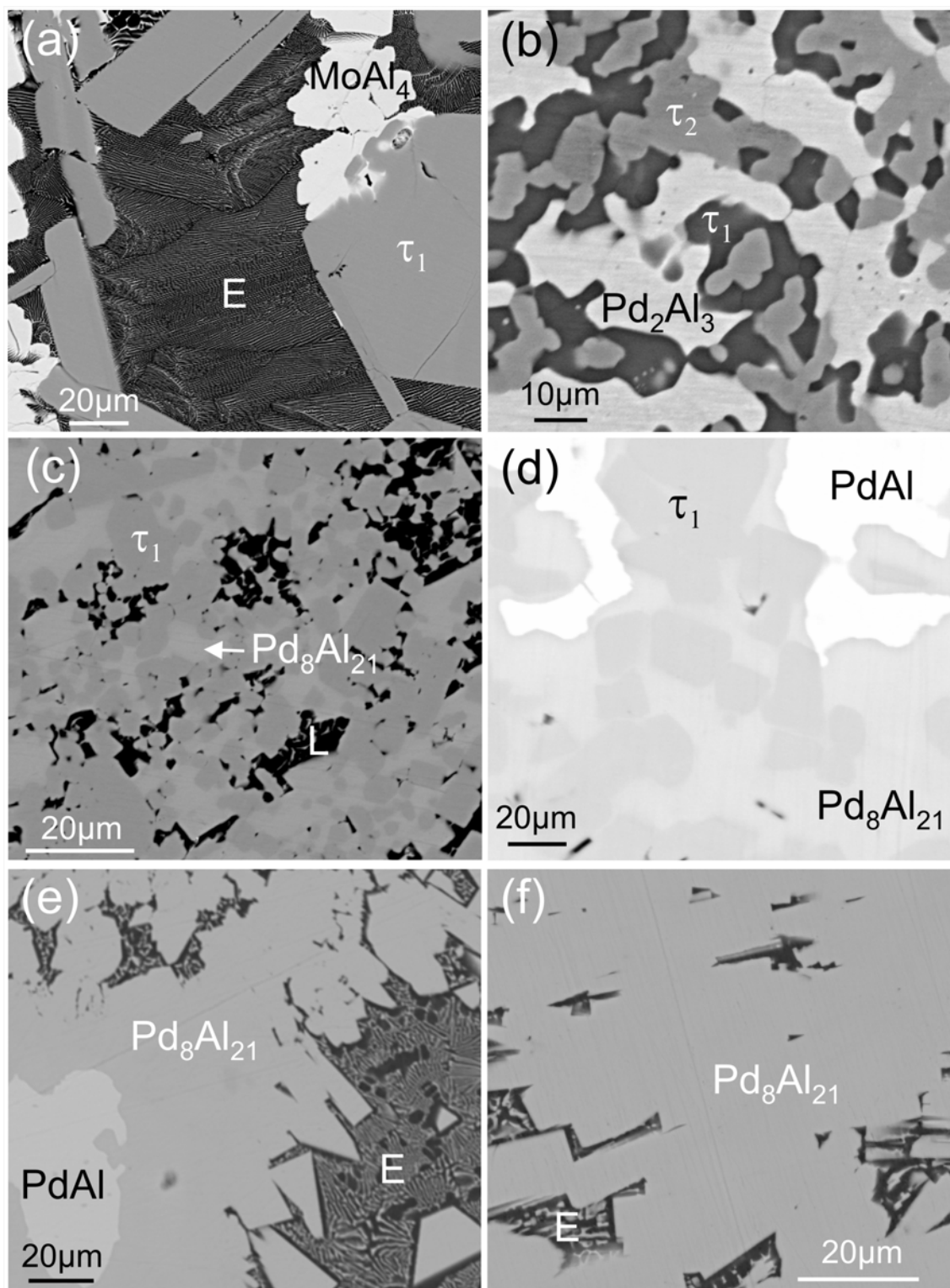
Fig. 8. Micrograph of various alloys of the Mo-Pd-Al system at 860 °C (all composition from EPMA); (a) $Mo_{9.2}Pd_{9.7}Al_{81.1}$, three-phase equilibrium τ_1 + E (Eutectic) + $MoAl_4$, (b) $Mo_{7.7}Pd_{26.6}Al_{65.7}$, three-phase equilibrium τ_1 + τ_2 + Pd_2Al_3, (c) $Mo_{5.4}Pd_{18.6}Al_{76.0}$, three-phase equilibrium τ_1 + Pd_8Al_{21} + L (Liquid), (d) $Mo_{6.1}Pd_{22.9}Al_{71.0}$, three-phase equilibrium τ_1 + Pd_2Al_3 + Pd_8Al_{21}, (e) $Pd_{23.3}Al_{76.7}$ (annealed for 1 hour), non-

equilibrium state Pd_2Al_3 + E (Eutectic) + Pd_8Al_{21}, (f) $Pd_{23.3}Al_{76.7}$ (annealed for 20 hours), two phase equilibrium Pd_8Al_{21} + E (Eutectic).
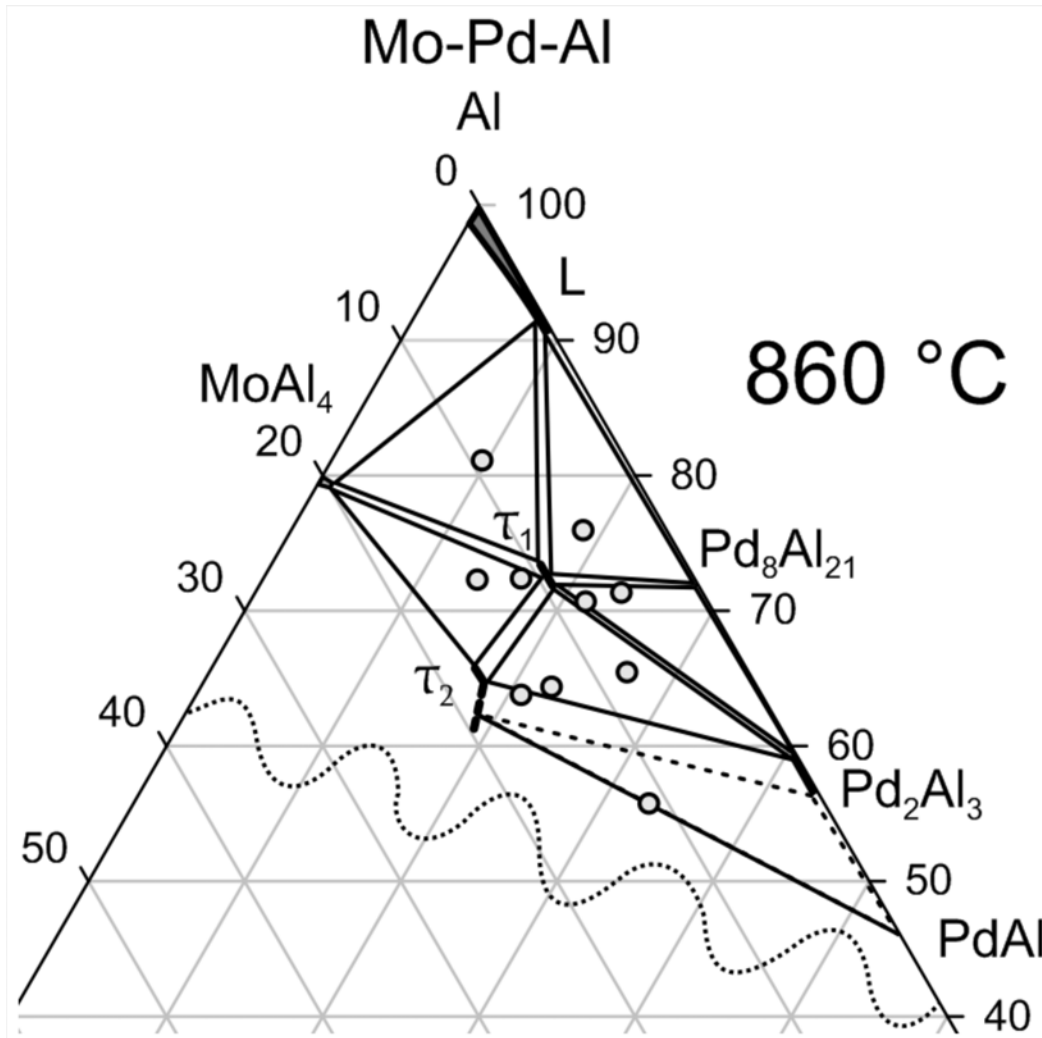
Fig. 9. Partial isothermal section of the Mo-Pd-Al system at 860 °C.

Although, the phase relations according to Massalski [15] show instability of the Pd_8Al_{21}-phase above at 790°C, we clearly observed the presence of this phase at 860°C along with τ_1 ($Mo_{9.1}Pd_{19.0}Al_{71.9}$) and Pd_2Al_3 ($Pd_{40.5}Al_{59.5}$) (Fig. 8d). To confirm the presence of this phase in the binary Pd-Al system, a sample with composition $Pd_{23.3}Al_{76.7}$ was annealed at 860 °C and checked after one hour but was not in equilibrium and showed the presence of three phases (Fig. 8e). However, annealing at 860 °C for 20 hours served to attain equilibrium and clearly showed that Pd_8Al_{21} ($Pd_{28.3}Al_{71.7}$) is present in large amounts in equilibrium with the liquid ($Pd_{8.5}Al_{91.5}$) (Fig.

8f). It is important to note that this composition of liquid is considerably different from the one reported by Massalski [15] with 23 at. % Pd.

Fig. 9 represents the partial isothermal section in the Al-rich corner of the Mo-Pd-Al system at 860 °C. The mutual solid solubility of Mo, Pd in the binary Al-rich phases is very low (<1 at. %).

7.4. Hardness of τ_1-MoPd$_{2-x}$Al$_{8+x}$.

The Vickers's hardness data (H$_V$), as measured for the orthorhombic compound τ_1-MoPd$_{2-x}$Al$_{8+x}$ are presented in Table 3. For comparison, we included our data measured for Ni$_2$Al$_3$, which are in fine agreement with those reported in the literature (~900 MPa [16]). Vicker's hardness value for τ_1 is listed in Table 3. Although this compound is rich in aluminium, its hardness is about five times higher than for pure aluminium for which a Vicker's hardness is reported [17] around ~180 MPa. As our phase is in equilibrium with (Al), it is expected that the presence of fine grains of the τ_1-phase inside an Al matrix can improve the hardness of the matrix. It must be noted that fracture toughness was not determined because of irregular lengths of side cracks to the Vicker's indents.

Table 3: Vickers's micro-hardness.

Compound	Composition			Average diagonal length (mm)	H$_V$ (MPa)	References
	Mo	Ni/Pd	Al			
τ_1-MoPd$_{2-x}$Al$_{8+x}$, x = 0.067.	9.3	17.7	73.0	0.02123	842 ±40	[This work]
Ni$_2$Al$_3$	0.0	39.2	60.8	0.02026	925 ±20	[4]
Ni$_2$Al$_3$	-	-	-	-	~900	[16]
Al	Pure Al (99.99 %)			-	~180	[17]

7.5. Conclusion.

The crystal structures of three Al-rich compounds have been solved from X-ray single crystal diffractometry: τ_1-MoPd$_{2-x}$Al$_{8+x}$ (x=0.067; *Pbcm*); τ_7-Zr(Cu$_{1-x}$Al$_x$)$_{12}$ (x = 0.514; *I4/mmm*) and τ_9-ZrCu$_{1-x}$Al$_4$ (x = 0.144; *P4/nmm*) of which τ_1 and τ_9 crystallize in unique structure types, whereas the structure of τ_7-Zr(Cu$_{1-x}$Al$_x$)$_{12}$ is isotypic with the ThMn$_{12}$ type. Details on the atom site preference show that all phases are partially ordered and random distribution of two atom species (Al+Pd) and (Cu+Al) appear in at least

one of the crystallographic sites except for τ_9-ZrCu$_{1-x}$Al$_4$ which exhibits a defect in the Cu-sites. Bärnighausen trees have been constructed to reveal the crystallographic group-subgroup relations that connect the structures of Mo(Cu$_x$Al$_{1-x}$)$_6$Al$_4$ and τ_1 and the structures of Cu and τ_9-ZrCu$_{1-x}$Al$_4$. The ZrCu$_{1-x}$Al$_4$ type (n=3) is part of a series of structures which follow a simple building principle assembling fcc-Cu-type units in a row of various members: Cu (n=1), TiAl$_3$ (n=2), ZrCu$_{1-x}$Al$_4$ (n=3), τ_5-TiNi$_{2-x}$Al$_5$ (n=4), HfGa$_2$ (n=6) and Cu$_3$Pd (n=7).

For the Al-rich part of the Mo-Pd-Al system phase equilibria have been established in an isothermal section at 860 °C comprising two ternary compounds, τ_1-MoPd$_{2-x}$Al$_{8+x}$ and τ_2. Vickers hardness (H$_v$) for τ_1 was determined to be 842 ±40 MPa, which is about five times higher than that of pure aluminium.

References

[1]   A.U. Khan, X. Yan, P. Rogl and A. Saccone, Intermetallics **17**, 2009, p. 1000-1006.

[2]   Atta U. Khan, J. Bursik, A. Grytsiv, V. Pomjakushin, H. Effenberger and P. Rogl, Intermetallics **19**, 2011, p. 1340-1347.

[3]   Atta U. Khan, A. Grytsiv, X. Yan, P. Rogl, A. Saccone, V. Pomjakushin and G. Giester, Inorganic Chem. **50**, 2011, p. 4537-4547.

[4]   Atta U. Khan, A. Grytsiv, G. Giester and P. Rogl, Intermetallics, submitted **2011**.

[5]   V.Y. Markiv and V.V. Burnashova, Poroshk. Metall, **12**, 1970, p. 53-58.

[6]   D. Soares and F. Castro, J. Chim. Phys. **94**, 1997, p. 958-963.

[7]   L. Tretyachenko, G. Effenberg, S. Ilyenko (ed.), Materials Science International Team MSIT. SpringerMaterials - The Landolt-Börnstein Database, Volume 11A2, part 2, 2003, DOI: 10.1007/10915967_14.

[8]   D.F. Soares and F.P. de Castro, Ber. Bunsenges. Phys. Chem. **102**, 1998, p. 1181-1184.

[9]   L.M. Gelato, E. J. Parthé, Appl. Crystallogr. **20**, 1987, p. 139-143.

[10]   E. Koch and W. Fischer, PC versions 9/1997, Z. Kristallogr. **211** (1996), p. 251-253.

[11]   P. Villars, K. Cenzual, Pearson's Crystal Data, Release 20010/11, ASM International, Materials Park, Ohio, USA.

[12]   J.V. Florio, R.E. Rundle and A.I. Snow, Acta Crystallographica **5**, 1952, p. 449-457.

[13]   M. Pötzschke, K. Schubert, Zeitschrift für Metallkunde **53**, 1962, p. 474-488.

[14]   K. Okamura, Jour. of the Physical Society of Japan **28**, 1970, p. 1005-1014.

[15]   T.B. Massalski, 2nd Edition, ASM International, Materials Park, Ohio, 1990, 1, 189-192.

[16]   H.Y. Kim, D.S. Chung, S.H. Hong, Materials Science and Engineering A 2005, 396**,** 376-384.

[17]   C. Xu, T.G. Langdon, J. Mater. Sci. **42,** 2007, 1542-1550.

8. Boron site preference in ternary Ta and Nb boron silicides

8.1. Introduction

It is already reported that particularly the solid solution phases $(TM1,TM2)_5(Si,B)_3$ exhibit good oxidation resistance, high temperature strength and good creep-resistance [1,2,3,4]. Furthermore the $(TM)_3(Si,B)$ phases are found in equilibrium with the parent metal matrix in some systems, providing a good base for the development of high-temperature structural materials. In contrast to the Ta-Si-B system, extended efforts focused on phase equilibria in the Nb-Si-B system [5,6,7,8,9], for which a critical assessment was presented by K. Korniyenko et al. [10]. A recent thermodynamic modeling of the Nb-rich part of Nb-Si-B system includes a liquidus projection [11].

However, for both systems a lack of data exists on detailed crystal structure investigation. Due to the low atomic number of B, it is difficult to precisely locate this element via X-ray powder diffraction techniques. As a task of current investigation, Neutron Powder Diffraction (NPD) and/or X-ray single crystal (XSC) analyses have been employed to shed more light on the B/Si site occupation.

8.2. Experimental Details

Alloys were prepared from metal ingots of Ta, Nb and pieces of Si and B (purity 99.998 and 99.5 mass %, respectively, Alfa Johnson Matthey GmbH, D) by repeated arc melting under argon (weight loss less than 0.1 %). The reguli were then annealed at 1800 °C for 6 hours in case of the Nb-Si-B alloys and at 1900 °C for 120 hours for alloys from the Ta-Si-B system. Lattice parameters and standard deviations were determined by least squares refinements of room temperature X-ray powder Diffraction (XRD) data obtained from a Guinier-Huber image plate employing monochromatic Cu Kα_1 radiation and Ge as internal standards. XRD-Rietveld refinements were performed with the FULLPROF program [for details see Chapter 2] with the use of its internal tables for atom scattering factors. Annealed samples were polished using standard procedures and were examined by scanning electron microscopy (SEM). Wavelength dispersive X-ray analysis (WDX) with an electron beam current of about 15 nA was used for

composition analysis. Pure elements served as standards to carry out the deconvolution of overlapping peaks and background subtraction. Finally the X-ray intensities were corrected for ZAF effects using the INCA-Energy 300 software package [for details see Chapter 2]. Overall composition of the samples derived from EPMA area scans agree with the nominal values within 1.0 at. %.

Single crystals of $Ta_3(Si,B)$ and $Ta_5(Si,B)_3$ were isolated via mechanical fragmentation of a specimen with nominal composition $Ta_{65.0}Si_{20.0}B_{15.0}$, which was annealed at 1900 °C for 120 hours while the single crystal for Ta_5Si_3 was selected from an as cast sample with nominal composition Ta_5Si_3. All crystals were inspected on an AXS-GADDS texture goniometer for quality and crystal symmetry prior to X-ray single crystal (XSC) intensity data collection on a four-circle Nonius Kappa diffractometer (CCD area detector and graphite monochromated Mo K_α radiation, $\lambda = 0.071069$ nm). Orientation matrix and unit cell parameters were derived using the program DENZO [for details see Chapter 2]. No individual absorption correction was necessary because of the rather regular crystal shape and small dimensions of the investigated specimens. The structures were solved by direct methods and refined with the SHELXS-97 and SHELXL-97 programs [for details see Chapter 2], respectively.

Two samples with nominal compositions Nb57.0Si10.0B33.0 and Nb62.0Si22.0B16.0 were prepared from 11B (purity 99.8 % with 95% isotopic enrichment) for neutron powder diffraction (NPD) by annealing at 1800°C for 6 hours and were powdered to a grain size below 40 μm in order to reduce preferential orientation effects. Neutron powder diffraction at room temperature was performed at the ORPHEE 14MW-reactor (CEA-Saclay) using the 3T2 double-axis multi-detector neutron powder diffractometer (resolution $\Delta d/d \geq 4 \times 10^{-3}$; $\lambda_{neutron} = 0.12251$ nm) [12]. Preferred orientation effects were minimized by powdering the samples in a steel mortar to a grain size smaller than 30 μm. Further details concerning the experiments are summarized in Table I. Precise atom parameters, occupation numbers, individual isotropic thermal factors, and profile parameters were derived from a least squares full matrix Rietveld refinement routine (FULLPROF program [for details see Chapter 2] with internal neutron scattering lengths). The various reliability factors calculated are defined in Table I.

8.3. Results and discussion

8.3.1. The crystal structure of $Ta_3(Si_{1-x}B_x)$, x = 0.112 (Ti_3P-type)

Although the structure of binary Ta_3Si (Ti_3P-type) has already been resolved from X-ray powder diffraction [13], no data on site preference and solubility of B in Ta_3Si have been reported. Therefore, a single crystal was selected from a three-phase sample with nominal composition $Ta_{65.0}Si_{20.0}B_{15.0}$ (at. %, annealed at 1900 °C) assuring that the composition determined by EPMA ($Ta_{75.2}Si_{21.3}B_{3.5}$) corresponds to the maximum solubility of B in binary Ta_3Si at this temperature. Lattice parameters obtained from a single crystal [a = 1.0183(5) and c = 0.5169(3) nm] were close to those reported in the literature for binary Ta_3Si [a = 1.017-1.0193 and c = 0.516-0.5183 nm] [13,14,15,16] indicating a rather low amount of B in solid solution. Systematic extinctions revealed a primitive unit cell with one possible space group symmetry $P4_2/n$ (No. 86). In total, 4 crystallographic sites (all 8g) were obtained, out of which three were fully occupied by Ta and one was a position (M) randomly shared by a mix of 88.8% of Si and 11.2 % of B atoms (Table 1). The refined composition ($Ta_{75.0}Si_{22.2}B_{2.8}$) is close to the EPMA value ($Ta_{75.2}Si_{21.3}B_{3.5}$). With anisotropic displacement parameters, the structure refinement finally converged to R_{F2} = 0.022 with little residual electron density (2.59 and -2.38 $e^-/10^{-3}nm^3$). Positional parameters (x, y, z) and interatomic distances obtained in the present study were very close to those obtained for binary Ta_3Si [13,14,15,16]. Using the DIDODATA program [18], which defines the Voronoi polyhedra, we confirmed the coordination figures for the individual atom sites as hitherto described, however, we found 15 ligands for Ta2 (Fig. 1a) in contrast to the descriptions in the literature [19].

Table 1a: XSC data for $Ta_3(Si_{1-x}B_x)$, x = 0.112, Ta_5Si_{3-x}, x = 0.08 and $Ta_5(Si_{1-x}B_x)_3$, x = 0.568, standardized with program *Structure Tidy* [17] and NPD data for $Nb_5(Si_{1-x}B_x)_3$, x = 0.592 and $Nb_5Si_3B_{1-x}$, x = 0.292. Anisotropic displacement parameters in 10^2nm^2.

Parameter/compound	$Ta_3(Si_{1-x}B_x)$, x = 0.112	Ta_5Si_{3-x}, x = 0.08	$Ta_5(Si_{1-x}B_x)_3$, x = 0.568	$Nb_5(Si_{1-x}B_x)_3$, x = 0.592	$Nb_5Si_3B_{1-x}$, x = 0.292
Method	XSC	XSC	XSC	NPD	NPD
Structure type	Ti_3P	Cr_5B_3	Cr_5B_3	Cr_5B_3	Ti_5Ga_4
Space Group	$P4_2/n$, #86	$I4/mcm$, #140	$I4/mcm$, #140	$I4/mcm$, #140	$P6_3/mcm$, #193
Composition from EPMA	$Ta_{75.2}Si_{21.3}B_{3.5}$	$Ta_{62.6}Si_{37.4}$	$Ta_{62.6}Si_{15.5}B_{21.9}$	$Nb_{62.7}Si_{15.8}B_{21.5}$	$Nb_{56.2}Si_{35.8}B_8$
Composition from refinement	$Ta_{75.0}Si_{22.2}B_{2.8}$	$Ta_{63.1}Si_{36.9}$	$Ta_{62.5}Si_{16.2}B_{21.3}$	$Nb_{62.5}Si_{15.3}B_{22.2}$	$Nb_{57.4}Si_{34.5}B_{8.1}$
Formula from refinement	$Ta_3(Si_{1-x}B_x)$, x = 0.112	Ta_5Si_{3-x}, x = 0.08	$Ta_5(Si_{1-x}B_x)_3$, x = 0.568	$Nb_5(Si_{1-x}B_x)_3$, x = 0.592	$Nb_5Si_3B_{1-x}$, x = 0.292

	Mo Kα	Mo Kα	Mo Kα	$\lambda_n = 0.12251$	$\lambda_n = 0.12251$
Radiations, λ (nm)	Mo Kα	Mo Kα	Mo Kα	$\lambda_n = 0.12251$	$\lambda_n = 0.12251$
a (nm)	1.0183(5)	0.65246(5)	0.62603(2)	0.62740(4)	0.75762(1)
c (nm)	0.5169(3)	1.18853(3)	1.16008(4)	1.16443(9)	0.52750(1)
Reflections in refinement	1144≥4σ(F_o) of 1185	302≥4σ(F_o) of 332	269≥4σ(F_o) of 308	250	186
Number of variables	36	17	16	31	28
$R_F = \Sigma|F_0\text{-}F_c|/\Sigma F_0$	-	-	-	0.0276	0.0164
$R_B = \Sigma|I_0\text{-}I_c|/\Sigma I_0$	-	-	-	0.0503	0.0218
$R_{wP} = [\Sigma w_i|y_{0i}\text{-}y_{ci}|^2/\Sigma w_i|y_{0i}|^2]^{1/2}$	-	-	-	0.0869	0.0466
$R_P = \Sigma|y_{0i}\text{-}y_{ci}|/\Sigma|y_{0i}|$	-	-	-	0.0657	0.0359
$R_e = [(N\text{-}P+C)/\Sigma w_i y_{0i}^2]^{1/2}$	-	-	-	0.0237	0.0217
$R_F^2 = \Sigma|F_0^2\text{-}F_c^2|/\Sigma F_0^2$	0.022	0.036	0.028	-	-
R_{Int}	0.059	0.049	0.024	-	-
wR2	0.048	0.095	0.079	-	-
GOF	1.232	1.133	1.321	-	-
Extinction	0.00253(7)	0.0062(5)	0.0010(2)	-	-
Residual density e⁻/Å³; max; min.	2.59; -2.38	7.32; -4.88	3.60; -5.94	-	-
Atom parameters					
Atom site 1	8g (x, y, z)	16l (x, x+ ½, z)	16l (x, x+ ½, z)	16l (x, x+ ½, z)	4d (⅓, ⅔, 0)
Occ.;	1.00 **Ta1**	1.00 **Ta1**	1.00 **Ta1**	1.00 **Nb1**	1.00 **Nb1**
x, y, z;	0.14704(2), 0.66251(2), 0.22260(5)	0.16438(5), 0.15039(4)	0.16696(5), 0.14102(3)	0.1686(1), 0.1396(1)	-
U_{11}; U_{22}; U_{33}	0.0056(1), 0.0043(1); 0.0048(1)	$U_{11} = U_{22} = 0.0039(3), U_{33} = 0.0026(4)$	$U_{11} = U_{22} = 0.0041(2), U_{33} = 0.0015(3)$	-	-
U_{23}; U_{13}; U_{12};	0.00049(7), -0.00031(7), -0.00072(7)	$U_{23} = U_{13} = -0.00034(8), U_{12} = -0.0001(1)$	$U_{23} = U_{13} = -0.00044(8), U_{12} = 0.0007(1)$	$B_{iso}^1 = 0.21(1)$	$B_{iso} = 0.21(1)$
Atom site 2	8g (x, y, z)	4c (0, 0, 0)	4c (0, 0, 0)	4c (0, 0, 0)	6g (x, 0, ¼)
Occ.;	1.00 **Ta2**	1.00 **Ta2**	1.00 **Ta2**	1.00 **Nb2**	1.00 **Nb2**
x, y, z;	0.10542(2), 0.23058(2), 0.52127(5)	-	-	-	0.24651(6)
U_{11}; U_{22}; U_{33};	0.0039(1), 0.0072(1); 0.0047(1)	$U_{11} = U_{22} = 0.0029(3), U_{33} = 0.0035(4)$;	$U_{11} = U_{22} = 0.0031(2), U_{33} = 0.0007(3)$;	-	-
U_{23}; U_{13}; U_{12};	0.00063(7), -0.00012(7), -0.00080(7)	$U_{23} = U_{13} = U_{12} = 0$	$U_{23} = U_{13} = U_{12} = 0$	$B_{iso} = 0.10(3)$	$B_{iso} = 0.20(1)$
Atom site 3	8g (x, y, z)	4a (0, 0, ¼)	4a (0, 0, ¼)	4a (0, 0, ¼)	6g (x, 0, ¼)
Occ.;	1.00 **Ta3**	0.92(4) **Si1**	1.00 **Si1**	1.00 **Si1**	1.00 **Si1**
x, y, z;	0.53598(2), 0.06267(2), 0.26293(4)	-	-	-	0.6018(1)
U_{11}; U_{22}; U_{33};	0.0033(1), 0.0041(1); 0.0024(1)	$U_{11} = U_{22} = 0.006(2), U_{33} = 0.005(3)$	$U_{11} = U_{22} = 0.006(1), U_{33} = 0.004(2)$	-	-
U_{23}; U_{13}; U_{12};	0.00023(7), 0.00007(7), 0.00007(7)	$U_{23} = U_{13} = U_{12} = 0$	$U_{23} = U_{13} = U_{12} = 0$	$B_{iso} = 0.11(5)$	$B_{iso} = 0.32(2)$

Atom site [4]	8g (x, y, z)	8h (x, x+ ½, 0)	8h (x, x+ ½, 0)	8h (x, x+ ½, 0)	2b (0, 0, 0)
Occ.;	0.888(4) **Si** + 0.112 **B**	1.00 **Si2**	0.854(4) **B** + 0.146 **Si**	0.89(3) **B** + 0.11 **Si**	0.708(3) **B1**
x, y, z;	0.0457(2), 0.2195(2), 0.0277(4)	0.6298(5)	0.622(1)	0.622(1)	-
U_{11}; U_{22}; U_{33};	0.0039(8), 0.0050(8); 0.0031(7)	$U_{11}=U_{22}$ =0.003(1), $U_{33}=0.007(2)$	$U_{11}=0.003(2)$	-	-
U_{23}; U_{13}; U_{12};	0.0000(6), 0.0000(6), -0.0011(5)	$U_{23}=U_{13}=0$, $U_{12}=-0.001(1)$	-	$B_{iso}=0.05(4)$	$B_{iso}=0.13(2)$

[1]B_{iso} is given in $(10^2\ nm^2)$.

Table 1b: Interatomic distances (nm) for $Ta_3(Si_{1-x}B_x)$, x = 0.112, standard deviation ≤ 0.0002.

Ta1–	1M	0.2589	CN = 15	–1M	0.2605	Ta3–	1M	0.2566		–1Ta1	0.3225
CN = 14	–1M	0.2640		–1M	0.2625	CN = 15	–1M	0.2663		–1Ta2	0.3630
	–1Ta1	0.2752		–1M	0.2690		–1M	0.2823		–1M	0.3805
	–1Ta3	0.2934		–1Ta3	0.2879		–1Ta3	0.2859	M–	1Ta3	0.2566
	–1Ta3	0.2962		–1Ta3	0.2901		–1Ta2	0.2879	CN = 9	–1Ta2	0.2570
	–1Ta3	0.3063		–1Ta2	0.2971		–1Ta2	0.2901		–1Ta1	0.2589
	–1Ta2	0.3090		–1Ta1	0.3090		–1Ta1	0.2934		–1Ta2	0.2605
	–1Ta2	0.3124		–1Ta3	0.3117		–1Ta1	0.2962		–1Ta2	0.2625
	–1Ta3	0.3189		–1Ta1	0.3124		–1Ta1	0.3063		–1Ta1	0.2640
	–1Ta3	0.3225		–2Ta2	0.3163		–1Ta3	0.3091		–1Ta3	0.2663
	–4Ta1	0.3235		–2Ta2	0.3504		–1Ta2	0.3117		–1Ta2	0.2690
Ta2–	1M	0.2570		–1Ta3	0.3630		–1Ta1	0.3189		–1Ta3	0.2823

Ta_5Si_{3-x}, x = 0.08

Ta1–	1Si2	0.2606		–1Ta1	0.3034		–8Ta1	0.3023		–2Ta1	0.2608
CN = 15	–2Si2	0.2634		–2Ta1	0.3195	Si1–	8Ta1	0.2710		–4Ta1	0.2633
	–2Si2	0.2710		–4Ta1	0.3448	CN = 10	–2Ta2	0.2971			
	–1Ta1	0.2846	Ta2–	4Si2	0.2558	Si2–	1Si2	0.2396			
	–2Ta2	0.3023	CN = 14	–2Si2	0.2971	CN = 9	–2Si2	0.2559			

$Ta_5(Si_{1-x}B_x)_3$, x = 0.568

Ta1–	2M	0.2456		–1Ta1	0.2956	CN = 14	–8Ta1	0.2849	M–	1M	0.2163
CN = 16	–1M	0.2482		–1Ta1	0.3272		–2Si1	0.2900	CN = 9	–4Ta1	0.2456
	–2Si1	0.2653		–2Ta1	0.3281	Si1–	8Ta1	0.2653		–2Ta1	0.2482
	–2Ta2	0.2849		–4Ta1	0.3298	CN = 10	–2Ta2	0.2900		–2Ta2	0.2486
	–1Ta1	0.2925	Ta2–	4M	0.2486						

$Nb_5(Si_{1-x}B_x)_3$, x = 0.592

Nb1–	2M	0.2440		–1Nb1	0.2992	CN = 14	–8Nb1	0.2843	M–	1M	0.2071
CN = 16	–1M	0.2504		–1Nb1	0.3252		–2Si1	0.2911	CN = 9	–4Nb1	0.2440
	–2Si1	0.2663		–2Nb1	0.3329	Si1–	8Nb1	0.2663		–2Nb1	0.2504
	–2Nb2	0.2843		–4Nb1	0.3299	CN = 10	–2Nb2	0.2911		–2Nb2	0.2514
	–1Nb1	0.2948	Nb2–	4M	0.2514						

$Nb_5Si_3B_{1-x}$, x = 0.292

Nb1–	2Nb1	0.2637		–1Si1	0.2692	Si1–	2Nb2	0.2637	B1–	6Nb2	0.2286
CN = 14	–6Si1	0.2668		–2Si1	0.2877	CN = 11	–4Nb1	0.2668	CN = 6		
	–6Nb2	0.3195		–4Nb1	0.3195		–1Nb2	0.2692			
Nb2–	2B1	0.2286		–4Nb2	0.3232		–2Nb2	0.2877			
CN = 17	–2Si1	0.2637		–2Nb2	0.3235		–2Si1	0.3056			

8.3.2. The crystal structure of Ta_5Si_{3-x}, x = 0.08 (Cr_5B_3-type)

Similar to Ta_3Si, the structure of binary Ta_5Si_3 with Cr_5B_3-type is already known in the literature including a Rietveld refinement of x-ray powder diffraction data [16,20,21,22,23]. In order to provide a set of atom positional parameters of higher precision for Ta_5Si_3, single crystal X-ray intensity CCD data were collected. Lattice parameters obtained from the single crystal [a = 0.65246(5) and c = 1.18853(3) nm] are close to those hitherto reported for the Ta_5Si_3-phase [a = 0.6511-0.6519 and c = 1.1873-1.1887 nm] [16,20,21,22,23]. Systematic extinctions revealed a body centered unit cell with three possible space group symmetries, *I*4/*mcm*, *I*-4*c*2 and *I*4*cm*. As structure determination using direct methods in all these space groups revealed practically identical solutions, we describe the structure in the space group with the highest symmetry *I*4/*mcm* (No. 140).

In total, 4 crystallographic sites were obtained, out of which, Si occupied the 4*a* and 8*h* sites while sites 4*c* and 16*l* were fully occupied by Ta. A small defect was found in the 4*a* site occupied by Si (see Table 1). The refined composition ($Ta_{63.1}Si_{36.9}$) was close to the composition ($Ta_{62.6}Si_{37.4}$) obtained from EPMA. With anisotropic displacement parameters, the structure refinement finally converged to R_{F2} = 0.033 with small residual electron density (7.32 and –4.88 $e^-/10^{-3}nm^3$). Fig. 1b shows the coordination polyhedra for Ta_5Si_{3-x}, x = 0.08. By using the program DIDO95 [18], we calculated the Voronoi coordination polyhedra and the distances from the next nearest neighbours for all the atom sites in the crystal structure (Table 1). The Voronoi analysis excludes the rather longer Ta1-Ta1 bond (0.3575 nm) with a very small Voronoi face area (0.10 compared to the maximum area of 4.05) and thus limits the coordination shell for Ta1 to 15 ligands. This is important to mention, because particularly The Ta1-Ta1 ligand needs to be included again in the Ta1 polyhedron, when Si is replaced by B in $Ta_5(Si_{1-x}B_x)$ (see section 3.3).
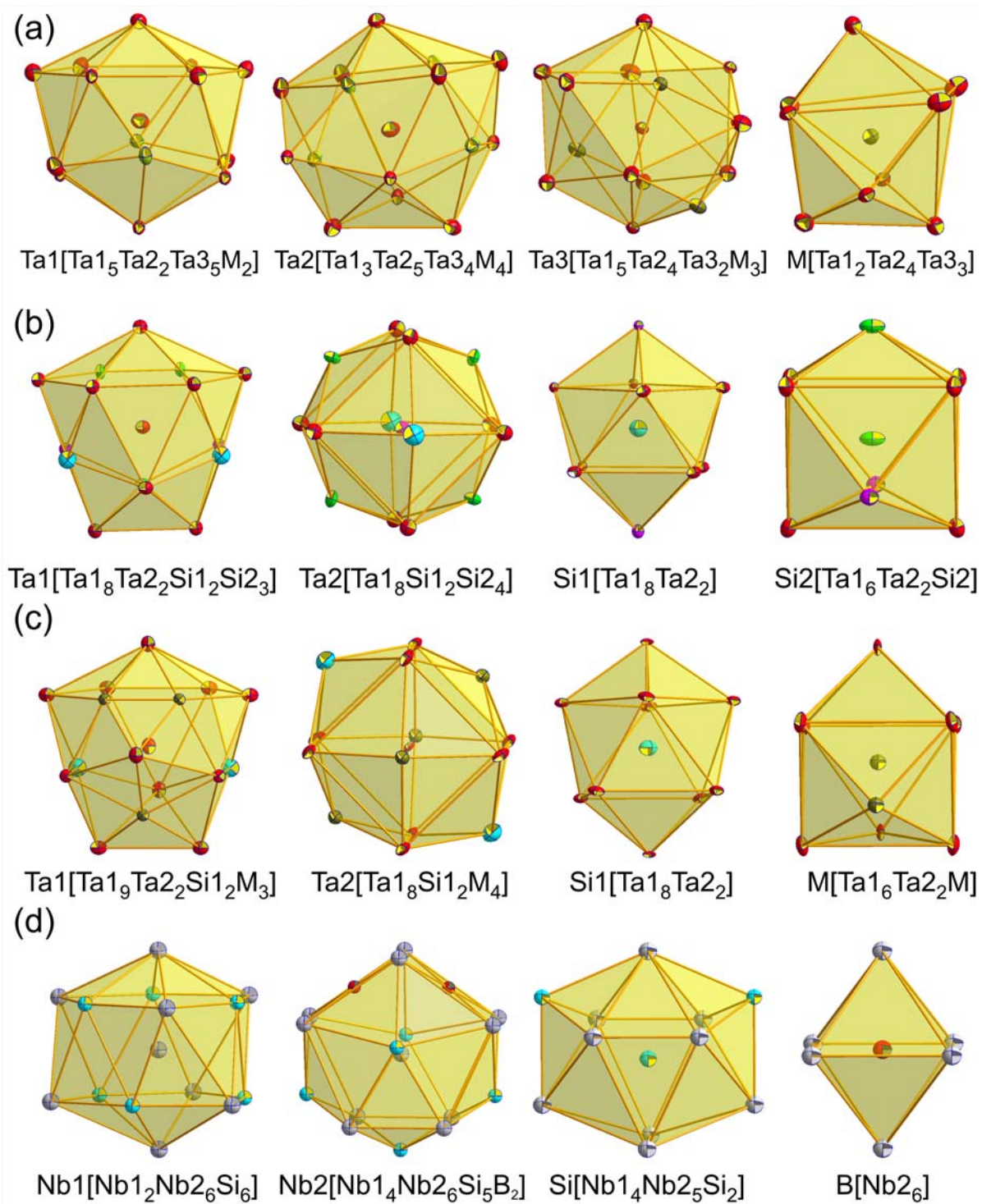
Fig. 1; Coordination polyhedra (a) in $Ta_3(Si_{1-x}B_x)$, $x = 0.112$, (b) in Ta_5Si_{3-x}, $x = 0.08$, (c) in $Ta_5(Si_{1-x}B_x)_3$, $x = 0.568$ and (d) in $Nb_5Si_3B_{1-x}$, $x = 0.292$.

8.3.3. The crystal structure of $Ta_5(Si_{1-x}B_x)_3$, $x = 0.568$ (Cr_5B_3- type)

No details on the site preference of B-atoms within the isotypic solid solution $Ta_5(Si_{1-x}B_x)_3$ have been reported in the literature. In order to elucidate boron incorporation into the lattice of parent Ta_5Si_3, X-ray structure analysis was employed on a single crystal selected from a multi-phase sample with nominal composition $Ta_{65.0}Si_{20.0}B_{15.0}$ (at. %, annealed at 1900 °C). Lattice parameters obtained from the single crystal [a = 0.62603(2) and c = 1.16008(4) nm] were considerably smaller than those reported in the literature for binary Ta_5Si_3 [a = 0.6511-0.6519 and c = 1.1873-1.1887 nm] [21,25,26,27,28] as well as those in section 3.2, indicating a significant solubility of B. Systematic extinctions confirmed a body centered unit cell with three possible space group symmetries, $I4/mcm$, $I\text{-}4c2$ and $I4cm$. As structure determination using direct methods in all these space groups revealed practically identical solutions, we describe the structure in the space group with the highest symmetry $I4/mcm$ (No. 140). In total, 4 crystallographic sites were obtained out of which, 4a was fully occupied by Si, 4c and 16l were fully occupied by Ta, but the 8h site clearly revealed a mixed position occupied by 14.5 % of Si and 85.4 % of B atoms (Table 1). At this atom arrangement, the refined composition ($Ta_{62.5}Si_{16.2}B_{21.3}$) was close to the EPMA value ($Ta_{62.6}Si_{15.5}B_{21.9}$). With anisotropic displacement parameters, the structure refinement finally converged to R_{F2} = 0.028 with little residual electron density (3.60 and –5.94 e$^-$/10^{-3}nm^3). Comparing structural parameters for the binary and ternary phases, we can see a significant decrease for the lattice parameters (Table 1) and for the positional parameters of the 8h site associated with the Si/B substitution. The shortest bond ($d_{M\text{-}M}$=0.2163 nm) is observed between atoms located in the mixed site M (8h). Due to the high boron occupation of 85.4 % B, the shortest distances between two 8h sites (0.2163 nm) are significantly shorter than the corresponding distances in binary Ta_5Si_3 (0.2396 nm). The decrease of the overall atom size in the 8h site also influences the positional parameters for the next-nearest Ta1 site (16l) and the corresponding distances for the coordination polyhedron of the Ta1 atom (Fig. 1c). The longest Ta1-Ta1 distance (0.3575 nm), which was excluded in binary Ta_5Si_3 (section 3.2), becomes considerably shorter (0.3272 nm, Table 1b) and again becomes part of the polyhedron around Ta1 now having 16 ligands. All other polyhedra keep their shape, bit it is noteworthy that several Ta1-M(Si/B) distances also shrink significantly (0.2456 nm) as compared to the binary Ta1-Si distances (0.2606 nm), whereas some Ta-Ta distances increase slightly.

It may be noted here, that due to similar atomic size of Nb and Ta, the lattice parameters of $Ta_5(Si_{1-x}B_x)_3$ fit to the compositional dependence of the isotypic Nb-based solid solution, $Nb_5(Si_{1-x}B_x)_3$ [8].

8.3.4. The crystal structure of $Nb_5(Si_{1-x}B_x)_3$, x = 0.592 (Cr_5B_3-type)

A sample with nominal composition $Nb_{62}Si_{16}B_{22}$ (at. %, annealed at 1800 °C) was used for NPD. Lattice parameters [a = 0.62740(4), c = 1.16443(9) nm] at a B content of 22.2 % (after EPMA) fits well with the compositional dependence of parameters for this phase as defined by several authors [5,7,8]. Rietveld refinement of the spectrum confirmed the Cr_5B_3-type (Fig. 2, Table 1) and showed that B shares the $8h$ site with Si (0.89B + 0.11Si) revealing a composition $Nb_{62.5}Si_{15.3}B_{22.2}$ (at. %). This composition is slightly lower than the maximum amount of B in this phase (25 %) [8,9] and it seems that Si will entirely be replaced by B at the limit of the solid solution.
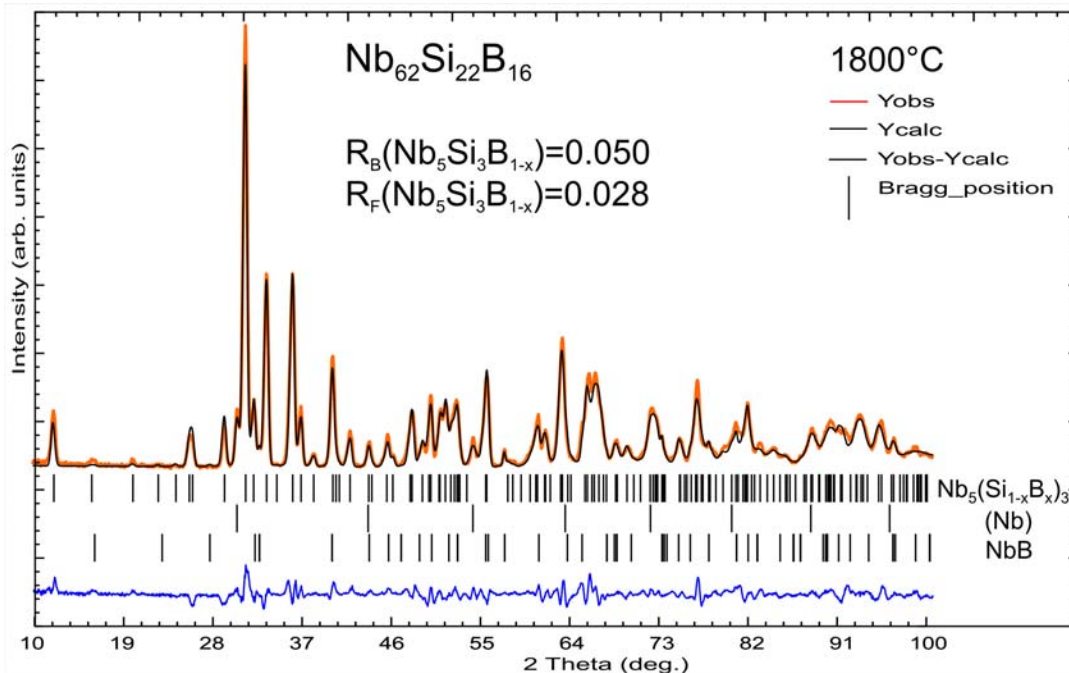

Fig. 2. Rietveld refinement of the NPD spectrum of $Nb_{62}Si_{22}B_{16}$ (nominal composition in at. %) revealing the presence of three phases: $Nb_5(Si_{0.41}B_{0.59})_3$, (Nb) and NbB.

It must be noted that no B was found in the $4a$ site (Si1) and thus the boron site preference in this phase is similar to the isotypic solid solution $Ta_5(Si_{1-x}B_x)_3$, (x = 0.568) in the Ta-Si-B system.

123

Consequently, the influence of Si/B substitution on structural parameters is similar to that observed for the isotypic Ta phase (see section 3.3). The coordination polyhedra for this phase are similar to $Ta_5(Si_{0.43}B_{0.57})_3$ and therefore are not shown here.

8.3.5. The crystal structure of $Nb_5Si_3B_{1-x}$, x = 0.292 (Ti$_5$Ga$_4$-type)

In order to elucidate atom site occupation via NPD for boron atoms incorporated in Nb_5Si_3, a sample of nominal composition $Nb_{57}Si_{10}B_{33}$ (at. %) was annealed at 1800 °C. Although we were able to index all the diffraction peaks on the basis of a hexagonal lattice that suggested isotypism with the Mn_5Si_3 type, the intensity of some of the peaks was considerably different. Further refinement of this spectrum showed that the void in the Mn_5Si_3 structure at site $2b$ (0, 0, 0) is partially filled by B (71.0 %). Therefore the structure can be considered as a partially filled Mn_5Si_3-type as was first reported by H. Nowotny et al. [5] (D8$_8$ type). Actually, this phase crystallises in the defect Ti$_5$Ga$_4$-type [24]. No Si/B exchange was observed.
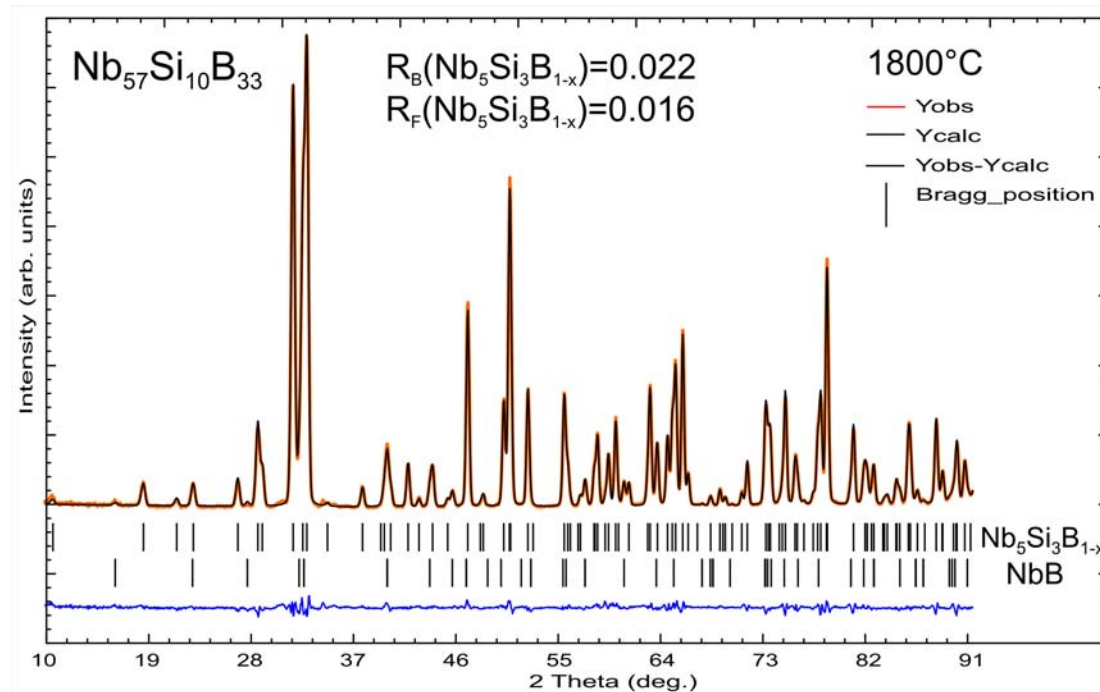

Fig. 3. Rietveld refinement of the NPD spectrum of $Nb_{57}Si_{10}B_{33}$ (nominal composition in at. %) showing the presence of two phases: $Nb_5Si_3B_{0.79}$ and NbB.

The formula obtained from refinement, $Nb_5Si_3B_{1-x}$ (x = 0.292), yielded a composition $Nb_{57.4}Si_{34.5}B_{8.1}$, which is in good accord with data from EPMA ($Nb_{56.2}Si_{35.8}B_{8.0}$) (see Table 1).

Furthermore, the refined composition is very close to the point composition shown in the isothermal section by Nunes et al. [9] at 1700 °C and lies inside the homogeneity region presented by H. Nowotny et al. [5] at 1600 °C. No B content was found for the $6d$ site occupied by Si (Fig. 3) constituting a fully ordered structure except for the B-defects in the $2b$ site.

To calculate the atomic environment and the distances from the next nearest neighbours, we used the DIDO95 program [18]. Nb1 atoms have only 14 next nearest neighbours. Interestingly, the program yielded 17 next nearest neighbours for Nb2 (Fig. 1), including B atoms at the centre of two square faces in this polyhedron. The coordination polyhedron of B is an octahedron with 6 next nearest neighbours. Although, the calculation prompts 14 nearest neighbours for B, we take only the 6 Nb2 because the distances for the other 8 ligands are rather long (B-B = 0.2637 nm and B-Si = 0.3292 nm) and cannot be considered as bonding distances.

8.4. Conclusion.

The crystal structures of a series of compounds have been solved from X-ray single crystal diffractometry revealing details on the boron incorporation in binary and ternary structures. $Ta_3(Si_{1-x}B_x)$ (x = 0.112) crystallizes with the Ti_3P-type where B and Si atoms randomly share the $8g$ site. Ta_5Si_{3-x} (x = 0.08) crystallizes with the Cr_5B_3-type and exhibits a small amount of vacancies on the $4a$ site. $Ta_5(Si_{1-x}B_x)_3$ (x = 0.568; Cr_5B_3-type) is part of the solid solution of Ta_5Si_3 into the ternary Ta-Si-B system with B replacing Si on the $8h$ site. The crystal structures of $Nb_5(Si_{1-x}B_x)_3$ (x = 0.592; Cr_5B_3-type) and of $Nb_5Si_3B_{1-x}$ (x = 0.292; Ti_5Ga_4-type) were solved from neutron powder diffraction data. In $Nb_5(Si_{1-x}B_x)_3$ B-atoms substitute for Si on the $8h$ site, whereas with B-atoms in $Nb_5Si_3B_{1-x}$ partially fill the octahedral voids in the $2b$ site of the parent Mn_5Si_3-type structure.

References

[1]   M.K. Meyer, M.J. Kramer and M. Akinc, Intermetallics **4** (1996), p. 273-281.

[2]   M.K. Meyer and M. Akinc, J. Am. Ceram. Soc. **79(4)** (1996), p. 938-944.

[3]   M.K. Meyer and M. Akinc, J. Am. Ceram. Soc. **79(10)** (1996), p. 2763-2766.

[4]   T.A. Parthasarathy, M.G. Mendiratta and D.M. Dimiduk, Acta Materialia **50** (2002), p. 1857-1868.

[5]   H. Nowotny, F. Benesovsky, E. Rudy and A. Wittman, Monatshefte für Chemie, **91**, (1960), p. 975-990.

[6]   D.M.P. Junior, C.A. Nunes, G.C. Coelho and F. Ferreira, Intermetallics, **11**, (2003), p. 251-255.

[7]   G. Rodrigues, C.A. Nunes, P.A. Suzuki and G.C. Coelho, Intermetallics, **12**, (2004), p. 181-188.

[8]   S. Katrych, A. Grytsiv, A. Bondar, P. Rogl, T. Velikanova and M. Bohn, Journal of Solid State Chemistry, **177**, (2004), p. 493-497.

[9]   C.A. Nunes, D.M.P. Junior, G.C. Coelho, P.A. Suzuki, A.A.A.P. da Silva and R.B. Tomasiello, Journal of Phase Equilibria and Diffusion **32(2)** (2011), p. 92-96.

[10] K. Korniyenko, P. Rogl and T. Velikanova, MSIT, G. Effenberg and S. Ilyenko (ed.), SpringerMaterials – The Landolt-Börstein Database. Springer-Verlag Berlin Heidelberg, (2010), DOI: 10.1007/978-3-642-02700-0_8.

[11] Z. Sun, Y. Yang, X. Guo, C. Zhang and Y.A. Chang **19** (2011), p. 26-34.

[12] M.C. Bellisent-Funel, Neutron News **3(1)** (1992) p. 7.

[13] W. Rossteutscher and K. Schubert, Zeitschrift für Metallkunde **56** (1965), p. 813-822.

[14] K. Schubert, A. Raman and W. Rossteutscher, Naturwissenschaften **51** (1964), p. 506-507.

[15] D.K. Deardorff, R.E. Siemens, P.A. Romans and R.A. McCune, Journal of less-Common Metals **18** (1969), p. 11-26.

[16] Y.A. Kocherzhinskii, O.C. Kulik and E.A. Shishkin, Doklady Akademii Nauk SSSR **261** (1981), p. 464-465.

[17] L.M. Gelato, E. J. Parthé, Appl. Crystallogr. **20**, (1987), 139-143.

[18] E. Koch and W. Fischer, PC versions 9/1997, Z. Kristallogr. **211** (1996), p. 251-253.

[19] P. Villars, K. Cenzual, Pearson's Crystal Data, ASM International, Ohio, USA, Release 2010/11.

[20] E. Parthe, H. Nowotny and H. Schmid, Monatshefte für Chemie **86** (1955), p. 385-396.

[21] E. Parthe, B. Lux and H. Nowotny, Monatshefte für Chemie **86** (1955), p. 859-867.

[22] H. Nowotny, C. Brukl and F. Benesovsky, Monatshefte für Chemie **92** (1961), p. 116-127.

[23] H. Nowotny and E. Laube, Planseeberichte für Pulvermetallurgie **9** (1961), p. 54-59.

[24] M. Pötzschke and K. Schubert, Zeitschrift für Metallkunde **53**, (1962), 474-488.

9. The system Ta-V-Si: Crystal structure and phase relations.

9.1. Introduction

Information on phases and equilibria in the Ta-V-Si system has been collected by several research groups. J.J. English [1] presented the first isothermal section of the Ta-V-Si system at 1400 °C, which exhibited two continuous solid solutions $(Ta_xV_{1-x})Si_2$ [2] and $(Ta_xV_{1-x})_5Si_3$, but did not reveal any ternary phase. Later, E. Ganglberger [3] and R. Mittal [4] reported a $MgZn_2$ type Laves phase, Ta_2V_3Si. A further ternary phase $Ta_{1.5}V_{3.5}Si_3$ with Mn_5Si_3 type was characterized by J. Steinmetz et al. [5] and in a second article, another ternary phase $Ta_2V_4Si_5$ [6] was defined as part of a solid solution starting from binary V_6Si_5. A linear lattice parameter dependence on the Ta-content was derived for the solution $(Ta_xV_{1-x})_3Si$ at 1650°C ($0 \leq x \leq 0.13$) [7].

All these investigations appearing after J.J. English [1] raised serious questions and demand a renewed study of the phase relations in the Ta-V-Si system. Furthermore, there is a lack of complete structure determinations for ternary Laves and Mn_5Si_3 type structures. Therefore the present investigation intends to provide a comprehensive evaluation of the equilibria and crystal structures for ternary phases in the Ta-V-Si system.

9.2. Experimental details

Alloys were prepared (each of 1-2 grams) by argon arc melting from metal ingots of Ta, V and pieces of Si all with purity higher than 99.9 mass % (Alfa Johnson Matthey GmbH, Germany) and were melted three times for homogenization (weight loss less than 0.1 %). As-cast alloys were annealed for 7-15 days at 1500 °C and subsequently at 1200 °C (for 7-15 days) in a high vacuum furnace and then were radiation cooled. In many cases, it was difficult to get equilibrium even after 10 days of annealing at 1500 °C. So repeated grinding, compacting and annealing of samples served to attain equilibrium. Lattice parameters and standard deviations were determined by least squares refinements of room temperature X-ray powder diffraction (XPD) data obtained from a Guinier-Huber image plate employing monochromatic Cu $K\alpha_1$ radiation with Ge as internal standard. Samples were polished using standard procedures and were

examined by optical metallography and scanning electron microscopy (SEM). Composition of particular phases was measured using a JEOL JSM 6460 scanning electron microscope equipped with both energy- and wavelength dispersive X-ray analytical systems INCA Energy and INCA Wave by Oxford Instruments. An acceleration voltage of 20 kV was used. Reliable evaluation of the Si content in the Ta-V-Si alloys is hindered by a strong overlap of the Si K_α peak at 1.740 keV and the Ta M_α peak at 1.710 keV in energy dispersive X-ray (EDX) spectra. Thus wavelength dispersive X-ray analysis (WDX) with well-separated wavelengths needs to be used for accurate composition measurements. Si K_α, V K_α and Ta L_α were used for quantification at an electron beam current of about 15 nA. The full width at half maximum of the Si K_α peak measured experimentally in WDX is only about 2 eV, hence no overlap with M_α Ta peak can occur. Pure elements served as standards to quantify. Finally the X-ray intensities were corrected for ZAF effects. Single crystals of τ_2-Ta(Ta,V,Si)$_2$ (MgZn$_2$-type Laves phase) suitable for X-ray diffraction were mechanically isolated from an arc-melted specimen Ta$_{33.3}$V$_{50}$Si$_{16.7}$ (nominal composition in at. %) that was annealed at 1500 °C for 10 days. The crystals were inspected on an AXS-GADDS texture goniometer for quality and crystal symmetry prior to X-ray intensity data collection on a four-circle Nonius Kappa diffractometer (CCD area detector and graphite monochromated Mo K_α radiation, λ = 0.071069 nm). Orientation matrix and unit cell parameters were derived using the program DENZO [For details, see chapter 2]. No absorption correction was necessary because of the rather regular crystal shape and small dimensions of the investigated specimens (30×30×35 μm^3). The structure was solved by direct methods and refined with the SHELXS-97 and SHELXL-97 programs [For details, see chapter 2] respectively.

9.3. Results and discussion

9.3.1. Binary boundary systems

Some controversy exists for the Ta-V binary phase diagram. The critical assessment in Massalski [8] shows a continuous bcc-type solid solution (Ta,V) at high temperatures and a binary Laves phase with MgCu$_2$ structure (C15) below a critical point at 1310 °C. In contrast to the version by Massalski, which is backed by four out of five independent investigations, A. Nefeolov et al. [9] reported the additional formation of a hexagonal Laves phase with MgZn$_2$-type (C14) in a limited temperature range from 1125 to 1430°C and this phase was included in the binary phase

diagram by Savitskii et al. [10]. The most recent attempts for a thermodynamic modeling of the Ta-V binary system by Pavlu et al. [11], and a similar assessment by Danon et al. [12], relied on the phase relations given by Savitskii et al. [10]. However, in the present investigation we could not confirm the hexagonal Laves phase in the binary Ta-V system in samples annealed at 1200 °C for 5 days. For the Ta-Si system we accept the thermodynamic assessment of Z. Guo et al. [13]. A thermodynamic modeling of the system V-Si is due to C. Zhang et al. [14], reviewed by H. Okamoto [15]. It should be emphasized, that although the Nb_6Sn_5 type structure (space group *Immm*) was assigned by J. Hallais et al. [16] to the V_6Si_5-phase, V_6Si_5, however, adopts its own structure type (space group *Ibam*), as derived from single crystal X-ray data presented by P. Spinat et al. [17] and J. Hallais [18]. All crystal data on solid unary and binary phases pertinent to the Ta-V-Si system are summarized in Table 1.

Table 1. Experimental crystallographic data of solid phases in the Ta-V-Si system.

Phase Temperature range (°C)	Space group Prototype	Lattice parameters (nm)			Comments
		a	b	c	
$(Ta_{1-x}V_x)$	*Im-3m* W	0.3305-0.3325			[19,20] (see Figure 5)
(Ta); < 3020 [8]		0.33030			[8]
(V); < 1910 [8]		0.3024			[8]
$(V_{1-x}Si_x)$		0.30232-0.303			0 < x < 0.03 [21]
(Si) < 1414 [8]	*Fd-3m* C (Diamond)	0.54306			[8]
TaV_2 ≤ 1310 [8]	*Fd-3m* $MgCu_2$	0.7157			[22]
TaV_2 1435-1127 and ≤ 370 [34]	$P6_3/mmc$ $MgZn_2$	0.5058(5)		0.8250(5)	[9]
$(Ta_{1-x}V_x)_3Si$ Ta_3Si; < 2340 [13]	$P4_2/n$ Ti_3P	1.00903(9) 1.0184		0.51276(9) 0.5183	x_{max}[1]= 0.160, [This work] 0 ≤ x ≤ 0.160, [This work] [23]
$(Ta_{1-x}V_x)_2Si$ Ta_2Si; < 2440 [13]	*I4/mcm* $CuAl_2$	0.61454(7) 0.61623(8) 0.6172		0.50431(7) 0.50574(7) 0.505	x_{max}[1]= 0.123, [This work] x = 0, [This work] [23]
$(Ta_{1-x}V_x)_5Si_3$ Ta_5Si_3; < 2160 [13]	*I4/mcm* Cr_5B_3	0.64430(7) 0.65154(5) 0.6519		1.19154(9) 1.18753(9) 1.187	x_{max}[1]= 0.128, [This work] x = 0, [This work] [23]
$(Ta_{1-x}V_x)Si_2$ $TaSi_2$; < 2034 [13] VSi_2; < 1683 [14]	$P6_222$ $CrSi_2$	0.4574-0.4766 0.4784 0.4573		0.6357-0.6549 0.6568 0.6374	0 < x < 1, graph given Annealed at 1300 °C [33] [24] [24]
$(Ta_xV_{1-x})_3Si$ V_3Si; < 1921 [14]	*Pm-3n* Cr_3Si	0.4755(4) 0.4763 0.4725 0.4727			x_{max}[1]= 0.086, [This work] x_{max}= 0.147 at 1650 °C [10] x = 0, [10] [25]
$(Ta_xV_{1-x})_5Si_3$ V_5Si_3 < 1987 [14] Ta_5Si_3 2543-2160 [13]	*I4/mcm* W_5Si_3	0.94674(7) 0.94264(4) 0.9383 0.9892		0.47752(6) 0.47585(3) 0.4760 0.5042	x = 0.048, [This work] x = 0, [This work] [26] [23]
V_6Si_5	*Immm*	0.4858	1.5966	0.7501	[16] Incorrect structure type

1667-459 [14]	Nb_6Sn_5				
$(Ta_xV_{1-x})_6Si_5$	*Ibam* V_6Si_5	0.7625(5) 0.7643(7)	1.609(1) 1.6078(5)	0.4936(3) 0.4939(5)	$x_{1200°C}$ = 0.333 [6] x_{max}[1]= 0.367, [This work]
V_6Si_5		0.7501	1.5966	0.4858	x = 0, [17]
1667-459 [14]		0.7501	1.5966	0.4858	x = 0, [18]
τ_1-$(Ta_xV_{1-x})_5Si_3$	*P6₃/mcm* Mn_5Si_3	0.7258(6) 0.71976-0.73914		0.4926(3) 0.48906-0.50135	$Ta_{1.5}V_{3.5}Si_3$ [4] $0.0816 \le x_{1500°C} \le 0.614$
τ_2-Ta_2V_3Si	*P6₃/mmc* $MgZn_2$	0.500(3) 0.505		0.826(0) 0.823	[3] Annealed at 1000 °C [4]
τ_3-$Ta(Ta_xV_{1-x-y}Si_y)_2$	*Fd-3m* $MgCu_2$	0.71510(1)			Annealed at 1500 °C [This work]

[1] Maximal solubility at 1500°C

9.3.2. Crystal structure of τ_2-Ta(Ta,V,Si)₂ (MgZn₂-type Laves phase)

A ternary compound with the $MgZn_2$-type structure was reported by E. Gangelberger [3] and R. Mittal [4] at 1000 °C to be present in a sample with the nominal composition Ta_2V_3Si for which R. Mittal [4] also reported small amounts of secondary phases. However, only the lattice parameters were published for this phase. Our sample with composition Ta_2V_3Si annealed at 1500 °C turned out to be three-phase as it contains τ_1-$(Ta_xV_{1-x})_5Si_3$ (Mn_5Si_3 type) and $(Ta_xV_{1-x})_3Si$ as secondary phases, but lattice parameters for the Laves phase (labeled τ_2, a = 0.50158(2), c = 0.82642(3) nm) are close to the values given by E. Gangelberger [3] [a = 0.500, c = 0.826 nm] and R. Mittal [4] [a = 0.505, c = 0.823 nm].

Systematic extinctions for a single crystal selected from this sample prompted the space group types *P6₃/mmc, P-62c* and *P6₃mc*. As practically identical solutions were found, we describe the structure in the space group with highest symmetry *P6₃/mmc* (194). Structural refinement results in a solution with R-factor R_{F2}=0.015 and negligible residual electron densities (1.36, -1.40 e⁻/Å³). Table 2 comprises the results of the single crystal refinement. Sites 4*f* and 6*h* are fully occupied by Ta and V, respectively, whereas ADP's (atom displacement parameters) for site 2*a*, however, indicate a statistical mixture. A statistical mixture of only two atoms (V and Si) on this site resulted in a significant deviation of the composition by a deficiency of about 4 at. % Si from the EPMA data. This simple model could furthermore not explain the homogeneity region of the τ_2-phase revealing a Ta content of more than 33.3 at. %, which clearly suggested that Ta should be present at sites 2*a* or 6*h* in addition to the 4*f* site. Ta in site 6*h* was not accepted by the refinement. However, when Ta was introduced to the 2*a* site, the amount of Si increased. Therefore we fixed the Si content in this site according to the EPMA data and refined the

130

occupation of Ta and V. The final composition from single crystal refinement, $Ta_{33.9}V_{53.8}Si_{12.3}$, is in good agreement with EPMA ($Ta_{34.4}V_{53.3}Si_{12.3}$). Furthermore, the structure solution obtained, $Ta_2V_3(Ta,V,Si)_1$, fits well with the X-ray powder diffraction data. Figure 1 presents the coordination polyhedra for the τ_2-phase.

Table 2a: X-ray single crystal data for τ_2-$Ta_2V_3(Ta_{0.034}V_{0.228}Si_{0.738})$, $2°\leq2\Theta\leq70°$; ω-scans, scan width 2°, 150 sec/frame and results of Rietveld refinement of τ_1 and τ_3. All structures are standardized with program *Structure Tidy* [27]. Anisotropic displacement parameters are in $10^2 nm^2$.

Parameter/compound	τ_1	τ_2	τ_3
Method	XPD (Cu Kα1)	XSC (Mo Kα)	XPD (Cu Kα1)
Structure type	Mn_5Si_3	$MgZn_2$	$MgCu_2$
Space Group	$P6_3/mcm$, #193	$P6_3/mmc$, #194	Fd-$3m$, #227
Composition from EPMA	$Ta_{19.0}V_{43.5}Si_{37.5}$[1]	$Ta_{34.4}V_{53.3}Si_{12.3}$	$Ta_{36.1}V_{60.0}Si_{3.9}$
Composition from refinement	$Ta_{18.0}V_{44.5}Si_{37.5}$	$Ta_{33.9}V_{53.8}Si_{12.3}$	$Ta_{36.3}V_{59.8}Si_{3.9}$
Formula from refinement	$(Ta_xV_{1-x})_5Si_3$, x = 0.288	$Ta(Ta_xV_{1-x-y}Si_y)_2$, x = 0.009, y = 0.184	$Ta(Ta_xV_{1-x-y}Si_y)_2$, x = 0.022, y = 0.030
a (nm)	0.72545(2)	0.50158(2)	0.71510(1)
b (nm)	0.72545(2)	0.50158(2)	0.71510(1)
c (nm)	0.49259(1)	0.82642(3)	0.71510(1)
Reflections in refinement	60	188≥4σ(F_o) of 195	18
Mosaicity	-	0.51	-
Number of variables	19	16	19
$R_F = \Sigma|F_0-F_c|/\Sigma F_0$	0.033	-	0.058
$R_B = \Sigma|I_0-I_c|/\Sigma I_0$	0.029	-	0.038
$R_{wP}=[\Sigma w_i|y_{0i}-y_{ci}|^2/\Sigma w_i|y_{0i}|^2]^{1/2}$	0.032	-	0.046
$R_P = \Sigma|y_{0i}-y_{ci}|/\Sigma|y_{0i}|$	0.025	-	0.035
$R_e = [(N-P+C)/\Sigma w_i y_{0i}^2]^{1/2}$	0.013	-	0.021
$\chi^2 = (R_{wP}/R_e)^2$	7.76	-	4.80
$R_F^2 = \Sigma|F_0^2-F_c^2|/\Sigma F_0^2$	-	0.015	-
R_{Int}	-	0.016	-
wR2	-	0.035	-
GOF	-	1.204	-
Extinction (Zachariasen)	-	0.0037(6)	-
Residual density e⁻/$Å^3$; max; min.	-	1.36; -1.40	-
Atom parameters			
Atom site 1	4d (⅓, ⅔, 0);	2a (0, 0, 0);	8b (⅜, ⅜, ⅜);
Occ.	1.00 V	0.033(4) Ta + 0.226 V + 0.741 Si[2]	1.00 Ta
$U_{11}=U_{22}$; U_{33}	-	0.0050(7); 0.0052(9)	-
$U_{23}=U_{13}=0$, U_{12}	B_{iso} = 0.653	0.0025(4)	B_{iso} = 0.693
Atom site 2	6g (x, 0, ¼)	4f (⅓, ⅔, z)	16c (0, 0, 0)
Occ.	0.48(3) Ta + 0.52 V	1.00 Ta	0.044(3) Ta + 0.897 V + 0.059 Si[2]
x, z;	x = 0.23805(6)	z = 0.56126(4)	-
$U_{11}=U_{22}$; U_{33}	-	0.0045(1); 0.0039(1)	-
$U_{23}=U_{13}=0$, U_{12}	B_{iso} = 0.714	0.0023(1)	B_{iso} = 0.621
Atom site 3	6g (x, 0, ¼);	6h (x, 2x, ¼);	-
Occ.	1.00 Si	1.00 V	-
x;	0.5943(2)	0.1707(1)	-
U_{11}; U_{22}; U_{33}	-	0.0040(3); 0.0030(4)	-
$U_{23}=U_{13}=0$, U_{12}	B_{iso} = 0.725	0.0015(2)	-

[1] Composition from graph in Fig. 4.
[2] Si content fixed after EMPA.

Table 2b: Interatomic distances (nm) for $Ta_2V_3(Ta_{0.034}V_{0.228}Si_{0.738})$ from XSC. Standard deviation ≤0.0001.

Ta–	3V	0.2935		−1Ta	0.3120		−2Ta	0.2935

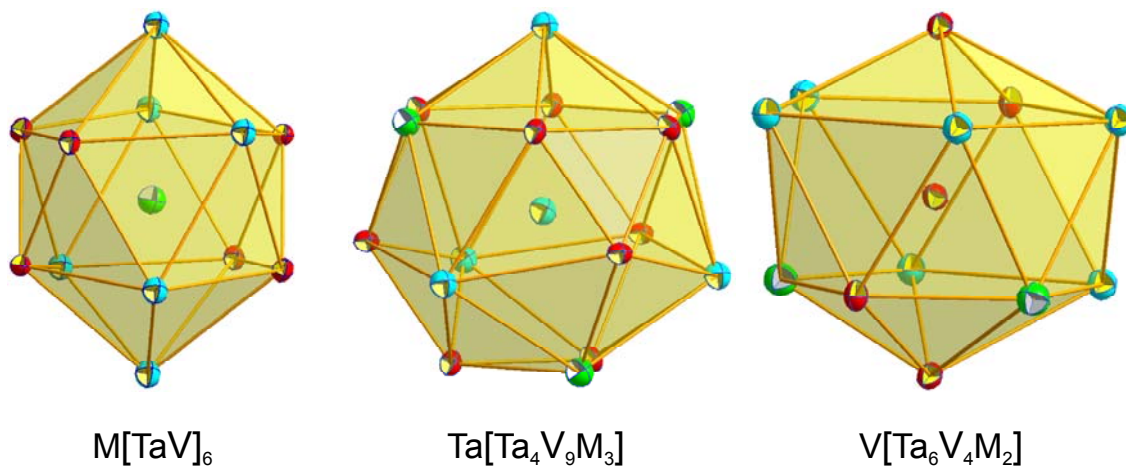| CN = 16	–3M	0.2940	V–	2V	0.2448		–4Ta	0.2954
	–6V	0.2954	CN = 12	–2M	0.2543	M–	6V	0.2543
	–3Ta	0.3068		–2V	0.2568	CN = 12	–6Ta	0.2940

M[TaV]$_6$ Ta[Ta$_4$V$_9$M$_3$] V[Ta$_6$V$_4$M$_2$]

Fig. 1. Coordination polyhedra of τ_2-Ta(TaVSi)$_2$ showing atoms with anisotropic displacement parameters from X-ray single crystal refinement. Green (gray in black & white) shows the mixed position occupied by Ta, V and Si atoms; blue (white in black & white) represents Ta atoms and red (black in black & white) represents V atoms.

9.3.3. Rietveld refinements of τ_3-Ta(Ta$_x$V$_{1-x-y}$Si$_y$)$_2$ (MgCu$_2$-type) and τ_1-(Ta$_x$V$_{1-x}$)$_5$Si$_3$ (Mn$_5$Si$_3$-type)

Detailed inspection of the phase equilibria at 1500 °C revealed a Laves phase with MgCu$_2$ type (τ_3-phase). The Rietveld refinement of the X-ray powder spectrum of the alloy Ta$_{36.1}$V$_{60.0}$Si$_{3.9}$ (EPMA, at. %) in Fig. 2 confirms the τ_3-phase in equilibrium with the solid solution (Ta,V) and with traces of τ_2. The refinement shows that the 16c site is shared by all three elements Ta, V and Si, whilst the 8b site is fully occupied by Ta only (Table 2). Thus the Si content was fixed and Ta and V amounts were refined for this site. Compositions obtained from the refinement (Ta$_{36.3}$V$_{59.8}$Si$_{3.9}$) and from EPMA (Ta$_{36.1}$V$_{60.0}$Si$_{3.9}$) are in good agreement with each other.

X-ray intensities of a powder spectrum of (Ta$_{0.3}$V$_{0.7}$)$_5$Si$_3$ (Ta$_{1.5}$V$_{3.5}$Si$_3$, Mn$_5$Si$_3$ type) were reported by J. Steinmetz et al. [5] to be consistent with a statistical mixture of 3 Ta and 3 V atoms sharing the 6g position, however, no further structural details were given. Our Rietveld X-ray powder data refinement (see Fig. 3) of a sample with composition Ta$_{20}$V$_{40}$Si$_{40}$ [τ_1-phase; (Ta$_{0.3}$V$_{0.7}$)$_5$Si$_3$] confirmed the Mn$_5$Si$_3$ type as well as the preferred partial occupation of the 6g-

site by Ta-atoms. Mn_5Si_3 type phases are known to be stabilized by various impurities (B, C, O etc.) and therefore were frequently observed in Ta-Si and V-Si binary systems by several research groups [28,29,30,31]. In the present study, we did not encounter this phase in binary samples, however, the τ_1-$(Ta_xV_{1-x})_5Si_3$ phase with Mn_5Si_3 type was clearly obtained in ternary alloys.
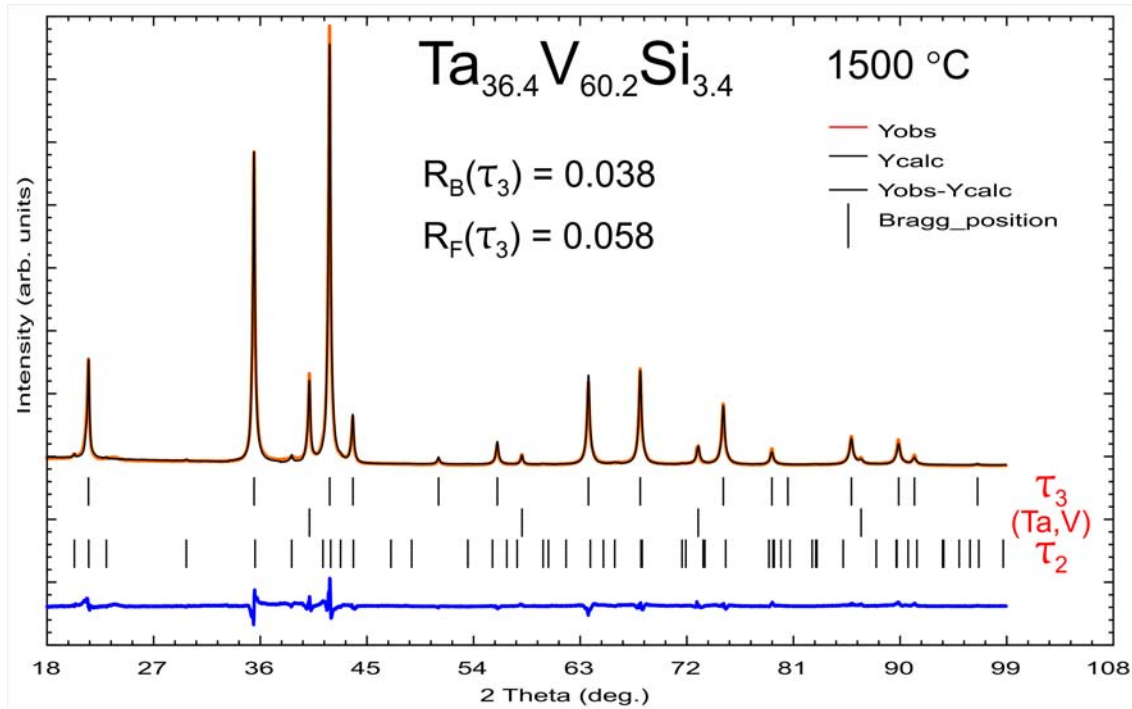

Fig. 2. Refinement of $Ta_{36.4}V_{60.2}Si_{3.4}$ (alloy annealed at 1500 °C; composition from EPMA in at. %); equilibrium between τ_3-$(Ta_{36.1}V_{60.0}Si_{3.9})$ + $(Ta_{50.3}V_{49.7})$ + τ_2 (traces).

Rietveld refinement of the τ_1-phase; $(Ta_{0.3}V_{0.7})_5Si_3$ did not reveal any significant residual electron density in the sites for the octahedral voids in $2b$ (0, 0, 0) excluding contamination. Furthermore, the interatomic distances from the centre of these voids are unfavourable for the incorporation of Si/V atoms ($d_{2b\text{-metal}}$= 0.212153 nm) in terms of a Ti_5Ga_4-type [32] and EPMA for this phase measured on various alloys confirms the metal/Si ratio $(Ta_xV_{1-x})_5Si_3$ ±1 at.%. It can thus be safely assumed that the τ_1-$(Ta_xV_{1-x})_5Si_3$ phase is a truly ternary phase with stoichiometry M_5Si_3. Table 2 summarizes the structural parameters for τ_1-$(Ta_{0.3}V_{0.7})_5Si_3$.

The τ_1-phase exhibits a large homogeneity region extending at 1500 °C from $Ta_{5.1}V_{57.4}Si_{37.5}$ (at. %) to $Ta_{38.5}V_{24.0}Si_{37.5}$ (at. %). It is interesting to note that the Ta-rich solubility limit at 1500 °C

133

practically coincides with a full occupation of Ta in the 6g site yielding the ordered composition Ta$_3$V$_2$Si$_3$ (Ta$_{37.5}$V$_{25}$Si$_{37.5}$ at. %). It must be noted that the amount of Ta for this phase in the as cast samples, however, exceeds the stoichiometric limit for a fully ordered composition Ta$_3$V$_2$Si$_3$. Refinement for alloys on the Ta-rich side of the homogeneity region showed Ta entering the 4d site after complete replacement of V by Ta in the 6g site.
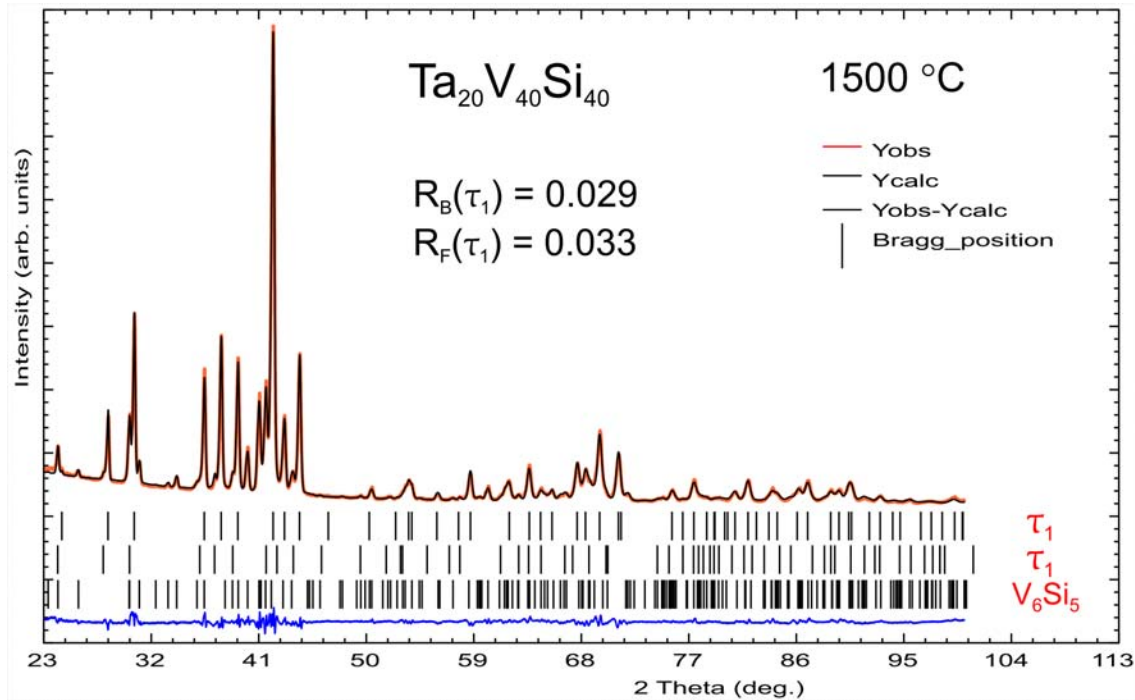

Fig. 3. Refinement of Ta$_{20}$V$_{40}$Si$_{40}$ (alloy annealed at 1500 °C after repeated grinding and compacting; EPMA in at. %). τ_1-phase shows two lattice parameters due to initial inhomogeneity of the as cast sample, which did not disappear even after repeated grinding, compacting and annealing.

9.3.4. Isothermal section of the Ta-V-Si system at 1500 °C

Although the MgCu$_2$ type Laves phase is not present in the Ta-V binary system at 1500 °C, it was observed in the Ta-V-Si ternary at this temperature with a rather small homogeneity range (~ 3 to 4 at. % Si content and 1 to 2 at. % Ta/V exchange). This phase (τ_3) is clearly separated from the binary system revealing a two-phase equilibrium with the Si-saturated solid solution of (Ta,V). In view of the existence of binary TaV$_2$ with MgCu$_2$-type far below 1500 °C, the small amounts of Si are conceived to significantly increase the stability of the cubic Laves phase.

134

Both, E. Ganglberger et al. [3] and R. Mittal et al. [4] reported the composition Ta_2V_3Si for the τ_2-phase with $MgZn_2$-type at 1000 °C. At 1500 °C we observed τ_2 with a considerable homogeneity region from ~ 8 to 12 at. % Si and from ~ 34 to 37 at. % Ta, however, excluding the stoichiometric composition Ta_2V_3Si.
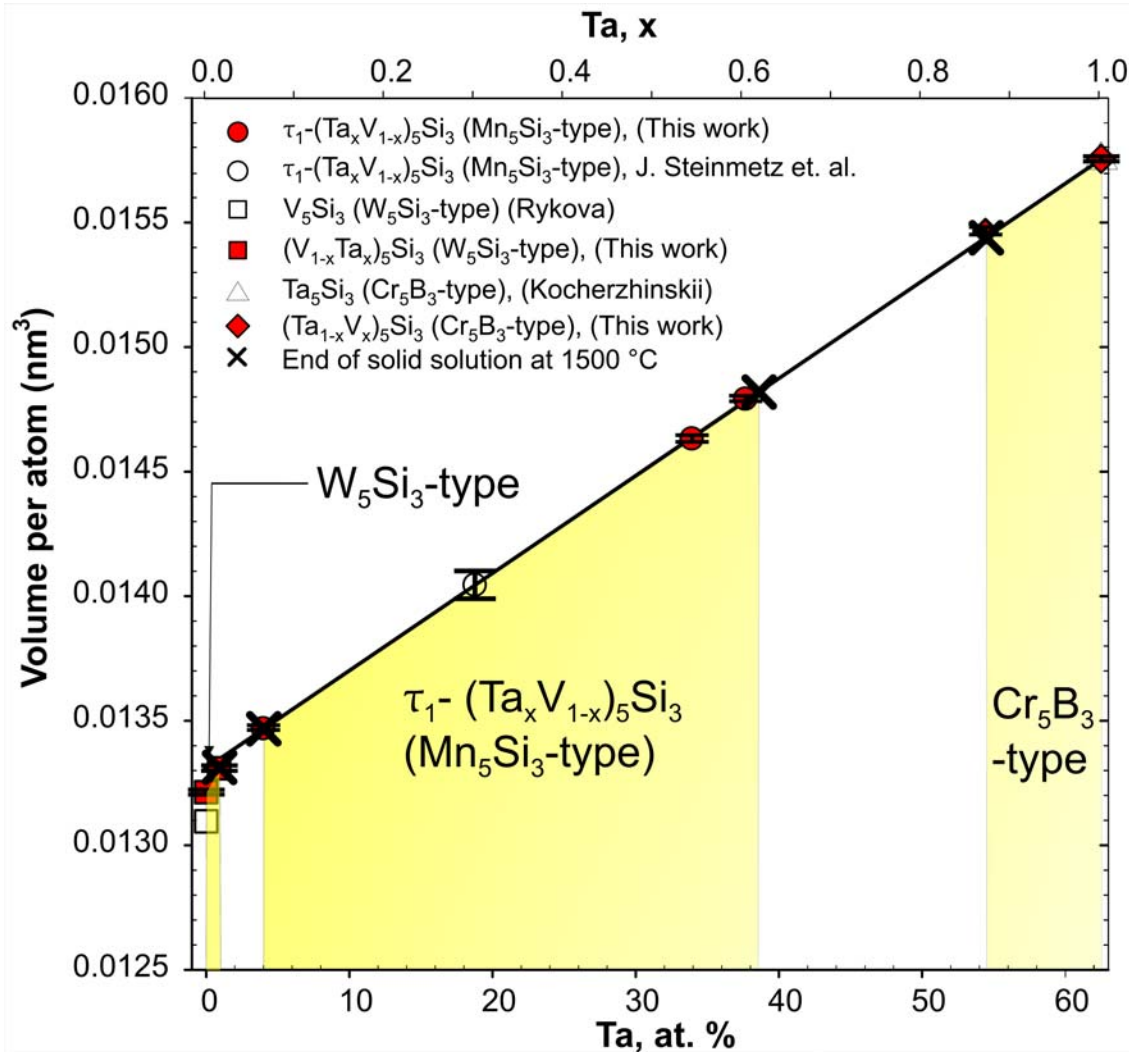

Fig. 4. Volume per atom (nm^3) vs composition for the section $(Ta_xV_{1-x})_5Si_3$. Data for τ_1-$(Ta_xV_{1-x})_5Si_3$ (Mn_5Si_3 type) given by J. Steinmetz et al. [5], for binary V_5Si_3 (W_5Si_3-type) given by M. Rykova et al. [26] and for Ta_5Si_3 (Cr_5B_3-type) given by Y. Kocherzhinskii et al [23] are also shown.

At 1500 °C τ_1-$(Ta_xV_{1-x})_5Si_3$ exists in a large homogeneity region extending from $Ta_4V_{58.5}Si_{37.5}$ (x=0.064) to $Ta_{39}V_{23.5}Si_{37.5}$ (x=0.624). The compositional dependences for the average volume per atom for the solutions along the isopleth Ta_5Si_3-V_5Si_3 with Mn_5Si_3-, W_5Si_3- and Cr_5B_3-types

show almost linear dependence (Fig. 4) and agree well with the data of J. Steinmetz et al. [5] for τ_1-$(Ta_{0.3}V_{0.7})_5Si_3$ (Mn_5Si_3-type).

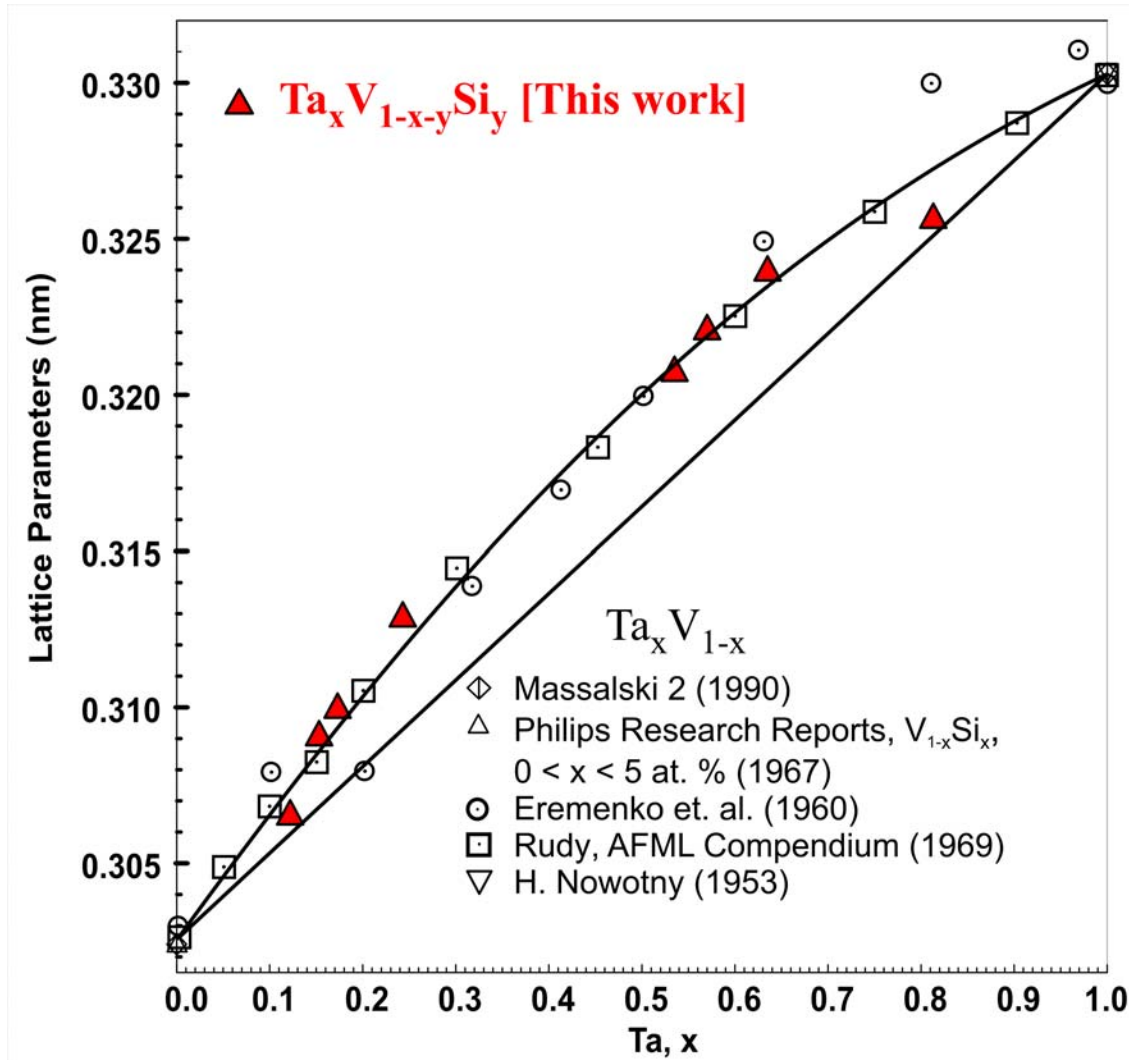Fig. 5. Compositional dependence for lattice parameters of the ternary $Ta_xV_{1-x-y}Si_y$ and binary Ta_xV_{1-x} phase; filled symbols [this work] and open symbols from refs. [8,19,20,21,30].

Lattice parameters as a function of composition for the binary (Ta_xV_{1-x}) and ternary ($Ta_xV_{1-x-y}Si_y$) are presented in Figure 5. Literature data for binary (Ta_xV_{1-x}) [19,20] are close to lattice parameters determined for the ternary Si-saturated (Ta,V)-solid solution ($Ta_xV_{1-x-y}Si_y$). The dependences (Fig. 4 and 5) are used to determine the composition of the phases via their lattice parameters in those samples for which EPMA was difficult to perform (powdered and sintered samples) and thereby help to define the extent of the three solid solutions in the isopleth Ta_5Si_3-

V5Si3. The continuous solid solution between TaSi2 and VSi2 phase, reported by H. Nowotny et al. [2] at 1300 °C, is confirmed to exist at 1500 °C.

A phase with unknown structure type and with a composition ranging from Ta47V37Si16 to Ta49.5V32.5Si18 (at. %) was observed in as cast samples, but it disappears after continuous grinding, compacting and annealing of these samples and thus is not present at 1500 °C.
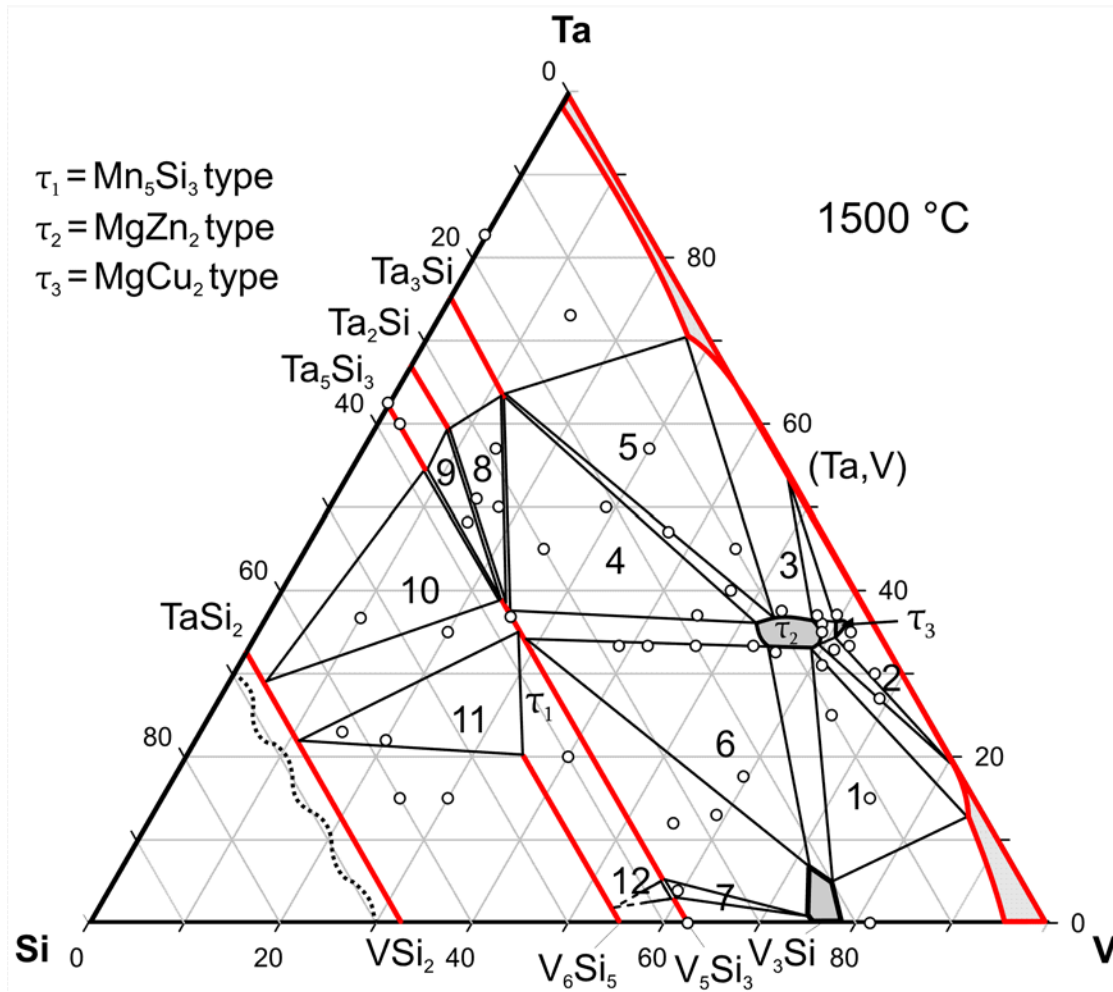

Fig. 6. Isothermal section of Ta-V-Si system at 1500 °C. Sample location is shown by open circles. Numbs in three-phase fields relate to the numbering in Table 3.

Figure 6 shows the isothermal section of the Ta-V-Si system at 1500 °C. Composition of vertices and the phases found in all triangles are summarized in Table 3. The numbering shown in the isothermal section in Figure 6 corresponds to the same numbers for the three-phase regions listed in Table 3.

137

Table 3: Data on alloys for three-phase regions in the Ta-V-Si system at 1500 °C.

Three phase regions	Phase	Structure type	Lattice parameters (nm)			Composition (at. %)		
			a	b	c	Ta	V	Si
τ_2 + $(Ta_xV_{1-x})_3Si$ + (Ta,V) (1)[1]	τ_2	$MgZn_2$	0.50215(6)	-	0.82102(4)	33.9	58.1	8.0
	$(Ta_xV_{1-x})_3Si$	Cr_3Si	0.47525(4)	-	-	4.5	75.1	20.4
	(Ta,V)	W	0.30656(5)	-	-	13.0	85.0	2.0
τ_2 + τ_3 + (Ta,V) (2)	τ_2	$MgZn_2$	0.50321(6)	-	0.82668(8)	34.6	60.3	5.1
	τ_3	$MgCu_2$	0.71279(2)	-	-	34.4	58.8	6.8
	(V,Ta)	W	0.30976(14)	-	-	18.4	80.3	1.3
τ_2 + τ_3 + (Ta,V) (3)	τ_2	$MgZn_2$	0.50586(7)	-	0.82555(15)	37.8	57.2	5.0
	τ_3	$MgCu_2$	0.71559(6)	-	-	37.5	58.3	4.2
	(Ta,V)	W	0.32076(6)	-	-	53.5	46.5	0.0
τ_1 + τ_2 + $(Ta_xV_{1-x})_3Si$ (6)	τ_2	$MgZn_2$	0.50099(3)	-	0.82565(9)	34.5	53.0	12.5
	τ_1	Mn_5Si_3	0.73615(5)	-	0.49888(6)	33.7	28.8	37.5
	$(Ta_xV_{1-x})_3Si$	Cr_3Si	0.47554(1)	-	-	6.8	71.9	21.3
τ_1 + $(Ta_xV_{1-x})_5Si_3$ + $(Ta_xV_{1-x})_3Si$ (7)	τ_1	Mn_5Si_3	0.71986(7)	-	0.48936(6)	5.1	57.4	37.5
	$(Ta_xV_{1-x})_5Si_3$	W_5Si_3	0.94674(7)	-	0.47752(6)	3.0	59.5	37.5
	$(Ta_xV_{1-x})_3Si$	Cr_3Si	-	-	0.47285(3)	0.6	74.2	25.2
τ_2 + $(Ta_xV_{1-x})_3Si$ + (Ta,V) (5)	τ_2	$MgZn_2$	0.50261(3)	-	0.82736(3)	37.1	52.8	10.1
	$(Ta_{1-x}V_x)_3Si$	Ti_3P	1.01128(6)	-	0.51351(7)	63.0	12.0	25.0
	(Ta,V)	W	0.32340(1)	-	-	69.0	31.0	0.0
τ_1 + τ_2 + $(Ta_{1-x}V_x)_3Si$ (4)	τ_1	Mn_5Si_3	0.73792(8)	-	0.50176(7)	37.7[2]	24.8	37.5
	τ_2	$MgZn_2$	0.50171(7)	-	0.82587(6)	34.9	52.4	12.7
	$(Ta_{1-x}V_x)_3Si$	Ti_3P	1.00903(9)	-	0.51276(9)	63.0	12.0	25.0
τ_1 + $(Ta_{1-x}V_x)_2Si$ + $(Ta_{1-x}V_x)_3Si$ (8)	τ_1	Mn_5Si_3	0.73912(9)	-	0.50100(9)	38.4	24.1	37.5
	$(Ta_{1-x}V_x)_2Si$	$CuAl_2$	0.61454(7)	-	0.50431(7)	58.5	8.2	33.3
	$(Ta_{1-x}V_x)_3Si$	Ti_3P	-	-	-	62.9	12.1	25.0
τ_1 + $(Ta_{1-x}V_x)_2Si$ + $(Ta_{1-x}V_x)_5Si_3$ (9)	τ_1	Mn_5Si_3	0.73914(7)	-	0.50135(9)	39.0[2]	23.5	37.5
	$(Ta_{1-x}V_x)_2Si$	$CuAl_2$	0.61352(6)	-	0.50343(8)	58.6	8.1	33.3
	$(Ta_{1-x}V_x)_5Si_3$	Cr_5B_3	0.64430(7)	-	1.19154(9)	54.5[2]	8.0	37.5
τ_1 + $(Ta_{1-x}V_x)_5Si_3$ + $(Ta_{1-x}V_x)Si_2$ (10)	τ_1	Mn_5Si_3	0.73834(9)	-	0.50233(8)	38.6[2]	23.9	37.5
	$(Ta_{1-x}V_x)_5Si_3$	Cr_5B_3	0.64308(6)	-	1.19042(8)	54.5[2]	8.0	37.5
	$(Ta_{1-x}V_x)Si_2$	$CrSi_2$	0.47585(3)	-	0.65492(9)	29.8[2]	3.5	66.7
τ_1 + $(Ta_xV_{1-x})_6Si_5$ + $(Ta_{1-x}V_x)Si_2$ (11)	τ_1	Mn_5Si_3	0.73781(7)	-	0.49995(6)	35.0[2]	27.5	37.5
	$(Ta_xV_{1-x})_6Si_5$	V_6Si_5	0.76214(8)	1.60989(8)	0.49380(5)	20.0	35.0	45.0
	$(Ta_{1-x}V_x)Si_2$	$CrSi_2$	0.47202(8)	-	0.65125(7)	22.0[2]	11.3	66.7
τ_1 + $(Ta_xV_{1-x})_6Si_5$ + $(Ta_xV_{1-x})_5Si_3$ (12)	τ_1	Mn_5Si_3	0.71976(5)	-	0.48906(7)	5.1	57.4	37.5
	$Ta_xV_{1-x})_6Si_5$	V_6Si_5	-	-	-	2.5[3]	52.0	45.5
	$Ta_xV_{1-x})_5Si_3$	W_5Si_3	0.94624(5)	-	0.47732(5)	3.0	59.5	37.5

[1] Corresponding no. of triangles shown in isothermal section at 1500 °C in Fig. 6.

[2] Composition of phases evaluated from Fig. 4,5.

[3] Estimated value for triangle, which is dotted in the isothermal section at 1500 °C.
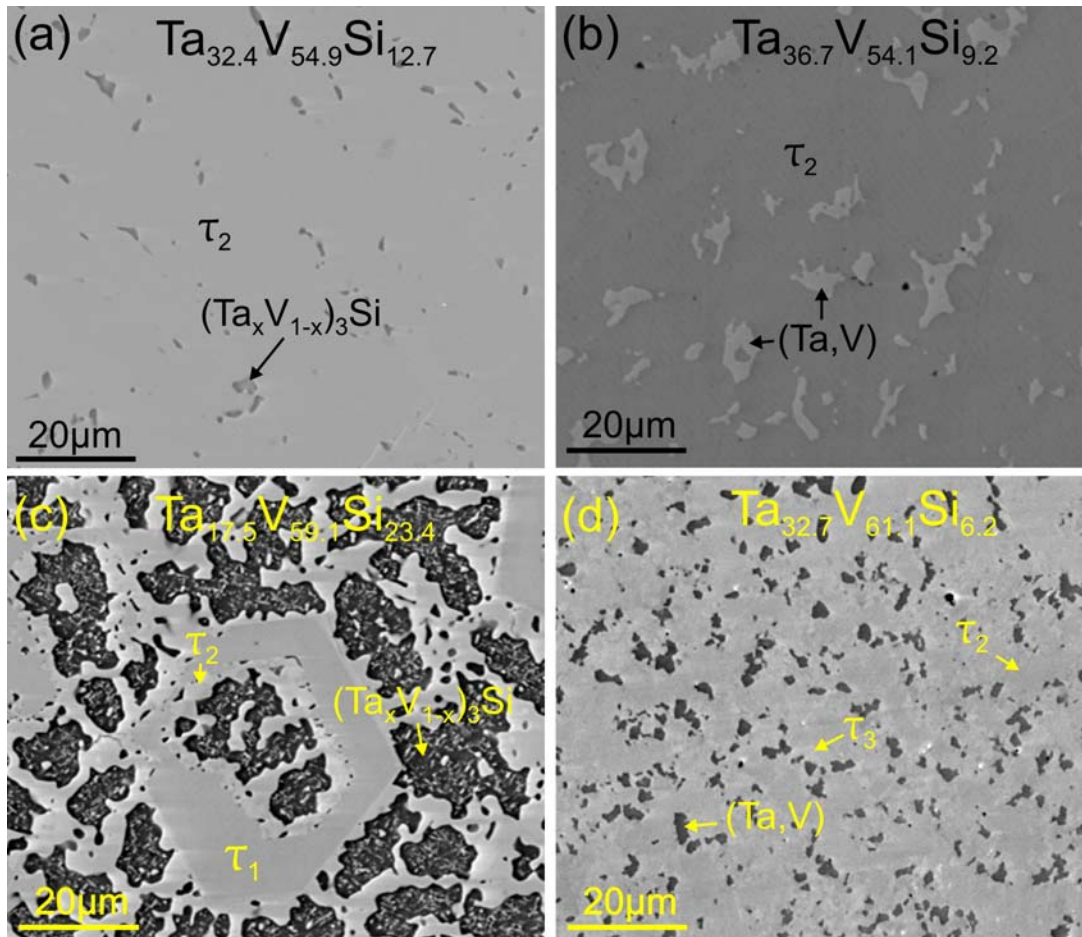
138

Fig. 7. Micrographs of selected samples annealed at 1500 °C. (a) $Ta_{32.4}V_{54.9}Si_{12.7}$; τ_2 + $(Ta_xV_{1-x})_3Si$, (b) $Ta_{36.7}V_{54.1}Si_{9.2}$; τ_2 + (Ta,V), (c) $Ta_{17.5}V_{23.4}Si_{59.1}$; τ_1 + τ_2 + $(Ta_xV_{1-x})_3Si$ and (d) $Ta_{32.7}V_{61.1}Si_{6.2}$; τ_2 + τ_3 + (Ta,V).

Figure 7 shows the micrographs of selected samples annealed at 1500 °C. Figure 7a represents $Ta_{32.4}V_{54.9}Si_{12.7}$ which shows a two-phase equilibrium between τ_2 + $(Ta_xV_{1-x})_3Si$. Figure 7b also represents a two-phase equilibrium between τ_2 + (Ta,V) in $Ta_{36.7}V_{54.1}Si_{9.2}$. A three-phase equilibrium τ_1 + τ_2 + $(Ta_xV_{1-x})_3Si$ was obtained in the sample with composition $Ta_{17.5}V_{59.1}Si_{23.4}$ (Fig. 7c). Another three-phase equilibrium was observed among τ_2 + τ_3 + (Ta,V) in alloy $Ta_{32.7}V_{61.1}Si_{6.2}$ (Fig. 7d). Equilibrium among $(Ta_xV_{1-x})_6Si_5$ + τ_1 + $(Ta_{1-x}V_x)Si_2$ was finally achieved by continuous grinding, compacting and annealing. Due to the impossibility to employ EPMA on sinter-bodies, the compositions at the vertices of the three-phase equilibrium were defined via lattice parameters using the graph in Fig. 4 for τ_1 and the graph reported by H.

Nowotny et. al. [2] for $(Ta_{1-x}V_x)Si_2$. The composition of the $(V_{1-x}Ta_x)_6Si_5$ phase was reliably measured by EPMA along with the lattice parameters.

9.3.5. Isothermal section of the Ta-V-Si system at 1200 °C

Our main focus at 1200 °C was on the homogeneity region of the two Laves phases, τ_2 and τ_3, and their connection with the binary Ta-V system. Savitskii et al. [10] showed the presence of two corresponding binary Laves phases: TaV_2 with $MgCu_2$-type for the low-temperature form and with the $MgZn_2$-type for the high-temperature modification.
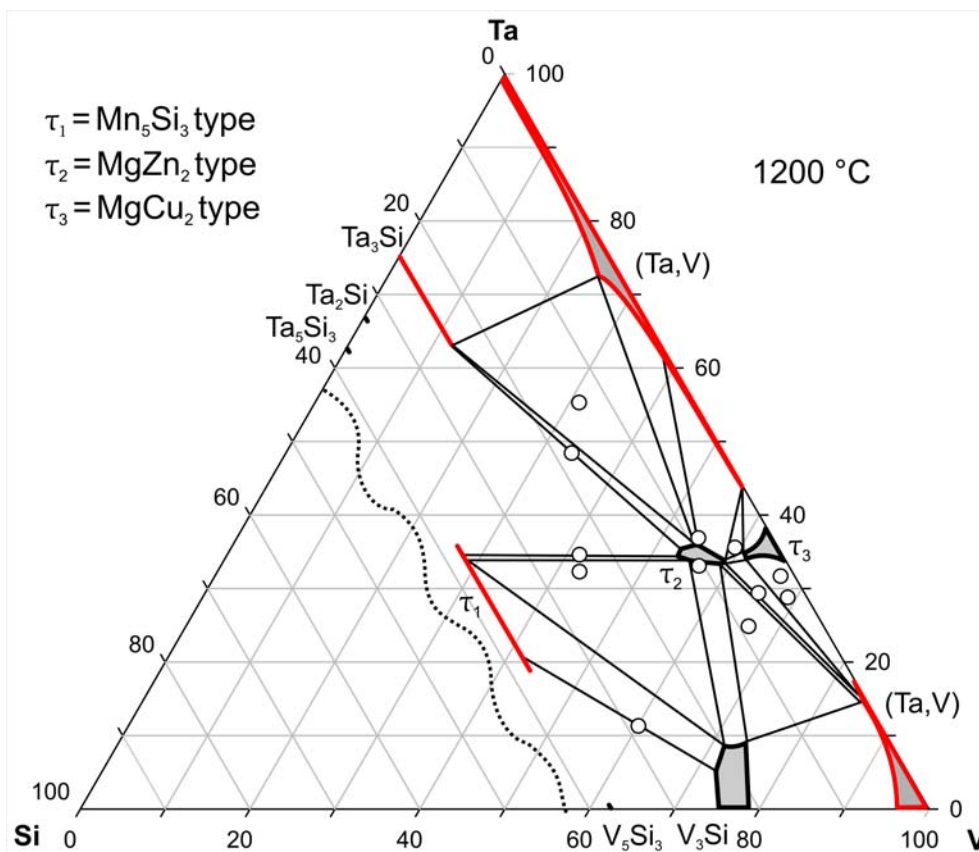

Fig. 8. Isothermal section of the Ta-V-Si system at 1200 °C. Sample location is shown by open circles.

The Ta-V phase diagram calculated by Pavlu et al. [11] refers to this data. However, we could not find any connection of τ_2 present in the ternary Ta-V-Si system with the corresponding isotypic binary Ta-V phase. In fact, our binary Ta,V-samples annealed at 1200 °C did not reveal

any presence of the hT-MgZn$_2$-type Laves phase (see also section "Binary boundary systems"). The partial isothermal section based on our results is shown in Figure 8. τ_2 has a rather small homogeneity region at 1200 °C as compared to it's extent at 1500 °C but τ_2 is still present in equilibrium with τ_1 and (Ta$_x$V$_{1-x}$)$_3$Si. However, τ_3 is connected with the Ta-V binary and exhibits a solubility of Si up to ~ 4 at. %. τ_3 is present in equilibrium with (Ta,V) on both sides in contrast to the isothermal section at 1500 °C where a continuous solid solution was observed between Ta and V and τ_3 was observed as truly ternary phase without any connection to the binary Ta-V section.

Both isothermal sections experimentally evaluated at 1500 °C and 1200 °C are in good agreement with the thermodynamically calculated isothermal sections [34].
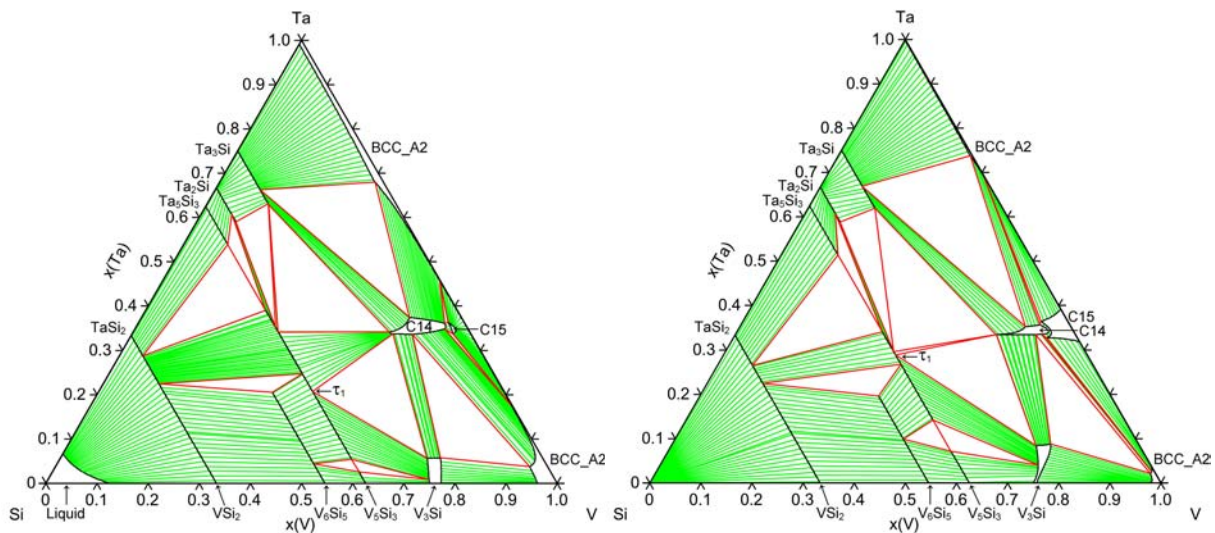

Fig. 9. Calculated phase diagrams of the Ta-V-Si system at 1500 °C (left) and 1200 °C (right) [34].

9.4. Conclusion

Phase relations in the Ta-V-Si system have been evaluated for the isothermal sections at 1500 °C and 1200 °C revealing three ternary phases: τ_1-(Ta,V)$_5$Si$_3$ (Mn$_5$Si$_3$-type) and the Laves phases τ_2-Ta(Ta,V,Si)$_2$ (MgZn$_2$-type) and τ_3-Ta(Ta,V,Si)$_2$ (MgCu$_2$-type). The crystal structures of the three phases were solved by single crystal diffraction (τ_2) or from X-ray powder diffraction data (τ_1 and τ_3). The homogeneity region at 1200 °C and 1500 °C obtained for the τ_2-phase does not include the stoichiometric composition Ta$_2$V$_3$Si. Although the τ_2-phase does not exist in the

binary Ta-V system at 1500 °C, it is present in the ternary system at this temperature. A large homogeneity range was found for τ_1-$(Ta_xV_{1-x})_5Si_3$ with Mn_5Si_3-type showing the exchange of Ta and V at a constant Si content. At 1500 °C, the end points of the τ_1-phase solution ($0.064{\leq}x{\leq}0.624$) are in equilibrium with $(Ta_{1-x}V_x)_5Si_3$ (Cr_5B_3 type, $0{\leq}x{\leq}0.128$) and with $(Ta_xV_{1-x})_5Si_3$ (W_5Si_3 type, $0{\leq}x{\leq}0.016$).

References

[1] J.J. English, AD 407987, Defense Documentation Center for Scientific and Technical information, **1** (1963).

[2] H. Nowotny, E. Dimakopoulou and H. Kudielka, Mh. Chem. **88** (1957), p. 180-192.

[3] E. Ganglberger, H. Nowotny and F. Benesovsky, Monatshefte für Chemie **96(5)** (1965), 1658-60.

[4] R.C. Mittal, S.K. Si and K.P. Gupta, Journal of Less Common Metals **60** (1978), 75-82.

[5] J. Steinmetz and B. Roques, C. R. Acad. Sc. Paris, Serie C, **283** (1976), p. 633-635.

[6] J. Steinmetz and B. Roques, Journal of Less-Common Metals **52** (1977), 247-258.

[7] N.Y. Alekseyevskiy, N.Y. Ageyev and V.F. Shamray, Physics of Metals and Metallography, translated from Fizika Metallov, Metallovedenie **43** (1977), p. 42-48.

[8] Binary Alloy Phase Diagrams, Second Edition, Ed. T.B. Massalski, ASM International, Materials Park, Ohio, **3**, (1990), p. 3364-3366.

[9] A.P. Nefeolov, E.M. Sokolovskaya, A.T. Grigor'ev, V.I. Chechernikov, I.G. Sokolova and L.S. Guzei, Vestnik Moskovskogo Universiteta, Seriya 2: Khimiya (1965), Issue 5, p. 42-47.

[10] E.M. Savitskii, J.V. Efimov, Monatshefte für Chemie **103** (1972), 270-287.

[11] J. Pavlu, J. Vrestal, X. –Q. Chen and P. Rogl, CALPHAD: Computer Coupling of Phase Diagrams and Thermochemistry **35** (2011), p. 103-108.

[12] C.A. Danon, C. Servant, Journal of Alloys and Compounds **366** (2004) p. 191-200.

[13] Z. Guo, W. Yuan, Y. Sun, Z. Cai and Z. Qiao, Journal of Phase Equilibria and Diffusion **30(5)** (2009) p. 564-570.

[14] C. Zhang, Y. Du, W. Xiong, H. Xu, P. Nash, Y. Ouyang and R. Hu, Computer Coupling of Phase Diagrams and Thermochemistry **32** (2008) p. 320-325.

[15] H. Okamoto, Journal of Phase Equilibria and Diffusion **31(4)** (2010) p. 409-410.

[16] J. Hallais, J.P. Senateur and R. Fruchart, C. R. Acad. Sc. Paris, Serie C, **264** (1967), p. 1947-1950.

[17] P. Spinat, R. Fruchart and P. Herpin, Bull. Soc. Fr. Mineral. Cristallogr. **93** (1970), 23-36.

[18] J. Hallais, Ann. Chim. **6** (1971), 321-330.

[19] V.N. Eremenko, L.A. Tret'yachenko and R.I. Yakhimovich, Russian Journal of Inorganic Chemistry, translated from Zhurnal Neorganicheskoi Khimii **5** (1960), p. 1110-1112.

[20] E. Rudy, Compendium of Phase Diagram Data, published as Tech. Rep. AD 689, 843 (1969), available from NTIS as document No. AFML-TR-65-2, part V.

[21] H.A.C.M. Bruning, Philips Research Reports **22(4)** (1967), p. 349-354.

[22] H. Müller and K. Weymann, Journal of the Less-Common Metals **119** (1986), p. 115-126.

[23] Y.A. Kocherzhinskii, O.C. Kulik and E.A. Shishkin, Doklady Chemistry, translated from Doklady Akademii Nauk SSSR, **261** (1981), p. 464-465.

[24] J.C. Lasjaunias, O. Laborde, U. Gottlieb, R. Madar and O. Thomas, Journal of Low Temperature Physics **92** (1993), p. 335-351.

[25] K. Kanematsu, Transactions of the Japan Institute of Metals **27** (1986), p. 225-232.

[26] M.A. Rykova, A.V. Sabirzyanov and P.V. Gel'd, Inorganic Materials, translated from Izvestiya Akademii Nauk SSSR, Neorganicheskie Materialy **10** (1974), p. 122-123.

[27] L.M. Gelato and E. Parthé, J. Appl. Crystallogr. **20** (1987), p. 139-43.

[28] H. Nowotny and E. Laube, Planseeberichte für Pulvermetallurgie, **9** (1961), p. 54-59.

[29] H. Nowotny, B. Lux and H. Kudielka, Monatshefte für Chemie **87** (1956), p. 447-470.

[30] H. Nowotny, H. Schachner, R. Kieffer and F. Benesovsky, Mh. Chem. **84(1)** (1953), p. 1-12.

[31] E. Parthé, H. Nowotny and H. Schmid, Mh. Chem. **86** (1955), p. 385-396.

[32] P. Villars, K. Cenzual, Pearson's Crystal Data, ASM International, Ohio, USA, Release 2010/11.

[33] H. Nowotny, B. Lux, and H. Kudielka, Monatshefte fuer Chemie, 87 (1956), p. 447-470.

[34] A.U. Khan, P. Broz, H. Niu, J. Bursik, A. Grytsiv, X.-Q. Chen, G. Giester and P. Rogl, Submitted to Journal of Solid State Chemistry, (2011).

10. Phase relations and crystal structures in the system Ta-V-Ge

10.1. Introduction

In continuation of our interest in refractory metal-based ternary systems [1,2], which might be potential candidates for high temperature applications, we report here our investigation on the system Ta-V-Ge. We recently reported on the phase equilibria and crystal structures of the Ta-V-Si homologous system [2]. For Ta-V-Ge neither a Ta-Ge binary phase diagram exists nor have phase relations been evaluated for the ternary system, although formation and crystal structure of several binary Ta-Ge phases are known including the low temperature and high temperature modifications of Ta_3Ge [3]. The only information on the Ta-V-Ge concerns the $MgZn_2$ type Laves phase Ta_2V_3Ge reported by Ganglberger et al. [4] for which lattice parameters were derived but no structure refinement was made.

As there is no information available on the phase relations as well as the crystal structure of the ternary Ta-V-Ge system at any temperature, the present investigation intends to provide a comprehensive evaluation of the equilibria and crystal structures for the ternary phases in the Ta-V-Ge system.

10.2. Experimental details

Alloys were prepared (each of 1-2 grams) by argon arc melting from metal ingots of Ta, V and pieces of Ge all with purity higher than 99.9 mass % (Alfa Johnson Matthey GmbH, Germany) and were melted three times for homogenization (weight loss less than 0.1 %). As-cast alloys were annealed for 7-15 days at 1500 °C in a high vacuum furnace and then were radiation cooled. Lattice parameters and standard deviations were determined by least squares refinements of room temperature X-ray powder diffraction (XPD) data obtained from a Guinier-Huber image plate employing monochromatic Cu $K\alpha_1$ radiation with Ge as internal standard. Samples were polished using standard procedures and were examined by optical metallography and scanning electron microscopy (SEM). Composition of particular phases was measured using a JEOL JSM 6460 scanning electron microscope equipped with both energy- and wavelength dispersive X-ray

(EDX and WDX) analytical systems INCA Energy and INCA Wave by Oxford Instruments. An acceleration voltage of 20 kV was used. Pure elements served as standards to quantify. Finally the X-ray intensities were corrected for ZAF effects.

Transmission Electron Microscopy (TEM) was used to corroborate unit cell, symmetry and formation of superstructures. A Philips CM12 STEM transmission electron microscope was used at 120 kV with an EDAX energy dispersive X-ray (EDX) analyser and Phoenix software. Samples for TEM were prepared by crunching a piece of sample with nominal composition $Ta_{37.0}V_{54.0}Ge_{9.0}$, putting the powder in the ethanol and transferring it on a thin holey carbon film supported by a copper grid.

10.3. Results and discussion

10.3.1. Binary boundary systems

A critical assessment of V-Ge based alloys mainly focused on superconducting properties [5]. A thermodynamic modelling of the V-Ge system with some experimental work on two eutectics close to the V-rich and Ge-rich sides is due to Yuan et al. [6]. The homogeneity region for the V_3Ge phase is experimentally evaluated in the present study. For the Ta-Ge system, there is no binary phase diagram yet available. Controversies in the Ta-V binary phase diagram concern the existence of a $MgZn_2$-type Laves phase. We herein follow the critical assessment in Massalski [7], which shows a continuous bcc-type solid solution (Ta,V) at high temperatures and a binary $MgCu_2$ type Laves phase (C15) below a critical point at 1310 °C (For a detailed discussion of the Ta-V binary see reference [2]). Table 1 summarizes the crystallographic data available for all the phases pertinent to the ternary Ta-V-Ge system.

Table 1. Crystallographic data of solid phases in the Ta-V-Ge system.

Phase Temperature range (°C)	Space group Prototype	Lattice parameters (nm)			Comments
		a	b	c	
$(Ta_{1-x}V_x)$	Im-$3m$ W	0.3305- 0.3325			[17,18]
(Ta); < 3020 [7]		0.33030			[7]
(V); < 1910 [7]		0.3024			[7]
(Ge); < 937 [6]	Fd-$3m$ C	0.56574			[7]
TaV_2 ≤ 1310 [7]	Fd-$3m$ $MgCu_2$	0.7157 0.7167			[19]

145

TaV$_2$ 1450-1205 and ≤ 370 [2]	*P6$_3$/mmc* MgZn$_2$	0.5058(5)		0.8250(5)	[16]
(Ta$_{1-x}$V$_x$)$_3$Ge Ta$_3$Ge; < 1550 [3]	*P4$_2$/n* Ti$_3$P	1.02508(8) 1.028		0.51202(6) 0.522	x$_{max}$[1]= 0.093, [This work] [8]
Ta$_3$Ge; > 1550 [3]	*I-4* Ni$_3$P	1.036 1.03421(3) 1.03421(3)		0.516 0.51531(2) 0.51532(2)	[8] [3] [9]
(Ta$_{1-x}$V$_x$)$_5$Ge$_3$ Ta$_5$Ge$_3$	*I4/mcm* Cr$_5$B$_3$	0.659(9)		1.201(0)	[10]
TaGe$_2$	*P6$_2$22* CrSi$_2$	0.4938		0.673	[11]
(Ta$_{1-x}$V$_x$)$_5$Ge$_3$ (Ta$_x$V$_{1-x}$)$_5$Ge$_3$ V$_5$Ge$_3$; < 1931 [6] Ta$_5$Ge$_3$	*I4/mcm* W$_5$Si$_3$	1.00448(8) 0.96688(7) 0.957 1.001(0)		0.51004(6) 0.48961(6) 0.484 0.515(0)	x = 0.136, [This work] x = 0.112, [This work] [12] [10]
(Ta$_x$V$_{1-x}$)$_3$Ge V$_3$Ge; < 1920 [6]	*Pm-3n* Cr$_3$Si	0.48170(3) 0.4764			x$_{max}$[1]= 0.113, [This work] [13]
(Ta$_x$V$_{1-x}$)$_{11}$Ge$_8$ V$_{11}$Ge$_8$; < 1622 [6]	*Pnma* Cr$_{11}$Ge$_8$	1.3803(1) 1.341	0.5117(1) 0.502	1.6572(1) 1.609	x$_{max}$[1]= 0.639, [This work] [14]
V$_{17}$Ge$_{31}$; < 961.1 [6]	*P-4n2* Cr$_{17}$Ge$_{31}$	0.591		0.8365	[15]
τ$_1$-(Ta$_x$V$_{1-x}$)$_5$Ge$_3$	*P6$_3$/mcm* Mn$_5$Si$_3$	0.73571(9)- 0.75149(8)		0.50031(7)- 0.51236(6)	0.208<x<0.632, at 1500 °C [This work]
τ$_2$-Ta(Ta$_x$V$_{1-x-y}$Ge$_y$)$_2$ x = 0.020, y = 0.121	*P6$_3$/mmc* MgZn$_2$	0.50506(4) 0.504(8)		0.82951(9) 0.827(8)	Annealed at 1500 °C [This work] For "Ta$_2$V$_3$Ge" [4]
τ$_3$-Ta$_{9-x+y}$V$_{4+x-y-z}$Ge$_{1+z}$ x = 0.325, y = 0.512, z = 0.975	*I4/mcm* Nb$_9$Co$_4$Ge	1.35165(1)		0.50910(1)	Annealed at 1500 °C [This work]
τ$_4$-(Ta,V)$_3$Ge					Structure unknown
C15-Ta(Ta$_x$V$_{1-x-y}$Ge$_y$)$_2$ x = 0.040, y = 0.054	*Fd-3m* MgCu$_2$	0.71584(4)			Annealed at 1500 °C [This work]

[1] Maximal solubility at 1500°C

10.3.2. Rietveld refinement of C15-Ta(Ta$_x$V$_{1-x-y}$Ge$_y$)$_2$ (MgCu$_2$-type)

Detailed inspection of the ternary phase relations at 1500 °C revealed the presence of a ternary Laves phase C15 (MgCu$_2$ type), which appears clearly separated by a two-phase equilibrium from the binary Ta-V system where the C15 (MgCu$_2$ type) phase is reported to exist below 1310 °C [7]. We have reported a similar case for the Ta-V-Si system [2]. The Rietveld refinement of the X-ray powder spectrum of the alloy Ta$_{32.7}$V$_{64.3}$Ge$_{3.0}$ (EPMA, at. %) confirmed the C15-phase in equilibrium with the solid solution (Ta,V) and τ$_2$ with the MgZn$_2$ type (Fig. 1). Initially, we refined the structure with Ta atoms in the 8a sites and a statistical mixture of V and Ge atoms in the 16*c* site of space group *Fd$\bar{3}$m*. However, the Electron Probe Microanalyzer (EPMA) composition of 36.0 at. % Ta requests a higher Ta-concentration, which can only be achieved via a statistical mixture of all three elements (Ta,V,Ge) in the 16*c* positions. Thus we fixed the Ta content and refined the V and Ge occupancy only. The final composition Ta$_{36.0}$V$_{60.4}$Ge$_{3.6}$ resulting from the Rietveld refinement was in good agreement with the composition

146

$Ta_{36.0}V_{60.1}Ge_{3.9}$ obtained from EPMA (Table 2). The calculated X-rays intensity data match well the experimental X-ray spectrum (Fig. 1).
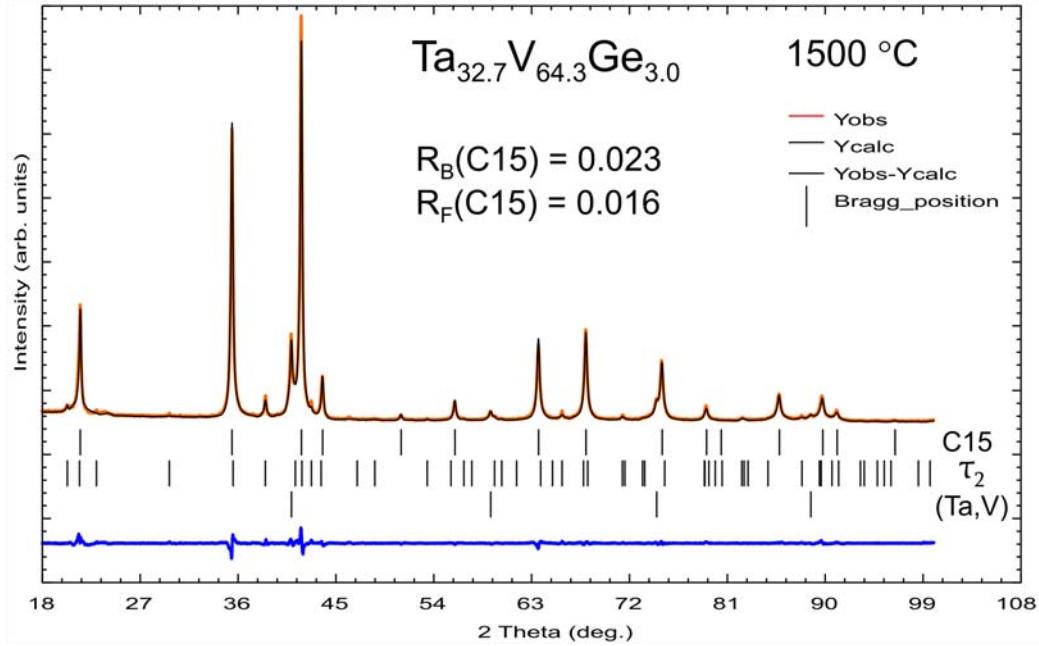

Fig. 1. Refinement of a sample with composition $Ta_{32.7}V_{64.3}Ge_{3.0}$ (at. %, EPMA) revealing the presence of C15-Ta(Ta,V,Ge)$_2$ in equilibrium with τ_2-Ta(Ta,V,Ge)$_2$ and (Ta,V).

Table 2: Results of Rietveld refinement of C15-Ta(Ta$_x$V$_{1-x-y}$Ge$_y$)$_2$, x = 0.040, y = 0.054, τ_1-(Ta$_x$V$_{1-x}$)$_5$Ge$_3$, x = 0.619, τ_2-Ta(Ta$_x$V$_{1-x-y}$Ge$_y$)$_2$, x = 0.020, y = 0.121 and τ_3-Ta$_{9-x+y}$V$_{4+x-y-z}$Ge$_{1+z}$, x = 0.325, y = 0.512, z = 0.975. All structures are standardized with program *Structure Tidy* [22].

Parameter/compound	C15	τ_1	τ_2	τ_3
Structure type	MgCu$_2$	Mn$_5$Si$_3$	MgZn$_2$	Nb$_9$Co$_4$Ge
Space Group	*Fd-3m*, #227	*P6$_3$/mcm*, #193	*P6$_3$/mmc*, #194	*I4/mcm*, #140
Composition from EPMA	$Ta_{36.0}V_{60.1}Ge_{3.9}$	$Ta_{37.4}V_{25.3}Ge_{37.3}$	$Ta_{35.0}V_{56.4}Ge_{8.6}$	$Ta_{64.2}V_{21.8}Ge_{14.0}$
Composition from refinement	$Ta_{36.0}V_{60.4}Ge_{3.6}$[1]	$Ta_{38.7}V_{23.8}Ge_{37.5}$	$Ta_{34.7}V_{57.2}Ge_{8.1}$	$Ta_{65.6}V_{20.3}Ge_{14.1}$
Formula from refinement	Ta(Ta$_x$V$_{1-x-y}$Ge$_y$)$_2$, x = 0.040, y = 0.054	(Ta$_x$V$_{1-x}$)$_5$Ge$_3$, x = 0.619	Ta(Ta$_x$V$_{1-x-y}$Ge$_y$)$_2$, x = 0.020, y = 0.121	Ta$_{9-x+y}$V$_{4+x-y-z}$Ge$_{1+z}$, x = 0.325, y = 0.512 , z = 0.975
a (nm)	0.71584(4)	0.74842(7)	0.50506(4)	1.35165(1)
b (nm)	0.71584(4)	0.74842(7)	0.50506(4)	1.35165(1)
c (nm)	0.71584(4)	0.50822(8)	0.82951(9)	0.50910(1)
Reflections in refinement	18	68	53	172
Number of variables	16	19	19	25
$R_F = \Sigma|F_0-F_c|/\Sigma F_0$	0.016	0.034	0.024	0.024
$R_B = \Sigma|I_0-I_c|/\Sigma I_0$	0.023	0.041	0.039	0.027
$R_{wP}=[\Sigma w_i|y_{0i}-y_{ci}|^2/\Sigma w_i|y_{0i}|^2]^{1/2}$	0.035	0.046	0.039	0.034
$R_P = \Sigma|y_{0i}-y_{ci}|/\Sigma|y_{0i}|$	0.023	0.037	0.025	0.025
$R_e = [(N-P+C)/\Sigma w_i y_{0i}^2]^{1/2}$	0.022	0.018	0.017	0.016
$\chi^2 = (R_{wP}/R_e)^2$	2.38	6.48	5.42	4.42
Atom parameters				

Atom site 1	8b (⅜, ⅜, ⅜);	4d (⅓, ⅔, 0);	2a (0, 0, 0);	16k (x, y, 0);
Occ.	1.00 Ta	0.15(3) Ta + 0.85 V	0.080 Ta + 0.435 V + 0.485 Ge[1]	1.00 Ta
x, y;	-	-	-	0.15874(4), 0.08413(3)
B_{iso};	0.21(2)	0.44(5)	0.84(4)	0.73(2)
Atom site 2	16c (0, 0, 0)	6g (x, 0, ¼)	4f (⅓, ⅔, z)	16k (x, y, 0);
Occ.	0.04 Ta + 0.906V + 0.054(3) Ge[1]	0.93(1) Ta + 0.07 V	1.00 Ta	1.00 Ta
x, y, z;	-	0.23353(7)	0.56063(4)	0.06489(5), 0.29147(5)
B_{iso};	0.68(3)	0.59(2)	0.29(1)	0.79(2)
Atom site 3	-	6g (x, 0, ¼);	6h (x, 2x, ¼);	4b (0, ½, ¼)
Occ.	-	1.00 Ge	1.00 V	0.650(4) Ta + 0.350 V
x;	-	0.5988(2)	0.1728(2)	-
B_{iso};	-	0.98(4)	0.19(2)	0.34(4)
Atom site 4	-	-	-	4a (0, 0, ¼)
Occ.	-	-	-	1.00 Ge
B_{iso};	-	-	-	0.90(7)
Atom site 5	-	-	-	8e (¼, ¼, ¼)
Occ.	-	-	-	0.512(1) V + 0.488 Ge
B_{iso};	-	-	-	0.63(7)
Atom site 6	-	-	-	8h (x, x + ½, 0)
Occ.	-	-	-	0.744(2) V + 0.256 Ta
x;	-	-	-	0.12880(7)
B_{iso};	-	-	-	0.33(3)

[1]Ta content fixed after EPMA.

10.3.3. Rietveld refinement of τ_1-$(Ta_xV_{1-x})_5Ge_3$ (Mn_5Si_3-type)

EPMA indicated a ternary phase with an extended homogeneity region at a constant Ge-content of ~38 at. % suggesting close similarity to the $(Ta,V)_5Si_3$ phase in the Ta-V-Si system [2]. Rietveld X-ray powder data refinement (see Fig. 2) of a sample with composition $Ta_{37.5}V_{23.5}Ge_{39.0}$ (at. %, EPMA) confirmed the Mn_5Si_3 type structure [τ_1-phase; $(Ta_xV_{1-x})_5Ge_3$, (x=0.619)]. Refinement revealed a preferred partial occupation of the 6g-site by Ta-atoms, with a small additional amount of Ta entering the 4d site. The homogeneity region of τ_1-phase (line compound at constant Ge-content) can be conceived on the basis of this statistical mixture in these two sites. Complete occupancy of Ta in the 6g site will result in a Ta content of 37.5 % yielding a fully ordered stoichiometry $Ta_3V_2Si_3$. However, the τ_1 homogeneity region at the Ta-rich end amounts at 1500°C to 39.5 at. % Ta slightly exceeding 37.5 % and thereby indicating that some Ta will occupy the 4d site. It should be noted that as cast samples exhibit a Ta content even higher than that at 1500 °C.

Mn_5Si_3 type phases are known to be stabilized by various impurities (B, C, O etc.) and these were already reported to exist in the Ta-Ge and V-Ge binary systems [23,24,25]. In the present study, we did not observe this phase in binary samples, however, the τ_1-$(Ta_xV_{1-x})_5Ge_3$ phase with Mn_5Si_3 type was clearly found in ternary alloys. Rietveld refinement of τ_1-$(Ta_xV_{1-x})_5Ge_3$

(x=0.619) did not reveal any significant residual electron density in the sites for the octahedral voids in 2*b* (0, 0, 0) excluding contamination. Furthermore, the EPMA for this phase measured on various alloys confirms the metal/Ge ratio $(Ta_xV_{1-x})_5Ge_3$ ±1 at.%. It can thus be safely assumed that the τ_1-$(Ta_xV_{1-x})_5Ge_3$ phase is a truly ternary phase with stoichiometry M_5Ge_3. Table 2 summarizes the structural parameters for τ_1-$(Ta_xV_{1-x})_5Ge_3$ (x=0.619).
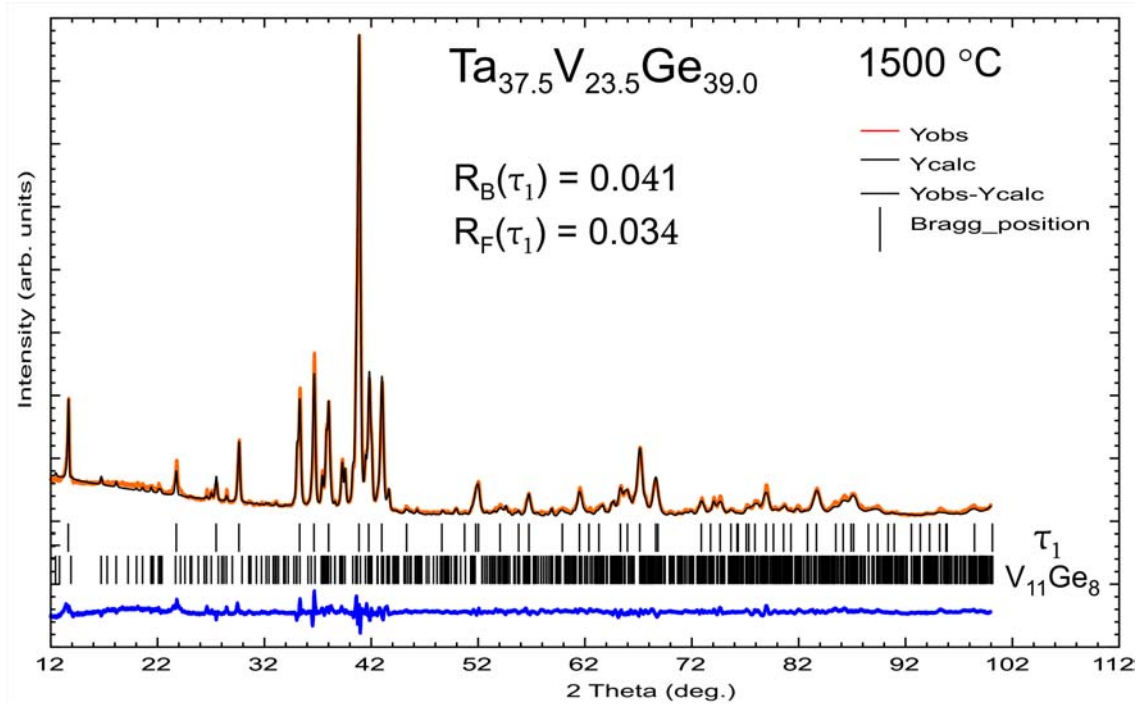
Fig. 2. Refinement of a sample with composition $Ta_{37.5}V_{23.5}Ge_{39.0}$ (at. %, EPMA) revealing the two-phase equilibrium between τ_1-$(Ta_xV_{1-x})_5Ge_3$ (x=0.632) and $(Ta_xV_{1-x})_{11}Ge_8$ (x=0.580).

10.3.4. Crystal structure of τ_2-Ta(Ta,V,Ge)$_2$ (MgZn$_2$-type Laves phase)

10.3.4.1. Rietveld refinement.

For the MgZn$_2$ type Laves phase with nominal composition Ta_2V_3Ge, reported by Ganglberger et al. [4], we only know the lattice parameters and that the X-ray pattern was not single phase. Our sample with composition Ta_2V_3Ge, annealed at 1500 °C, turned out to be three-phase containing τ_4-$(Ta_xV_{1-x})_3Ge$ (structure unknown) and $(Ta_xV_{1-x})_3Ge$ (Cr$_3$Si type) as secondary phases. Lattice parameters for the Laves phase [labeled τ_2, a = 0. 50463(8), c = 0.83005(9) nm] are slightly larger than the values reported earlier [4] [a = 0.504(8), c = 0.827(8) nm]. As the homogeneity

region obtained for τ_2 (for details see section 3.6) shows similarity to the homogeneity region reported for the isotypic phase in the Ta-V-Si system [2], we used the same structure model for refinement of τ_2-Ta(Ta,V,Ge)$_2$ which was derived from single crystal data for Ta(Ta,V,Si)$_2$. We fixed the Ta content in the $2a$ site according to the EPMA data as a starting value and refined the occupation of V and Ge. The Rietveld refinement of the X-ray powder diffraction data showed good agreement of calculated and experimental intensities (Fig. 3). The final composition obtained from Rietveld refinement Ta$_{34.7}$V$_{57.2}$Ge$_{8.1}$ is in good agreement with the composition obtained from EPMA (Ta$_{35.0}$V$_{56.4}$Ge$_{8.6}$) and yields a structure formula Ta(Ta$_x$V$_{1-x-y}$Ge$_y$)$_2$ (x=0.020, y=0.121). Table 2 summarizes the structural parameters for τ_2.

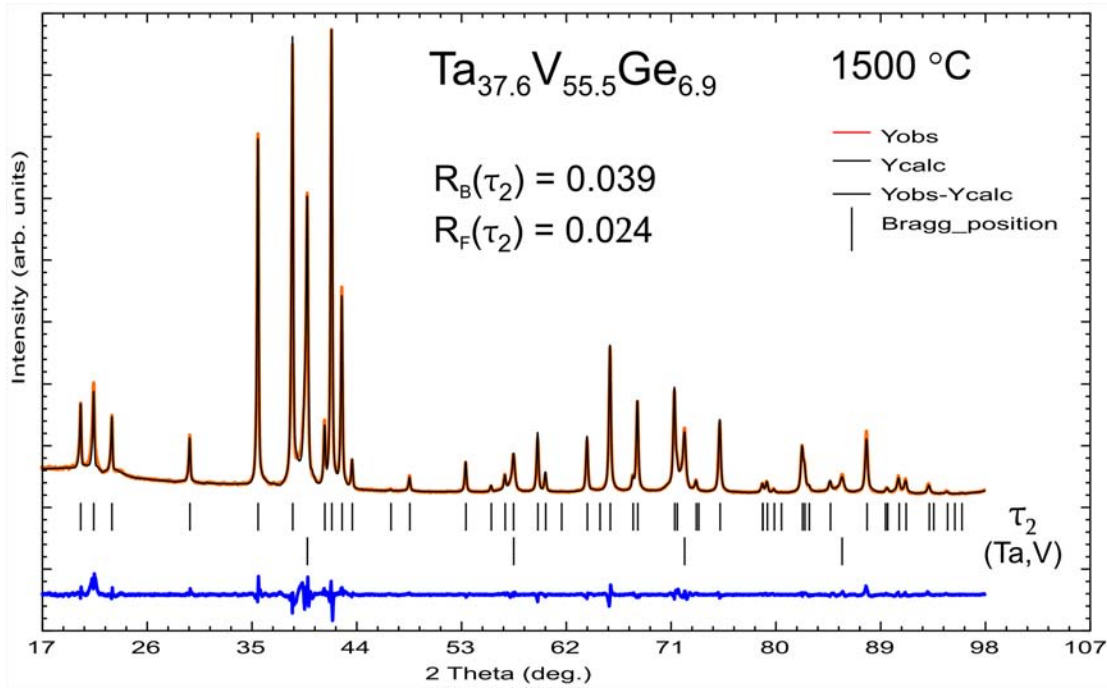

Fig. 3. Refinement of a sample with composition Ta$_{37.6}$V$_{55.5}$Ge$_{6.9}$ (at. %, EPMA) revealing the two phase equilibrium between τ_2-Ta(Ta,V,Ge)$_2$ and (Ta,V).

10.3.4.2. Transmission electron microscopy

As no single crystal study was performed for τ_2-Ta(Ta,V,Ge)$_2$ in the present work, we decided to confirm unit cell and symmetry employing TEM. Grains of the Laves phase were primarily detected by their composition measured by EDX analysis and being close to (Ta$_{36.0}$V$_{56.0}$Ge$_{8.0}$). A series of selected area diffraction (SAD) patterns were then taken at various sample tilts. Fig. 4

summarizes the most representative diffraction patterns with low index zone axes [100], [001] and [210] and their simulations using software JEMS [20]. All diffraction patterns were fully indexed using the hexagonal lattice parameters found by X-ray powder diffraction. No superstructure spots were detected confirming the unit cell dimensions given in Table 2. The observed intensities of diffraction spots correlate well with the simulations based on atomic positions given in Table 2.
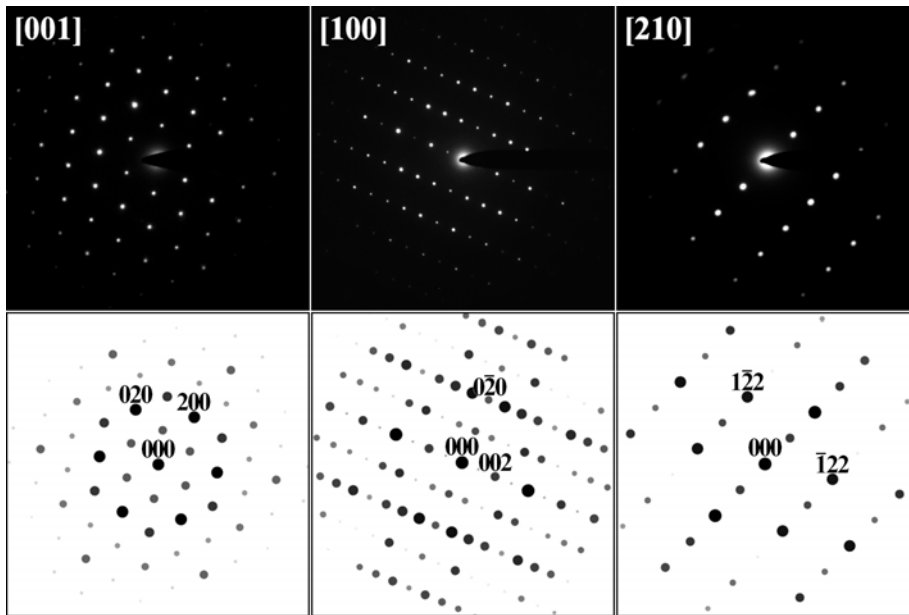

Fig. 4. τ_2-Ta(Ta,V,Ge)$_2$: TEM selected area diffraction patterns of low index zone axes [100], [001] and [210] together with their simulations.

10.3.5. Rietveld refinement of τ_3-Ta$_9$V$_3$Ge$_2$ (Nb$_9$Co$_4$Ge-type)

A phase labelled τ_3 was observed in Ta-rich corner of the Ta-V-Ge system with a considerably large homogeneity region (see section 3.6). We recognized a striking similarity in the powder diffraction pattern of τ_3 and the phase Nb$_9$Co$_4$Ge reported in the Nb-rich corner of the Nb-Co-Ge system [21]. Indexation of the powder diffraction spectrum of an alloy with composition Ta$_{62.6}$V$_{27.3}$Ge$_{10.1}$ (at. %, EPMA) having a majority of τ_3 and Rietveld refinement confirmed isotypism with Nb$_9$Co$_4$Ge. A close inspection of the homogeneity region of τ_3 suggests both Ta/V exchange as well as V/Ge exchange eventually combined with the presence of vacancies in the structure. The refinement clearly shows that two 16k sites are fully occupied by Ta and one

4a site is fully occupied by Ge atoms, which is consistent with the Nb_9Co_4Ge-type structure. However, we obtained a statistical mixture in three crystallographically different sites (4*b*, 8*e*, 8*h*) whereas the Nb_9Co_4Ge-type is a fully ordered structure [21]. Thus τ_3 resembles the $Nb_9Fe_3Ge_2$ phase which also adopts the Nb_9Co_4Ge-type structure but shows a statistical distribution of Fe + Ge atoms in two sites, 8*e* and 8*h*. Besides a random mixture of V + Ge in 8*e*, refinement of τ_3 reveals random disorder in the 4*b* (Ta + V) and the 8*h* (Ta +V) sites (Table 2). The structure formula obtained from Rietveld refinement can thus be represented as τ_3-$Ta_{9-x+y}V_{4+x-y-z}Ge_{1+z}$, x = 0.325, y = 0.512, z = 0.975 and is close to $Ta_{\sim 9}V_{\sim 3}Ge_{\sim 2}$. With this atom arrangement the Rietveld refinement of τ_3 showed good agreement of calculated and experimental intensities (Fig. 5). The final composition from Rietveld refinement, $Ta_{65.6}V_{20.3}Ge_{14.1}$, is in good agreement with EPMA ($Ta_{64.2}V_{21.8}Ge_{14.0}$).
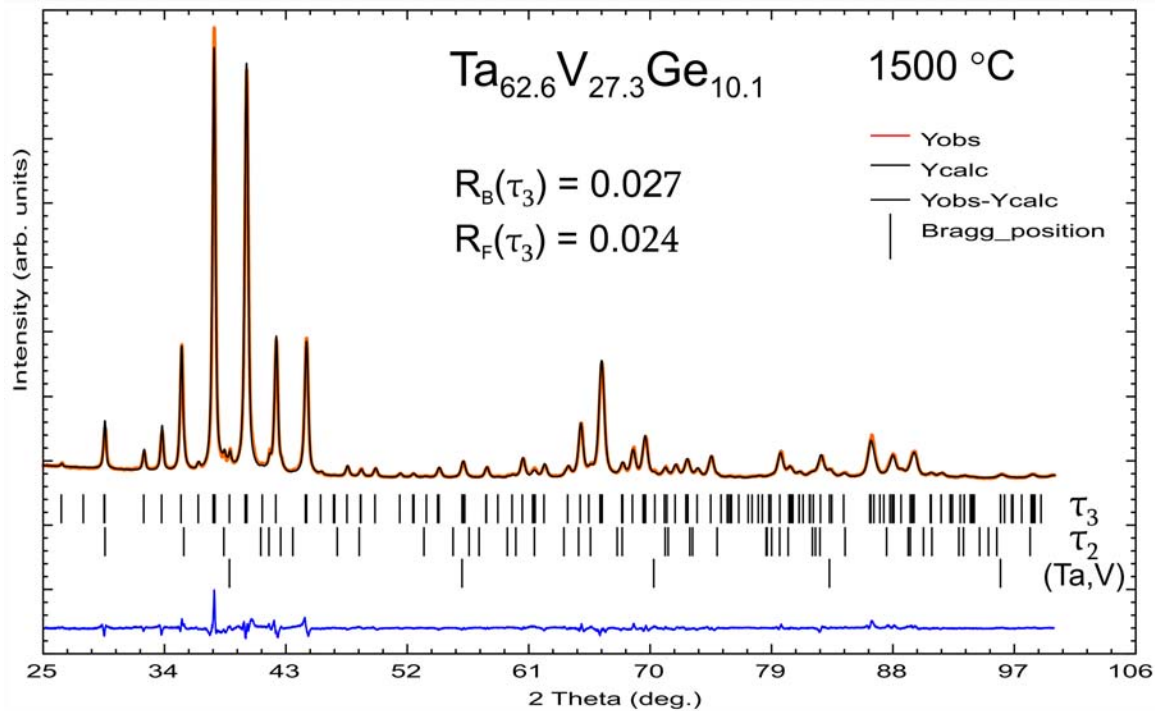

Fig. 5. Refinement of a sample with composition $Ta_{62.6}V_{27.3}Ge_{10.1}$ (at. %, EPMA) revealing the presence of τ_3-$Ta_9V_3Ge_2$ in equilibrium with τ_2-Ta(Ta,V,Ge)$_2$ and (Ta,V).

The largest Ta-Ta interatomic distances (0.3434 nm) observed in τ_3 are slightly larger than the largest Nb-Nb distances (0.3329 nm) in Nb_9Co_4Ge as expected because the atom radius of V is larger than that of Co, whereas Ta and Nb atoms have roughly the same size. Largest Ta-Ge

interatomic distances (0.2742 nm) are comparable to the largest Nb-Ge interatomic distances (0.2662 nm). Maximum distance of Ta atoms from the mixed site M1 is 0.3215 nm. It must be noted that M1 is occupied by 0.65 Ta +0.35 V. That's why, this distance is slightly smaller than the Ta-Ta maximum interatomic distance.

10.3.6. Isothermal section of the Ta-V-Ge system at 1500 °C

Combined X-ray and EPMA identified four ternary phases within the isothermal section at 1500°C. The $MgCu_2$ type Laves phase exhibits a rather small homogeneity range ($\sim$ 3 to 4 at. % Ge content and 1 to 2 at. % Ta/V exchange). This phase (C15) is clearly separated from the binary Ge-saturated solid solution of (Ta,V) by a two-phase equilibrium. As it is reported already [2,7] that this phase is not present in the Ta-V binary system, it can be concluded that the small amounts of Ge significantly increase the stability of this phase in a similar way as Si does [2]. Although the τ_2-phase with the $MgZn_2$-type exists at 1500°C in a considerable homogeneity region from $\sim$7 to 12 at. % Ge and from $\sim$34 to 36 at. % Ta, it does not comprise the stoichiometric composition "Ta_2V_3Ge" reported by Ganglberger et al. [4]. It seems that the Ta content in τ_2 increases with increasing Ge. The homogeneity region is similar to that of the homologous phase $Ta(Ta,V,Si)_2$.

At 1500 °C, τ_1-$(Ta_xV_{1-x})_5Ge_3$ exists in a large homogeneity region extending from $Ta_{13}V_{49.5}Ge_{37.5}$ (x=0.208) to $Ta_{39.5}V_{23}Ge_{37.5}$ (x=0.632) suggesting the exchange of Ta and V at a constant Ge content (see Rietveld refinement in section 3.3). The homogeneity region of τ_3-$Ta_{9-x+y}V_{4+x-y-z}Ge_{1+z}$ extends at 1500 °C from $\sim$ 61.5 to 68 % Ta and 11.5 to 14.5 % Ge including the stoichiometric composition $Ta_9V_3Ge_2$, which is similar to the formula obtained for $Nb_9Fe_3Ge_2$ [21]. The phase is in direct equilibrium with (Ta) and might be used for hardening of (Ta). No such phase was observed in Ta-V-Si system.

In addition to all these phases, another phase named τ_4-$(Ta,V)_3Ge$ was observed near τ_1. Its homogeneity extends from about 39.5 to 40 % Ta and $\sim$24.5 to 25.5 % Ge at 1500 °C. Its structure is yet unknown and requires further investigation. The continuous solid solution bcc-(Ta,V), similar to the Ta-V-Si system [2], reveals very little solubility of Ge (Table 3). In contrast to values given by Yuan et al. [6] our EPMA measurements indicate a larger homogeneity region for V_3Ge extending at 1500°C from 21 to 25 at% Ge. A large solubility of

Ta (up to 37 at. %) was observed in $V_{11}Ge_8$ annealed at 1500 °C as well as in the as cast samples. The maximum solubility of Ta in V_5Ge_3 was found to be ~ 7 at. % and the maximum solubility of V in Ta_5Ge_3 was ~ 8.5 at. % (see Table 3).

In the as cast samples, we observed a further phase with unknown structure type and with a composition ranging from $Ta_{42.5}V_{41.5}Ge_{16.0}$ to $Ta_{49}V_{35.0}Ge_{16.0}$ (at. %). This compound disappears after annealing and thus is not present at 1500 °C.

Table 3: Data on alloys for three-phase regions in the Ta-V-Ge system at 1500 °C.

Overall composition	Phase	Structure type	Lattice parameters (nm)			Composition EPMA (at. %)		
			a	b	c	Ta	V	Ge
$Ta_{8.0}V_{52.9}Ge_{39.1}$	τ_1	Mn_5Si_3	0.73591(7)	-	0.50049(7)	13.0	49.4	37.6
	$(Ta_xV_{1-x})_5Ge_3$	W_5Si_3	0.96608(8)	-	0.48920(9)	7.0	55.5	37.5
	$(Ta_xV_{1-x})_{11}Ge_8$	$Cr_{11}Ge_8$	1.34746(7)	0.50389(5)	1.62406(9)	6.1	51.8	42.1
$Ta_{7.6}V_{56.8}Ge_{35.6}$	τ_1	Mn_5Si_3	0.73571(9)	-	0.50031(7)	13.0	49.7	37.3
	$(Ta_xV_{1-x})_5Ge_3$	W_5Si_3	0.96688(7)	-	0.48961(6)	7.2	55.5	37.3
	$(Ta_xV_{1-x})_3Ge$	Cr_3Si	0.47858(8)	-	-	1.5	73.5	25.0
$Ta_{23.6}V_{66.4}Ge_{10.0}$	τ_2	$MgZn_2$	0.50467(4)	-	0.82795(9)	34.1	58.0	7.9
	$(Ta_xV_{1-x})_3Ge$	Cr_3Si	0.48170(3)	-	-	5.6	74.9	19.5
	(V,Ta)	W	0.31379(2)	-	-	20.1	78.2	1.7
$Ta_{26.6}V_{54.5}Ge_{18.9}$	τ_2	$MgZn_2$	0.50482(8)	-	0.83018(9)	35.0	53.0	12.0
	τ_4	Unknown	-	-	-	40.0	35.5	24.5
	$(Ta_xV_{1-x})_3Ge$	Cr_3Si	0.48343(5)	-	-	8.3	69.4	22.5
$Ta_{25.5}V_{45.5}Ge_{29.0}$	τ_1	Mn_5Si_3	0.74501(7)	-	0.50448(7)	31.3	31.3	37.4
	τ_4	Unknown	-	-	-	39.4	35.1	25.5
	$(Ta_xV_{1-x})_3Ge$	Cr_3Si	0.48280(8)	-	-	7.4	69.2	23.4
$Ta_{32.2}V_{63.8}Ge_{4.0}$	τ_2	$MgZn_2$	0.50609(7)	-	0.82689(9)	35.5	58.5	6.0
	C15	$MgCu_2$	0.71584(4)	-	-	35.5	64.4	4.1
	(V,Ta)	W	0.31175(1)	-	-	22.0	76.8	1.2
$Ta_{38.4}V_{57.7}Ge_{3.9}$	τ_2	$MgZn_2$	0.50597(3)	-	0.82846(9)	36.0	58.0	6.0
	C15	$MgCu_2$	0.71681(8)	-	-	36.1	59.7	4.2
	(Ta,V)	W	0.31910(3)	-	-	43.0	56.4	0.6
$Ta_{62.3}V_{27.2}Ge_{10.5}$	τ_2	$MgZn_2$	0.50609(7)	-	0.83127(7)	36.0	54.6	9.4
	τ_3	$Nb_9Co_4Zn_2$	1.35165(1)	-	0.50910(1)	63.0	25.0	12.0
	(Ta,V)	W	0.32608(3)	-	-	74.0	25.2	0.8
$Ta_{48.0}V_{38.0}Ge_{14.0}$	τ_2	$MgZn_2$	0.50545(5)	-	0.83079(9)	36.1	52.8	11.1
	τ_3	$Nb_9Co_4Zn_2$	1.34744(7)	-	0.50871(1)	61.0	25.7	13.3
	τ_4	Unknown	-	-	-	52.6	22.7	24.7
$Ta_{75.1}V_{11.2}Ge_{13.7}$	τ_3	$Nb_9Co_4Zn_2$	1.35877(8)	-	0.51206(8)	67.9	18.4	13.7
	$(Ta_{1-x}V_x)_3Ge$	Ti_3P	1.02947(7)	-	0.51371(8)	69.7	5.9	24.4
	(Ta,V)	W	0.32880(4)	-	-	86.6	1.2	12.2
$Ta_{64.7}V_{16.8}Ge_{18.5}$	τ_3	$Nb_9Co_4Zn_2$	1.34965(7)	-	0.50871(4)	62.9	22.7	14.4
	τ_4	Unknown	-	-	-	47.3	27.8	24.9
	$(Ta_{1-x}V_x)_3Ge$	Ti_3P	1.02636(9)	-	0.51445(9)	68.0	7.2	24.8
Dotted triangles[2]	τ_4	Unknown	-	-	-	47.2	26.8	26.0
	$(Ta_{1-x}V_x)_3Ge$	Ti_3P	1.02928(9)	-	0.51355(9)	69.9	6.0	25.1
	$(Ta_{1-x}V_x)_5Ge_3$	W_5Si_3	1.00707(9)	-	0.51365(8)	57.1	6.1	36.8
Dotted triangles[2]	τ_1	Mn_5Si_3	0.75373(8)	-	0.51234(6)	39.5	23.0	37.5
	τ_4	Unknown	-	-	-	47.0	27.0	26.0
	$(Ta_{1-x}V_x)_5Ge_3$	W_5Si_3	1.00580(7)	-	0.51188(9)	55.5	7.0	37.5
Dotted triangles[2]	τ_1	Mn_5Si_3	0.75149(8)	-	0.51236(6)	39.5	23.0	37.5
	$(Ta_{1-x}V_x)_5Ge_3$	W_5Si_3	1.00448(8)	-	0.51004(6)	54.0	8.5	37.5

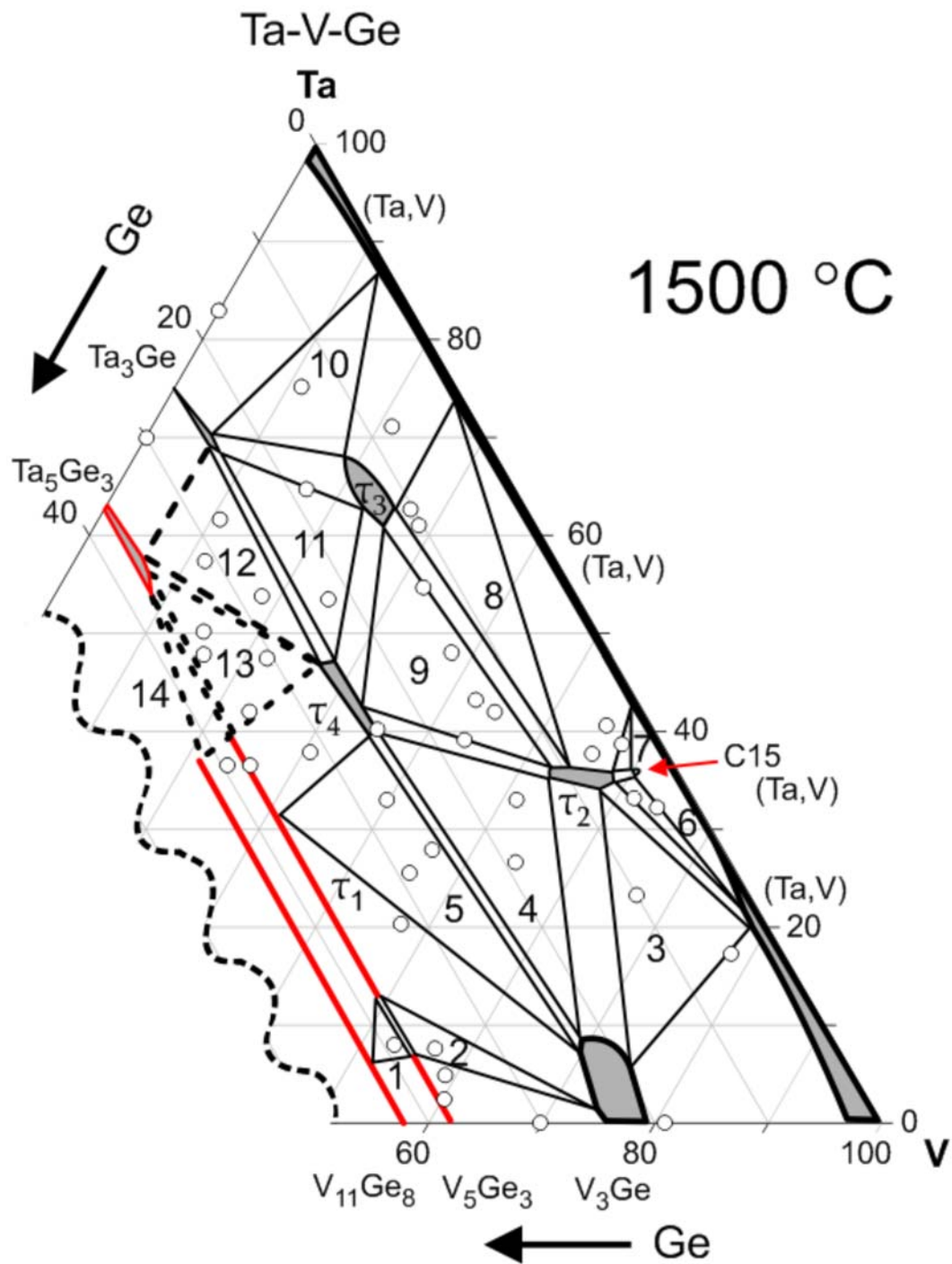| | $(Ta_xV_{1-x})_{11}Ge_8$ | $Cr_{11}Ge_8$ | 1.3803(1) | 0.5117(1) | 1.6572(1) | 37.0 | 20.9 | 42.1 |

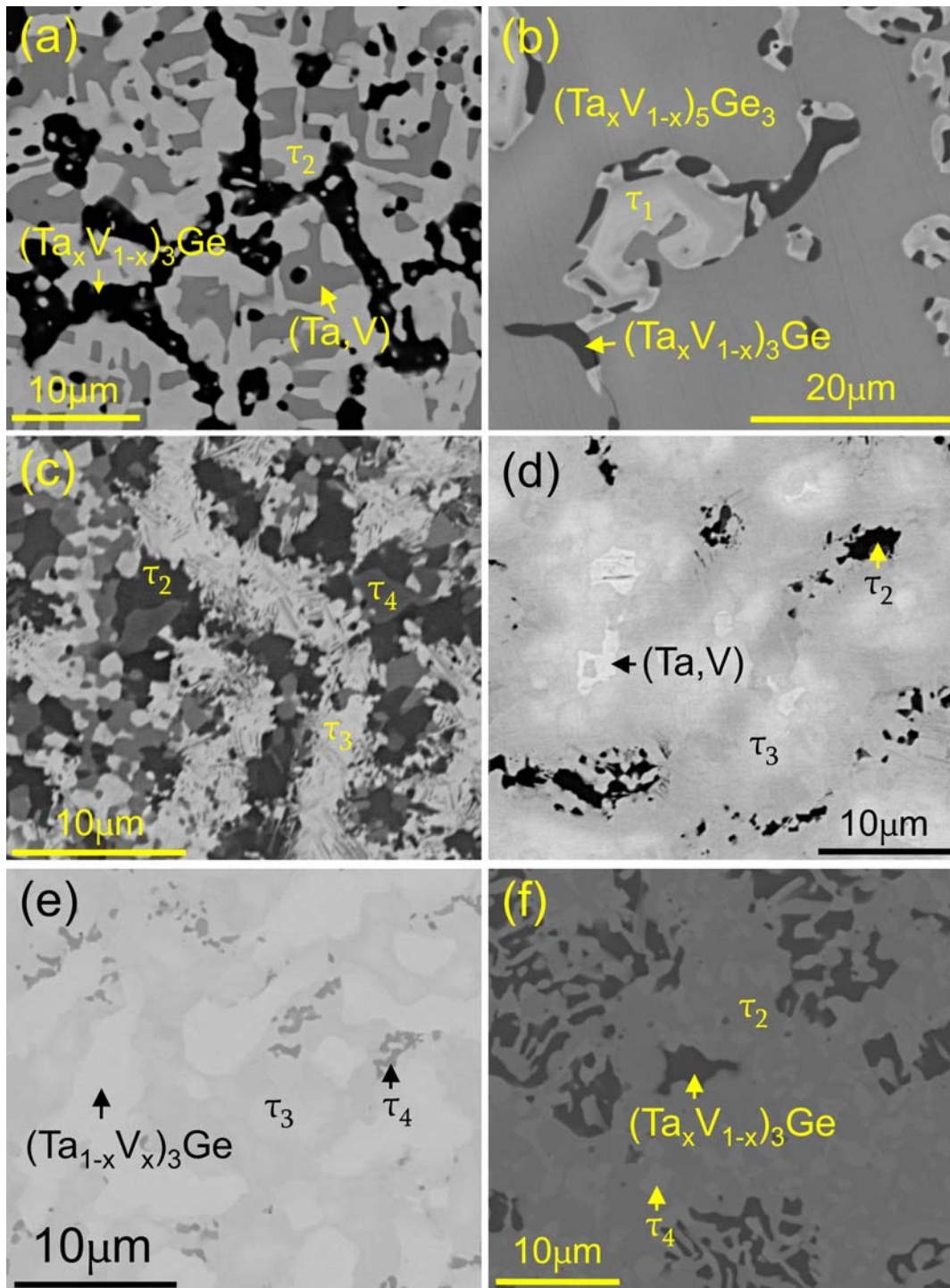Fig. 6. System Ta-V-Ge: partial isothermal section at 1500 °C.

Fig. 7. Micrographs of selected samples annealed at 1500 °C (for phase compositions, see Table 3). (a) $Ta_{23.6}V_{66.4}Ge_{10.0}$; τ_2 + $(Ta_xV_{1-x})_3Ge$ + (Ta,V), (b) $Ta_{7.6}V_{56.8}Ge_{35.6}$; τ_1 + $(Ta_xV_{1-x})_3Ge$ + $(Ta_xV_{1-x})_5Ge_3$, (c) $Ta_{48.0}V_{38.0}Ge_{14.0}$; τ_2 + τ_3 + τ_4, (d) $Ta_{62.3}V_{27.2}Ge_{10.5}$; τ_2 + τ_3 + (Ta,V), (e) $Ta_{64.7}V_{16.8}Ge_{18.5}$; τ_3 + τ_4 + $(Ta_{1-x}V_x)_3Ge$ and (f) $Ta_{26.6}V_{54.5}Ge_{18.9}$; τ_2 + τ_4 + $(Ta_xV_{1-x})_3Ge$.

156

Figure 6 shows the phase relations within the isothermal section of the Ta-V-Ge system at 1500 °C. Composition of vertices and the phases found in all triangles are summarized in Table 3. The numbering shown in the isothermal section in Figure 6 corresponds to the same numbers for the three-phase regions listed in Table 3. Figure 7 shows the micrographs of selected samples annealed at 1500 °C. Figure 7a represents $Ta_{23.6}V_{66.4}Ge_{10.0}$ which shows a three-phase equilibrium between τ_2 + $(Ta_xV_{1-x})_3Ge$ + (Ta,V). Figure 7b represents a three-phase equilibrium between τ_1 + $(Ta_xV_{1-x})_3Ge$ + $(Ta_xV_{1-x})_5Ge_3$ in a sample with composition $Ta_{7.6}V_{56.8}Ge_{35.6}$. Fig. 7c confirms the three-phase equilibrium τ_2 + τ_3 + τ_4 obtained in the sample with composition $Ta_{48.0}V_{38.0}Ge_{14.0}$. The three-phase equilibrium observed among τ_2 + τ_3 + (Ta,V) in alloy $Ta_{62.7}V_{23.7}Ge_{12.6}$ is documented in Fig. 7d. A sample with composition $Ta_{64.7}V_{16.8}Ge_{18.5}$ showed the presence of τ_3 in equilibrium with τ_4 + $(Ta_{1-x}V_x)_3Ge$. Equilibrium among τ_2 + τ_4 + $(Ta_xV_{1-x})_3Ge$ was achieved in a sample with composition $Ta_{26.6}V_{54.5}Ge_{18.9}$.

It must be noted that some triangles in the isothermal section are presented with dotted lines, due to the fact that annealing at 1500 °C for one week did not reveal equilibrium in any of these samples. Continuous grinding, compacting and annealing did not improve the situation due to two reasons: (i) diffusion was very small; (ii) Ge losses were considerable. Hence further investigations are required to get reliable phase relations for the dashed regions as well as to solve the crystal structure of τ_4-phase.

10.4. Conclusion

Phase relations in the Ta-V-Ge system have been evaluated for the isothermal section at 1500 °C revealing four ternary phases: τ_1-$(Ta,V)_5Ge_3$ (Mn_5Si_3-type), Laves phase τ_2-$Ta(Ta,V,Ge)_2$ ($MgZn_2$-type) and τ_3-$Ta_9V_3Ge_2$ (Nb_9Co_4Ge-type) whilst the structure of τ_4-$(Ta,V)_3Ge$ is yet unsolved. In addition to all these phases, small amounts of Ge stabilize a ternary C15-phase ($MgCu_2$-type) at 1500 °C, separated from the Ta-V binary. The crystal structures of the three phases τ_1 to τ_3 were solved from X-ray powder diffraction data. The homogeneity region at 1500 °C obtained for the τ_2-phase does not include the stoichiometric composition Ta_2V_3Ge. A large homogeneity range was found for τ_1-$(Ta_xV_{1-x})_5Ge_3$ with Mn_5Si_3-type showing the exchange of Ta and V at a constant Ge content.

References

[1] A.U. Khan, C.A. Nunes, G.C. Coelho, P.A. Suzuki, A. Grytsiv, F. Bourree, G. Giester and P. Rogl, Submitted to Journal of Solid State Chemistry, (2011).

[2] A.U. Khan, P. Broz, H. Niu, J. Bursik, A. Grytsiv, X.-Q. Chen, G. Giester and P. Rogl, Submitted to Jour. of Solid State Chemistry, (2011).

[3] J.-O. Willerström, Journal of the Less-Common Metals **86**, (1982), p. 85-104.

[4] E. Ganglberger, H. Nowotny and F. Benesovsky, Monatshefte für Chemie **96(5)** (1965), p. 1658-1660.

[5] T. Wolf, J.Q. Xu, R. Flükiger (ed.), W. Klose (ed.), Vol. 21E, SpringerMaterials – The Landolt-Börnstein Database, DOI: 10.1007/10086032_8.

[6] X. Yuan, W. Sun, Y. Chung, H. Xu, S. Liu, Y. Du, P. Nash and D. Zeng, Thermodynamica Acta **513** (2011), p. 100-105.

[7] Binary Alloy Phase Diagrams, Second Edition, T.B. Massalski (ed.), ASM International, Materials Park, Ohio (1990).

[8] W. Rossteutscher and K. Schubert, Zeitschrift für Metallkunde **56**, (1965), p. 813-822.

[9] J.-O. Willerström and S. Rundqvist, Journal of Solid State Chemistry **39**, (1981), p. 128-132.

[10] H. Nowotny, A.W. Searcy and J.E. Orr, Journal of Physical Chemistry **60**, (1956), p. 677-678.

[11] R. Kubiak, R. Horyn, H. Broda and K. Lukaszewicz, Bulletin de l'Academie Polonaise des Sciences, Serie des Sciences Chimiques **20**, (1972), p. 429-436.

[12] H. Holleck, H. Nowotny and F. Benesovsky, Monatshefte für Chemie **94**, (1963), p. 497-501.

[13] K. Kanematsu, Transactions of the Japan Institute of Metals **27**, (1986), p. 225-232.

[14] H. Völlenkle, A. Wittmann and H. Nowotny, Monatshefte für Chemie **95**, (1964), p. 1544-1549.

[15] H. Völlenkle, A. Preisinger, H. Nowotny and A. Wittmann, Zeitschrift für Kristallographie **124**, (1967), p. 9-25.

[16] A.P. Nefeolov, E.M. Sokolovskaya, A.T. Grigor'ev, V.I. Chechernikov, I.G. Sokolova and L.S. Guzei, Vestnik Moskovskogo Universiteta, Seriya 2: Khimiya (1965), Issue 5, p. 42-47.

[17] V.N. Eremenko, L.A. Tret'yachenko and R.I. Yakhimovich, Russian Journal of Inorganic Chemistry, translated from Zhurnal Neorganicheskoi Khimii **5** (1960), p. 1110-1112.

[18] E. Rudy, Compendium of Phase Diagram Data, published as Tech. Rep. AD 689, 843 (1969), available from NTIS as document No. AFML-TR-65-2, part V.

[19] H. Müller and K. Weymann, Journal of the Less-Common Metals **119** (1986), p. 115-126.

[20] P. Stadelmann: JEMS: Java Electron Microscopy Software. Available from http://cimewww.epfl.ch/people/stadelmann/jemswebsite/jems.html [accessed 31.03.11].

[21] R.R. Olenych, Y.P. Yarmolyuk and L.G. Akselrud, Dopov. Akad. Nauk Ukr. RSR, Ser. A **2** (1986), p. 65-67.

[22] L.M. Gelato and E. Parthé, J. Appl. Crystallogr. **20** (1987), p. 139-43.

[23] W. Jeitschko H. Nowotny and F. Benesovsky, Monatshefte für Chemie **95** (1964), p. 1242-1246.

[24] W. Rieger, H. Nowotny and F. Benesovsky, Monatshefte für Chemie **96** (1965), p. 98-103.

[25] H. Holleck, H. Nowotny and F. Benesovsky, Monatshefte für Chemie **94** (1963), p. 497-501.

11. The Mn-rich part of the Ti-Mn binary system: Crystal chemistry and phase equilibria.

11.1. Introduction

Although the Ti-Mn phase diagram is part of numerous ternary and higher order systems of technological importance such as hydrogen-storage [1,2,3], ductilisation of titanium aluminium duplex alloys by alloying with manganese for high strength intermetallics in aerospace and/or earth bound turbine applications [4], and high strength materials for biomedical applications [5], critical assessments [6,7] of the Ti-Mn equilibrium diagram are essentially based on the experimental work of Waterstrat et al. [8,9] and still leave many points open for experimental verification. Lack of information particularly concerns the Mn-rich part of the phase diagram for which Waterstrat et al. [8,9] reported the formation of two compounds, labelled as TiMn$_{\sim3}$ and TiMn$_{\sim4}$. Whereas the crystal structure of TiMn$_{\sim3}$ is still undetermined [7], the X-ray powder spectrum of TiMn$_{\sim4}$ was indexed on the basis of a rhombohedral lattice (a_{hex}=1.1003, c_{hex}=1.9446 nm for the alloy Ti$_{17}$Mn$_{83}$ in at.%) and X-ray powder intensities compared well [8,9] with the structure type of the so-called R-phase Mo$_{0.38}$Cr$_{0.16}$Co$_{0.46}$ [10]. Despite phase equilibria data are incomplete for Ti-Mn, thermodynamic calculations [6,11,12] have relied on the preliminary phase diagram. An attempt to solve phase relations in the Ti-Mn system was made by Krendelsberger [13]. As the crystal structures and homogeneity regions of both compounds, TiMn$_{\sim3}$ and TiMn$_{\sim4}$, are not clarified and as their temperature region of existance is disputed, the current investigation is an attempt (i) to perform a detailed crystal structure evaluation on the basis of single crystal X-ray diffraction data, (ii) to verify the phase equilibria involving TiMn$_{\sim3}$ and TiMn$_{\sim4}$, their peritectic formation and their eutectoid decomposition temperatures, and (iii) to evaluate the physical behaviour of the compound richest in Mn, TiMn$_{\sim4}$.

11.2. Experimental details:

Alloys were prepared (each of 1-2 grams) by argon arc melting from metal ingots of Ti with purity higher than 99.9 mass % (Alfa Johnson Matthey GmbH, Germany) and pieces of 99.9 mass % pure Mn (Alpha-Ventron, D), which prior to use were surface cleaned in HNO$_3$. The

metal blends were melted three times for homogenization. The reguli were then placed in alumina crucibles, sealed in evacuated quartz tubes and annealed for 1-15 days in the range of 1250 °C to 800 °C followed by quenching the capsules in cold water. Temperature at the position of samples was controlled by a high quality standard thermocouple.

Lattice parameters and standard deviations were determined by least squares refinements of room temperature X-ray powder diffraction (XRD) data obtained from a Guinier-Huber image plate employing monochromatic Fe Kα_1 radiation. Single crystals of TiMn$_{\sim3}$ suitable for X-ray diffraction were mechanically isolated from an arc-melted specimen Ti$_{23.5}$Mn$_{76.5}$, which was annealed at 1230°C for 1 hour, slowly cooled down to 1180 °C and then water quenched. Similarly single crystals of TiMn$_{\sim4}$ were mechanically isolated from an arc-melted specimen Ti$_{15.5}$Mn$_{84.5}$, which was annealed at 1200°C for 1 hour, slowly cooled down to 1050 °C and then water quenched. The crystals were inspected on an AXS-GADDS texture goniometer for quality and crystal symmetry prior to X-ray intensity data collection on a four-circle Nonius Kappa diffractometer (CCD area detector and graphite monochromated MoK$_\alpha$ radiation, $\lambda = 0.071069$ nm). Orientation matrix and unit cell parameters were derived using the program DENZO [For details, see chapter 2]. No absorption correction was necessary because of the rather regular crystal shape and small dimensions of the investigated specimens. The structures were solved by direct methods and refined with the SHELXS-97 and SHELXL-97 programs [For details, see chapter 2] respectively. Rietveld refinement of the X-ray diffraction data was performed with the FULLPROF program [For details, see chapter 2] with the use of its internal tables for atomic form factors.

Prior to electron microprobe analyses, microstructure of as-cast and annealed samples were inspected by optical and scanning electron microscopy (SEM) on smooth surfaces prepared by grinding (SiC-paper) and polishing the resin mounted alloys with diamond pastes down to 1/4 µm grain size. Compositions were determined by Electron Probe Micro-Analyzers (EPMA; Carl Zeiss EVO 40 and a Supra55), equipped with a Pentafet Link energy dispersive X-ray (EDX) system. Pure elements were used as standards to carry out the deconvolution of overlapping peaks and background subtraction. Finally the X-ray intensities were corrected for ZAF effects using the INCA-Energy 300 software package [For details, see chapter 2]. In some cases a CAMEBAX SX50 wavelength dispersive X-ray microanalyser (XMA) was used at an

acceleration voltage of 15 kV at 20 nA sample current employing spectrometer crystals such as PET for TiK$_\alpha$ and LiF for the MnK$_\alpha$ radiation.

DTA analyses were performed in a Netzsch type DTA under a stream of argon with a heating rate of 5 Kmin^{-1}. Because of reactions with the Ta-crucible material, Mn-rich alloys were contained in alumina crucibles sealed in Ta-crucibles and prior to the DTA-runs were either annealed for several hours at 50 K below expected solid-solid transition temperatures or used in the as-cast state.

Thermal expansion from 4.2 to 300 K was measured in a miniature capacitance dilatometer [14], using the tilted plate principle [15,16]. For the measurement the sample is placed in a hole of the lower ring-like silver capacitance plate, which is separated from the upper silver capacitor plate by two needle bearings. This equipment can also be used under magnetic fields up to 9 Tesla.

Electrical resistivity measurements in a temperature range from 4.2 to 300 K were carried out in a He4 cryostat, using a home made equipment (four point technique), at temperatures above 300 K the electrical resistivity and the Seebeck coefficient were measured simultaneously in an ULVAC (model ZEM-3, Japan) equipment [17]. For magnetic measurement measurements a SQUID susceptometer was used.

11.3. Results and Discussion

11.3.1. Structural Chemistry

11.3.1.1. The crystal structure of Ti$_6$(Ti$_{1-x}$Mn$_x$)$_6$Mn$_{25}$, x=0.462 ("TiMn$_{\sim3}$")

Single crystal X-ray intensity data of the TiMn$_{\sim3}$-phase were fully indexed on an orthorhombic unit cell with lattice parameters a = 0.79070(3), b = 2.5830(1), c = 0.47943(2) nm. The analysis of systematic extinctions yielded two space group types: *Pba*2 and *Pbam* for which structure solutions were received employing direct methods. As practically identical reliability factors and residual electron densities were obtained from these two structure refinements and as an analysis of missing symmetry by program PLATON confirmed *Pbam*, we describe the structure in the highest symmetry space group *Pbam (*No. 55*)*. In total, 16 Wyckoff positions were found, out of

which, 3 positions were completely occupied by Ti, 10 positions by Mn only but three sites were randomly shared by Ti and Mn atoms.
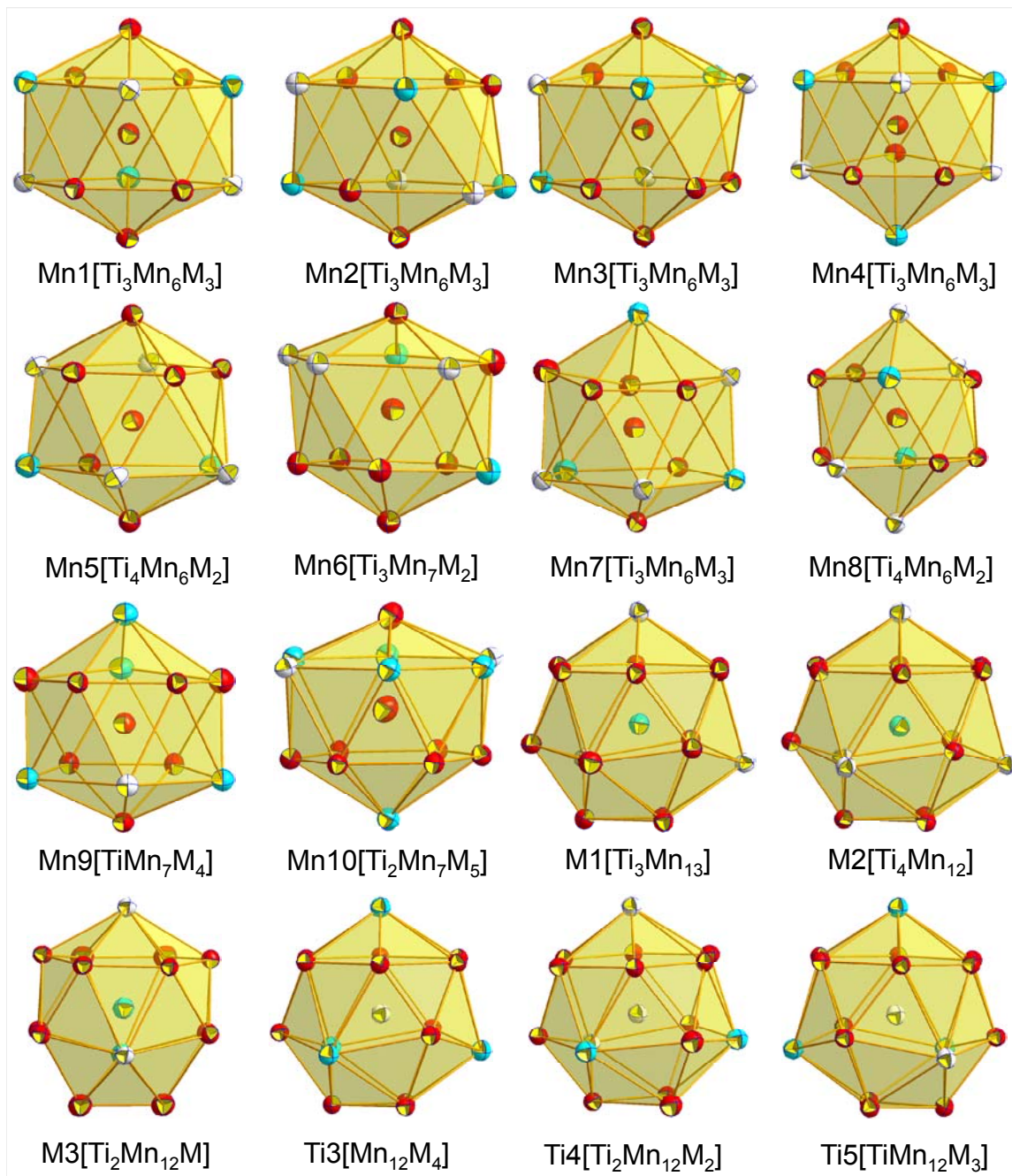

Fig. 1. Coordination polyhedra of $Ti_6(Ti_{1-x}Mn_x)_6Mn_{25}$, $x = 0.462$ ($TiMn_{\sim3}$) with anisotropic displacement parameters from X-ray single crystal refinement.

With the introduction of anisotropic displacement parameters, the structure refinement converged to R_{F2} = 0.0241 with negligible residual electron densities (1.57 and -1.49 e$^-$/10^{-3}nm^3). As there is a difference of only three electrons between Ti and Mn, it is very difficult to elucidate the exact ratio in the mixed site. Thus for sites M1 and M2 (Table 1), the ratio of Ti and Mn atoms in the statistical mixtures were fixed after EPMA but not M3 because even without constraints, temperature factors corresponded to M1 and M2.
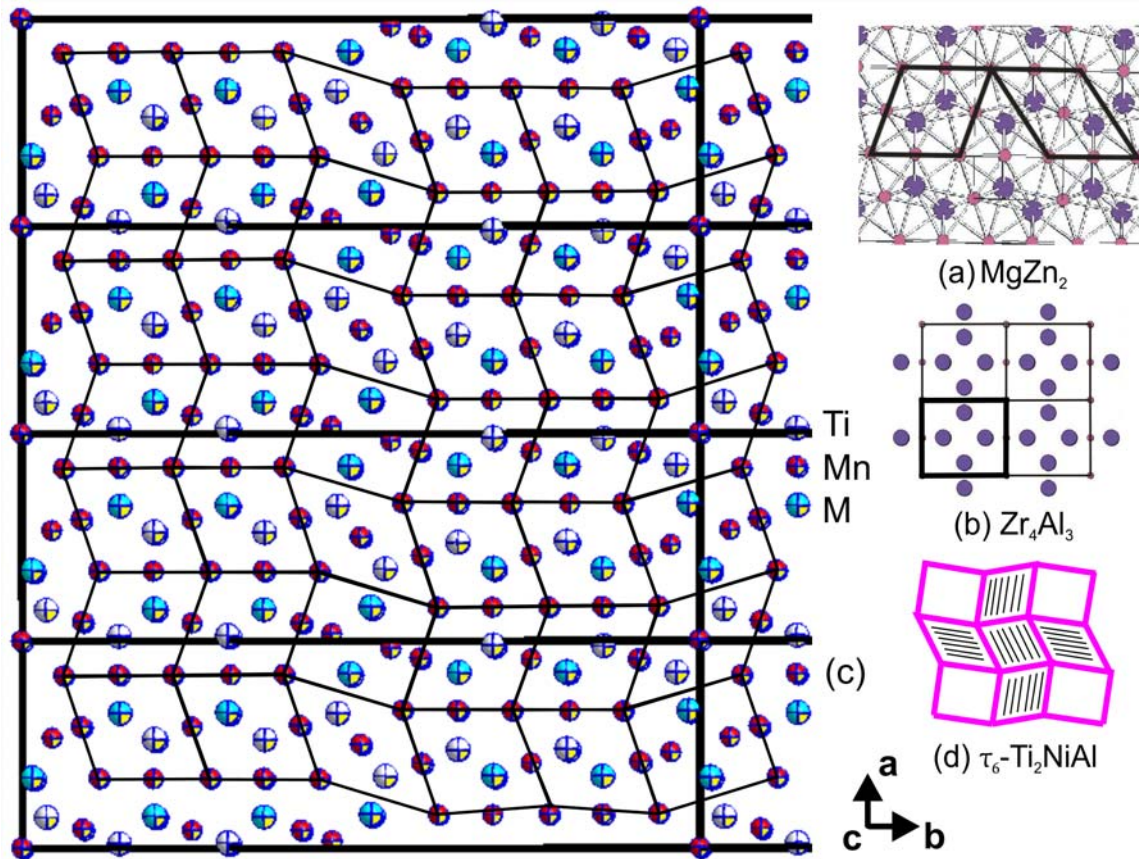

Fig. 2. Crystal structure of Ti$_6$(Ti$_{1-x}$Mn$_x$)$_6$Mn$_{25}$, x = 0.462 (TiMn$_{\sim3}$) as seen in projection along [001], a) solid thick lines highlight the building blocks of MgZn$_2$, b) Zr$_4$Al$_3$-unit highlighted with thick lines, c) multiple unit cells (thick lines) of Ti$_6$(Ti$_{1-x}$Mn$_x$)$_6$Mn$_{25}$, x = 0.462 shown in the left part, represent blocks of MgZn$_2$ and Zr$_4$Al$_3$ (thin lines) forming the structure of Ti$_6$(Ti$_{1-x}$Mn$_x$)$_6$Mn$_{25}$, x = 0.462, d) schematic arrangement of MgZn$_2$ (hexagonal ruled boxes) and Zr$_4$Al$_3$ units (square unruled boxes) as reported in Ti$_2$(Ti$_{0.16}$Ni$_{0.43}$Al$_{0.41}$)$_3$ [20].
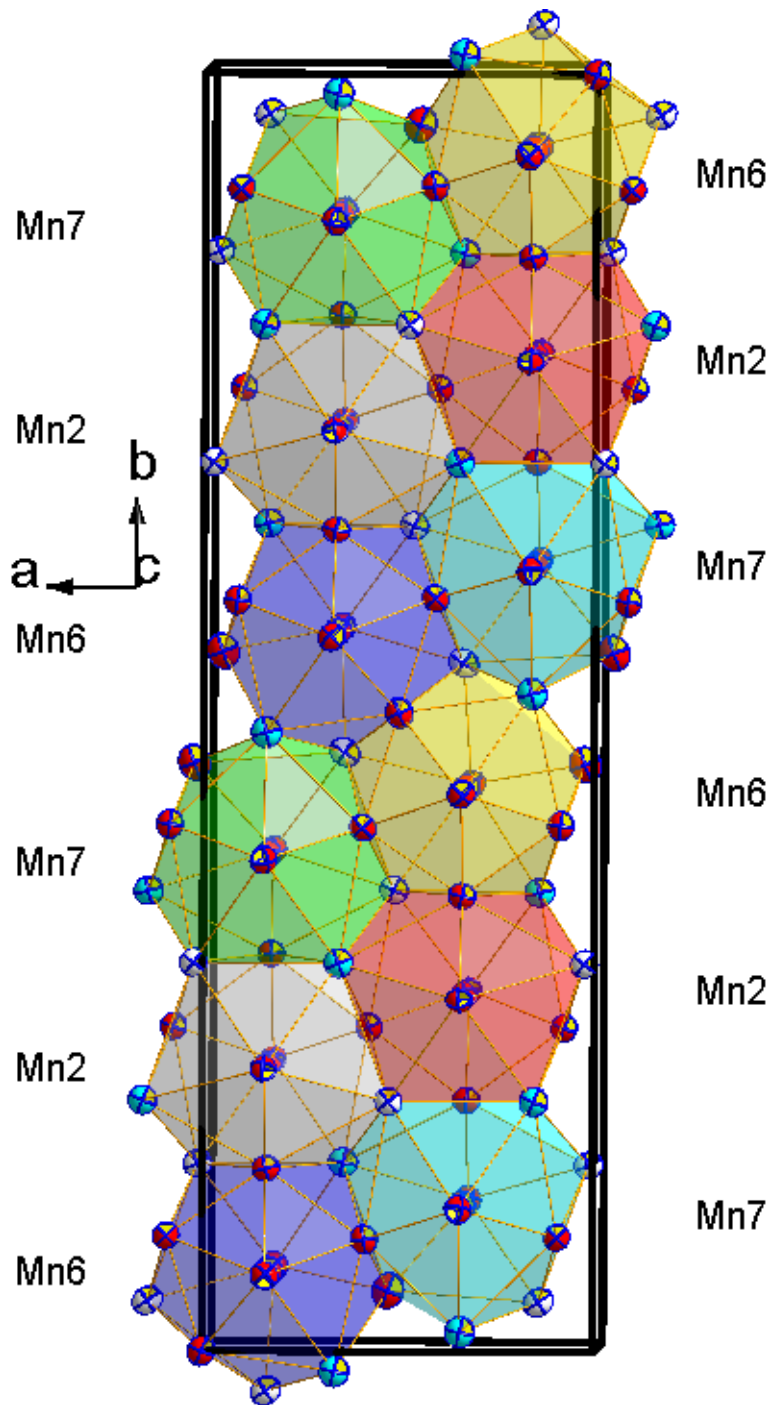
Fig. 3. Unit cell of $Ti_6(Ti_{1-x}Mn_x)_6Mn_{25}$, $x = 0.462$ ($TiMn_{\sim 3}$) presenting the stacking of various Frank-Kasper polyhedra.

From the refinement we arrive at a formula $Ti_6(Ti_{1-x}Mn_x)_6Mn_{25}$, $x = 0.462$ ($Ti_{24.9}Mn_{75.1}$), which is identical with the EPMA value and corresponds to the overall chemical formula $TiMn_3$. A full

set of crystallographic data is presented in Table 1. Coordination polyhedra for all crystallographically independent sites are shown in Fig. 1. A search for the structure type (Pearson symbol: oP88) in Pearson's Crystal Data [19] prompted no results suggesting $Ti_6(Ti_{1-x}Mn_x)_6Mn_{25}$ to be a unique structure type. Analyses of the atom arrangement in the unit cell of $Ti_6(Ti_{1-x}Mn_x)_6Mn_{25}$ revealed that this structure is made up of different layers which are perpendicular to the b-axis (Fig. 2). At the centre and at the border of the unit cell, perpendicular to the b-axis, a continuous layer is composed of alternate blocks of the hexagonal Laves phase structure ($MgZn_2$ type which is inherent to $TiMn_2$) and units of the Zr_4Al_3 structure in a ratio 50:50. Between these layers, there are two other layers, which are constructed purely from the building blocks of the $MgZn_2$ type. We have recently reported a similar structural arrangement of these building blocks for τ_6-$Ti_2(Ti_{0.16}Ni_{0.43}Al_{0.41})_3$ [20] (see also Fig. 2). Mn-Mn shortest interatomic distances of this phase (0.2213 nm) are comparable to the shortest Mn-Mn distances (0.2337 nm) observed for $TiMn_2$ [21] with $MgZn_2$ type and are close to those reported for $TiMn_{\sim4}$ (0.2291 nm) (see section 3.1.2). However, maximum Mn-Mn interatomic distances (0.2682 nm) are within those reported for $TiMn_2$ (0.2496 nm) and $TiMn_{\sim4}$ (0.2847 nm). Ti-Ti interatomic distances for this phase (0.2954-0.3010 nm) are very similar to $TiMn_2$ (0.2953-2970 nm) [21] as well as $TiMn_{\sim4}$ (0.2908-0.2939 nm). This small range between maximum and minimum interatomic distances proves a rather symmetric arrangement of Ti atoms inside the lattice.

Although Ti-Mn interatomic distances in $TiMn_{\sim3}$ (0.2729-0.3200 nm) are rather different from those reported in $TiMn_2$ (0.2832-0-2836 nm), they match those observed in $TiMn_{\sim4}$ (0.2665-0.3154 nm). Thus the similar interatomic distances in $TiMn_{\sim3}$ and $TiMn_{\sim4}$ reveal a closer structural relation between $TiMn_{\sim3}$ and $TiMn_{\sim4}$ than with $TiMn_2$.

The stacking of the coordination polyhedra in the unit cell of $Ti_6(Ti_{1-x}Mn_x)_6Mn_{25}$ is shown in Fig. 3. It should be noted that all the polyhedra shown have the coordination number 12 (distorted icosahedra).

11.3.1.2. The crystal structure of $Ti_8(Ti_xMn_{1-x})_6Mn_{39}$, x=0.187 ("TiMn$_{\sim4}$")

Although [8,9] defined the isotypism of $TiMn_{\sim4}$ with the structure type of the so-called R-phase $Mo_{0.38}Cr_{0.16}Co_{0.46}$ [10] from X-ray powder data, neither a detailed atom distribution nor

166

positional parameters specific for TiMn~4 were presented. From an alloy with nominal composition $Ti_{15.5}Mn_{84.5}$, which was annealed at 1200°C, we were able to select a single crystal suitable for X-ray structure determination. Lattice parameters obtained from the single crystal [a = 1.10070(2), c = 1.94411(4) nm] were in good agreement with those reported by Waterstrat [8] [a = 1.1003, 1.9446 nm]. Systematic extinctions confirmed the rhombohedral unit cell and proved consistency with two possible space group symmetries, *R*-3 and *R*3. As structure solution using direct methods in both these space groups revealed practically identical solutions, we describe the structure in the space group with the highest symmetry *R*-3 (No. 148). In total, 11 crystallographic sites were obtained out of which, 2 sites (6*c* and 18*f*) were fully occupied by Ti, 1 site (18*f*) was a statistical mixture of Ti and Mn and the rest were fully occupied by Mn. It should be mentioned, that by careful analyses of atomic displacement parameters (ADP) in combination with interatomic distances from a central atom to its ligands of the first coordination sphere it was possible to unambiguously define atom occupation in TiMn~4 despite the small differences in the scattering power of the atom species involved (3 electrons at *theta*=0). Introducing anisotropic displacement parameters, the structure refinement finally converged to R_{F2} = 0.029 with negligible residual electron density (1.42 and –1.19 $e^{-}/10^{-3}nm^3$). Results of the crystal structure determination are summarized in Table 1a,b. Lattice parameters, space group symmetry and Wyckoff symbol f^8c^2a confirm isotypism of $Ti_8(Ti_xMn_{1-x})_6Mn_{39}$, x = 0.187 with the so called R-phase reported in the Mo-Cr-Co system at $Mo_{0.38}Cr_{0.16}Co_{0.46}$ [10]. X-ray powder diffraction intensities collected from a polycrystalline sample are in good agreement with the intensities calculated from the structural model taken from the single crystal. Polyhedra for all sites are shown in Fig. 4. The formula from refinement is $Ti_8(Ti_xMn_{1-x})_6Mn_{39}$, x = 0.187 ($Ti_{17.2}Mn_{82.8}$) close to the EPMA value ($Ti_{16.3}Mn_{83.7}$). It must be noted that this phase has a considerable homogeneity region ranging from 16 to 20 % Ti in the temperature range from 900 °C to 1150 °C including the stoichiometric composition $TiMn_4$ at the Ti-rich boundary (see section 3.2). This homogeneity region arises from the randomly mixed position of Ti/Mn in 18*f*. Complete replacement of Ti by Mn in this site will result in a content of 15.1 at. % Ti, which corresponds well with the Mn-rich end of the homogeneity region of this phase at 16 % Ti. On the other hand, 50 % occupation of Ti on this site will result in 20.8 at % Ti, but the extension of the homogeneity region on the Ti-rich side is limited to 20 at. % Ti.

Table 1a: XSC data for $Ti_6(Ti_{1-x}Mn_x)_6Mn_{25}$, x = 0.462 (TiMn_~3), space group *Pbam*, #55 and $Ti_8(Ti_xMn_{1-x})_6Mn_{39}$, x = 0.187 (TiMn_~4), space group *R-3*, #148, standardized with program *Structure Tidy* [18]. Mo Kα-radiation 2Θ range (°) = 3≤2Θ≤70; ω-scans, Anisotropic displacement parameters in (10^2nm^2).

Parameter/compound	$Ti_6(Ti_{1-x}Mn_x)_6Mn_{25}$, x = 0.462	$Ti_8(Ti_xMn_{1-x})_6Mn_{39}$, x = 0.187
Composition from EPMA	$Ti_{24.9}Mn_{75.1}$	$Ti_{16.3}Mn_{83.7}$
Composition from refinement	$Ti_{24.9}Mn_{75.1}$	$Ti_{17.2}Mn_{82.8}$
Formula from refinement	$Ti_6(Ti_{1-x}Mn_x)_6Mn_{25}$, x = 0.462	$Ti_8(Ti_xMn_{1-x})_6Mn_{39}$, x = 0.187
a (nm)	0.79081(3)	a_{hex} = 1.1007(2)
b (nm)	2.58557(9)	b_{hex} = 1.1007(2)
c (nm)	0.47931(2)	c_{hex} = 1.94411(4)
Reflections in refinement	1867 Fo≥4σ(F_o) of 2353	1584≥4σ(F_o) of 1991
Number of variables	107	86
$R_F^2 = \Sigma|F_0^2-F_c^2|/\Sigma F_0^2$	0.0241	0.0293
R_{Int}	0.0135	0.0444
wR2	0.0581	0.0784
GOF	1.050	1.038
Extinction (Zachariasen)	0.00029(1)	0.0001(2)
Residual density e⁻/Å³; max; min.	1.57; -1.49	1.42; -1.19
Atom parameters		
Atom site 1	4*h*(x, y, ½)	6*c*(0, 0, z)
Occ.;	1.00 **Mn1**	1.00 **Ti1**
x, y, z;	0.08780(6), 0.24987(2)	0.42522(4)
U_{11}; U_{22}; U_{33}	0.0055(2); 0.0059(2); 0.0060(2)	0.0086(2); 0.0070(3)
$U_{23} = U_{13} = 0$; U_{12}	-0.0002(1)	0.0043(1)
Atom site 2	8*i*(x, y, z)	18*f*(x, y, z)
Occ.;	1.00 **Mn2**	1.00 **Mn1**
x, y, z;	0.33820(4), 0.27736(1), 0.24129(8)	0.24362(4), 0.42006(4), 0.16526(2)
U_{11}; U_{22}; U_{33}	0.0055(1); 0.0057(1); 0.0054(2)	0.0086(2); 0.0080(2)
U_{23}; U_{13}; U_{12}	0.0004(1), 0.0000(1), 0.0001(1)	0.0001(1), -0.0003(1), 0.0043(1)
Atom site 3	4*h*(x, y, ½)	18*f*(x, y, z)
Occ.;	1.00 **Mn3**	1.00 **Mn2**
x, y;	0.33776(6); 0.19291(2)	0. 19262(4), 0.22167(4), 0.23438(2)
U_{11}; U_{22}; U_{33}	0.0060(2); 0.0056(2); 0.0063(2)	0.0087(2); 0.0084(2); 0.0084(2)
$U_{23} = U_{13} = 0$; U_{12}	0.0000(1)	0.0004(1), 0.0001(1), 0.0040(1)
Atom site 4	4*h*(x, y, ½)	6*c*(0, 0, z)
Occ.;	**M1** = 0.64 **Ti** + 0.36 **Mn***	1.00 **Mn3**
x, y, z;	0.15214(7); 0.35590(2)	0.19459(4)
$U_{11}= U_{22}$; U_{33}	0.0089(2); 0.0082(2); 0.0086(3)	0.0089(2); 0.0087(3)
$U_{23} = U_{13} = 0$; U_{12}	-0.0001(2)	0.0045(1)
Atom site 5	4*g*(x, y, 0)	18*f*(x, y, z)
Occ.;	**M2** = 0.64 **Ti** + 0.36 **Mn***	1.00 **Ti2**
x, y;	0.15244(6); 0.19615(2)	0.10472(5), 0.39701(5), 0.28951(2)
U_{11}; U_{22}; U_{33}	0.0056(2); 0.0057(2); 0.0058(3)	0.0096(2); 0.0073(2); 0.0068(2)
$U_{23} = U_{13} = 0$; U_{12}	-0.0000(2)	0.0001(1), -0.0001(1), 0.0042(2)
Atom site 6	4*g*(x, y, 0)	18*f*(x, y, z)
Occ.;	1.00 **Ti3**	1.00 **Mn4**
x, y, z;	0.02385(7); 0.30412(2)	0.13914(4), 0.01949(4), 0.30480(2)
U_{11}; U_{22}; U_{33}	0.0061(2); 0.0061(2); 0.0060(3)	0.0084(2); 0.0083(2);

		0.0080(2)
$U_{23} = U_{13} = 0; U_{12}$	-0.0003(2)	0.0001(1), -0.0002(1), 0.0040(1)
Atom site 7	$4h$(x, y, ½)	$18f$(x, y, z)
Occ.;	1.00 **Ti4**	0.187(4) **Ti** + 0.813 **Mn**
x, y, z;	0.15168(7); 0.03516(2)	0.25766(4), 0.03674(4), 0.18145(2)
U_{11}; U_{22}; U_{33}	0.0074(2); 0.0067(2); 0.0060(3)	0.0092(2); 0.0100(2); 0.0103(2)
$U_{23} = U_{13} = 0; U_{12}$	-0.0010(2)	0.0002(1), 0.0010(1), 0.0047(1)
Atom site 8	$4h$(x, y, ½)	$18f$(x, y, z)
Occ.;	1.00 **Ti5**	1.00 **Mn6**
x, y, z;	0.02466(7); 0.14262(2)	0.10567(4), 0.38687(4), 0.06461(2)
U_{11}; U_{22}; U_{33}	0.0064(2); 0.0060(2); 0.0061(3)	0.0082(2); 0.0092(2); 0.0078(2)
$U_{23} = U_{13} = 0; U_{12}$	-0.0003(2)	0.0001(1), -0.0001(1), 0.0042(1)
Atom site 9	$4g$(x, y, 0)	$18f$(x, y, z)
Occ.;	1.00 **Mn4**	1.00 **Mn7**
x, y, z;	0.33713(6); 0.35695(2)	0.26519(4), 0.11339(4), 0.03567(2)
U_{11}; U_{22}; U_{33}	0.0060(2); 0.0055(2); 0.0063(2)	0.0093(2); 0.0109(2); 0.0099(2)
$U_{23} = U_{13} = 0; U_{12}$	0.0002(1)	0.0009(1), 0.0008(1), 0.0051(1)
Atom site 10	$4g$(x, y, 0)	$18f$(x, y, z)
Occ.;	1.00 **Mn5**	1.00 **Mn8**
x, y, z;	0.09203(6); 0.08999(2)	0.12788(4), 0.17501(4), 0.10203(2)
U_{11}; U_{22}; U_{33}	0.0058(2); 0.0058(2); 0.0064(2)	0.0116(2); 0.0113(2); 0.0090(2)
$U_{23} = U_{13} = 0; U_{12}$	-0.0003(2)	-0.0001(1), 0.0009(1), 0.0061(2)
Atom site 11	$8i$(x, y, z)	$3a$(0, 0, 0)
Occ.;	1.00 **Mn6**	1.00 **Mn9**
x, y, z;	0.33370(4); 0.43879(1); 0.26914(8)	-
$U_{11} = U_{22}$; U_{33}	0.0062(1); 0.0057(2)	0.0094(3); 0.0104(4)
$U_{23} = U_{13} = 0; U_{12}$	-0.0003(1)	0.0047(1)
Atom site 12	$8i$(x, y, z)	-
Occ.;	1.00 **Mn7**	-
x, y, z;	0.33927(4); 0.11345(1); 0.25448(7)	-
U_{11}; U_{22}; U_{33}	0.0060(1); 0.0064(1); 0.0060(2)	-
U_{23}; U_{13}; U_{12}	-0.0001(1); 0.0000(1); -0.0001(1)	-
Atom site 13	$2a$(0, 0, 0)	-
Occ.;	1.00 **Mn8**	-
U_{11}; U_{22}; U_{33}	0.0064(3); 0.0074(3); 0.0069(3)	-
$U_{23} = U_{13} = 0; U_{12}$	-0.0005(2)	-
Atom site 14	$4g$(x, y, 0)	-
Occ.;	1.00 **Mn9**	-
x, y;	0.08549(6); 0.41229(2)	-
U_{11}; U_{22}; U_{33}	0.0058(2); 0.0068(2); 0.0066(2)	-
$U_{23} = U_{13} = 0; U_{12}$	-0.0001(2)	-
Atom site 15	$4h$(x, y, ½)	-
Occ.;	1.00 **Ti5**	-
x, y;	0.03627(6); 0.45634(2)	-
U_{11}; U_{22}; U_{33}	0.0086(2); 0.0107(2); 0.0087(3)	-
$U_{23} = U_{13} = 0; U_{12}$	0.0009(2)	-

Atom site 16	4g(x, y, 0)	-
Occ.;	**M3** = 0.332(4) **Ti** + 0.668 **Mn**	-
x, y;	0.33938(6); 0.01551(2)	-
U_{11}; U_{22}; U_{33}	0.0075(2); 0.0082(2); 0.0084(2)	-
$U_{23} = U_{13} = 0$; U_{12}	-0.0001(2)	-

*Fixed after EPMA.

Table 1b: Interatomic distances (nm) for $Ti_8(Ti_xMn_{1-x})_6Mn_{39}$ (TiMn~4), Standard deviation ≤0.0002.

Interatomic distances [nm], Standard deviation ≤0.0020								
Ti1–	3Mn4	0.2747		−1Mn2	0.2771		−1Mn1	0.2490
	−3Mn1	0.2774		−1Mn6	0.2772		−1Mn7	0.2556
	−3Mn1	0.2803		−1Mn4	0.2796		−1Mn7	0.2566
	−3Mn6	0.2886		−1Mn1	0.2801		−1M2	0.2568
	−1Ti1	0.2908		−1Mn2	0.2816		−1Ti2	0.2750
	−3Ti2	0.2923		−1Mn6	0.2915		−1Ti2	0.2772
Mn1–	1Mn2	0.2380		−1Ti1	0.2923		−1M1	0.2844
	−2Mn1	0.2380		−1Ti2	0.2939		−1Ti1	0.2886
	−1Mn6	0.2390		−1M2	0.3028		−1Ti2	0.2915
	−1Mn6	0.2490		−1Mn7	0.3154	Mn7–	1Mn8	0.2331
	−1Mn8	0.2641	Mn4–	1Mn6	0.2291		−1Mn6	0.2556
	−1Ti2	0.2720		−1Mn2	0.2421		−1Mn6	0.2566
	−1M1	0.2768		−1Mn2	0.2442		−1Mn2	0.2616
	−1Ti1	0.2774		−2Mn4	0.2488		−1Mn4	0.2618
	−1M1	0.2775		−1Mn3	0.2579		−1Mn9	0.2630
	−1Ti2	0.2801		−1Mn7	0.2618		−1Ti2	0.2711
	−1Ti1	0.2803		−1Ti2	0.2665		−1Mn8	0.2821
Mn2–	1Mn6	0.2366		−1M1	0.2691		−1Mn8	0.2847
	−1Mn1	0.2380		−1Ti1	0.2747		−2Mn7	0.2891
	−1Mn4	0.2421		−1Ti2	0.2767		−1M1	0.2913
	−1Mn3	0.2424		−1Ti2	0.2796		−1M1	0.2946
	−1Mn4	0.2442	M1–	1M1	0.2554		−1Ti2	0.3154
	−1Mn7	0.2616		−1Mn8	0.2615	MN8–	1Mn7	0.2331
	−1M1	0.2638		−1Mn2	0.2638		−1Mn3	0.2494
	−1Mn8	0.2651		−1Mn3	0.2669		−1Mn6	0.2568
	−1M1	0.2678		−1Mn2	0.2678		−1M1	0.2615
	−1M1	0.2722		−1Mn4	0.2691		−1Mn9	0.2630
	−1Ti2	0.2771		−1Mn2	0.2722		−1Mn1	0.2641
	−1Ti2	0.2816		−1Ti2	0.2752		−1Mn2	0.2651
Mn3–	3Mn2	0.2424		−1Mn1	0.2768		−1Mn7	0.2821
	−3Mn8	0.2494		−1Mn1	0.2775		−1Mn7	0.2847
	−3Mn4	0.2579		−1Mn6	0.2844		−1M1	0.2857
	−3M1	0.2669		−1Mn8	0.2857		−1M1	0.2986
Ti2–	1Mn4	0.2665		−1Mn7	0.2913		−2Mn8	0.2990
	−1Mn7	0.2711		−1Mn7	0.2946		−1Ti2	0.3028
	−1Mn1	0.2720		−1Mn8	0.2986	Mn9–	6Mn8	0.2630
	−1Mn6	0.2750	Mn6–	1Mn4	0.2291		−6Mn7	0.2630
	−1M1	0.2752		−1Mn2	0.2366			
	−1Mn4	0.2767		−1Mn1	0.2390			

The crystal structure of the R-phase belongs to the socalled tetrahedrally close packed structures with interpenetrating Frank-Kasper polyhedra i.e. coordination polyhedra with 12, 14, 15 or 16 vertices which fill space completely leaving exclusively tetrahedral interstices. A complete listing of tetrahedrally closed structures (including also Zr_4Al_3 and $V_2(Co,Si)_3$) is presented in Typix [22]. Kumara et. al. [10] showed the stacking sequence of coordination polyhedra along the c-axis present in the Mo-Co-Cr R-phase CN 16-12-12-12-16. An identical sequence is present in $Ti_8(Ti_xMn_{1-x})_6Mn_{39}$ and is shown in Fig. 5 in comparison with $TiMn_2$ ($MgZn_2$ type) with stacking sequence of CN 12-12-12 and with $TiMn_{\sim3}$ with a stacking of polyhedra CN 12-12-12-12 along the b-axis. Figure 5 reveals the close structural relations between the Mn-rich compounds $TiMn_2$, $TiMn_{\sim3}$ and $TiMn_{\sim4}$.
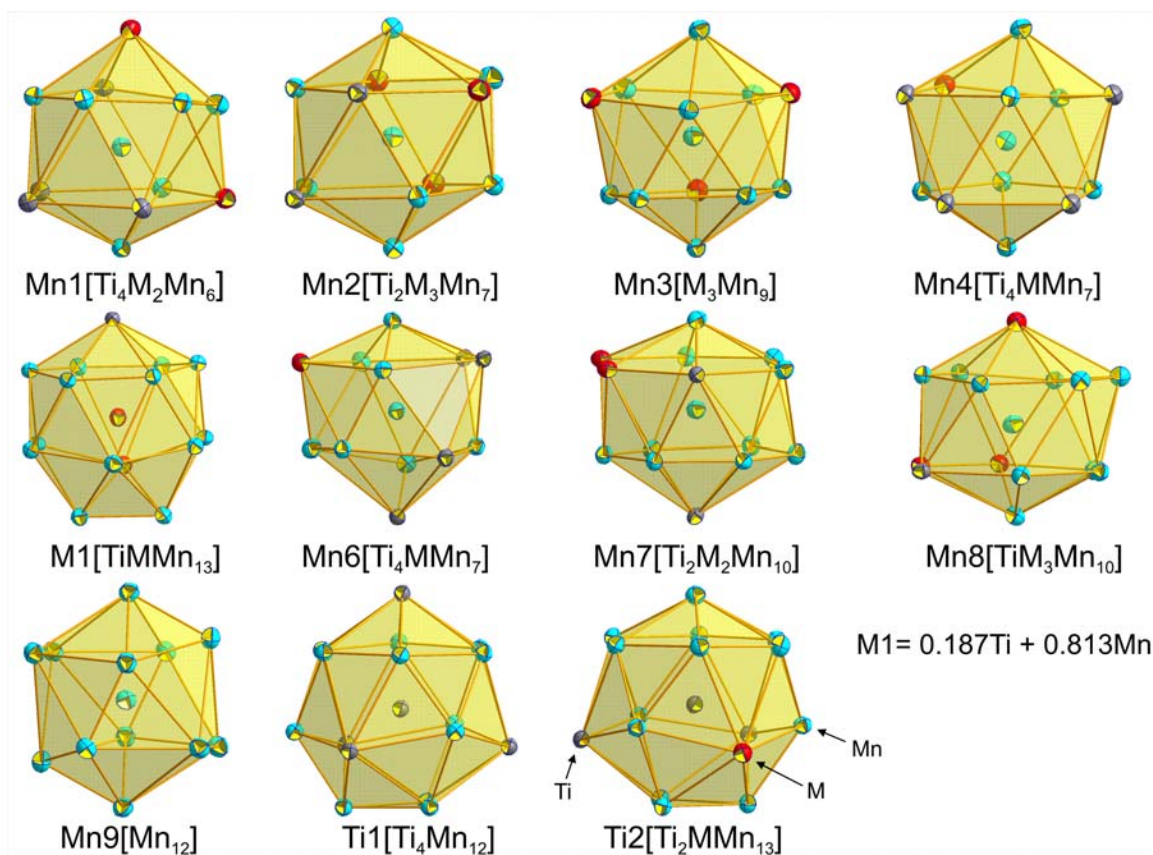
Fig. 4. Polyhedra of $Ti_8(Ti_xMn_{1-x})_6Mn_{39}$ ($TiMn_{\sim4}$) showing atoms with anisotropic displacement parameters from X-ray single crystal refinement.

It is interesting to note that besides $Ti_{17.2}Mn_{82.8}$, the only binary Mn-containing R-phase is found in the Mn-Si system at $Mn_{85.5}Si_{14.5}$ [23] where again the R-phase appears as a neighboring phase to the modifications of (Mn).
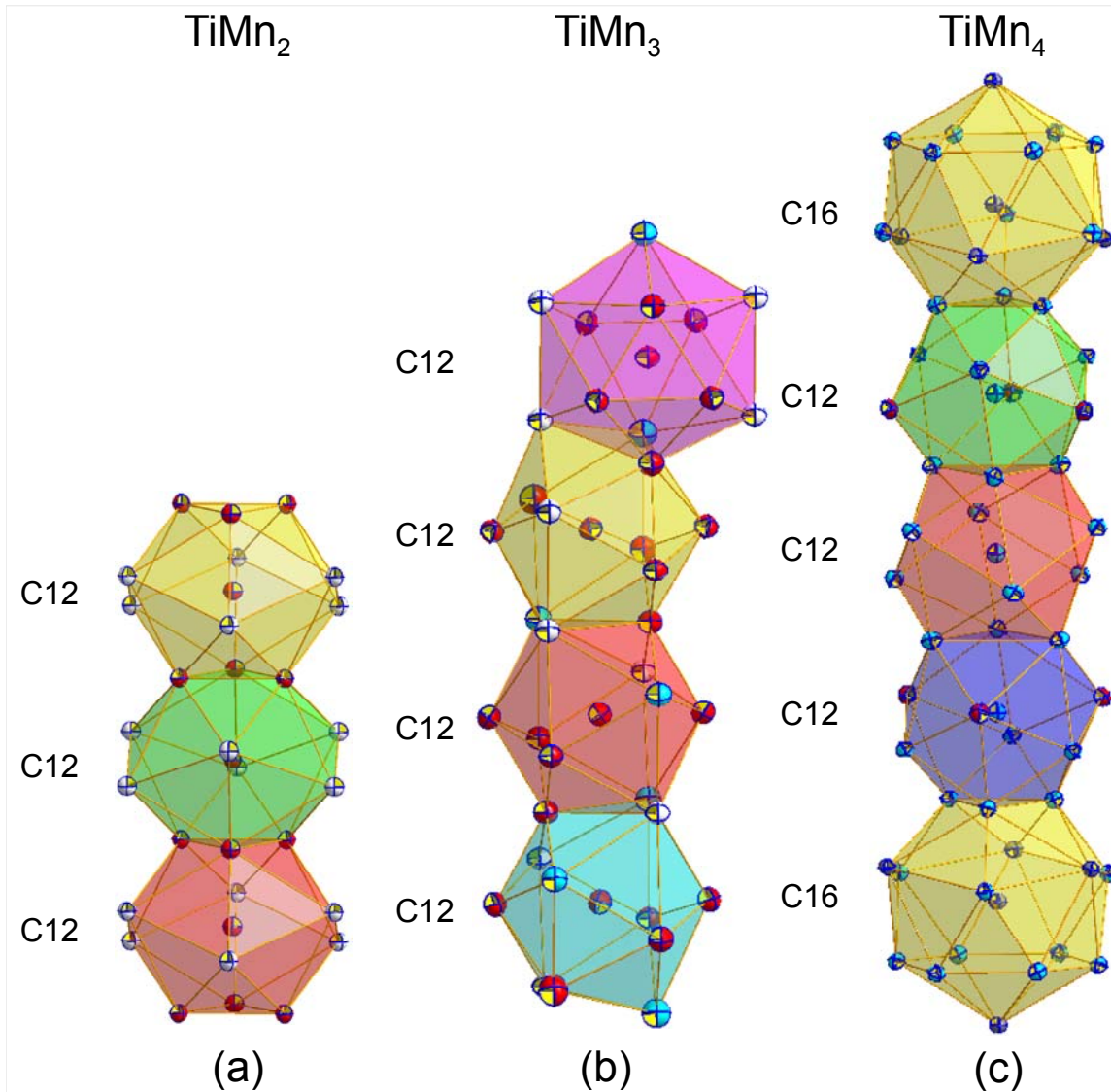

Fig. 5. Stacking of Frank-Kasper polyhedra in Mn-rich titanium manganides. a) stacking of polyhedra in $TiMn_2$ (MgZn$_2$ type) along c-axis, b) stacking of polyhedra in $TiMn_{\sim3}$ along b-axis, c) stacking of polyhedra in $TiMn_{\sim4}$ along c-axis.

11.3.2. Phase equilibria

All the phases, their range of existance and crystallographic data pertinent to the Mn-rich part of the phase diagram (>60 at.% Mn) are presented in Table 2. Our main focus in the present work was on the phase relations involving TiMn$_{\sim3}$ and TiMn$_{\sim4}$, their homogeneity ranges and their temperature range of existance. Figure 6 shows the Ti-Mn binary phase diagram based on the experimental results obtained in this study. Thermal analyses (DTA) on a number of samples, which were annealed at 800 °C prior to the DTA heating runs, were employed to determine the various reaction isotherms in the Mn-rich part of the Ti-Mn system. Table 3 summarizes the different DTA thermal effects observed and the conclusion made on the basis of these experiments. A temperature of 1209 °C was assigned to the eutectic reaction L$\Leftrightarrow$TiMn$_{\sim4}$+δ (Mn). Both compounds TiMn$_{\sim3}$ and TiMn$_4$ form through peritectic reactions at 1248 °C and 1225 °C, respectively (see Table 3b). All these temperatures are very close to those reported in the literature (see Table 2).

Table 2. Crystallographic data of solid phases in the Ti-Mn system.

Phase Temperature range (°C)	Space group Prototype	Lattice parameters (nm)			Comments
		a	b	c	
(αTi) ≤ 882 [24]	$P6_3/mmc$ Mg	0.29506		0.46835	[24]
(βTi$_{1-x}$Mn$_x$)	Im-$3m$ W	0.3182- 0.3247			0.05 ≤ x ≤ 0.18 at 800 °C [25]
(βTi) 1670-882 [24]		0.33065			[24]
(αMn)(rt) ≤ 727 [24]	I-$43m$ W	0.89126			[24]
(βMn)(ht1) ≤ 1100 [24]	$P4_132$ βMn	0.63152			[24]
(γMn)(ht2) ≤ 1138 [24]	Fm-$3m$ Cu	0.3860			[24]
(δMn)(ht3) ≤ 1246 [24]	Im-$3m$ W	0.29315			[24]
TiMn$_2$ ≤ 1246 [24]	$P6_3/mmc$ MgZn$_2$	0.4811 - 0.4880		0.7892 – 0.7992	[9] 32.0-44.2 % Ti content
TiMn$_{\sim3}$ 1250-960 [24]	*Pbam* Own	0.79081(3)	2.58557(9)	0.47931(2)	[This work]
TiMn$_{\sim4}$ 1230-930 [24]	$R\overline{3}$ Mo$_{0.38}$Cr$_{0.16}$Co$_{0.46}$	1.10003[1]		1.9446	[8]

[1]Hexagonal setting.

Table 3a. Thermal effects (DTA) observed in selected samples (nominal composition).

Mn	Ti	T (°C)	H.T.[*]	Comments
80	20	1211.7	800°C	Heating
		1249.7	800°C	Heating
		1254.1	800°C	Heating
		1272.6	800°C	Heating

85	15	1209.3	800°C	Heating
		1212.2	800°C	Heating
		1229	800°C	Heating
		1237	800°C	Heating
		1239.5	800°C	Heating
90	10	1142.6	800°C	Heating
		1209	800°C	Heating
		1212.2	800°C	Heating
		1219.5	800°C	Heating
		1221.9	800°C	Heating
92	8	1207.1	800°C	Heating
		1213	800°C	Heating
		1225	800°C	Heating
		1226.5	800°C	Heating
89.5	10.5	1204.9	800°C	Heating
		1211.3	800°C	Heating
		1216.7	800°C	Heating
90.5	9.5	1209.4	800°C	Heating
		1242.9	800°C	Heating

[*] Heat treatment.

Table 3b. Binary reaction isotherms.

Reaction	Temperature (°C)
$L+TiMn_2 \Leftrightarrow TiMn_{\sim 3}$	1248 ± 10
$L+TiMn_{\sim 3} \Leftrightarrow TiMn_{\sim 4}$	1225 ± 10
$L \Leftrightarrow TiMn_{\sim 4} + \delta(Mn)$	1209 ± 10
$TiMn_{\sim 4} + \delta(Mn) \Leftrightarrow \alpha(Mn)$	1160 ± 10
$\alpha(Mn) + \delta(Mn) \Leftrightarrow \beta(Mn)$	$\sim 1142\pm 15$

Decomposition on cooling of the $TiMn_{\sim 3}$ and $TiMn_{\sim 4}$ phases, however, was not observed in DTA, perhaps due to sluggish reaction kinetics. Therefore, an isothermal annealing and quenching technique was used instead. Although, $TiMn_{\sim 3}$ and $TiMn_{\sim 4}$ are reported in literature [9] to decompose at 960 °C and 930 °C, respectively, we did not observe any decomposition of these phases above 810 °C for 35 days in samples already annealed at 1180 °C. However, samples rich in $TiMn_{\sim 3}$ showed the appearance of $\alpha(Mn)$ at the grain boundaries after 30 days of annealing at 900 °C. No change was observed in the sample, containing a majority of $TiMn_{\sim 4}$ at 900 °C even after anneal at 810 °C for 35 days. As cast samples directly annealed at 800 °C consist of all the four phases [$TiMn_2$, $TiMn_{\sim 3}$, $TiMn_{\sim 4}$, $\alpha(Mn)$] present in this part of the phase diagram showing that the reaction kinetics is very slow in this temperature range and it is very difficult to reliably define the decomposition temperatures for these phases. In samples annealed at 1180 °C only two phases (80 % $TiMn_{\sim 3}$ + 20 % $TiMn_{\sim 4}$) have been detected by EPMA. Subsequent annealing at 1000 °C also revealed the presence of only two phases ($TiMn_{\sim 3}$ +

TiMn$_{\sim4}$). Whereas the composition for TiMn$_{\sim3}$ and TiMn$_{\sim4}$ remained almost same at both temperatures, the X-ray powder diffraction pattern for TiMn$_{\sim3}$ changed significantly at both temperatures with respect to the as cast condition, suggesting a phase transition to a low temperature modification of TiMn$_{\sim3}$. Waterstrat [9] also observed some effects in his alloys and suggested a profuse twinning or a martensitic structure. Further investigations are needed to define the exact transformation temperature for this phase as well as the crystal structure of the low temperature modification.
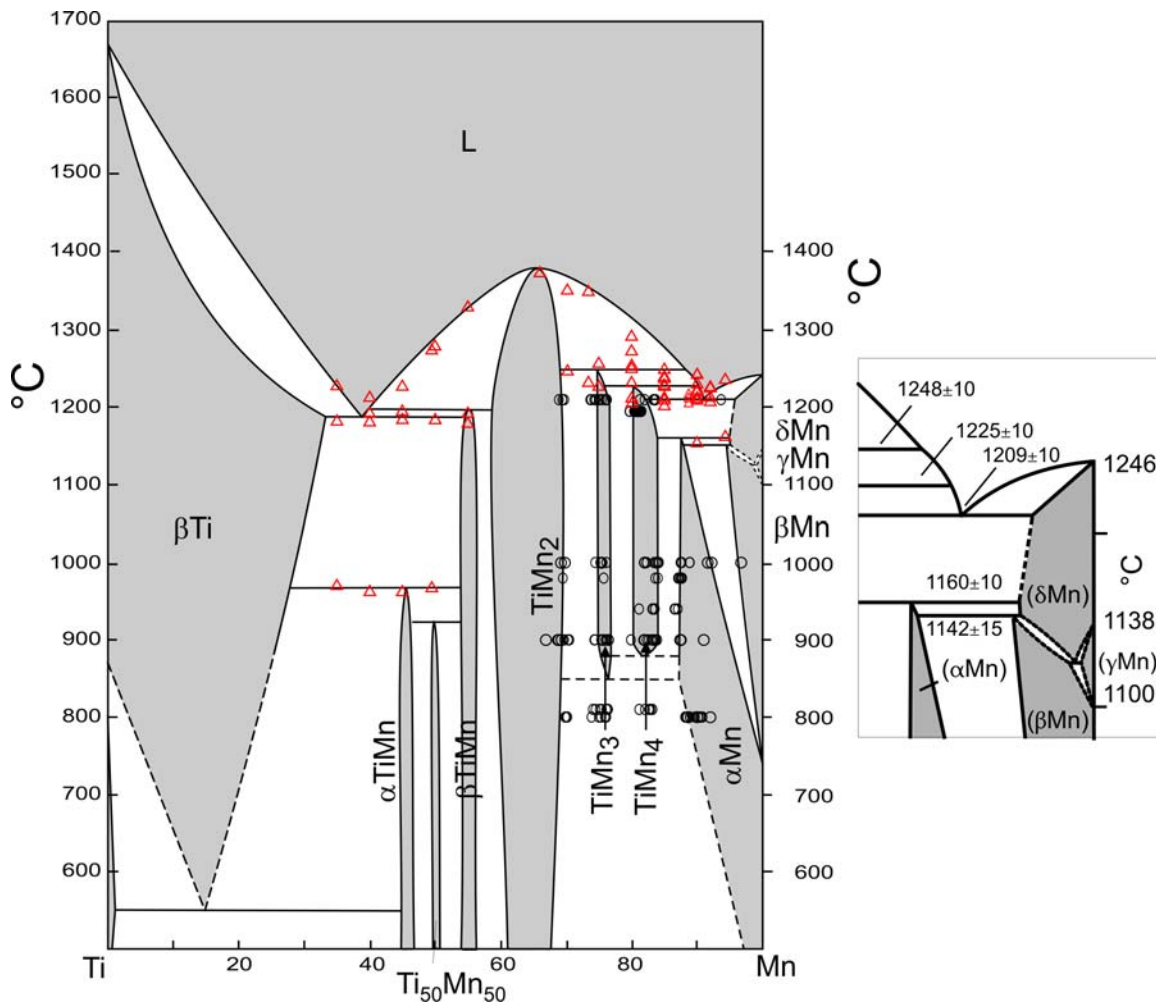
Fig. 6. Ti-Mn binary phase diagram in the Mn-rich corner. Circles show the measurement points obtained from EPMA while the triangles represent DTA data points on heating.
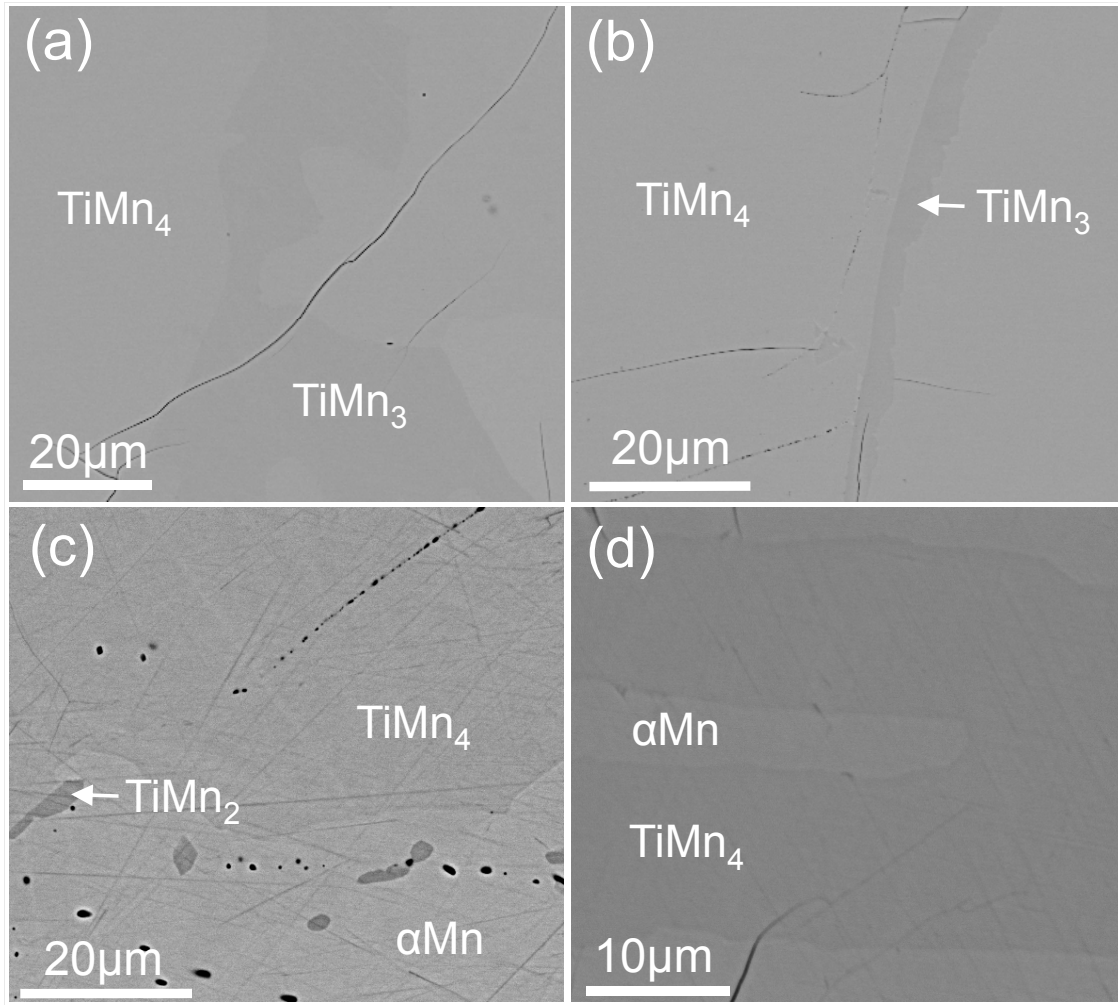
Fig. 7. Micrograph of selected alloys of the Ti-Mn system, (a) $Ti_{21.6}Mn_{78.4}$ (composition from EPMA, at. %, annealed at 1180 °C), reveals two-phase equilibrium $Ti_{19.6}Mn_{80.4}$ (shown as $TiMn_4$) + $Ti_{24.2}Mn_{75.8}$ (shown as $TiMn_3$), (b) $Ti_{20.1}Mn_{79.9}$ (composition from EPMA, at. %, first annealed at 1210 °C for two days and then at 810 °C for 35 days), represents two-phase equilibrium $Ti_{19.8}Mn_{80.2}$ (shown as $TiMn_4$) + $Ti_{23.7}Mn_{76.3}$ (shown as $TiMn_3$), (c) $Ti_{14.4}Mn_{85.6}$ (composition from EPMA, at. %, annealed at 1000 °C), shows $Ti_{15.6}Mn_{84.4}$ (shown as $TiMn_4$) + $Ti_{12.5}Mn_{87.5}$ (represented as αMn) and traces of $TiMn_2$, (d) $Ti_{11.7}Mn_{88.3}$ (composition from EPMA, at. %, after DTA), reveals two-phase equilibrium $Ti_{15.0}Mn_{85.0}$ (shown as $TiMn_4$) + $Ti_{9.5}Mn_{90.5}$ (represented as αMn).

$TiMn_{\sim3}$ and $TiMn_{\sim4}$ are shown as line compounds in the phase diagram given by Massalski [24]. However, we found considerable homogeneity regions for both, $TiMn_{\sim4}$ and $TiMn_{\sim3}$. For temperatures 900<T<1200°C, the range of existence of $TiMn_{\sim4}$ is in between 16.0 and 20 at. %

Ti, whereas TiMn$_{\sim3}$ has a slightly narrower homogeneity region and exists between 23.5 and 26 at. % Ti.

Micrographs of selected alloys are shown in Fig. 7. A sample Ti$_{21.6}$Mn$_{78.4}$ (compositions are given as obtained from EPMA, represented in at. % in all micrographs) annealed at 1180 °C reveals the equilibrium between TiMn$_{\sim3}$ (Ti$_{24.2}$Mn$_{75.8}$) and TiMn$_{\sim4}$ (Ti$_{19.6}$Mn$_{80.4}$) (Fig. 7a). To find the reliable decomposition temperature, one sample Ti$_{20.1}$Mn$_{79.9}$ was first annealed at 1210 °C for two days and then it was annealed at 810 °C for 35 days. It revealed a two-phase equilibrium between TiMn$_{\sim4}$ (Ti$_{19.8}$Mn$_{80.2}$) and TiMn$_{\sim3}$ (Ti$_{23.7}$Mn$_{76.3}$) without any sign of decomposition (Fig. 7b). Another sample Ti$_{14.4}$Mn$_{85.6}$, which was annealed at 1000 °C (directly from as cast) showed mainly two phases TiMn$_{\sim4}$ (Ti$_{15.6}$Mn$_{84.4}$) and αMn (Ti$_{12.5}$Mn$_{87.5}$) with some traces of TiMn$_2$ (Fig. 7c). One of the samples with composition Ti$_{11.7}$Mn$_{88.3}$ after runs in DTA is shown in Fig. 7d. It shows the presence of a two-phase equilibrium between TiMn$_{\sim4}$ (Ti$_{15.0}$Mn$_{85.0}$) and αMn (Ti$_{9.5}$Mn$_{90.5}$).

11.3.3. Physical properties of Ti$_8$(Ti$_x$Mn$_{1-x}$)$_6$Mn$_{39}$, x = 0.187 (TiMn$_{\sim4}$).

Figure 8 shows the thermal expansion Δl/l$_0$ of Ti$_8$(Ti$_x$Mn$_{1-x}$)$_6$Mn$_{39}$, x = 0.187 (TiMn$_{\sim4}$) as a function of temperature. It is obvious that Δl/l$_0$ decreases linearly from room temperature to about 150 K, whereas for temperatures below 150 K a nonlinear behavior is evident as also observed for skutterudites [26] or clathrates [27]. The thermal expansion coefficient α follows from a temperature derivative of the length change

$$\alpha = \left(\frac{\partial \Delta l}{\partial T} \right) \frac{1}{l_0} . \qquad\qquad (11.1)$$

i.e., α = 1.4*10^{-5} K^{-1} was calculated in the temperature range from 180 – 300 K.

The thermal expansion was analyzed as a function of temperature following the semi-classical treatment by Mukherjee (details are described in Ref. [28]) taking into account three- and four-phonon interactions and considering an anharmonic potential, using both the Debye model for the acoustic phonons, and the Einstein approximation for the optical modes. The length change Δl/l (T$_0$) is given by

$$\frac{\Delta l}{l(T_0)} = \frac{\langle x \rangle_T - \langle x \rangle_{T_0}}{x_0} \qquad \langle x \rangle_T = \frac{\gamma}{2}T^2 + \frac{3g}{4c^2}\left[\varepsilon - G\varepsilon^2 - F\varepsilon^3\right]$$

$$\varepsilon = \left\{ \left(\frac{3}{p}\right)3k_B T\left(\frac{T}{\theta_D}\right)^3 \int_0^{\frac{\theta_D}{T}} \frac{z^3 dz}{e^z - 1} + \left(\frac{p-3}{p}\right)\frac{k_B \theta_E}{e^{\theta_D/T} - 1} \right\} \qquad (11.2)$$

where γ is the electronic contribution to the average lattice displacement, θ_D is the Debye temperature, θ_E is the Einstein temperature and p is the average number of phonon branches actually excited over the temperature range. G, F, c and g are further material dependent constants. The Debye temperature, $\theta_D = 347$ K, was obtained from least square fits of equations (2) to the experimental data (Fig. 9), a value that differs not much from the one extracted from the resistivity fit ($\theta_D = 441$ K; see below). Magnetostriction measurements at 4.2 K with a magnetic field of 9 Tesla did not show any magnetic ordering.
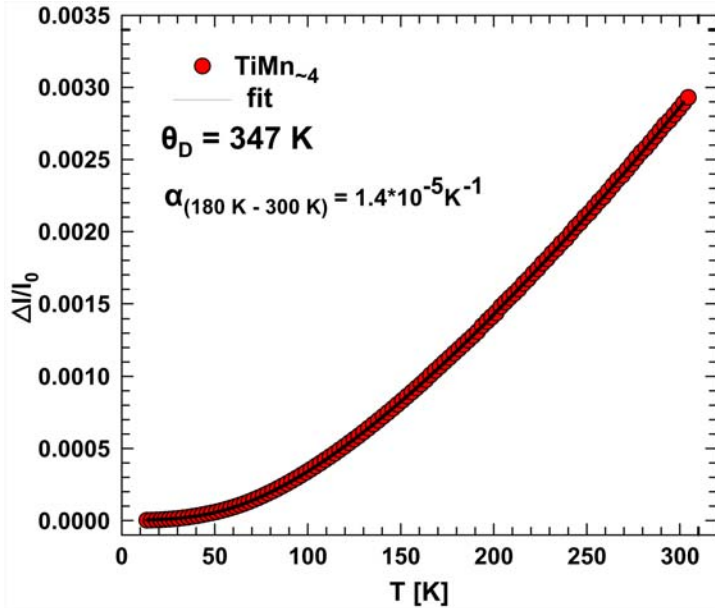

Fig. 8. Thermal expansion of TiMn$_{\sim4}$ versus temperature.

Figure 9 shows the magnetisation over the magnetic field in dependence of the temperature. At low temperatures paramagnetism is observed, revealing a susceptibility of $5.6*10^{-6}$ emu/mol. Ferromagnetic impurity, very unlikely to be intrinsic, could be determined with a Curie temperature at about 50 K. At higher temperatures and with higher magnetic fields

antiferromagnetic behaviour with a high T-Neel could be possible, but with the current fields and at the current temperatures this behaviour cannot be distinguished from paramagnetism.

In Fig. 9 (at the right hand side) linear magnetisation with a very small hysteresis at low fields ($<1\mu_0H$) was observed for all four temperatures (4 K, 8 K, 13 K, 18 K).
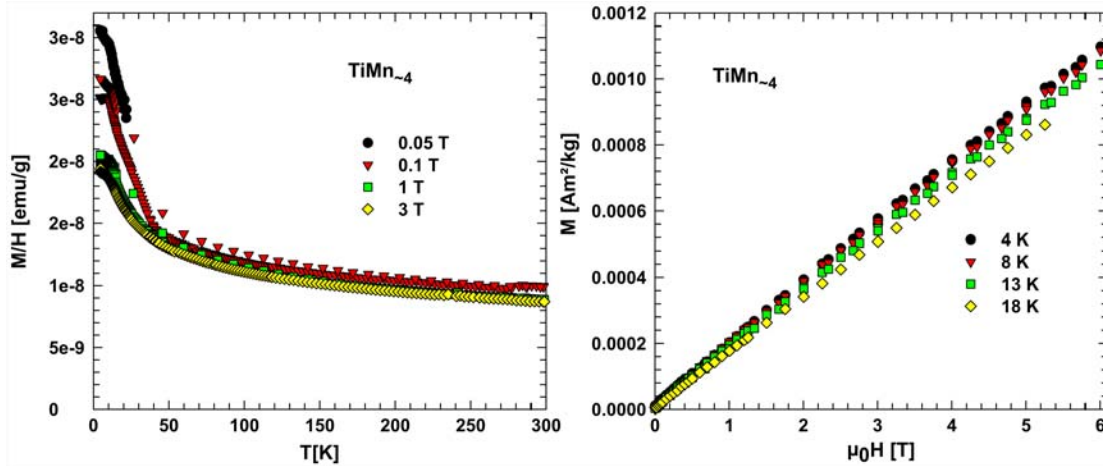

Fig. 9. M/H of TiMn$_{\sim4}$ versus temperature (left side). Graph on the right side represents isothermal magnetisation M of TiMn$_{\sim4}$ versus magnetic field for various temperatures.
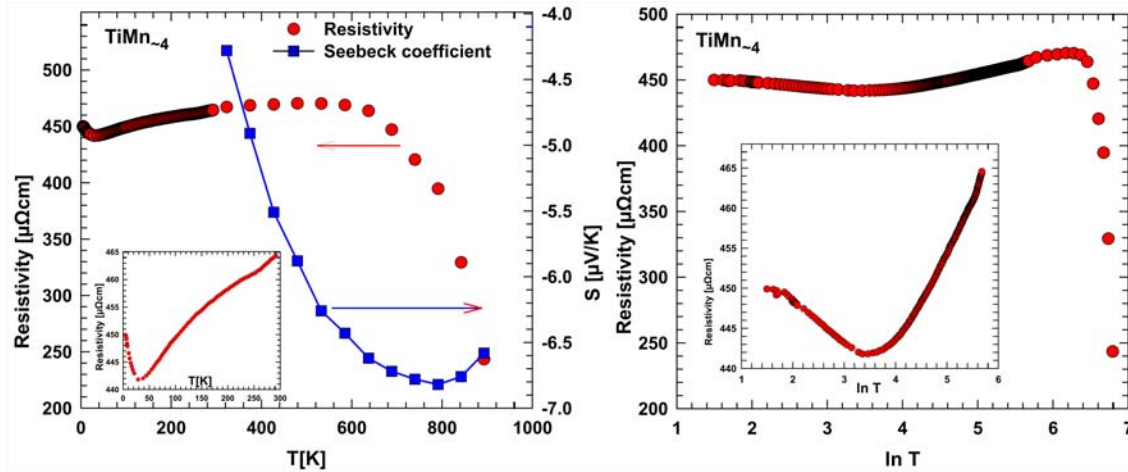

Fig. 10. Electrical resistivity and thermopower of TiMn$_{\sim4}$ in dependence of temperature (left side of figure). Insert: electrical resistivity versus temperature < 300 K. Graph on the right side represents electrical resistivity of TiMn$_{\sim4}$ in dependence of temperature (ln-scale). Insert: electrical resistivity versus temperature < 300 K.

Electrical resistivity (Fig.10, left) is increasing slightly above about 30 K with a plateau-like behavior between 500 and 620 K and a decrease for temperatures above 620 K. Ferromagnetic

impurities, as revealed from magnetic measurements, most likely cause a Kondo-type scattering of electrons at low temperatures, thus, triggering a negative logarithmic behavior for the electrical resistivity (Fig. 10, right). The negative Seebeck coefficient (see Fig. 10) reveals electron transport and is increasing with increasing temperature, after a maximum for 800 K thermopower is decreasing. Due to a very low thermopower the power factor (Fig.11) of TiMn$_{\sim4}$ is low, however it is increasing with increasing temperature almost linearly below 750 K. Above 750 K the increase is much stronger.
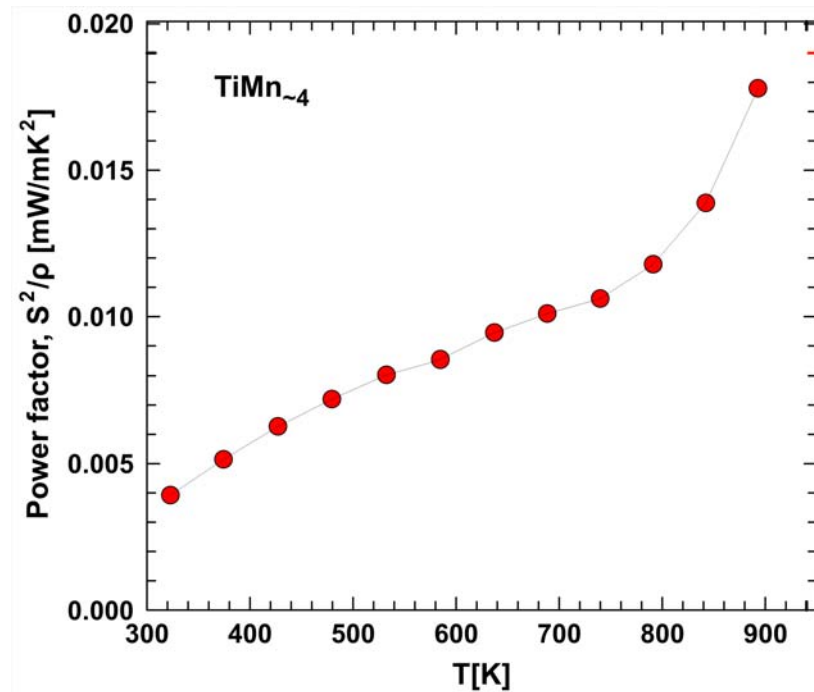

Fig. 11. Power factor of TiMn$_{\sim4}$ versus temperature.

11.4. Conclusion

The Mn-rich part in the Ti-Mn binary phase diagram is revised and considerable homogeneity regions have been defined for TiMn$_{\sim3}$ (from 23.5 to 26 at. % Ti) as well as for TiMn$_{\sim4}$ (from 16.0 to 20 at. % Ti). The crystal structures of Ti$_6$(Ti$_{1-x}$Mn$_x$)$_6$Mn$_{25}$, x = 0.462 and Ti$_8$(Ti$_x$Mn$_{1-x}$)$_6$Mn$_{39}$, x = 0.187 were solved by X-ray single crystal diffraction. Ti$_6$(Ti$_{1-x}$Mn$_x$)$_6$Mn$_{25}$, x = 0.462 (previously labeled as TiMn$_3$) adopts a new structure type made of two consecutive layers of Laves phase MgZn$_2$ type and a combined layer of alternate blocks of MgZn$_2$ type and Zr$_4$Al$_3$ type structure in a ratio of 50:50. The crystal structure of Ti$_8$(Ti$_x$Mn$_{1-x}$)$_6$Mn$_{39}$, x = 0.187

(previously labeled "$TiMn_{\sim4}$") is isotypic with the R-phase of prototype $Cr_{0.16}Mo_{0.38}Co_{0.46}$. Both structures belong to the socalled tetrahedrally close packed structures with interpenetrating Frank-Kasper polyhedra.

Thermal expansion of $Ti_8(Ti_xMn_{1-x})_6Mn_{39}$, $x = 0.187$ ($TiMn_{\sim4}$) shows a linear behavior at temperatures above 180 K revealing a thermal expansion coefficient $\alpha(180\text{-}300 \text{ K}) = 1.4*10^{-5} \text{ K}^{-1}$ and a Debye temperature $\theta_D = 347$ K. Paramagnetism with a susceptibility of $5.6*10^{-6}$ emu/mol, is observed at temperatures above 50 K, whereas a ferromagnetic impurity dominates the susceptibility below 50 K. The upturn of the susceptibility below 50 K is a fingerprint of a small amount of a ferromagnetic impurity. Electrical resistivity shows, most likely, a Kondo-type scattering of electrons at low temperatures. Seebeck coefficient measurements indicate electron transport (n-type). Although the power factor is low, it strongly increases above 750 K.

References:

[1]   T. Matsumura, H. Yukawa, M. Morinaga, J. Alloys Comp. **279**, (1998), p. 192.

[2]   S. Semboshi, N. Masahashi, S. Hanada, Acta Materialia, **49**, (2001), p. 927-935.

[3]   Y. Ji, X. Liu, J. Mi, X. Guo, Z. Li, L. Jiang, and S. Wang, Rare Metals, **29**, (2010), p. 589-592.

[4]   G. Sung, Y.W. Chang and N.J. Kim, Metals and Materials, **1(2)**, (1995), p. 107-115.

[5]   F. Zhang, A. Weidmann, J. B. Nebe, U. Beck, and E. Burkel, Journal of Biomedical Materials Research Part B: Applied Biomaterials, **94B**, (2010), p. 406-413.

[6]   J.L. Murray, Phase Diagrams of Binary Titanium Alloys, ASM International, Materials Park, OH, (1987), p. 159-168.

[7]   V. Ivanchenko, T. Pryadko, MSIT, G. Effenberg, S. Ilyenko (ed.), SpringerMaterials – The Landolt-Börnstein Database, (2008), DOI: 10.1007/978-3-540-78644-3_22.

[8]   R.M. Waterstrat, Trans. Metall. Soc. AIME, **221**, (1961), p. 687-690.

[9]   R.M., B.N. Das and P.A. Beck, Trans. Metall. Soc. AIME, **224**, (1962), p. 512-518.

[10]   Y. Komura, W.G. Sly and D.P. Shoemaker, Acta Cryst., **13**, (1960), p. 575-585.

[11]   N. Saunders, COST 507, Thermochemical Database for Light Metal Alloys, Vol. 2, European Commission, (1998), p. 241-244.

[12] L.Y. Chen, C.H. Li, K. Wang, H.Q. Dong, X.G. Lu and W.Z. Ding, CALPHAD: Computer Coupling of Phase Diagrams and Thermochemistry, **33**, (2009), p. 658-663.

[13] R. Krendelsberger, PhD Thesis, Univ. Vienna, Austria, (1997).

[14] M. Rotter, H. Müller, E. Gratz, M. Doerr, and M. Löewenhaupt, Rev. Sci. Instrum. **69(7)**, (1998), p. 2742.

[15] G. Brändli and R. Griessen, Cryogenics **13**, (1973), p. 299.

[16] J. Genossar and M. Steinitz, Rev. Sci. Instrum. **61**, (1990), p. 2469.

[17] G. Rogl, A. Grytsiv, E. Bauer, P. Rogl, M. Zehetbauer, Intermetallics, **18**, (2010), p. 57-60.

[18] L.M. Gelato, E. Parthé, J. Appl. Crystallogr. **20**, (1987), p. 139-143.

[19] P. Villars, K. Cenzual, Pearson's Crystal Data, Release 20010/11, ASM International, Materials Park, Ohio, USA.

[20] Atta U. Khan, A. Grytsiv, X. Yan, P. Rogl, A. Saccone, V. Pomjakushin and G. Giester, Inorganic Chem. **50**, (2011), p. 4537-4547.

[21] M.M.R. Costa and M.J.M. De Almeida, Portugaliae Physica **17**, (1986), p. 173-180.

[22] Gmelin Handbook of Inorganic and Organometallic Chemistry, Typix, Volume 1, (1993), p. 186.

[23] C.B. Shoemaker and D.P. Shoemaker, Acta Cryst., **B34**, (1978), p. 701-705.

[24] T.B. Massalski (ed.), 2nd Edition, ASM International, Materials Park, Ohio, **3**, (1990), p. 2615-2617.

[25] D.J. Maykuth, H.R. Ogden and R.I. Jaffee, Trans. Am. Inst. Min. Metall. Pet. Eng. **197** (1953), p. 225-230.

[26] G. Rogl, L. Zhang, P. Rogl, A. Grytsiv, M. Falmbigl, D. Rajs, M. Kriegisch, H. Müller, E. Bauer, J. Koppensteiner, W. Schranz, M. Zehetbauer, Z. Henkie, M. Maple, J. Appl. Phys. **107**, (2010), p. 043507.

[27] M. Falmbigl, G. Rogl, P. Rogl, M. Kriegisch, H. Müller, E. Bauer, M. Reinecker, W. Schranz, J. Appl. Phys. **108**, (2010), p. 043529.

[28] G.D. Mukherjee, C. Bansal, A. Chatterjee, Phys. Rev. Lett. **76**(11), (1996), p. 1876.

Summary

Crystal structure and phase relations has been studied in several different system based on X-ray Powder Diffraction (XPD), Neutron Powder Diffraction (NPD), X-ray Single Crystal Diffraction (XSC), Light Optical Microscopy (LOM), Scanning Electron Microscipe (SEM) and Electron Probe Micro-Analyzer (EPMA).

Several problems have been clarified in this work using combined XRD and neutron powder diffraction as well as EPMA analyses. Accurate temperatures were assigned to two four-phase reactions of transition type. The crystal structure of the two compounds in the Al-rich region (τ_5-TiNi$_{2-x}$Al$_5$, x = 0.48) and in the Ti-rich region [τ_6-Ti$_2$(Ti,Ni,Al)$_3$] of the Ti-Ni-Al system has been solved by X-ray single crystal diffraction (XSC) as well as combined refinement of X–ray powder (XPD) and combined with neutron powder diffraction (NPD). All phase relations related to the Ti-rich phase [τ_6-Ti$_2$(Ti,Ni,Al)$_3$] from formation to decomposition are clarified.

The crystal structures of the novel compounds in Mo(Cu$_x$Al$_{1-x}$)$_6$Al$_4$ (x=0.416), ReNi$_2$Al$_{8-x}$ (x = 0.033) and of homologous MoNi$_{2-x}$Al$_{8+x}$ (x = 0.166) and WNi$_{2-x-y}$Al$_{8+x-z}$, (x = 0.162, y = 0.015, z = 0.010) were defined from X-ray single crystal data. A superstructure was observed with formula MoCu$_2$Al$_{8-x}$, x = 0.080, which was defined by Rietveld refinement of X-ray powder diffraction data. A completely ordered structure was observed for ReNi$_2$Al$_{8-x}$ with small defects in the two 4g sites (Al). WNi$_{2-x-y}$Al$_{8+x-z}$ and partial phase equilibria at 930 °C for the Al-rich region of the W-Ni-Al phase diagram were reported.

The crystal structures of three compounds have been solved from X-ray single crystal diffractometry: τ_1-MoPd$_{2-x}$Al$_{8+x}$ (x=0.067; *Pbcm*); τ_7-Zr(Cu$_{1-x}$Al$_x$)$_{12}$ (x = 0.514; *I4/mmm*) and τ_9-ZrCu$_{1-x}$Al$_4$ (x = 0.144; *P4/nmm*). τ_1 and τ_9 crystallize in unique structure types, whereas the structure of τ_7-Zr(Cu$_{1-x}$Al$_x$)$_{12}$ is isotypic with the ThMn$_{12}$ type. Bärnighausen trees have been constructed that connect the structures of Mo(Cu$_x$Al$_{1-x}$)$_6$Al$_4$ and τ_1 and the structures of Cu and τ_9-ZrCu$_{1-x}$Al$_4$. The ZrCu$_{1-x}$Al$_4$ type (n=3) is a part of a series of structures, which appear by simple building principle assembling fcc-Cu-type units in one direction. An isothermal section at 860 °C for the Al-rich part of the Mo-Pd-Al system has been established comprising two ternary compounds, τ_1-MoPd$_{2-x}$Al$_{8+x}$ and τ_2. Vickers hardness (H$_v$) for τ_1 was determined to be 842 ±40 MPa, which is about five times higher than that of pure aluminium.

B site preference is evaluated in a series of structures using X-ray single crystal diffractometry. $Ta_3(Si_{1-x}B_x)$ (x = 0.112) crystallizes with the Ti_3P-type where B randomly share $8g$ site with Si atoms. Ta_5Si_{3-x} (x = 0.08) crystallizes with the Cr_5B_3-type and exhibits a small amount of vacancies on the $4a$ site. $Ta_5(Si_{1-x}B_x)_3$ (x = 0.568; Cr_5B_3-type) is a part of the solid solution of Ta_5Si_3 into the ternary Ta-Si-B system with B replacing Si on the $8h$ site. Neutron powder diffraction (NPD) was employed to find the exact location of B in the crystal structures of $Nb_5(Si_{1-x}B_x)_3$ (x = 0.592; Cr_5B_3-type) and of $Nb_5Si_3B_{1-x}$ (x = 0.292; Ti_5Ga_4-type). In $Nb_5(Si_{1-x}B_x)_3$ B-atoms substitute for Si on the $8h$ site, whereas with B-atoms in $Nb_5Si_3B_{1-x}$ partially fill the octahedral voids in the $2b$ site of the parent Mn_5Si_3-type structure.

Two isothermal section are constructed for the Ta-V-Si system at 1500 °C and 1200 °C revealing three ternary phases: τ_1-$(Ta,V)_5Si_3$ (Mn_5Si_3-type) and the Laves phases τ_2-$Ta(Ta,V,Si)_2$ ($MgZn_2$-type) and τ_3-$Ta(Ta,V,Si)_2$ ($MgCu_2$-type). The crystal structure of the τ_2 was solved by X-ray single crystal diffraction while the crystal structures of τ_1 and τ_3 from X-ray powder diffraction (XPD) data. Although the τ_2-phase does not exist in the binary Ta-V system at 1500 °C, it is present in the ternary system at this temperature. τ_1-$(Ta_xV_{1-x})_5Si_3$ with Mn_5Si_3-type has a large homogeneity range showing the exchange of Ta and V at a constant Si content.

Phase relations in the Ta-V-Ge system have been evaluated and an isothermal section at 1500 °C is established revealing four ternary phases: τ_1-$(Ta,V)_5Ge_3$ (Mn_5Si_3-type), Laves phase τ_2-$Ta(Ta,V,Ge)_2$ ($MgZn_2$-type) and τ_3-$Ta_9V_3Ge_2$ (Nb_9Co_4Ge-type) and τ_4-$(Ta,V)_3Ge$ (unknown structure). Ge stabilizes a ternary C15-phase ($MgCu_2$-type) at 1500 °C, separated from the Ta-V binary. The crystal structures of the three phases τ_1 to τ_3 were solved from X-ray powder diffraction data. A large homogeneity range was observed for the τ_1-$(Ta_xV_{1-x})_5Ge_3$ with Mn_5Si_3-type showing the exchange of Ta and V at a constant Ge content.

The Mn-rich part in the Ti-Mn binary phase diagram is reevaluated and homogeneity regions have been defined for $TiMn_{\sim3}$ (from 23.5 to 26 at. % Ti) as well as for $TiMn_{\sim4}$ (from 16.0 to 20 at. % Ti). The crystal structures of $Ti_6(Ti_{1-x}Mn_x)_6Mn_{25}$, x = 0.462 and $Ti_8(Ti_xMn_{1-x})_6Mn_{39}$, x = 0.187 were solved by X-ray single crystal diffraction (XSC). $Ti_6(Ti_{1-x}Mn_x)_6Mn_{25}$, x = 0.462 (previously labeled as $TiMn_3$) adopts a new structure type made of two consecutive layers of Laves phase $MgZn_2$ type and a layer of alternate blocks of $MgZn_2$ type and Zr_4Al_3 type structure. $Ti_8(Ti_xMn_{1-x})_6Mn_{39}$, x = 0.187 (previously labeled "$TiMn_{\sim4}$") is isotypic with the R-phase of prototype $Cr_{0.16}Mo_{0.38}Co_{0.46}$.

Linear behavior at temperatures above 180 K is observed for $Ti_8(Ti_xMn_{1-x})_6Mn_{39}$, x = 0.187 ($TiMn_{\sim4}$) revealing a thermal expansion coefficient α(180-300 K) = $1.4*10^{-5}$ K^{-1} and a Debye temperature θ_D = 347 K. It reveals Paramagnetism with a susceptibility of $5.6*10^{-6}$ emu/mol at temperatures above 50 K, whereas a ferromagnetic impurity dominates the susceptibility below 50 K. Electrical resistivity shows, most likely, a Kondo-type scattering of electrons at low temperatures. Seebeck coefficient measurements indicate electron transport (n-type) but the power factor is low.

List of publications

1)   "On the four-phase reactions in the Ti-Ni-Al system"

A.U. Khan, X. Yan, P. Rogl and A. Saccone, Intermetallics **17**, (2009), p. 1000-1006.

2)   "Crystal Structure of τ_5-TiNi$_{2-x}$Al$_5$ (x= 0.48) and Isotypic {Zr,Hf}Ni$_{2-x}$Al$_{5-y}$"

Atta U. Khan, J. Bursik, A. Grytsiv, V. Pomjakushin, H. Effenberger and P. Rogl, Intermetallics 19, (2011), p. 1340-1347.

3)   "Phase Relations and Crystal Structure of τ_6-Ti$_2$(Ti$_{0.16}$Ni$_{0.43}$Al$_{0.41}$)$_3$"

Atta U. Khan, A. Grytsiv, X. Yan, P. Rogl, A. Saccone, V. Pomjakushin and G. Giester, Inorganic Chemistry **50**, (2011), p. 4537-4547.

4)   "Crystal structures and hardness of novel compounds: hexagonal Mo(Cu$_x$Al$_{1-x}$)$_6$Al$_4$, MoCu$_2$Al$_{8-x}$ and orthorhombic {Mo,W,Re}Ni$_{2-x}$Al$_{8+x}$"

Atta U. Khan, A. Grytsiv, P. Rogl and G. Giester, submitted to Intermetallics, (2011).

5)   "Crystal structure of novel compounds in the systems Zr-Cu-Al, Mo-Pd-Al and partial phase equilibria in the Mo-Pd-Al system"

Atta U. Khan, P. Rogl and G. Giester, submitted to Dalton Transactions, (2011).

6)   "Boron site preference in ternary Ta and Nb boron silicides"

Atta U. Khan, Carlos A. Nunes, Gilberto Carvalho Coelho, Paulo Atsushi Suzuki, Andriy Grytsiv, Francoise Bourreé, Gerald Giester and Peter Rogl, submitted to J. Solid State Chem., (2011).

7)   "The system Ta-V-Si: Crystal structure, phase equilibria, first principle calculations and thermodynamic modeling"

A. U. Khan, P. Broz, H. Niu, J. Bursik, A. Grytsiv, X.-Q. Chen, G. Giester and P. Rogl, submitted to J. Solid State Chem., (2011).

8)   "Phase relations and crystal structures in the system Ta-V-Ge"

Atta U. Khan, J. Bursik and P. Rogl, (to be submitted).

9)   "The Mn-rich part of the Ti-Mn binary system: Crystal chemistry and phase equilibria and selected properties"

Atta U. Khan, G. Rogl, M. Kriegisch, H. Michor, E. Bauer, X. Yan, A. Grytsiv, G. Giester, D. Maccio, A. Saccone and P. Rogl, (to be submitted).

Oral presentations

CALPHAD 2009

Calculation of Phase Diagram 2009

Prague, Czech Republic, 17-22 May, 2009.

"**On the four-phase reactions in the Ti-Ni-Al system**"

<u>A.Ullah Khan</u>, X. Yan, A. Grytsiv, P. Rogl, and A. Saccone.

MSE 2010

Materials Science and Engineering 2010

Darmstadt, Germany, 24-26 Aug. 2010

"**τ_6-Ti$_2$(Ti$_{0.22}$Ni$_{0.43}$Al$_{0.35}$)$_3$, a Novel Phase in the Ti-rich part of the phase diagram: crystal structure and phase equilibria**"

<u>Atta Ullah Khan</u>, Xinlin Yan, Andri Grytsiv, Peter Rogl and Adriana Saccone.

TOFA 2010

Thermodynamics Of Alloys 2010

Porto, Portugal, 12-16 Sep, 2010.

"**τ_6-Ti$_2$(Ti$_{0.22}$Ni$_{0.43}$Al$_{0.35}$)$_3$, a novel phase in the Ti-rich part of the phase diagram: crystal structure and phase equilibria**"

<u>Atta Ullah Khan</u>, Xinlin Yan, Andri Grytsiv, Peter Rogl, Adriana Saccone.

MRS 2010

Materials Research Society 2010

Boston, USA, 29Nov-03Dec, 2010.

"Two novel phases in the Ti and Al-rick part of the TiNiAl phase diagram: Phase equilibria and crystal structure"

Atta Ullah Khan, Xinlin Yan, Andri Grytsiv, Peter Rogl, Adriana Saccone, G. Giester.

CALPHAD 2011

Calculation of Phase Diagram 2011

Rio de Janeiro, Brazil, 22-27 May, 2011

"The phase diagram of Ta-V-Si"

Atta Ullah Khan, P. Broz, H. Niu, X. Chen, P. Rogl.

Poster

CALPHAD 2011

Calculation of Phase Diagram 2011

Rio de Janeiro, Brazil, 22-27 May, 2011

"The study of Z-phase in Ternary Cr-Nb-N and Cr-V-N systems"

Kroupa Ales, Legut Dominik, Zemanova Adela, Khan Atta Ullah.

CURRICULUM VITAE

Name: Atta Ullah Khan

Father's Name: Muhammad Manzoor

Nationality: Pakistan

Religion: Islam

Date of birth: 28-12-1983

CURRICULAR:

2006.03-2007-12: Shift Engineer (Dyeing Department), Sapphire Textile Mills, 3.5 Kil., Raiwind Manga Road, Kasoor, Pakistan.

2005: Master of Science (M. Sc), Chemistry, University of Punjab, Lahore, Pakistan.

2003: Bachelor of Science (B.Sc), University of Punjab, Pakistan.

2001: Millat College, Jhang, Pakistan.

1998: Secondary School Certificate, Govt. High School Haveli Lal, Pakistan.

Awards

Award for Ph. D studies Abroad (Austria), Higher Education Commission of Pakistan.